Robust orbit control for proximity operations around asteroids

Luigi Serra

Delft University of Technology

TU Delft

Robust orbit control for proximity operations around asteroids

by

Luigi Serra

to obtain the degree of Master of Science in Aerospace
Engineering at Delft University of Technology,
to be defended publicly on Friday, December 13, 2024, at 14:00.

Student number:	5863147	
Project Duration:	March, 2024 - December, 2024	
Thesis Committee:	Prof.dr. L.L.A. Vermeersen,	TU Delft, Chair
	Dr. ir. E. Mooij,	TU Delft, Supervisor
	Dr. ir. E. Smeur,	TU Delft, Independent examiner
Faculty:	Faculty of Aerospace Engineering, Delft	

Cover: Eros as seen by NEAR, courtesy of NASA.
Style: TU Delft Report Style, with modifications by Daan Zwaneveld

TU Delft

Preface

This thesis marks the conclusion of my five-year academic journey in Aerospace Engineering—a journey that has taken me from Italy to the Netherlands, with a stop in Germany. While it has been a path filled with challenges and difficult moments, it has also been deeply rewarding and fulfilling.

Firstly, I would like to express my deepest gratitude to my supervisor, Dr. Ir. Erwin Mooij, for his guidance throughout this project. His weekly availability, insightful feedback, and positive attitude were invaluable in helping me navigate the complexities of this work and motivating me to tackle the challenges with confidence.

My most heartfelt thank you goes to my parents and grandparents, whose constant support and encouragement have been essential throughout this journey. Their understanding and reassurance made it easier for me to pursue my goals away from home.

I am also profoundly grateful to a group of special people who made my time in Delft truly extraordinary. Francesco, Giacomo, Giuseppe, João, Ludovica, and Riccardo — your friendship turned the last nine months in the Netherlands into some of the most memorable of my life. You are the reason why leaving TU Delft will be so bittersweet. A special mention goes to Jacopo, a dear friend with whom I shared the daily challenges of this thesis journey, despite the physical distance.

Lastly, to the flatmates of Poppesteeg 1D, both past and present, thank you for making our shared home a place of laughter, unforgettable memories, and, most importantly, great food.

Luigi Serra
Delft, November 2024

Summary

Proximity operations around asteroids are currently at the forefront of space research and industry due to their strategic and scientific relevance. These small bodies have been orbiting the Sun since the very formation of the Solar System, thus collecting precious information on its origin and holding valuable materials that could be exploited by humans. By now, there have been more than five space missions that have successfully performed close proximity operations with a Near Earth object. However, all these missions heavily relied on frequent support from the ground segment, thus demanding a very cautious and slow approach. This type of mission architecture is not only very expensive but also likely to become unfeasible in the future due to the increasing demand for space monitoring. Consequently, the scientific community has been working to develop mission architectures with increasingly higher degrees of autonomy.

In this regard, the problem of orbiting around an asteroid without support from the ground represents a significant challenge. Nonetheless, most orbit control literature focuses on planetary applications, with limited attention given to the safe maintenance of orbits around asteroids. While planetary scenarios are also affected by uncertainties and perturbations, the solar and gravitational perturbations that characterize the asteroid environment create the most perturbed dynamical conditions of the Solar System. As a consequence, certain regions of space are characterized by unstable motion which can quickly deteriorate in an impact or escape trajectory. Developing a robust orbit control system thus represents a key step in evolving the current mission architecture to a more autonomous status.

This research aims to design a functional orbit control system that is able to guarantee safe station-keeping on highly perturbed orbits while proving robust against injection, navigation, and execution errors. A key requirement considered throughout this work is ensuring that the designed system allows for sufficiently long time windows during which the spacecraft is coasting, and thus capable of performing science operations. By using a linear sliding surface and a first-order reaching law, a sliding mode controller is used to generate a continuous control law that is exploited to perform impulsive orbit maintenance maneuvers through an adequate thrust quantization logic. To increase the efficiency of the orbit control system, the conventional two-satellite formation control approach used in the orbit control literature to generate the reference trajectory is overcome by a line-of-sight tracking mode, which allows to remove time parametrization from the target orbit by adaptively changing the reference state based on the closest point to the spacecraft position. The designed system proves capable of maintaining the spacecraft within the desired distance from the asteroid and inclination from the Sun-terminator plane, allowing it to reach altitudes as low as 2 km from Eros's surface, provided that the onboard computer receives an update on the spacecraft's state once every 5 minutes.

Robust Design principles are then applied to improve the performance of the system and investigate how it is affected by the choice of the target orbit and the environment model used for onboard dynamics propagation. Results show that for low-altitude orbits, inclination can have a major impact on all performance parameters, with equatorial, prograde orbits requiring the highest station-keeping cost due to the frequent encounters with Eros's lobes. It is also found that the use of a triaxial ellipsoid gravity model or a spherical harmonic expansion limited to C_{20} and C_{22} coefficients is able to significantly increase the robustness of the system to navigation errors, leading to successful simulations even when the update measurement frequency is increased to 2 hours.

Recommendations for future work include the integration of the developed simulator with both attitude control and a navigation filter. The latter could be used to improve the knowledge of the environment and thus improve the efficiency of the control system.

Contents

Nomenclature

List of acronyms

Acronym	Definition
ACAF	Asteroid-centered asteroid-fixed
ACI	Asteroid-centered inertial
ACOF	Asteroid-centered orbit-fixed
ADCS	Attitude Determination and Control System
ANOVA	Analysis of variance
AOCS	Attitude and Orbit Control System
ATE	Asteroid true equator
CKBO	Classical Kuiper belt object
CPU	Central processing unit
DSN	Deep Space Network
D/O	Degree and order
DOE	Design of experiments
DOF	Degree of freedom
EH	Ellipsoidal harmonics
EHE	Ellipsoidal harmonic expansion
EKF	Extended Kalman filter
ESA	European Space Agency
FD	Factorial design
FFD	Fractional factorial design
GCP-NAV	Guidance control points navigation
GEO	Geosynchronous equatorial orbit
GNC	Guidance Navigation and Control
GNSS	Global navigation satellite system
GPS	Global positioning system
GRACE	Gravity Recovery and Climate Experiment
GRADS	Generic Rendezvous and Docking Simulator
GVE	Gauss variational equations
HPNAV	Home position navigation
IKF	Iterative Kalman filter
IMU	Inertial measurement unit
JAXA	Japan Aerospace eXploration Agency
JPL	Jet Propulsion Laboratory
LAMO	Low-altitude mapping orbit
LEO	Low Earth orbit
LOS	Line of sight
LQG	Linear quadratic Gaussian
LQR	Linear quadratic regulator
LTI	Linear time-invariant
MC	Monte Carlo
MEE	Modified equinoctial elements
MIMO	Multi-input multi-output

Acronym	Definition
MSI	Multi spectral imager
MOID	Minimum orbit intersection distance
MPC	Model predictive control
NASA	National Aeronautics and Space Administration
NEA	Near-Earth asteroid
NEAR	Near Earth Asteroid Rendezvous
NEO	Near-Earth object
NLR	Near laser rangefinder
OCM	Orbit correction maneuver
OCK	Orbit control kit
OH	Oblate harmonics
OIM	Orbit insertion maneuver
OMM	Orbit maintenance maneuver
OSIRIS-REx	Origins, Spectral Interpretation, Resource Identification, and Security – Regolith Explorer
PDS	Planetary Data System
PH	Prolate harmonics
PHA	Potentially hazardous object
PID	Proportional-integral-derivative
QP	Quadratic programming
RAAN	Right ascension of the ascending node
RCS	Reaction control system
RK4	Runge-Kutta 4
RLQR	Robust linear quadratic regulator
RMS	Root mean square
RSQ	Research sub-question
RTN	Radial-transverse-normal
SBN	Small Bodies Node
SDO	Scattered disk object
SH	Spherical harmonics
SHE	Spherical harmonic expansion
SISO	Single-input single-output
SMC	Sliding mode control
S/N	Signal-to-noise
SOI	Sphere of influence
SOSC	Second-order sliding mode control
SPOS	Sun plane-of-sky
SRP	Solar radiation pressure
SSSB	Small Solar System bodies
SSTL	Surrey Satellite Technology Limited
STM	State transition matrix
TAG	Touch-and-go
TCM	Trajectory correction maneuver
TPA	Target point approach
TNO	Trans-Neptunian object
TUDAT	TU Delft Astrodynamics Toolbox
TVBL	Time-varying boundary layer
UAV	Unmanned aerial vehicle
UKF	Unscented Kalman filter
WP	Work package

Acronym	Definition
WBS	Work breakdown structure
YORP	Yarkovsky–O'Keefe–Radzievskii–Paddack

Symbols

Symbol	Definition	Unit
a	Semi-major axis	[m]
$\boldsymbol{a}$	Acceleration vector	[m/s^2]
$\boldsymbol{a}_d$	Target acceleration vector	[m/s^2]
$\boldsymbol{a}_g$	Gravity acceleration	[m/s^2]
$\boldsymbol{a}_{g,ns}$	Non-spherical component of the gravity acceleration	[m/s^2]
$\boldsymbol{a}_{g,pm}$	Gravity acceleration due to point mass	[m/s^2]
$\boldsymbol{a}_{SRP}$	Solar radiation pressure acceleration	[m/s^2]
$\boldsymbol{a}_T$	Thrust acceleration	[m/s^2]
$\boldsymbol{a}_{3BP}$	Third-body gravity acceleration	[m/s^2]
A	Spacecraft reference surface	[m^2]
c	Speed of light	[m/s]
C_r	Reflectance of the spacecraft surface	[-]
C_{20}	Oblateness coefficient	[-]
C_{22}	Ellipticity coefficient	[-]
$\boldsymbol{C}$	Rotation matrix	[-]
e	Eccentricity	[-]
$\boldsymbol{e}$	Eccentricity vector	[-]
E	Eccentric anomaly	[rad]
$\boldsymbol{E}_e$	Edge dyad	[-]
$\boldsymbol{F}$	Force vector	[N]
$\boldsymbol{F}_f$	Face dyad	[-]
g_0	Earth gravitational acceleration on the surface	[m/s^2]
G	Gravitational constant	[Nm^2/kg^2]
h	Specific angular momentum (per unit of mass)	[m^2/s]
$\boldsymbol{h}$	Specific angular momentum vector	[m^2/s]
i	Inclination	[rad]
I_{sp}	Specific impulse	[s]
L_e	Edge potential	[-]
m	Spacecraft mass	[kg]
M	Celestial body mass	[kg]
P_{nm}	Associated Legendre functions of the first kind	[-]
q_a	Aphelion	[m]
q_p	Perihelion	[m]
r	Distance	[m]
r_H	Radius of the sphere of Hill	[m]
r_{SOI}	Radius of the sphere of influence	[m]
$\boldsymbol{r}$	Position vector of the spacecraft	[m]
$\boldsymbol{r}_d$	Target position vector	[m]
$\boldsymbol{r}_\odot$	Position vector of the Sun	[m]
R_e	Equatorial radius	[m]
$\boldsymbol{s}$	Sliding surface	[m/s]
t	Time	[s]

Symbol	Definition	Unit
T	Orbital period	[s]
T_{obs}	Coasting time	[s]
T_s	Onboard computer frequency	[Hz]
$\boldsymbol{T}$	Thrust vector	[N]
$\boldsymbol{u}$	Control vector	[m/s^2]
v	Speed	[m/s]
$\boldsymbol{v}$	Velocity vector of the spacecraft	[m/s]
$\boldsymbol{v}_d$	Target velocity vector	[m/s]
V	Volume	[m^3]
W	Prime meridian	[rad]
α	Pole right ascension	[rad]
β	Solar phase angle	[rad]
δ	Pole declination	[rad]
Δt	Integration time step	[s]
ΔV	Delta-v	[m/s]
η	Signal-to-noise ratio	[dB]
θ	True anomaly	[rad]
λ	Longitude	[rad]
$\tilde{\lambda}$	Co-rotating longitude	[rad]
μ	Gravitational parameter	[m^3/s^2]
$\mu_\odot$	Gravitational parameter of the Sun	[m^3/s^2]
ν	True longitude	[rad]
ρ	Density	[kg/m^3]
σ	Standard deviation	[-]
ϕ	Latitude	[rad]
Φ	Boundary layer width	[-]
ψ_0	Solar constant	[W/m^2]
$\boldsymbol{\Psi}$	State transition matrix	[-]
ω	Longitude of the periapsis	[rad]
ω_A	Angular velocity of the asteroid	[rad/s]
ω_f	Solid angle	[sr]
Ω	Right ascension of the ascending node	[rad]

1

Introduction

Centuries-old knowledge about the small celestial bodies orbiting our Solar System has been documented. In 1680, the first comet was discovered by the German astronomer Gottfried Kirch, and approximately 120 years later Giuseppe Piazzi identified the first asteroid, Ceres, although at the time it was mistakenly considered to be the eighth planet. Despite the perception that a potential collision threat between Earth and one of these bodies might appear as a recent phenomenon, in 1799 Pierre-Simon Laplace wrote:

> *However, the small probability of a similar encounter [of the Earth with a comet], can become very great in adding up over a huge sequence of centuries. It is easy to picture to oneself the effects of this impact upon the Earth. The axis and the motion of rotation changed; the seas abandoning their old position to throw themselves toward the new equator; a large part of men and animals drowned in this universal deluge, or destroyed by the violent tremor imparted to the terrestrial globe.*

thus proving that awareness about the catastrophic impact that such an event would cause was already present in the scientific community at the time.

1.1 Scientific and strategic interest in asteroids

By 2024, approximately 1.3 million asteroids and more than 3800 comets have been discovered and identified [1]. A fraction of these bodies follow perturbed trajectories around the Sun that cross the orbits of Earth and other planets, making the likelihood of an impact hazard very real, regardless of how small it may be (Hall and Ross, 1997). One of the first studies explicitly dealing with this matter dates back to 1941, when Fletcher Watson published an estimate of the rate of impacts on the Earth, based on the discovery of the first three Earth-approaching asteroids (Apollo, Adonis, and Hermes). Nevertheless, it was not until 1980 that the matter gained public relevance with the publication of a study by Alvarez et al. (1980). In this work, the authors provided substantial evidence suggesting that the impact of an asteroid on Earth could have led to large-scale extinctions, effectively ending the age of dinosaurs. Widespread interest in both the scientific and political world followed this publication, which culminated in 1991 with the near-Earth object (NEO) Interception Workshop, organized upon request of the U.S. Congress and sponsored by NASA (National Aeronautics and Space Administration). The proceedings from this workshop recommended that in addition to *deflection missions*, aimed at diverting or destroying threatening asteroids, also *exploratory missions* should be considered to investigate these bodies and determine their physical properties (Morrison, 1992).

Indeed, the interest in asteroids and comets does not arise exclusively from the evaluation of mitigation strategies for protecting Earth, but also from the large scientific value that these bodies hold. In fact, the

[1] `https://science.nasa.gov/asteroids-comets-meteors/`, accessed on 20/03/2024

transformation processes that have radically altered the composition and internal structure of the planets and their moons did not affect the small bodies. As a result, they have remained virtually unprocessed since their formation from the solar protodisk, thereby representing fully-fledged *fossils* of the Solar System (Cui and Qiao, 2014). It follows that the study of their composition and motion can provide crucial information for improving our understanding of the Solar System's evolution and the processes that led to its formation. Specifically, their investigation could provide additional information to address questions regarding planetary formation, delivery of water and organics to the early Earth, as well as the emergence of life (Ieva et al., 2020). Moreover, data collected at asteroids is generally beneficial to our understanding of how these bodies could impact Earth, as it improves our ability to predict their ephemerides in the long term (Beshore et al., 2015).

In addition to planetary defense and scientific relevance, a third major reason of interest in these bodies has gradually developed in parallel: asteroid mining. The idea of extracting useful resources from asteroids was originally proposed in the 20th century by Konstantin Tsiolkovsky (Calla et al., 2019). In particular, starting from the 1970s, the wave of enthusiasm generated by the Moon landing combined with growing concerns about the over-exploitation of Earth's natural resources led the science community to take this seriously into consideration. As a matter of fact, approximately 5% of the near-Earth asteroids (NEAs) represent the most readily accessible extraterrestrial bodies for exploration by spacecraft (National Research Council, 1998; Scheeres, 2012c), and the likely abundant presence of substances such as water, metals, semiconductors, and even exotic materials could make the endeavor economically feasible.

1.2 Technical challenges in asteroid exploration

Given the three main reasons of interest outlined in the previous section, it is clear that proximity operations around asteroids are a highly relevant topic in today's space industry, with more than five space missions successfully achieving orbit around small bodies to date. During these missions, scientific operations were possible only after an extensive, local characterization phase (Calla et al., 2019). In fact, the most significant technical challenges of small bodies exploration emerge once close proximity operations are considered, as the asteroid environment can arguably be regarded as the most strongly perturbed location of the Solar System (Scheeres, 2014). This environment is particularly perturbed due to a variety of factors, including the irregular shape and mass distribution of the asteroid, a weak and non-homogeneous gravity field, and strong solar perturbations from both gravity and radiation pressure. The superposition of these effects can lead to complex, non-periodic orbital trajectories, whose stability is bounded to a limited range of latitudes and distances from the asteroid (Lara and Scheeres, 2002). The highly perturbed gravity field that characterizes this environment can thus be regarded as a double-edged sword: on one side, it significantly reduces the propulsive effort required to perform the desired maneuvers; on the other, it increases the sensitivity to external perturbations and modeling inaccuracies, thereby emphasizing the consequences of any other force acting on the spacecraft. Ultimately, this results in the possibility that the spacecraft may either escape from a bounded orbit or be captured by the asteroid starting from a hyperbolic trajectory (Scheeres et al., 1996), hence the need for very tight and challenging navigation requirements. In parallel, the a-priori knowledge about small bodies is inherently limited by their size and distance from Earth, as observations through ground-based telescopes can only constrain the asteroid's size and mass with less than 100% and 2000% errors, respectively (Takahashi and Scheeres, 2021). As a consequence, it is very challenging to predict the motion of the spacecraft with sufficient accuracy, and a long reconnaissance phase is needed to guarantee safety later during operations.

Nonetheless, the characterization of the asteroid environment *in loco* is generally a time-consuming and expensive operation. In fact, the long Earth-asteroid distance implies that a signal can require up to 40 minutes to execute a round-trip between the ground station on Earth and the spacecraft (Ono et al., 2020), ultimately resulting in a delay of several months between the spacecraft's arrival and the actual beginning of operations (Khoroshylov and Redka, 2021). During this time, the spacecraft is kept relatively far

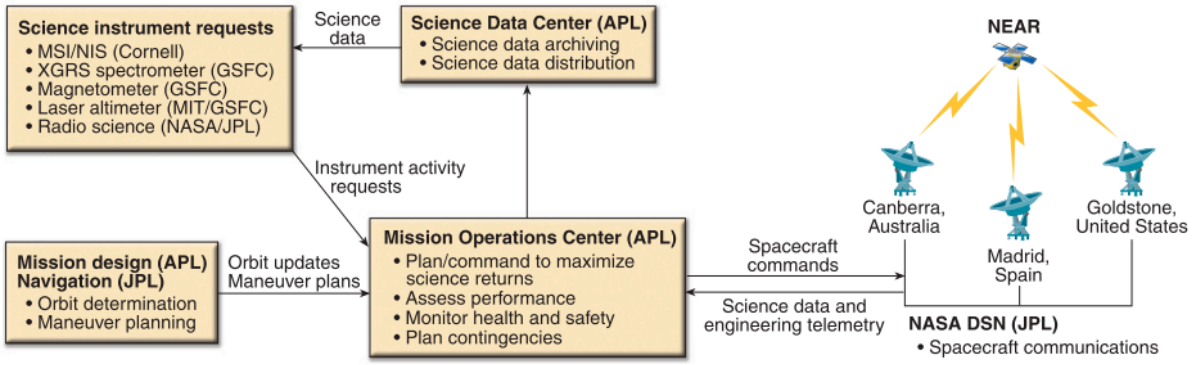

Figure 1.1: Representative workflow between the spacecraft and the ground for an asteroid mission (Holdridge, 2002).

from the asteroid to ensure safety, while navigation data is processed by operators on the ground to build accurate models of the asteroid environment and plan correction maneuvers. As summarized in Fig. 1.1, the nominal mission approach largely relies on ground-based systems that process the radiometric tracking data collected via the Deep Space Network (DSN), and combine it with local observations performed by the spacecraft sensors and instruments. This is operationally complex, and will gradually become less feasible in the future as ground segments are saturated by the increasing number of satellites in orbit and more scheduling conflicts with other space missions arise. Moreover, it is inherently slow-paced, as the communication gaps determined by DSN availability and/or Earth occultation imply that spacecraft must wait long periods before receiving navigation, shape, and gravity estimation solutions, ultimately dictating a very cautious approach to the mission that can mitigate the risks associated with the lack of real-time control of the spacecraft. Finally, it is also extremely expensive: according to NASA's Mission Operations and Communications Services[2], using a 70m antenna 10 hours a day for four consecutive weeks should cost between 2.5 and 3 million dollars [3], on top of which one has to consider all the costs related to the personnel. Furthermore, mission designers need to take into account the evolving characterization of the asteroid's environment, which inevitably leads to the need to re-plan orbital maneuvers multiple times.

1.3 Problem statement

From the previous section, it follows that there is great interest in research to evolve the traditional architecture used for asteroid missions, which heavily relies on human intervention, to a fully autonomous status that is not reliant on ground-based measurements. The capacity of a spacecraft to successfully execute close proximity operations in autonomy ultimately depends on the design of the Guidance, Navigation, and Control (GNC) subsystem. Specifically, autonomous navigation shall enable the spacecraft to estimate its relative state and characterize the environment by observing the asteroid from multiple orbits exhibiting a wide range of inclinations and radii. In parallel, autonomous orbit control shall compute in real-time the commands required to maintain the spacecraft on these orbits and transfer from one to the other according to a predefined mission plan. Ideally, the existence of specific orbital regimes that prove to be stable against perturbations has been widely proven in the literature. In practice, the uncertainty and sensitivity of the environment imply that it is not practical to entirely rely on these open-loop solutions, thus demanding active, closed-loop orbit control.

The overall interest in making orbital operations autonomous dates back to the 1990s, with the first flight demonstration of a fully autonomous, onboard orbit control system on the Surrey Satellite Technology

[2] `https://deepspace.jpl.nasa.gov/files/NASA_MO&CS.pdf`

[3] Data extracted using the cost algorithm tool that can be downloaded from `http://deepspace.jpl.nasa.gov/advmiss`.

Limited (SSTL) UoSAT-12 spacecraft (Wertz, 2003). Since then, the problem has been widely investigated in the context of Earth applications, and later also for libration point orbits (Shirobokov et al., 2017). However, these applications differ very much from the unique dynamical and operational conditions encountered within the proximity of an asteroid. Such conditions raise specific challenges to be solved and demand for new, innovative solutions. Based on these considerations, the research objective of this thesis is to *design a robust, autonomous orbit control strategy that can ensure safe operations in an uncertain, strongly perturbed environment*. The research question that will drive this thesis is stated hereafter:

Research Question

How can autonomous orbit control guarantee safe station-keeping around an irregularly shaped asteroid in the presence of uncertainties and perturbations?

Four research sub-questions (RSQ) which clarify the scope of the project and help address the main research question have also been identified:

RSQ-1: What is a robust control scheme that can maintain a spacecraft close to a reference orbit through impulsive commands?

RSQ-2: How is the orbit control performance affected by the orbital parameters of the target orbit?

RSQ-3: How can we generate a reference trajectory that improves the efficiency of the orbit control system?

RSQ-4: How do navigation errors and onboard environment modeling affect the performance of the orbit control system?

As a final note, it is anticipated that within this work, the expressions *orbit maintenance* and *station-keeping* are considered identical, although it is acknowledged that the former is typically used for orbit control applied to Low Earth Orbits (LEOs), whereas the latter is preferred for geosynchronous equatorial orbit (GEO) applications (Tavakoli and Assadian, 2014).

1.4 Report outline

This report is divided into 8 chapters including the introduction:

Mission heritage
Chapter 2 presents the context of asteroid missions. A concise overview of small Solar System bodies (SSSB) and their main features is given, followed by an excursus of the most relevant asteroid missions and the corresponding strategies used for navigation and guidance. A summary of the current research status for autonomous orbit control around asteroids is also given. The chapter concludes with the definition of a mission that will be used as a case study during this research, thereby identifying a target asteroid, a reference vehicle, and the mission and system requirements.

Flight dynamics
Chapter 3 outlines the dynamical model that describes the asteroid environment. Reference frames, coordinate systems, and transformations are first introduced. Subsequently, the mathematical models that describe the forces acting within the asteroid environment are presented, followed by a concise overview of how these perturbations affect the dynamics of a vehicle. The chapter concludes by stating the equations of motion.

Nonlinear control
Chapter 4 describes the theoretical background of nonlinear control theory for systems affected by uncertainties and disturbances. A comparative overview of methods taken from the field of orbit control

is given, followed by a trade-off analysis. The chapter concludes by illustrating the mathematical background of sliding mode control and the target point approach.

Simulator design and verification
Chapter 5 presents the software architecture of the simulator, focusing first on the high-level blocks, and then highlighting lower-level components. A verification plan is presented, and the results of the most relevant tests are reported.

Orbit control
Chapter 6 describes the design of the orbit control scheme. The formulation of the controllers is introduced, followed by the description of the approach used to generate a reference trajectory. The problem is analyzed first in continuous form, then a quantization logic is employed to achieve impulsive control. The chapter concludes by performing Monte Carlo simulations for given station-keeping and transfer scenarios.

Robust analysis and design
Chapter 7 contains the results obtained by applying robust design principles to the orbit control algorithm outlined in the previous chapter. Control parameters are refined, and performance comparisons are reported. The same methodology is applied to investigate how the orbit control system is affected by the type of orbit and the onboard environment model. Subsequently, the designed control scheme is also applied to perform station-keeping around two additional asteroids. Finally, a comparison with the target point approach is provided.

Conclusions and recommendations
Chapter 8 presents the conclusions of this work together with a series of recommendations for future research.

Appendices
This work is concluded by three appendices. Appendix A outlines the research plan that was used to structure the thesis for the allocated timeframe, along with the adjustments made during its execution. Appendix B illustrates the implementation of the triaxial ellipsoid gravity field model using Carlson's algorithms to compute elliptic integrals. Finally, Appendix C contains the structure and interaction table for the L27 orthogonal array.

2

Mission heritage

The close exploration of small celestial bodies began only in the 1990s, despite the interest in asteroids and comets being high since the beginning of the second half of 20th century, and rendezvous missions to NEAs being proposed as early as 1963 (Ohman, 1963). In fact, the cost that was envisioned at the time for such missions was not lower than half a billion dollars, too much considering the already ongoing Apollo program (Dunham et al., 2002b). Therefore, approximately 40 years had to pass before the first mission to ever orbit and land on an asteroid was accomplished: in 1996 the Near Earth Asteroid Rendezvous (NEAR) spacecraft was launched, and after four years of interplanetary cruise it became the first vehicle to orbit and land on an asteroid. In the following 25 years, multiple other missions were successfully operated with increasingly complex operations, involving touch-and-go (TAG) maneuvers, soft landing, and even sample return.

This chapter seeks to establish the overall context within which this thesis is situated. Section 2.1 outlines the definitions, classifications, and properties of small Solar System bodies to explain how asteroids collocate in the Solar System population. Section 2.2 presents a comprehensive overview of previous space missions to asteroids, with a focus on mission design and GNC strategies. In Sec. 2.3, a concise overview of the current research status on the topics inherent to this thesis is given. Finally, Sec. 2.4 concludes the chapter by defining a reference mission, which includes a detailed description of the target asteroid, spacecraft, and system requirements.

2.1 Small Solar System bodies

According to the International Astronomical Union (IAU), asteroids belong to the category of small Solar System bodies, which are defined as irregularly shaped, rocky bodies orbiting the Sun that do not qualify as a planet, a dwarf planet, or a natural satellite. According to the definition given by the IAU, a natural body needs to satisfy the following three criteria to be considered as a planet[1]:

1. It is in orbit around the Sun.
2. It has sufficient mass for its self-gravity to overcome rigid body forces so that it assumes a hydrostatic equilibrium (a nearly round shape).
3. It has cleared the neighborhood around its orbit from smaller celestial bodies.

The convention established by the IAU also states that a dwarf planet adheres to the first two criteria, but not the third. SSSBs include also comets, trojans, centaurs, and the trans-Neptunian objects (with the exception of Pluto, Eris, Haumea, and Makemake, which are dwarf planets).

[1] `https://www.iau.org/public/themes/pluto/`, accessed on 29/03/2024

2.1.1 Classification

Small bodies can be classified based on several criteria. One of these is the orbital niche in which they are located:

- **Main asteroid belt**: located between the orbits of Mars and Jupiter, it is where most of the known asteroids reside. This group is strongly affected by the gravity of Jupiter, which is the reason why there are evident gaps in the bodies' distribution across the belt. These are known as Kirkwood gaps and coincide with resonance locations with Jupiter. Here, the cumulative gravitational influence of the gas giant forces asteroids' eccentricities to values high enough to cross (and impact) the orbits of rocky planets or to be ejected toward interstellar space.
- **Near-Earth objects**: all asteroids and comets that have perihelia inside 1.3 au, and thus represent a special observed because of the danger they pose to Earth. The majority of this category is occupied by the Near Earth Asteroids. These bodies are inevitably bound to be ejected into interstellar space or be thermally eroded by the Sun (and in a smaller percentage, to collide with planets and moons), hence their dynamical lifetime is relatively short (less than 10^7 years). However, the NEO population is constantly being replenished from multiple sources, the most relevant being the Kirkwood gaps.
- **Trojans**: asteroids located near Jupiter's L_4 and L_5 triangular Lagrangian points. It is thought that also Neptune may hold a considerable population of asteroids at its Lagrangian points, but because of their faintness, only nine are known.
- **Trans-Neptunian objects** (TNOs): small bodies whose orbits lie entirely, or in part, beyond the distance of Neptune. They represent the largest percentage of small bodies within the Solar System and include the dwarf planet Pluto. Half of the known TNOs are classical Kuiper Belt Objects (CKBOs), which travel on low-eccentricity orbits exterior to Neptune. A second group of TNOs is referred to as scattered disk objects (SDOs), which include small bodies traveling on high-eccentricity, non-resonant orbits with perihelia beyond the orbit of Neptune.
- **Centaurs**: located between the orbits of Jupiter and Neptune, they travel on highly inclined and/or eccentric orbits. They reside in chaotic, planet-crossing orbits, suggesting that they originated among TNOs, especially from the population of SDOs.

NEOs are the most inexpensive bodies to rendezvous with as a class due to their proximity to Earth (Scheeres, 2012b). For the same reason, they represent the group of bodies with the highest probability of impacting our planet, thus justifying the large interest in their exploration. In particular, NEAs are divided into four groups[2] based on their perihelion (q_p), aphelion (q_a) and their semi-major axes (a), as shown in Table 2.1.

Only Atens and Apollos are Earth-crossing asteroids, and when their minimum orbit intersection distance (MOID) with the Earth is less than 0.05 au they are referred to as potentially hazardous asteroids (PHAs). As of January 2024, 2396 of the 34143 known NEAs have a trajectory and a size sufficient to be classified as potentially hazardous.

Table 2.1: NEAs classification.

Group	Perihelion [au]	Aphelion [au]	Semi-major axis [au]
Amors	$1.017 < q_p < 1.3$	-	$a > 1.0$
Apollos	$q_p < 1.017$	-	$a > 1.0$
Atens	-	$q_a > 0.983$	$a < 1.0$
Atiras	-	$q_a < 0.983$	$a < 1.0$

[2] `https://cneos.jpl.nasa.gov/about/neo_groups.html`, accessed on 30/03/2024

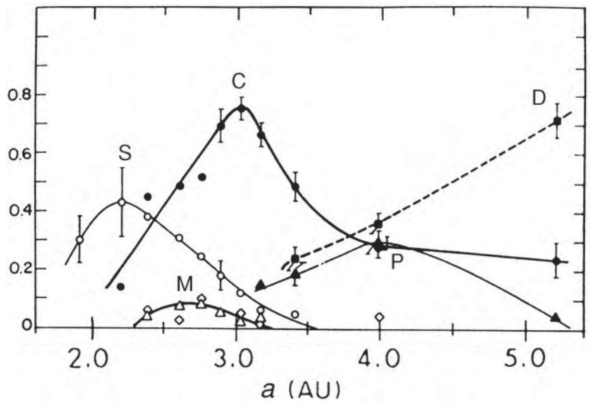

Figure 2.1: Distribution of the asteroid taxonomic classes as a function of distance (Lissauer and de Pater, 2019).

2.1.2 Taxonomy

Studying the composition of asteroids and comets provides a means for investigating the origin of the Solar System. Based on the observation of the albedos and reflectance spectra of asteroids, spectroscopy allows to classify these bodies among three main taxonomic classes:

- **C-type**: carbonaceous asteroids, the largest fraction of the known asteroids (roughly 40%). They are dark bodies that appear to be low-temperature condensates and occupy mainly the outer belt (> 2.7 au).
- **S-type**: stony asteroids, mainly composed of silicates and present in the inner-central belt. They are fairly bright and have a reddish appearance due to the content of iron and nickel. They represent the second largest class of cataloged asteroids (30-35%).
- **M-type**: Stony-iron or iron asteroids, which have undergone a noticeable transformation due to thermal processes.

There is an unquestionable correlation between these taxonomic classes and the spatial distribution of asteroids in the Solar System, as highlighted by Fig. 2.1. This is likely a primordial effect: the distribution in space of these bodies can be used to infer information on the thermo-chemical environment that characterized the solar nebula.

2.2 Missions to asteroids

Missions to asteroids can be distinguished according to the operations that were executed at the location of the small body. A first distinction has to be made between those missions that simply performed an interplanetary flyby, during which the spacecraft distance from the asteroid remains in the order of thousands of km, and those that operated an actual rendezvous by executing an orbit insertion maneuver (OIM). The former, while being essentially fuel-free, can generally provide only limited information on the mass and shape of the small body (Scheeres, 2012b). Instead, rendezvous missions, also referred to as proximity operations missions, allow for a significant scientific return, while entailing higher risks and fuel costs. Intuitively, these operations take place within the Hill's sphere of the asteroid, which is where the balance between the Sun's and the asteroid's gravitational pulls allows for bounded motion. Proximity operations can be classified in the following categories:

- Orbiting, where the spacecraft follows perturbed Keplerian paths around the small body, with orbit sizes varying greatly based on asteroid scale - from a few kilometers (e.g., Bennu) to tens or even hundreds of kilometers (e.g., Eros).
- Slow, sequential hyperbolic flybys, achieving passes over the asteroid at altitudes of a few kilometers, and with very low excess velocities (e.g., Rosetta).

- Hovering, which can be *inertial* or *body-fixed*, depending on whether the spacecraft remains fixed with respect to the rotating asteroid or not.
- Landing, which can entail either proper soft landing (required terminal velocity smaller than 3 m/s (Dunham et al., 2002a)) or TAG maneuvers, where the spacecraft descends only to grab a sample and then takes off.

Table 2.2 summarizes the main features of relevant small body missions. While sample collection is likely the most sought-after goal of any mission, it must be preceded by thorough environmental characterization to ensure operational safety near the asteroid. This phase typically involves either orbiting the body or hovering over a fixed location, sometimes complemented by slow hyperbolic flybys to gather additional data.

A comprehensive summary of the asteroid missions that achieved closed orbits around asteroids is included hereafter, with the addition of Hayabusa missions. Considerations are raised about the specific challenges that these missions had to deal with, and how they affected the navigation and guidance systems. An overview of the mission design is given to enhance the understanding of how navigation and scientific requirements drive the orbital profile. First, a short comparison between the orbiting and hovering approach is provided.

2.2.1 Orbiting and Hovering

In the majority of space missions that performed proximity operations with asteroids, controlled motion was achieved by orbiting the body at various distances and inclinations. However, scientific exploration of small bodies can be - in some cases - simplified by adopting a hovering approach. In this scenario, the spacecraft maintains fixed its position relative to the asteroid either with respect to the asteroid-Sun reference frame (*near-inertial* hovering) or with respect to the asteroid-fixed rotating frame (*body-fixed* hovering). This quasi-stationary position is guaranteed by regular thruster firings which compensate

Table 2.2: Summary of missions to Small Solar System bodies. Missions that failed, are still en route, or only planned are not included.

Mission	Launch	Target	Classification	Approach	Dates
Galileo	1989	Gaspra	Inner AB	Flyby	1991
		Ida	Outer AB	Flyby	1993
NEAR	1996	Mathilde	Middle AB	Flyby	1997
		Eros	NEA (Amor)	Orbiter/Lander	2000-2001
Deep Space 1	1997	Braille	Inner AB	Flyby	1999
Stardust	1999	Annefrank	Inner AB	Flyby	2002
Hayabusa	2003	Itokawa	NEA (Apollo)	Hover/Sampler[b]	2005-2007
Rosetta	2004	Šteins	Inner AB	Flyby	2008
		Lutetia	Inner AB	Flyby	2010
		67P/Churyumov-Gerasimenko	Jupiter-family comet	Orbiter/Lander	2014-2016
Dawn	2007	Vesta	Inner AB	Orbiter	2011-2012
		Ceres[a]	Middle AB	Orbiter	2015
Chang'e-2	2010	Toutatis	NEA (Apollo)	Flyby	2013
Hayabusa 2	2014	Ryugu	NEA (Apollo)	Orbiter/Sampler	2018-2019
OSIRIS-REx	2016	Bennu	NEA (Apollo)	Orbiter/Sampler	2018-2021
DART/LICIACube	2021	Dimorphos	NEA (Apollo)	Impactor	2022

[a] Ceres was reclassified as a dwarf planet in 2006.
[b] Sampler is here used to refer to a spacecraft that executes a TAG maneuver to collect a sample from the body surface.

for both gravitational and, in the case of body-fixed hovering, non-inertial accelerations. This approach does not require complicated maneuvers while still allowing a precious scientific output, including high-resolution measurements and even samples from the bodies' surface, thus simplifying in many ways the design of the mission (Scheeres, 2014). However, it is extremely challenging to obtain accurate measures of the asteroid's mass and gravity field, since the frequent maneuvers will generally overshadow the signature of high-order gravity field terms, as was the case for Hayabusa (Yoshikawa et al., 2006). This is not only a drawback for the scientific output of the mission but also an important operational limitation for subsequent mission phases where the spacecraft has to get closer to the asteroid's surface. In addition to this, body-fixed hovering also implies periods during which the spacecraft is in shadow, with inherent limitations in terms of power generation, optical navigation, and communications.

Ultimately, the feasibility of a hovering approach is strictly dependent on the size (and mass) of the asteroid to be explored. In fact, while the cost of inertial hovering can be theoretically zero at a given altitude, this latter may be too large for the payload and sensors to work correctly. Indeed, had NEAR spacecraft followed an inertial hovering approach at the altitude of 50 km (the nominal orbit radius during the actual mission), over 15 m/s of ΔV would have been required every day, resulting in approximately 4 km/s for the nine-month mission (Scheeres, 2014). Hovering thus represents a reasonable approach only for very small bodies, such as those explored by Hayabusa missions.

2.2.2 NEAR Shoemaker

Even though Galileo executed two flybys at 951 Gaspra and 243 Ida between 1991 and 1993, thus becoming the first space mission to perform operations with an asteroid according to the broader meaning of the term, it is to the Near Earth Asteroid Rendezvous mission, later renamed NEAR Shoemaker, that goes the achievement of orbiting and landing on an asteroid for the first time.

On 14 February 2000, NEAR spacecraft correctly performed the OIM and entered a bounded orbit around Eros. While this initial orbit was originally planned to be 500 km high, the vehicle was inserted into a 321x366 km elliptical orbit. It is relevant for the scope of the present research to note that this shortcoming did not originate from maneuver inaccuracy (the OIM ΔV error was -0.26%) but from the uncertainty in Eros's mass. Indeed, NEAR was the first space mission that had to explicitly deal with the issue of navigating in an environment affected by such a significant uncertainty over its physical properties before arrival. The challenge resided in the need to continuously adapt the orbit plan based on the estimation of Eros's physical parameters, which were crucial to computing trajectory correction maneuvers (TCMs).

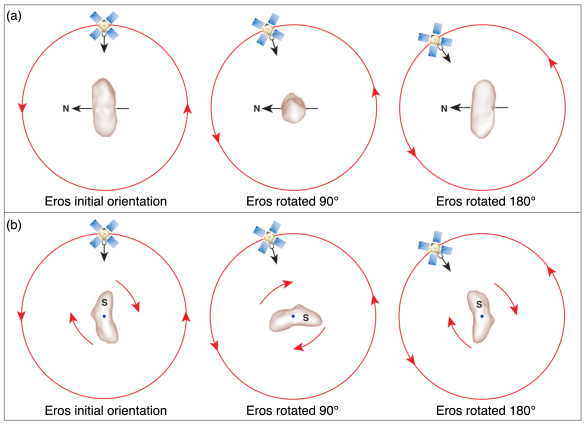

(a) Eros orbital geometry at NEAR arrival (a) and departure (b) as seen from the Sun. In (a) Eros spin axis is perpendicular to the Sun-Eros line, while in (b) it is aligned with it, and the northern hemisphere is in darkness (Dunham et al., 2002b).

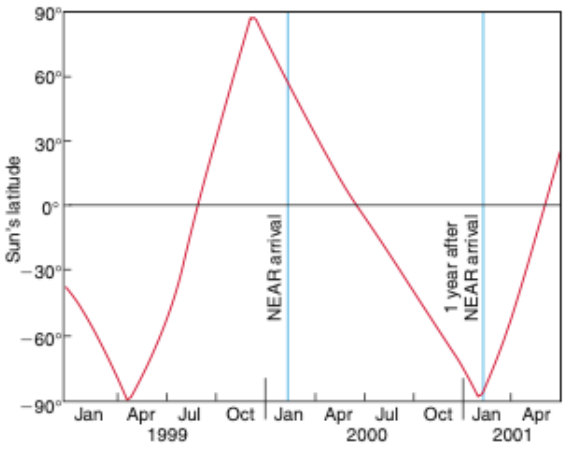

(b) The Sun's latitude above Eros's equator (Dunham et al., 2002b).

Figure 2.2: The orientation of Eros's pole during one heliocentric revolution.

The NEAR navigation system relied on the Deep Space Network (DSN)[3] for radiometric Doppler and range tracking, supplemented by optical landmark tracking and laser ranging. The landmark tracker identified surface features, or landmarks, which were used in subsequent images to estimate both the orbit and landmark positions. Instead, the laser altimeter provided range measurements to validate orbits derived from DSN data and to create an accurate shape model of Eros. Overall, NEAR operated with minimal autonomy, relying almost entirely on continuous ground support. The tracking from DSN used a 34-m antenna nearly continuously during the first 30 days and 20 hours a day thereafter, supported by daily eight-hour contacts with the larger 70-m antenna (Holdridge, 2002).

The orbital strategy followed by NEAR, summarized in Table 2.3, was designed in adherence to scientific, navigation, and stability requirements. A major constraint consisted of maintaining the desired illumination conditions to ensure the correct functioning of the solar panels, the instruments, and the optical sensors, all of which had a fixed orientation. Given that the instruments needed to always point to the nadir, and the explicit constraint to never fly into the shadow of Eros, the orbit plane orientation was severely constrained (Antreasian et al., 1998). In particular, the orbit normal was required to remain within 30° of the Sun direction. This is equivalent to saying that the solar phase angle, namely the angle between the spacecraft-asteroid and asteroid-Sun vectors, had to remain within 60° and 120°.

Based on these considerations, the orbital plane could be designed by choosing an appropriate combination of the orbit inclination and longitude of the ascending node. However, mission designers had to consider that because the spin axis of Eros nearly lies along the plane of its orbit, the illumination conditions along an orbit of a given orientation would change dramatically in time, as clarified by Figs. 2.2a and 2.2b. Therefore, they established a plan that allowed the spacecraft to achieve multiple inclinations around the asteroid, illustrated in Table 2.3, while remaining always within 30 degrees from the *Sun plane-of-sky* (Dunham et al., 2002b). This plane, also referred to as *terminator* plane, passes through the asteroid's center of mass and is perpendicular to the Sun-asteroid line. It provides very good illumination conditions to view the asteroid, as well as the right geometry for solar panels, which had to remain illuminated at less than a 30° incidence angle (Williams, 2002).

Table 2.3: Orbital plan for NEAR mission. ATE stands for asteroid true equator, SPOS for Sun plane-of-sky. Data has been reconstructed from Williams (2002) and Miller et al. (2002). When data was not available, N.A. has been noted.

Orbit (km × km)	Inclination (deg) ATE	Inclination (deg) SPOS	Orbit (km × km)	Inclination (deg) ATE	Inclination (deg) SPOS
321 × 366	35	176	100 × 103	115	150
204 × 365	34	172	50 × 98	130	179
203 × 206	37	171	50 × 52	133	178
100 × 209	55	178	19 × 51	133	168
99 × 101	59	177	64 × 203	145	N.A.
50 × 101	64	179	194 × 196	147	N.A.
49 × 52	90	160	34 × 193	179	N.A.
35 × 51	90	165	34 × 38	179	N.A.
35 × 39	90	163	22 × 35	179	N.A.
36 × 56	90	161	19 × 37	179	N.A.
49 × 52	90	159	35 × 36	179	N.A.
50 × 52	105	178	36 × 36	179	N.A.
49 × 102	113	179	36 × 36	179	N.A.

[3]The Deep Space Network consists of three communication complexes, spaced evenly around the Earth, ensuring continuous spacecraft visibility as the Earth rotates.

Over the course of one year, 25 orbital correction maneuvers (OCMs) were conducted to guide the spacecraft through various orbital distances and inclinations, with a remarkably low total ΔV of only 17.2 m/s (Dunham et al., 2002b). The lowest orbit achieved was a 35×35 km polar orbit, maintained for 10 days, while the closest passes to the asteroid occurred in eccentric elliptical orbits, with periapsis as low as 2.7 km above the surface. Notably, each OCM required approximately one week of ground operations preparation before execution (Antreasian et al., 1998).

The early orbit phase entailed the use of high-altitude orbits to perform global mapping of the asteroid, enabling the refinement of navigation models and the estimation of physical parameters such as shape, size, and spin state. In the absence of autonomous orbit control, the navigation team had to replan the orbit phase seven times after orbit insertion (Holdridge, 2002), leveraging improved navigation accuracy to target progressively smaller orbits. Additionally, inclinations were carefully increased and maintained above 90 degrees, ideally near 180 degrees. The reader may already observe from Table 2.3 that no direct orbits (orbits with inclination lower than 90°) were designed below 50 km. This precaution, as further discussed in Sec. 3.4.3, was necessary because the irregular gravity field of Eros makes prograde orbits unstable at semi-major axes smaller than 50 km (Scheeres et al., 2002). As a consequence, the orientation of the orbit had to be chosen not only in compliance with the requirements described before but also by considering the unique dynamical effects present in the asteroid environment. Finally, one may notice in Table 2.3 that as a result of maneuver errors and environment uncertainty, the actual orbits that were achieved were almost never perfectly circular (e.g., 49×52 km rather than 50×50 km).

2.2.3 Rosetta

Rosetta was a mission launched in 2004 by the European Space Agency (ESA) with the purpose of exploring comet 67P/Churyumov–Gerasimenko. One of the most notable aspects of Rosetta was the orbital profile during the approach phase, shown in Fig. 2.4. Here, the spacecraft had not been yet captured by the comet and had to fly along three consecutive hyperbolic arcs of two triangular (really, tetrahedral) orbits around the comet. It was during this phase that the first landmark observations were processed and the mass and rotational state of the comet were roughly determined. Following this initial characterization, it was possible to transition to a mapping phase, during which the spacecraft became actively captured by the comet's gravity. A series of maneuvers progressively reduced Rosetta's distance and circularized the orbit around the comet up to a 10 km-altitude circular orbit. During nominal operations, orbit maintenance was performed by a ground-controlled orbit control system, which ensured low-amplitude, short (1-2 minutes) correction maneuvers in the order of a few cm/s generated by 10 N thrusters (Reuilh et al., 2007).

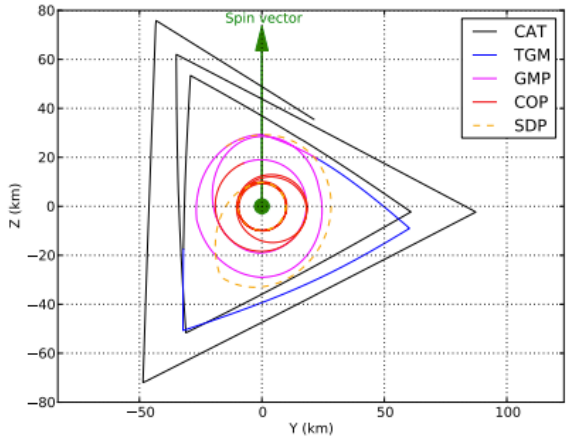

Figure 2.4: The orbit profile as seen from the Sun during proximity operations with the comet (Godard et al., 2015).

2.2.4 Dawn

Dawn was a space mission launched in September 2007 and part of NASA's Discovery Program. Its main purpose was to investigate the two largest objects of the asteroid belt: Vesta and Ceres. The successful outcome of the mission led Dawn to become the first space mission ever to orbit two different extraterrestrial bodies and the first one to visit and orbit a dwarf planet (Ceres).

For both Vesta and Ceres, four science orbits were defined at different altitudes. The relatively large and nearly spherical shape of the two bodies implied that the environment was less perturbed compared with other asteroids, thus three of these orbits were left completely free to evolve with time, causing deviations in radius up to 5 km over 17 days (Parcher, 2011). Instead, the low-altitude mapping orbit (LAMO) was particularly sensitive to the irregularities of the gravity field, as well as to the small velocity changes imparted from the asymmetric burns required for momentum wheels desaturation [4].

As a result, orbit maintenance maneuvers (OMMs) were planned in advance to correct the natural drift in phase angle and prevent the spacecraft from entering shadow. Fig. 2.5 illustrates a typical maintenance sequence involving two OMMs: the first reverses the phase angle rate so that it returns to its nominal value over time, while the second halts the rate to maintain the desired orbit. Since these maneuvers were ground-planned rather than autonomously computed onboard, sufficient margins were included to account for a possible failure of the second OMM, allowing at least 25 days for operators to respond a second time and prevent the spacecraft from entering the shadow.

A main aspect that drove the mission design of Dawn was its reliance on an ion propulsion system, which was used both for the interplanetary cruise and orbital transfers. However, along the science orbits the spacecraft was coasting, as thrusting is generally incompatible with performing science observations and data transfers (Mastrodemos et al., 2011). The use of low-thrust propulsion also introduced unique challenges for scheduling DSN antenna time: since the distribution of thrusting and coasting arcs could not be accurately predicted in advance, it was not possible to determine a preliminary schedule with sufficient anticipation. Initially, continuous DSN coverage was requested for the entire operational period at Vesta, a solution that was viable only because no other missions of similar priority overlapped with Dawn. However, when Dawn reached Ceres, the onset of the New Horizons mission made this approach unsustainable. As a result, DSN scheduling was revised to prioritize tracking during transfer sequences and science orbits, albeit at the risk of insufficient tracking capacity in case of a critical spacecraft anomaly (Han et al., 2017).

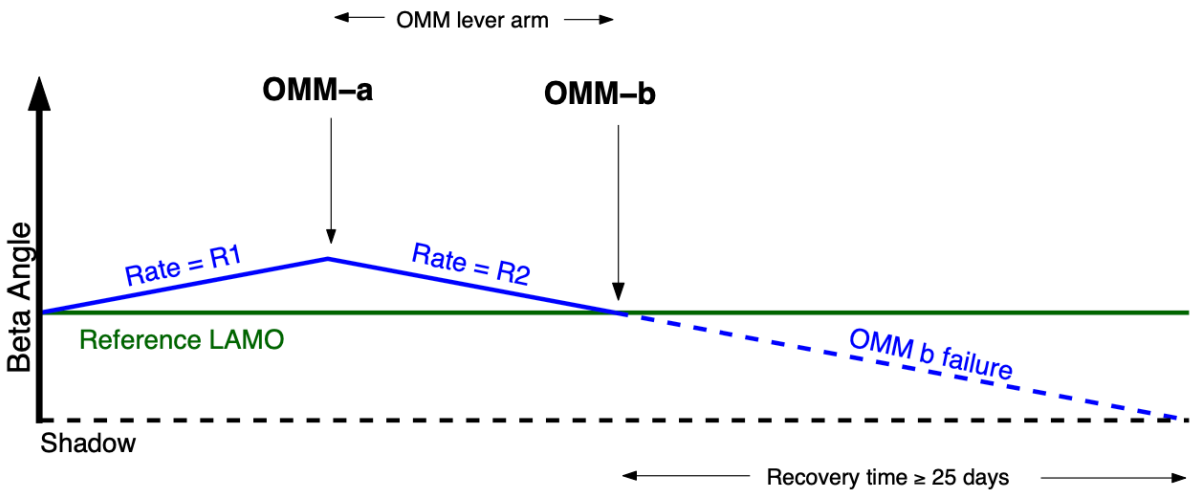

Figure 2.5: Orbit maintenance strategy for low-altitude orbits at Vesta (Parcher, 2011).

[4]Momentum wheels are used as attitude control mechanisms to counteract the angular momentum buildup from solar radiation pressure, but they have to be controlled not to reach saturation speed.

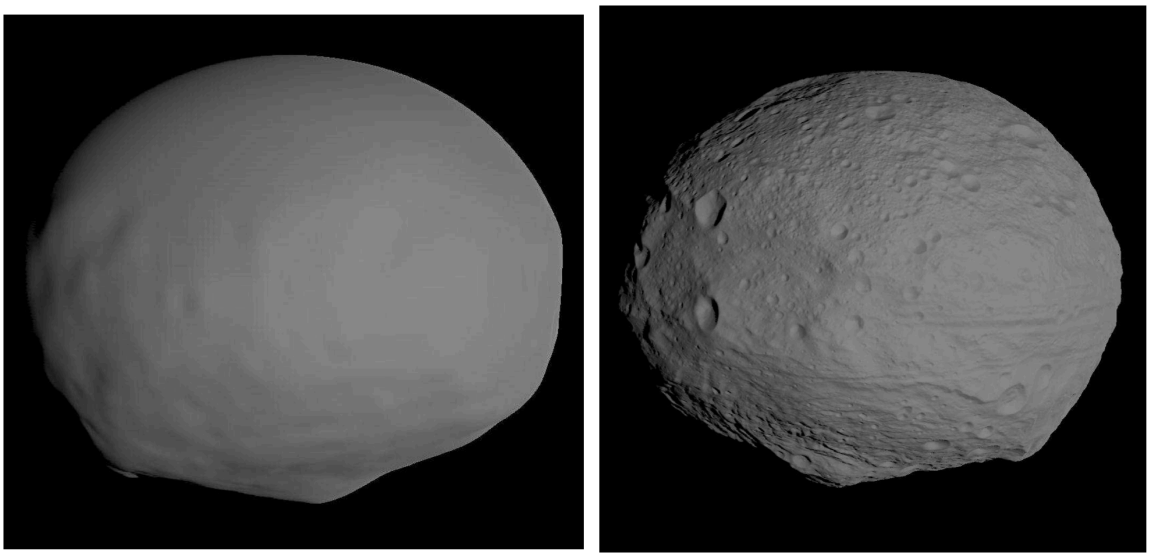

Figure 2.6: Equatorial view of Vesta's shape model after initial approach (left) and at the end of high-altitude mapping (right) (Han et al., 2017).

Similarly to previous missions, Dawn employed a twofold navigation approach where radiometric range and Doppler data were complemented by optical navigation, which was based on landmark tracking through the images acquired by the onboard camera. A comparison between the shape model of Vesta at the arrival of Dawn and after the mapping campaign is presented in Fig. 2.6. This shows that while topographic details are available only after proximity operations, the overall size of the asteroid can be roughly determined with sufficient accuracy at a very early stage of the mission.

2.2.5 Hayabusa and Hayabusa 2

Hayabusa 1 and 2 were two very successful missions conducted by the Japan Aerospace eXploration Agency (JAXA) and aimed at the exploration of asteroids Itokawa and Ryugu, respectively. In 2010, Hayabusa returned to Earth with a collected soil sample from Itokawa, becoming the first successful sample return mission. Approximately 10 years later, Hayabusa 2 delivered samples from Ryugu in a capsule, before continuing its journey in deep space towards asteroid 1998 KY26, which it is expected to encounter in 2031. The Hayabusa missions had a unique station-keeping approach in the context of asteroid missions, being the only ones to opt for hovering instead of orbiting. Both missions implemented a mixture of inertial and body-fixed hovering, maintaining an orbit-fixed location when far from the asteroid and transitioning into a body-fixed frame during descent operations.

It was decided to report the GNC strategy of Hayabusa 2 only, not exclusively for conciseness reasons, but also because it builds upon the successful legacy of its predecessor Hayabusa, hence providing a complete picture. As summarized by Table 2.3, Hayabusa 2 employed two main GNC strategies: one for nominal position-keeping operations (HPNAV), and one for critical actions, including close access to the asteroid surface (GCP-NAV).

It is of particular interest to summarize the workflow during GPC-NAV mode, as illustrated by Ono et al. (2020). The process would start with an image taken from the navigation camera and sent to a ground station. After the 20-minute travel time, operators in the control room elaborated this image to produce an estimate of the spacecraft state, which was then fed to the on-ground Kalman filter. This measurement update improved the prediction of the filter, which propagated the dynamics for 65 minutes to amount for the total time required by the image downlink, processing (25 mins), and ΔV command uplink (20 mins). The predicted state was then compared to a reference state, and a sliding mode controller (SMC) produced the required ΔV, which was uplinked to the spacecraft. This process was iterated every 10 minutes.

Table 2.3: Comparison of Hayabusa 2 GNC modes (Ono et al., 2020; Takei et al., 2020).

	HPNAV	**GCP-NAV**	
	-	On-ground	On-board
Operation	Regular HP keeping	Critical operations, including descent	
Control frequency	1 ΔV per day	1 ΔV per 10 mins	1 ΔV per 2 mins
Gravity model of the asteroid	Point mass	Point mass + spherical harmonics of order 8	
SRP model	Cannonball	Cannonball	
Navigation	Centroid-based optical	Landmark-based	lidar-based
State estimation	Batch least squares	Sequential Kalman filtering (extended)	
Guidance	Optimal ΔV from shooting method	Feedback control on reference trajectory	
Control law	-	PD controller	Sliding mode control

Below 5 km of altitude, the control rate that this ground-based strategy could guarantee was clearly not adequate, for which reason the spacecraft performed autonomously 6-DOF (degrees of freedom) control using the onboard system. During this final phase of the descent, the state was estimated with an extended Kalman filter using measurement data provided by the onboard optical sensors. Finally, it is interesting to mention that according to Ono et al. (2020), the design decision to keep human operators in the loop even in the GCP-NAV mode was guided by the idea that *recognition and determination abilities of humans are flexible and reliable under unexpected situations*.

2.2.6 OSIRIS-REx

The NASA Origins, Spectral Interpretation, Resource Identification, and Security–Regolith Explorer (OSIRIS-REx) is a mission from NASA that launched in 2016 and visited asteroid Bennu. The main purpose of the mission was to collect a sample of the asteroid's surface, which was successfully brought back to Earth in 2023. To support this activity, the spacecraft spent almost two years in close proximity to the asteroid to characterize its environment and identify suitable collection locations. As Bennu is one of the smallest objects ever visited by a spacecraft, the challenges associated with navigation were even higher than with other asteroids. In particular, the nominal orbital velocity around Bennu is 7.2 cm/s, implying that a 2 cm/s change in velocity can result in a change of the periapsis altitude by more than 500 m. Over almost two years of operations, more than 80 propulsive maneuvers were conducted for a total ΔV of approximately 22 m/s (Williams et al., 2018).

Proximity operations at Bennu consisted of a sequence of progressively complex trajectories, including close flybys at low altitudes for reconnaissance of specific sites, captured orbits, and descending trajectories to collect samples from the surface. Navigation requirements included at least 8 hours of tracking per day plus near-continuous coverage of maneuvers and observation phases (Williams et al., 2018).

Figure 2.7 provides a schematic overview of the mission phases. Initially, onboard cameras conducted optical surveys to assess the asteroid's environment, aided by ground-based image processing for navigation. This allowed to build the initial shape model over more than 80% of the surface to less than 1 m resolution. At the end of the Approach phase, three hyperbolic flybys were executed to satisfy navigation requirements, which required reducing the uncertainty in the asteroid's mass to within 2%. The most relevant scientific activities were done on two circular orbits (A and B), respectively 1.5 and 1 km in radius. It is important to mention that the location of orbits A and B was chosen based on careful considerations regarding orbital stability and scientific requirements. In fact, developing an accurate gravity model for such a small asteroid required the orbits to be very close to the surface, while being stable enough to al-

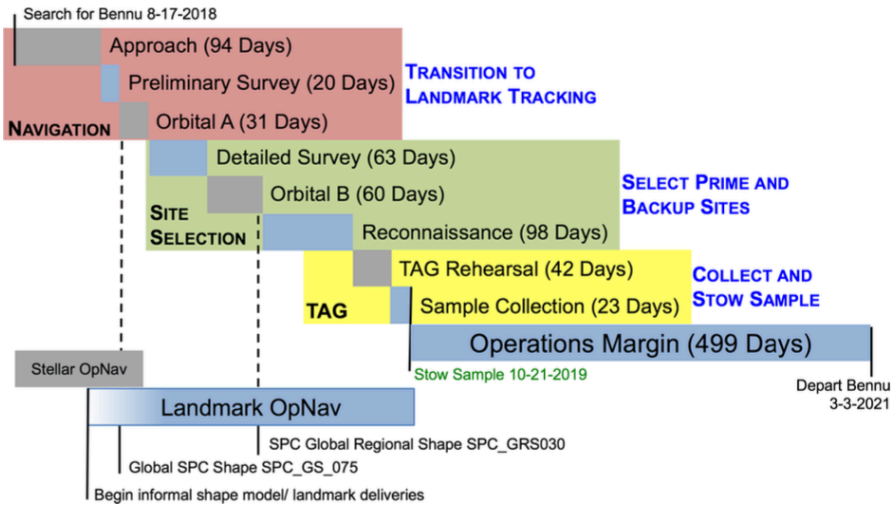

Figure 2.7: Overview of OSIRIS-REx mission phases during proximity operations with Bennu (Williams et al., 2018).

low for relatively long periods of time without correction maneuvers, a necessary condition to detect the small perturbations caused by the high-order terms of Bennu's gravity field. Hence, similarly to NEAR, both orbits were placed on the solar terminator plane, given its known stability properties. In addition, their semi-major axis was chosen in adherence to specific limits, in particular between 0.7 km and 2.5 km, as it was known that outside of these bounds the spacecraft would have escaped or collided with the asteroid (Scheeres et al., 2013). The theory behind these stability considerations will be presented later in Sec. 3.4.3.

A proper onboard guidance algorithm for the translational motion was used only for the descent procedures, during which real-time control over the spacecraft was needed due to the impossibility of relying on ground support as with the remaining phases of the mission. OSIRIS-REx was thus equipped with a closed-loop onboard scheme that used a two-dimensional polynomial relationship between the state predictions and lidar measurements to provide simple maneuver corrections (Berry et al., 2015).

2.2.7 General considerations

All the asteroid missions illustrated until now employed a similar strategy for proximity operations. A slow approach phase was first conducted to estimate key physical parameters of the asteroid, namely its gravitational parameter, rotation period, and pole orientation. This reconnaissance phase was followed by thorough observation and mapping campaigns, where enhanced environmental knowledge enabled safer spacecraft navigation near the asteroid.

These missions were heavily reliant on ground communication, with continuous DSN coverage during observations to collect radiometric tracking data, including Doppler shifts and range measurements. Combined with data from onboard sensors like laser altimeters and cameras, these measurements allowed to characterize the asteroid's environment and spacecraft state. The collected data was always processed on the ground through batch estimation techniques to obtain a navigation solution, which then was used by operators to predict the spacecraft's trajectory.

Typically, the necessity for active orbit-keeping was reduced to a minimum by choosing proper orbital profiles that exploit the stability regions around the asteroid. Still, the combination of various sources of uncertainty required regular orbit maintenance, which was achieved through nearly-impulsive maneuvers that were computed on the ground by operators and then uplinked to the spacecraft. In general, the low-gravity environment does not require significant ΔVs, thus both OCMs and OMMs were generally executed by using the reaction control system (RCS).

Table 2.4: Causes and effects of the main uncertainties affecting asteroid missions.

	Dynamical model	**Navigation**	**Maneuvers**
Cause	Impossibility in measuring the physical properties of the target small body from Earth.	Inaccuracy in the dynamical model, time delays in communications, and imprecision of the optical sensors.	Hardware and actuator errors, pointing errors.
Effect	Models used to predict the dynamics can become very inaccurate in the long term; computed commands can have undesired effects.	There is a difference between the real state of the spacecraft and the one known onboard; state-feedback commands are inevitably inaccurate.	Executed maneuvers differ from the commanded ones.

In conclusion, the key uncertainties in asteroid missions can be grouped into three main categories, as summarized in Table 2.4 and in the following:

1. **Modeling errors**: they arise mainly from the inaccurate knowledge of the asteroid's internal structure and rotational state (angular velocity and pole orientation), which translate into uncertainty over the gravitational parameter and the high-order gravity terms. Depending on the asteroid, another primary error may come from the inaccuracy in the SRP coefficient.
2. **Navigation errors**: they represent the difference between the real spacecraft state and the one estimated either on the ground through an orbit determination process or onboard via sequential filtering.
3. **Maneuver errors**: they are caused by the chain of errors that accumulate between the moment in which the command is computed, and that in which it is executed. Additionally, also the inaccuracy in the spacecraft attitude generally implies a misalignment with respect to the desired burn direction. It should be highlighted that execution errors are the main reason why it is required that the spacecraft is coasting during gravity estimation. In fact, in a scenario where the magnitude and direction of the maneuvers are known exactly, it would be possible to account for it within the orbit determination process and thus isolate its effect. Instead, in a realistic scenario, it becomes hard to distinguish the gravity signature from the execution errors - impossible for asteroids, since gravity is often orders of magnitude lower than the maneuver errors themselves.

2.3 Current research status

2.3.1 Orbit control around asteroids

One of the first to work on orbit control for asteroids was Reyhanoglu et al. (2012), who implemented a feedback control law with PD logic and static gains to perform both attitude and orbit control on an equatorial orbit around Eros. Winkler et al. (2012) expanded on this by employing a linear quadratic regulator (LQR) approach to track four low-altitude, circular orbits at different inclinations around Eros. The LQR was designed on a fully linearized dynamics model with all the nonlinear forces lumped in a perturbation vector. A disturbance-rejection technique was applied to decrease the control effort to acceptable levels, successfully reducing the amplitude of the control accelerations. More recently, Tiwari et al. (2023) developed a nonlinear adaptive controller that is able to track orbits around small bodies virtually without any model knowledge. The control law is given by a nonlinear PID (proportional-integral-derivative) which updates the integral and proportional gains according to the position error. A completely different strategy was proposed by Shi et al. (2020), who compared an impulsive method based on differential correction with a discrete LQR controller for orbit-keeping around binary asteroids. Both algorithms were tested against maneuvering and state uncertainties, showing a station-keeping accuracy in the order of 100 m for 10-12 impulses per revolution.

Other authors employed more advanced control methods which draw from the theory of robust and adaptive control. Zhang et al. (2015) proposed a robust version of the linear quadratic regulator (RLQR) to achieve stable orbital motion around the tumbling asteroid Toutatis without the necessity to have an a-priori rotation model of the small body. The control law is composed of a feedforward control term, which counteracts the known perturbations, and an adaptive integral compensator that ensures stability against uncertainties in the dynamical model. Lee and Singh (2019a) recently developed and compared an adaptive, a supertwisting, and a supertwisting adaptive control law for spacecraft orbit-keeping around asteroids Eros and Ida. All three algorithms were proven to successfully track a reference circular trajectory while assuming the mass and moments of inertia of these latter to be not known. In more recent publications, the adaptive mechanism present in these control laws was augmented by additional algebraic functions to obtain stronger stability properties. These adaptive controllers have been proposed by Lee and Singh (2019b, 2023) and applied to the same scenario of Eros and Ida with the mass and moments of inertia of the small bodies not known. These unknown terms are estimated by an integral adaptation law combined with state-dependent nonlinear functions. Simulation results showed that the implemented system is able to track a reference orbit with negligible steady-state error, although the continuous control law exhibits a rapid oscillatory behavior that is strictly dependent on tuning parameters. Another version of an adaptive supertwisting control algorithm was developed by Zhang et al. (2020), who employed a disturbance observer to estimate online the perturbations from the gravity field and achieve a smooth control law. In particular, the algorithm proved very efficient to drive the spacecraft to the reference orbit within finite time even for large discrepancies in the initial state.

A simple, yet more specialized strategy was proposed by Guelman (2015), who developed a closed-loop guidance law that is able to target any circular orbit of given angular momentum and radius while assuming a point mass gravity model of the central body and continuous thrust. In a later publication (Guelman, 2017), the same author improved the control law with an additional term that allows to control the orbit radius independently from the angular momentum. The robustness of this latter formulation was proved against unrealistic large values for the C_{20},C_{22} gravity coefficients, achieving a maximum error of 2% on the commanded orbit radius, although other sources of uncertainty were neglected. Building upon this heritage, Negri and de Almeida Prado (2020, 2022) developed a more flexible and robust approach based on a sliding surface defined in terms of the angular momentum and the eccentricity vectors.

To provide comprehensive coverage, it's relevant to also mention the work from Oguri and Mcmahon (2019), who proposed a state-dependent Lyapunov control law that uses SRP[5] through attitude adjustments for orbit maintenance and transfers. Inspired by the Qlaw, the control law minimizes a Lyapunov function weighing deviations in orbital elements through a feedback gain matrix. In a later publication, Oguri and McMahon (2021) introduced a stochastic optimal control framework for maintaining resonant transfer orbits, which are specific periodic orbits derived from the Hill approximation that naturally avoid eclipses. The authors devised a two-step process combining convex optimization and nonlinear programming to design robust, real-time guidance policies for onboard implementation.

Most of the studies that have been described until now tested the robustness of the respective orbit control strategy only against unmodeled dynamics, often limited to gravitational effects and not including solar perturbations. Additionally, many assumed perfect knowledge of the spacecraft state, thus neglecting navigation uncertainties. Lastly, they approached the problem from a purely control perspective, not considering the specific operational constraints that characterize the given application scenario, and regarding the orbit-keeping problem around an asteroid as a general reference-tracking problem in a nonlinear environment. In many cases, the generated control laws did not consider maneuvering errors, or thrust saturation, and exhibited a continuous, often rapidly oscillating behavior that is not feasible in practice. Especially this latter aspect represents a criticality since the spacecraft should perform station-keeping in a discrete way, with long time windows in between maneuvers to allow for scientific observations.

[5] It is noted that the successful applicability of this method while assuming a nominal spacecraft area-to-mass ratio (thus, not considering the presence of solar sails) is possible in this case because the target asteroid, Bennu, is small enough for SRP to be the dominant perturbation even when relatively close to the asteroid (for more information, see Fig. 3.2).

Most importantly, to the knowledge of the author, there is no study in the literature that has investigated how orbit control is affected by the choice of a particular target orbit. Indeed, asteroid missions are characterized by the use of several orbits with very different characteristics; in contrast, classic orbit control literature (Earth and libration point orbits) typically focuses on a specific orbit for a given satellite. Therefore, the robustness of the orbit control system should be tested not only against the uncertainties and errors that are present in the asteroid environment but also against different types of orbits. The importance of observing how the performance of the orbit-keeping strategy is affected by the choice of the orbit geometry and orientation is even more when considering the specific stable and unstable orbital regimes that can be found in the proximity of an asteroid, as Sec. 3.4.3 will highlight.

2.3.2 Integrated guidance and navigation

A reduced number of recent publications focused on orbit control at asteroids with simultaneous estimation of the spacecraft state and environment parameters. Feng et al. (2021) proposed an integrated framework consisting of station-keeping, autonomous navigation, and estimation of the gravity field, while considering uncertainty over a wide variety of factors, including the thrust magnitude, the asteroid spin rate, and the spherical harmonic coefficients. For asteroid Lutetia, the designed system achieved convergence to a reference orbit in under 1.5 hours, with steady-state position errors below 1%.

A more conventional approach is that of including the uncertain parameters within the navigation solution, as proposed by Takahashi and Scheeres (2021). They introduced an autonomous exploration scheme for global mapping campaigns via near-inertial hovering, integrating ΔV measurements into an augmented state vector to support optical navigation and break scale invariance present in the images. They used an iterative Kalman filter (IKF) to overcome the potential stability issues of the extended Kalman filter (EKF) and employed a two-point boundary value problem for translational guidance.

Sanchez et al. (2022) developed a 6-DOF autonomous guidance scheme using model predictive control (MPC) enhanced by a learning-based approach for orbit-attitude station-keeping. The inherent model dependency of MPC is overcome by employing an unscented Kalman filter (UKF), which allows for in-situ gravity field estimation and proves to improve controller performance over time. By modeling dynamics with Gauss variational equations, the designed system tracks only the semi-major axis and eccentricity through a combination of radial and tangential thrust, thus decoupling in-track from cross-track control. Lastly, Negri et al. (2024) implemented the previously mentioned control law in combination with a batch-sequential least-squares filter to estimate the gravitational parameter and solar radiation pressure coefficient onboard. Simulations around asteroids Bennu and Eros demonstrated robustness against unmodeled perturbations and reduced the asteroid mass uncertainty below 2%.

2.3.3 Thesis heritage

There have been multiple research efforts on autonomous proximity operations with asteroids at the Aerospace Engineering faculty of TU Delft over the past years. Specifically, there has been great interest in onboard navigation and estimation through sequential filtering, which requires less memory and computational effort than batch estimators and fits well within the framework of autonomous space missions.

Razgus (2016) developed a navigation algorithm based on relative pose dynamics, comparing nominal and dual quaternion state representations. While the EKF performance was found to be similar for both, dual quaternions showed better transient behavior. Simulations were conducted using a polyhedron gravity model for asteroids Kleopatra and Itokawa. Subsequently, Bourgeaux (2020) implemented a UKF for autonomous gravity field estimation around asteroid Eros, demonstrating better convergence than an EKF despite higher computational demands. Specifically, the UKF's ability to estimate spherical harmonics gravity coefficients without requiring analytical Jacobian matrices represented a key advantage of this method. A detailed analysis revealed that equatorial orbits at altitudes of 200–300 km were optimal for gravitational parameter estimation, while polar, low-altitude orbits were better suited for

higher-order coefficients, as they maximize surface coverage and allow the spacecraft to feel the effect of every gravity component.

Building upon these two works, Spee (2022) investigated navigation within the circumscribing sphere of an asteroid by making use of an EKF based on a *masscon* (mass concentrations) gravity model. Since stable orbits could not be found at the tested low altitudes, the asteroid had to be modeled as non-rotating. While all the previous authors focused on single asteroids, Elffers (2023) developed a vision-based navigation system for binary asteroids based on the use of optical and laser ranging measurements. An EKF applied to a landing scenario showed robustness against high Sun phase angles, which significantly impact optical navigation performance. Finally, Munuera Vilalta (2024) conducted a thorough study of how a UKF can be exploited in combination with a satellite constellation to improve gravity field estimation.

In parallel, there has been interest also in guidance strategies for proximity operations with asteroids. Canale (2018) adapted a Lyapunov-based real-time guidance law, originally designed for orbit raising in the two-body problem, to asteroid proximity operations. The formulation was augmented to include constraints on minimum distance (non-impact condition) and the C_{20} gravity term, though its applicability was limited to low-thrust missions. Trullas (2018) focused on the use of dual quaternions within a 6-DOF controller for a spacecraft that had to orbit, hover, and land at asteroid Bennu. These trajectories were tracked by using a linear PD controller with gains tuned by trial and error. Finally, Hazra (2019) developed a guidance system for an asteroid TAG descent based on successive convexification and dual-quaternions.

These research studies did not consider the mutual relation between navigation and guidance. Specifically, the authors who worked on autonomous navigation did not use the estimated solution as input for orbit control, and those who instead focused on guidance assumed perfect knowledge of the state coming directly from the integration of the equations of motion. To provide a natural continuation to this previous work, one of the objectives of this thesis is to formulate a strategy for orbit control that is robust to navigation uncertainty while accommodating the needs that characterize gravity estimation experiments.

2.3.4 Earth applications

The development of autonomous orbit control strategies initially focused on Earth applications. One of the earliest examples, the Orbit Control Kit (OCK) by Microcosm Inc., was flight-tested on UoSAT-12 in 1999, achieving in-track position control within ±1 km accuracy while using less propellant than traditional methods (Wertz, 2003). Over the past three decades, the increasing number of satellites has exposed the limitations of ground-in-the-loop approaches, which require frequent, ground-based control actions to counter atmospheric drag and other perturbations, significantly impacting mission costs and risks. Autonomous station-keeping addresses these challenges by enhancing system performance and reducing reliance on ground operations.

While asteroid missions share some of these motivations, their context differs significantly. Therefore, many design considerations for Earth orbit control systems are not directly applicable to asteroid environments. The primary discrepancies are outlined as follows:

- The level of uncertainty in the dynamic environment: the degree of accuracy in understanding the Earth's gravitational field and other factors influencing spacecraft motion is very high. As a consequence, it is possible to generate a reference orbit that already accounts for the main perturbing effects (De Florio and D'Amico, 2009).
- The navigation solution quality: global navigation satellite system (GNSS) provides satellites with very accurate knowledge of their state.
- The perturbations affecting the dynamics: the motion of a spacecraft orbiting Earth is very well approximated by the point mass and oblateness gravity terms.

- The operational context: satellites located along Earth orbits have typically tight position and maneuvering margins to avoid collisions with other space assets, or to enable precise scientific experiments. Therefore, the size of the station-keeping window needs to be relatively small.

The factors listed above lead to the applicability of simpler control designs for Earth applications, where PD controllers with gain-scheduling (Bonaventure et al., 2005) and LQRs (De Florio et al., 2012) represent very valid choices. Generally, the orbit control problem can be addressed based on either Cartesian coordinates or orbital elements. In both cases, a linearized model of the dynamics is available, either via the Hills equations or the linearized Gauss variational equations (GVE). Specifically, when controlling directly the orbital elements it is possible to use their mean formulation to avoid compensating for the tracking errors generated by the short-term periodic gravitational disturbances (Schaub et al., 2000).

For Earth-orbiting satellites, it is typically necessary to track all components of the reference trajectory. Therefore, both cross-track and in-track maneuvers are required to control the orbit plane's orientation and the spacecraft's position within the plane, respectively. Linearization allows to consider these controls as decoupled, with in-track control managed by the main engine and cross-track control performed using smaller impulsive thrusters (Garulli et al., 2011). In particular, maintaining the in-track phase of the spacecraft is essential to predict in advance the position of the spacecraft at all future times (Wertz, 2003). As a consequence, a commonly used approach consists of simulating a virtual target that moves along a reference, unperturbed orbit, and formulating the control problem as a leader-follower formation flying scenario (De Florio and D'Amico, 2009).

Evidently, many of the aforementioned considerations lose their validity when applied to the orbit control problem around asteroids. The use of linear models is not reliable, and the in-track and cross-track control of the spacecraft are strongly coupled. Additionally, the phasing of the orbit is far less relevant than for Earth satellites. In fact, since the spacecraft operates alone and given the short orbital periods, there is no justification for controlling its position along the orbit (i.e., tracking the true anomaly). Thus, the leader-follower approach may not represent an adequate strategy to generate a reference trajectory.

2.4 Reference mission

The mission envisioned for this study is based on the legacy of the asteroid missions that have been presented at the beginning of this chapter, with Eros chosen as the target small body. Even prior to NEAR Shoemaker mission, Eros used to be the most observed object in the Solar System among those of its size. The extensive data gathered during NEAR campaign facilitated a thorough characterization of its physical properties, allowing studies to have a consistent, realistic scenario in which to develop and test their models. More than 25 years after NEAR's launch and subsequent asteroid missions, Eros remains the standard case study for testing GNC designs for autonomous operations around asteroids. It provides a well-known baseline, which enables meaningful comparisons with other methods present in the literature. Assuming that the target of the reference mission is a single body shall not be considered a limitation, as this is the nominal scenario for most asteroids (85 % of the NEAs population is composed of single asteroids (Cheng et al., 2009)).

The operations that will be considered are limited to a range of altitudes between 20 and 50 km. In fact, this is the most relevant flight zone for scientific purposes, especially gravity field estimation, given that the perturbations from the asteroid's gravity field become non-negligible. In turn, this makes it necessary for the presence of an active orbit control system. Unlike most studies present in the literature, an effort will be made to test the designed system on a variety of possible orbits, rather than focusing on only one. Specifically, the main object of interest for this study will be circular orbits, which are the most widely used to perform observation of small bodies, although elliptical orbits will also be considered since they can allow for low-altitude flyovers.

2.4.1 433 Eros

433 Eros, a near-Earth asteroid belonging to the Amor group, was first discovered in 1898 by Carl Gustav Witt. The asteroid passes relatively close to the Earth, but does not intersect its orbit and is thus not regarded as a PHO. Primarily composed of silicates, it falls under the S-class category. It possesses a highly irregular shape, with one dimension exceeding double the length of the other two. Indeed, the most prominent feature of the small body is its elongated shape and two lobes, with the three largest craters being Himeros (9.0 km), Shoemaker (7.6 km), and Psyche (5.3 km). Through a joint analysis of the gravity field measurements and the pictures of the surface features, it was possible to infer that Eros is a consolidated body, and not an aggregate of smaller debris or a rubble pile, thus suggesting it is a collisional fragment from a larger parent body. In addition, it was determined that the offset between the center of the figure and the center of mass is only about 30 m, indicating that Eros has a remarkably uniform mass-density distribution (1% variation) on a large scale. Finally, Eros appears to be rotating with relatively uniform angular speed about its maximum moment of inertia, thus being classified as a uniform rotator. As a matter of fact, no wobble greater than 0.02° has been detected in the pole direction.

Table 2.5 presents Eros's main physical parameters as reported by Miller et al. (2002). Prior to NEAR mission, ground-based telescope observations had been able to determine with high accuracy only the rotation rate (from light curves) of the asteroid and its orbital elements, while the other parameters remained very poorly known until the spacecraft reached the asteroid. The a-priori knowledge of the gravitational parameter and pole orientation was refined during the approach phase to the asteroid, where it was possible to reduce the uncertainty (1σ) over these parameters to 10% and to 2-5 degrees, respectively (Miller et al., 2002). Based on the gravitational parameter, it is immediate to estimate that for a 50x50 km orbit, the velocity is about 3 m/s, making it intuitive to understand how even small perturbations can have such a destabilizing effect and lead to either escape or impact with the surface. Table 2.6 shows the Kepler elements for Eros's orbit around the Sun according to the small body database [6]. The asteroid's trajectory has a perihelion distance of 1.13 au and an aphelion distance of 1.78 au. The large obliquity of the asteroid (89 degrees) implies that the pole lies nearly in its orbit plane, therefore the seasons of dark and light at either pole persist for several months.

Table 2.5: Eros's physical parameters as reported by Miller et al. (2002). The orientation of Eros (prime meridian, right ascension, and declination) is described with respect to the J2000 reference frame.

Parameter	Symbol	Value	Unit
Gravitational parameter	μ	$4.4631 \cdot 10^{-4}$	km^3/s^2
Bulk density	ρ	2.67	g/cm^3
Volume	V	2503	km^3
$a \times b \times c$	-	34.4x12x12	km
Rotation rate	ω_A	1639.34	deg/day
Rotation period	T	5.27	hrs
Prime meridian	W	326.06	deg
Right ascension	α	11.36	deg
Declination	δ	17.23	deg

Table 2.6: Eros's orbital parameters, given with respect to a Sun-centered inertial frame aligned with J2000.

Semi-major axis [au]	Eccentricity [-]	Inclination [deg]	RAAN [deg]	AoP [deg]
1.458	0.2227	10.83	304.28	178.90

[6] `https://ssd.jpl.nasa.gov/tools/sbdb_lookup.html/?sstr=433`, accessed on 08/05/2024.

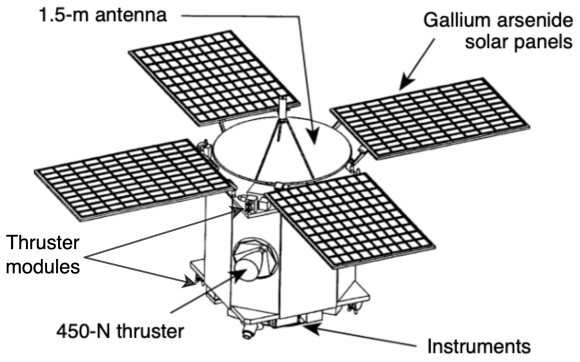

Figure 2.8: Schmeatic view of NEAR spacecraft, adapted from Santo et al. (1995).

2.4.2 Spacecraft

The spacecraft that will be used as a reference during the simulations is the one from NEAR mission, as shown in Fig. 2.8. The main propulsion system consists of a 470N bipropellant thruster using nitrogen tetroxide (N_2O_4) and hydrazine (N_2H_4). Conversely, the reaction control system is made of four 21N and seven 3.5N monopropellant thrusters that use hydrazine as propellant. These thrusters are arranged in six modules mounted to the fore and aft decks of the spacecraft, which allow to provide torque around all axes and small ΔV maneuvers in all directions (Santo et al., 1995). The RCS is used for OCMs and OMMs, but it can also control the rotational motion (e.g., to dump angular momentum from the reaction wheels). Nominal attitude control is achieved through a set of four reaction wheels, out of which three are sufficient to guarantee three-axis control, and one is redundant. For power generation, the spacecraft relies on four solar panels attached to the sides of the main spacecraft bus. This latter has the shape of an octagonal prism, approximately 1.7 m on a side. The total propellant mass carried by the spacecraft is 318 kg, which guarantees a maximum ΔV of 1450 m/s, out of which 245 m/s can be achieved in monopropellant mode.

The guidance and control system provides closed-loop control for attitude only. For this, the spacecraft can rely on the use of five solar sensors, an inertial measurement unit (IMU), and a star tracker. The IMU contains four gyros and four accelerometers aligned such that any three are sufficient for three-axis rate/acceleration measurement. Thus a single failure of a gyro or accelerometer can be accommodated.

2.4.3 Requirements

Based on the considerations that have been made throughout this chapter, a list of mission and system requirements is generated to drive the design of the orbit control system. The mission requirements identify the main aspects of the mission plan, which is inspired by NEAR and based on the general considerations that were made at the beginning of this section. In particular, it is noted that the mission profile entails the observation of the asteroid through standard Kepler orbits. As it will be shown in Sec. 3.4.3, the asteroid environment can theoretically be modeled through specific versions of the three-body problem, rather than a perturbed two-body problem, which allows to infer the presence of specific families of periodic orbits. While there has been ongoing research in regard to this matter (Broschart et al., 2014; Kikuchi et al., 2017), it will be shown in the next chapter that for Eros, the perturbed two-body problem represents the most convenient way of modeling proximity dynamics with the asteroid, thereby making Keplerian orbits the most natural choice for observation purposes (i.e., targeting orbits which are far from the reality will generally increase the station-keeping cost (Howell and Pernicka, 1993)). Furthermore, high relevance is given to the orbit inclination from which the asteroid is observed. In fact, based on the outcome of multiple studies (Bourgeaux, 2020; Pasquale et al., 2022), achieving a polar orbit is essential to guarantee the accurate estimation of the irregular gravity field.

Mission requirements
MIS-REQ-01: The periapsis radius of the observation orbits shall be within 25 km and 35 km.
MIS-REQ-02: The eccentricity of the observation orbits shall be within 0 and 0.3.
MIS-REQ-03: The inclination of the observation orbits shall span the full available space, thus ranging from 0° to 180°.
MIS-REQ-04: The observation orbits shall all lie to within 10° from the Sun-terminator plane.
MIS-REQ-05: Elliptical orbits enabling pole flyovers of Eros at an altitude of 2 km shall be included in the mission design plan.

System requirements
OC-REQ-01: The orbit control algorithm shall not rely on onboard optimization.
OC-REQ-02: The orbit control system shall not depend on commands sent from the ground.
OC-REQ-03: The orbit control system shall be robust against injection errors (1σ) of 1 km in position and 1 m/s in velocity.
OC-REQ-04: The orbit control system shall be robust against navigation errors (1σ) of 10 m in position and 0.1m/s in velocity.
OC-REQ-05: The orbit control system shall be robust against maneuvering errors (1σ) of 3% in magnitude and 0.5° in direction.
OC-REQ-06: The orbit control system shall be able to counteract the disturbing forces generated by the irregular gravity field, the solar radiation pressure, and the solar tide.
OC-REQ-07: Orbit control shall be achieved by impulsive maneuvers.
OC-REQ-08: The orbit control algorithm shall allow for coasting time windows longer than 30 minutes.
OC-REQ-09: The orbit control algorithm shall not rely on any environment information outside of the asteroid's gravitational parameter.
OC-REQ-10: The orbit control system shall be able to maintain the spacecraft within the desired region of space for all orbits included in the mission design plan.

Finally, a list of boundary conditions for the mission scenario is also provided:

BC1: The gravitational parameter is assumed to be fully known. Given the low altitude of the orbits that will be investigated, it can be safely assumed that in a real mission, the mass of the small body would have been already estimated with a negligible residual error.
BC2: Attitude dynamics and control will not be simulated. It is assumed that the spacecraft is able to autonomously point the science deck at the asteroid to support autonomous navigation. Specifically, the reference attitude for the spacecraft is nadir-pointing, which is consistent with the scientific nature of the reference mission.
BC3: The motion of Eros around the Sun is described by an unperturbed Kepler orbit. This is a model simplification since additional perturbations arise from the gravitational attraction of the planets. However, this assumption is generally a good one over a timespan of a few orbit periods around the Sun (Scheeres, 2012b).
BC4: While it is one of the primary purposes of this work that of investigating the performance of the guidance subsystem under the presence of navigation errors/uncertainties, simulating a full navigation architecture falls outside the overall scope. For this reason, it is assumed that the spacecraft can exclusively rely on the use of onboard devices, such as cameras and lidar, which can ensure autonomous, vision-based, relative navigation. These sensors will not be implemented, and the reader can refer to the work of Razgus (2016), Bourgeaux (2020), and Munuera Vilalta (2024) for the corresponding mathematical models. In addition, an image processing algorithm was developed and is described in the work of Elffers (2023).
BC5: It is not within the scope of this thesis to also implement an autonomous mission planning algorithm. While onboard trajectory generation is an active field of research, it is noted that once an asteroid is identified for a mission, there is sufficient information to design the large-scale framework of mission objectives based on ground observations (Takahashi and Scheeres, 2021). For this reason, it is assumed that a reference, feasible mission plan that the orbit control has to adhere to can be generated in advance.

BC6: Since ground-based optical observations can establish with high accuracy the rotation rate of an asteroid (Miller et al., 2002), this has been assumed to be known exactly by the time the spacecraft has begun proximity operations (indeed, Williams (2002) report an uncertainty in the order of 10^{-9} deg/s). For the same reason, also uncertainties in the asteroid's pole orientation have not been considered.

3

Flight dynamics

This chapter discusses the kinematics and dynamics that characterize the motion in the proximity of an asteroid. Section 3.1 defines the reference frames used throughout the thesis, while Sec. 3.2 presents different sets of elements to represent the spacecraft's translational state. In Sec. 3.3, the transformations that describe the relative orientation between the reference frames are introduced. Section 3.4 provides an extensive overview and comparison of the models used to describe the forces acting on the spacecraft, followed by a qualitative discussion of the main dynamics effects that a vehicle can experience in the proximity of a uniformly rotating, irregular small body. Finally, the equations of motion are presented in Sec. 3.5.

3.1 Reference frames

The state of the spacecraft at a certain moment has to be expressed with respect to a given reference frame, which is defined by the position of its origin and the orientation of its three axes [1]. Usually, reference frames are based on the rotation axis of a given celestial body, whose points of intersection with the body's surface are referred to as *north* and *south pole*.

J2000 Earth Ecliptic (J2000)
The origin of this reference frame is located at the asteroid's center of mass, with the X_{J2000}-axis pointing towards the mean vernal equinox. The Z_{J2000}-axis is aligned with the Earth's rotation axis (thus pointing towards the celestial north pole), while the Y_{J2000}-axis completes a right-handed coordinate system. This reference frame is particularly useful for describing Eros's attitude relative to the Sun, as the orientation of the small body's pole is typically expressed with respect to it. The J2000 reference frame is identified by the symbol $\mathcal{F}_{J2000}$, and its basis vectors are labelled as $\hat{\boldsymbol{x}}_{J2000}$, $\hat{\boldsymbol{y}}_{J2000}$, and $\hat{\boldsymbol{z}}_{J2000}$.

Asteroid-centered inertial (ACI)
Its origin O_I is located at the center of mass of the asteroid, with the Z_I-axis along the rotation axis (assumed to be also the direction of the maximum moment of inertia). The direction of the X_I-axis is generally a degree of freedom; a possible solution is to choose the axis corresponding to the minimum moment of inertia at a given time. Therefore, following the same convention used for NEAR mission[2], X_I is oriented such that, at time zero, it aligns with one of Eros's lobes, with longitude increasing to 90° near Himeros and 270° near Psyche. The Y_I-axis completes the right-handed coordinate system, and the $O_I X_I Y_I$ plane is referred to as *equatorial plane*. This reference frame is identified by the symbol $\mathcal{F}_I$, and its basis vectors are labelled as $\hat{\boldsymbol{x}}_I$, $\hat{\boldsymbol{y}}_I$, and $\hat{\boldsymbol{z}}_I$. For the sake of precision, it should be noted that it would be more appropriate to refer to this reference frame as *pseudo*-inertial, rather than inertial. In fact,

[1] It is noted that the definition given here is technically that of a *reference system* rather than of a reference frame.
[2] `https://sbn.psi.edu/pds/resource/near/NEAR_Coordinate_Systems.txt`, accessed on 30/04/2024.

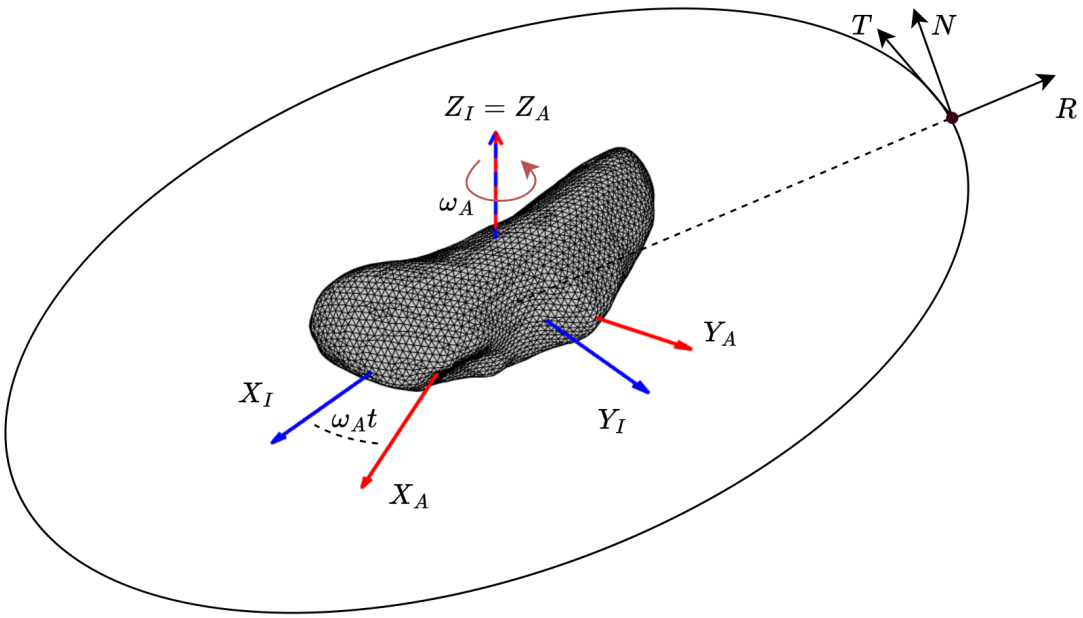

Figure 3.1: Representation of $\mathcal{F}_I$, $\mathcal{F}_A$ and $\mathcal{F}_R$.

the asteroid has an acceleration about the Sun as it orbits around it. However, the relative motion of the body around the Sun is in the order of degrees per day at the fastest, meaning the position can be safely assumed nearly inertial over relatively short periods (Scheeres, 2014). In other words, since the orbital period of Eros is roughly two years, the time scale associated with this motion is not comparable to the duration of the simulations that will be performed, therefore this frame can be regarded as inertial for all practical purposes.

Asteroid-centered asteroid-fixed (ACAF)
Its origin O_A is located at the center of mass of the asteroid, and its Z_A-axis is aligned with the rotation axis of the asteroid, thus coinciding with $\hat{\boldsymbol{z}}_I$. At time zero, the X_A-axis coincides with X_I, and the Y_A-axis completes the right-handed reference system. This frame is fixed to the asteroid and thus the $O_A X_A Y_A$ plane rotates about the Z_A axis with constant angular velocity ω_A (Eros has uniform angular speed). This reference frame is identified by the symbol $\mathcal{F}_A$, and its basis vectors are labelled as $\hat{\boldsymbol{x}}_A$, $\hat{\boldsymbol{y}}_A$, and $\hat{\boldsymbol{z}}_A$. As displayed in Fig. 3.1, the angle between X_I and X_A grows with the linear law $\omega_A t$ since the asteroid is assumed to be rotating uniformly.

Asteroid-centered orbit-fixed (ACOF)
Its origin O_O is located at the center of mass of the asteroid, but its orientation with respect to the asteroid changes as this latter revolves around the Sun. The X_O-axis lies along the Sun-asteroid line and points away from the Sun, while the Z_O-axis is normal to the plane of Eros's heliocentric orbit, in the same direction of the angular momentum. The Y_O-axis completes the right-handed system. This reference frame is particularly useful because it allows to identify Sun-terminator orbits, which lie on the plane $O_O Y_O Z_O$. It is identified by the symbol $\mathcal{F}_O$, and its basis vectors are labelled as $\hat{\boldsymbol{x}}_O$, $\hat{\boldsymbol{y}}_O$, and $\hat{\boldsymbol{z}}_O$.

Perifocal (PWQ)
Its origin O_P is located at the center of mass of the asteroid. The X_P-axis is directed towards the periapsis of the spacecraft orbit, positive away from the asteroid, whereas the Z_P-axis is parallel to the angular momentum vector, and thus orthogonal to the plane in which the spacecraft orbits the asteroid. The Y_P-axis completes the right-handed system. This frame is identified by the symbol $\mathcal{F}_P$, and its basis vector are labelled as $\hat{\boldsymbol{p}}$, $\hat{\boldsymbol{w}}$, and $\hat{\boldsymbol{q}}$.

Radial-transverse-normal (RTN)
Its origin O_R is located at the center of mass of the spacecraft. The R-axis (radial) points away from the center of the asteroid and along the radial component of the gravitational acceleration, while the N-axis (normal, or *cross-track*) is normal to the orbit plane in the direction of the angular momentum. The T-axis (transverse, or *along-track*) completes the right-handed system. In general, the along-track direction does not coincide with the velocity, although this is the case for circular orbits. This reference frame is identified by the symbol $\mathcal{F}_R$, and its basis vectors are labelled as $\hat{\boldsymbol{r}}$, $\hat{\boldsymbol{t}}$, and $\hat{\boldsymbol{n}}$.

Body
The body frame is fixed to the spacecraft. Its origin O_B coincides with the center of mass of the vehicle, while the axes X_B, Y_B, and Z_B lie along the spacecraft's main axes of inertia. In particular, the Z_B-axis is aligned with the science deck. This reference frame is mainly used to describe the rotational motion of the vehicle, especially the pointing direction of the instruments (camera, lidar), the solar panels, the antenna, and the thrusters. Despite attitude dynamics will not be simulated, the body reference frame is still required because it identifies the directions available for thrusting, as the engines of the RCS are aligned with the spacecraft body axes. This reference frame is identified by the symbol $\mathcal{F}_B$, and its basis vectors are labelled as $\hat{\boldsymbol{x}}_B$, $\hat{\boldsymbol{y}}_B$, and $\hat{\boldsymbol{z}}_B$.

3.2 State representation

Since only the translational motion will be modeled, the state of the spacecraft is uniquely identified by six components, three for the position and three for the velocity. Three coordinate sets will be used throughout this work to represent the spacecraft's state:

- Cartesian coordinates ($\mathcal{C}$): these provide the simplest and most flexible way to describe the equations of motion in an inertial frame. They are employed both for propagating dynamics and computing guidance commands.
- Spherical coordinates ($\mathcal{S}$): these are employed exclusively to compute the gravitational acceleration exerted by the asteroid.
- Orbital elements ($\mathcal{O}$): these are used to model the motion of Eros around the Sun. Furthermore, this representation improves the quality of the analysis, as it offers deeper insights into the physics of the problem.

Cartesian coordinates
Cartesian coordinates are generally used to describe the position and velocity of the spacecraft with respect to either the ACI or ACAF frame. Position $\boldsymbol{r}$ and velocity $\boldsymbol{v}$ are identified by the following variables:

$$\boldsymbol{r} = \begin{pmatrix} x & y & z \end{pmatrix}^T \qquad \boldsymbol{v} = \begin{pmatrix} v_x & v_y & v_z \end{pmatrix}^T \tag{3.1}$$

The norms of the position and velocity are identified by r and v.

Spherical coordinates
Only the spherical position is of interest for this work, thus the spherical velocity components are not introduced:

$$\boldsymbol{r} = \begin{pmatrix} r & \phi & \lambda \end{pmatrix}^T \tag{3.2}$$

where r is the distance between the center of mass of the vehicle and the origin of the reference frame, ϕ is the latitude and λ is the longitude. The longitude is measured positively from East to West ($0° \leq \lambda \leq 360°$), while the latitude is positive in the north direction and negative to the south ($-90° \leq \phi \leq 90°$). As will be shown later, it is common to express spherical coordinates with respect to a rotating frame such as the ACAF frame. In this case, the symbol $\tilde{\lambda}$ will be used to refer to the co-rotating longitude, which is simply:

$$\tilde{\lambda} = \lambda + \omega_A t \tag{3.3}$$

Orbital elements
The solution to the two-body problem is a conic section which is uniquely identified by a set of six orbital elements, or Kepler elements. The state vector in terms of Kepler elements is the following:

$$\boldsymbol{x} = \begin{pmatrix} a & e & i & \Omega & \omega & \theta \end{pmatrix}^T \tag{3.4}$$

where a is the semi-major axis, e is the eccentricity, i the inclination, Ω the right ascension of the ascending node (RAAN), ω the argument of periapsis and θ the true anomaly. The semi-major axis describes the size of the orbit, while the eccentricity defines its shape. The orientation of the orbital plane in space is given by i and Ω, while ω describes how the orbit is oriented within the orbital plane. Finally, θ describes the position of the spacecraft along the orbit. Other relevant quantities to describe a Kepler orbit are the eccentricity vector $\boldsymbol{e}$ and the angular momentum vector $\boldsymbol{h}$, defined as:

$$\boldsymbol{e} = \frac{\boldsymbol{v} \times \boldsymbol{h}}{\mu} - \frac{\boldsymbol{r}}{r} \tag{3.5}$$

$$\boldsymbol{h} = \boldsymbol{r} \times \boldsymbol{v} \tag{3.6}$$

3.3 Coordinate and frame transformations

3.3.1 State conversions

Cartesian - Orbital ($\mathcal{C} \leftrightarrow \mathcal{O}$)
To compute the orbital elements from a given Cartesian state, the following procedure has to be followed:

$$a = \frac{1}{2}v^2 - \frac{\mu}{r} \tag{3.7}$$

$$e = ||\boldsymbol{e}|| \tag{3.8}$$

$$i = \arccos\left(\frac{\boldsymbol{h} \cdot \boldsymbol{z}_I}{\boldsymbol{h}}\right) \tag{3.9}$$

$$\Omega = \begin{cases} \arccos\left(\hat{\boldsymbol{N}} \cdot \boldsymbol{x}_I\right) & \Omega \in [0, \pi] \\ 2\pi - \arccos\left(\hat{\boldsymbol{N}} \cdot \boldsymbol{x}_I\right) & \Omega \in [\pi, 2\pi] \end{cases} \tag{3.10}$$

$$\omega = \begin{cases} \arccos\left(\frac{\boldsymbol{e} \cdot \hat{\boldsymbol{N}}}{e}\right) & \omega \in [0, \pi] \\ 2\pi - \arccos\left(\frac{\boldsymbol{e} \cdot \hat{\boldsymbol{N}}}{e}\right) & \omega \in [\pi, 2\pi] \end{cases} \tag{3.11}$$

$$\theta = \begin{cases} \arccos\left(\frac{\boldsymbol{r} \cdot \boldsymbol{e}}{re}\right) & \theta \in [0, \pi] \\ 2\pi - \arccos\left(\frac{\boldsymbol{r} \cdot \boldsymbol{e}}{re}\right) & \theta \in [\pi, 2\pi] \end{cases} \tag{3.12}$$

where $\hat{\boldsymbol{N}}$ is the unit vector along the line of nodes, defined as $\hat{\boldsymbol{N}} = \frac{\boldsymbol{z}_I \times \boldsymbol{h}}{||\boldsymbol{z}_I \times \boldsymbol{h}||}$. The opposite procedure instead requires to rotate the state into the PWQ frame:

$$\boldsymbol{r}^P = \frac{a(1-e^2)}{1 + e\cos\theta} \begin{pmatrix} \cos\theta \\ \sin\theta \\ 0 \end{pmatrix} \qquad \boldsymbol{v}^P = \sqrt{\frac{\mu}{a(1-e^2)}} \begin{pmatrix} -\sin\theta \\ e + \cos\theta \\ 0 \end{pmatrix} \tag{3.13}$$

Cartesian - Spherical ($\mathcal{C} \leftrightarrow \mathcal{S}$)
The following relations can be used to move between spherical and Cartesian position representations:

$$\begin{cases} r &= \sqrt{x^2+y^2+z^2} \\ \phi &= \arccos \frac{z}{r} \\ \lambda &= \arccos \frac{x}{\sqrt{x^2+y^2}} \end{cases} \quad \begin{cases} x &= r\cos\phi\cos\lambda \\ y &= r\cos\phi\sin\lambda \\ z &= r\sin\phi \end{cases} \tag{3.14}$$

3.3.2 Frame rotations

The transformation from a generic A-frame to an equally generic B-frame can be expressed through the use of a rotation matrix $\boldsymbol{C}_{B/A}$. This matrix is always orthonormal, therefore the inverse transformation can be obtained by using $\boldsymbol{C}_{A/B} = \boldsymbol{C}_{B/A}^T$. In particular, any transformation can always be expressed as a series of sequential unit-axis rotations, which means that any rotation matrix can always be obtained as the product of at most three rotation matrices:

$$\boldsymbol{C}_X(\Theta) = \begin{bmatrix} 1 & 0 & 0 \\ 0 & \cos\Theta & \sin\Theta \\ 0 & -\sin\Theta & \cos\Theta \end{bmatrix} \boldsymbol{C}_Y(\Theta) = \begin{bmatrix} \cos\Theta & 0 & -\sin\Theta \\ 0 & 1 & 0 \\ \sin\Theta & 0 & \cos\Theta \end{bmatrix} \boldsymbol{C}_Z(\Theta) = \begin{bmatrix} \cos\Theta & \sin\Theta & 0 \\ -\sin\Theta & \cos\Theta & 0 \\ 0 & 0 & 1 \end{bmatrix} \tag{3.15}$$

The matrices above describe a rotation about an arbitrary angle Θ around the $X-$, $Y-$, and Z-axis of a generic reference frame. The specific rotation matrices for the frames involved within this work are described briefly hereafter. Also, a summary is provided in Table 3.1.

J2000 to asteroid inertial ($\mathcal{F}_{J2000} \rightarrow \mathcal{F}_I$)
This matrix describes the attitude of the asteroid body with respect to the J2000 frame, and it is based on the longitude of Eros's prime meridian at J2000, the declination, and the right ascension of its pole. It is based on the conventions established in Archinal et al. (2018).

$$\begin{aligned} \boldsymbol{C}_{I/J2000} &= \boldsymbol{C}_Z(W)\boldsymbol{C}_X\left(\frac{\pi}{2}-\delta\right)\boldsymbol{C}_Z\left(\frac{\pi}{2}+\alpha\right) = \\ &= \begin{bmatrix} -\cos W\sin\alpha - \cos\alpha\sin W\sin\delta & \cos W\cos\alpha - \sin W\sin\alpha\sin\delta & \cos\delta\sin W \\ \sin W\sin\alpha - \cos W\cos\alpha\sin\delta & -\cos\alpha\sin W - \cos W\sin\alpha\sin\delta & \cos W\cos\delta \\ \cos\alpha\cos\delta & \cos\delta\sin\alpha & \sin\delta \end{bmatrix} \end{aligned} \tag{3.16}$$

Asteroid-fixed to asteroid inertial ($\mathcal{F}_A \rightarrow \mathcal{F}_I$)
Assuming that at the initial epoch, the axis X_A is aligned with X_I, it follows that the rotation matrix to convert a vector from the ACAF frame to the ACI corresponds to a rotation about the Z-axis:

$$\boldsymbol{C}_{I/A} = \boldsymbol{C}_Z(-\omega_A t) = \begin{bmatrix} \cos\omega_A t & -\sin\omega_A t & 0 \\ \sin\omega_A t & \cos\omega_A t & 0 \\ 0 & 0 & 1 \end{bmatrix} \tag{3.17}$$

Applying this transformation to an inertial, Cartesian position vector is equivalent to moving between the inertial and co-rotating spherical coordinates, as mentioned previously.

Orbit-fixed to J2000/radial-transverse-normal to asteroid inertial ($\mathcal{F}_O \rightarrow \mathcal{F}_{J2000}/\mathcal{F}_R \rightarrow \mathcal{F}_I$)
The RTN and ACOF frames share the same orientation but have different origins (the spacecraft and the asteroid, respectively). It is possible to derive the rotation matrix in terms of orbital elements by applying three consecutive rotations: the first one about the angular momentum vector by an angle $-\nu$, the second one about axis $\boldsymbol{X}_I$ by an angle $-i$, and the last one about $\boldsymbol{Z}_I$ by an angle $-\Omega$.

$$\begin{aligned} \boldsymbol{C}_{J2000/O} &= \boldsymbol{C}_{I/R} = \boldsymbol{C}_Z(-\Omega)\boldsymbol{C}_X(-i)\boldsymbol{C}_Z(-\nu) = \\ &= \begin{bmatrix} \cos\nu\cos\Omega - \sin\nu\cos i\sin\Omega & -\sin\nu\cos\Omega - \cos\nu\cos i\sin\Omega & \sin i\sin\Omega \\ \cos\nu\sin\Omega + \sin\nu\cos i\cos\Omega & -\sin\nu\sin\Omega + \cos\nu\cos i\cos\Omega & -\sin i\cos\Omega \\ \sin\nu\sin i & \cos\nu\sin i & \cos i \end{bmatrix} \end{aligned} \tag{3.18}$$

where $\nu = \omega + \theta$ is referred to as true longitude. When considering the orbit-fixed frame, then the orbital elements shall be those corresponding to Eros's orbit, and the obtained vector is in the J2000 frame. In the case of the RTN frame, they shall represent the spacecraft orbit around the asteroid, and the computed vector is relative to the ACI frame.

This rotation matrix can be computed in a second manner. In fact, it is relatively easy to obtain the components of the unit vectors that describe the ACOF/RTN frame with respect to the J2000/ACI frame based on the spacecraft/asteroid state vector at a given time:

$$\hat{\boldsymbol{r}} = \frac{\boldsymbol{r}}{||\boldsymbol{r}||} \quad \hat{\boldsymbol{n}} = \frac{\boldsymbol{r} \times \boldsymbol{v}}{||\boldsymbol{r} \times \boldsymbol{v}||} \quad \hat{\boldsymbol{t}} = \hat{\boldsymbol{r}} \times \hat{\boldsymbol{n}} \tag{3.19}$$

The components of these unit vectors are referred to as direction cosines, therefore the rotation matrix is simply obtained by applying the definition of direction cosine matrix:

$$\boldsymbol{C}_{J2000/O} = \boldsymbol{C}_{I/R} = \begin{bmatrix} \hat{\boldsymbol{r}} & \hat{\boldsymbol{t}} & \hat{\boldsymbol{n}} \end{bmatrix} \tag{3.20}$$

Perifocal to asteroid inertial ($\mathcal{F}_P \rightarrow \mathcal{F}_I$)
The transformation is essentially the same as for the RTN frame, but the rotation about the angular momentum vector is simply by an angle $-\omega$:

$$\boldsymbol{C}_{I/P} = \boldsymbol{C}_Z(-\Omega)\boldsymbol{C}_X(-i)\boldsymbol{C}_Z(-\omega) \tag{3.21}$$

Table 3.1: List of relevant reference frames and corresponding transformations.

Acronym	Symbol	Description	Transformation
ACI	$\mathcal{F}_I$	Asteroid-centered, inertial	-
J2000	$\mathcal{F}_{J2000}$	Asteroid-centered, inertial	$\boldsymbol{C}_{I/J2000} = \boldsymbol{C}_Z(W)\boldsymbol{C}_X\left(\frac{\pi}{2} - \delta\right)\boldsymbol{C}_Z\left(\frac{\pi}{2} + \alpha\right)$
ACAF	$\mathcal{F}_A$	Asteroid-centered, asteroid-fixed	$\boldsymbol{C}_{I/A} = \boldsymbol{C}_Z(-\omega_A t)$
ACOF	$\mathcal{F}_O$	Asteroid-centered, orbit-fixed	$\boldsymbol{C}_{J2000/O} = \boldsymbol{C}_X(-i)\boldsymbol{C}_Z(-\Omega)\boldsymbol{C}_Z(-\nu)$
RTN	$\mathcal{F}_R$	Spacecraft-centered	$\boldsymbol{C}_{I/R} = \boldsymbol{C}_X(-i)\boldsymbol{C}_Z(-\Omega)\boldsymbol{C}_Z(-\nu)$
PWQ	$\mathcal{F}_P$	Asteroid-centered, perifocal	$\boldsymbol{C}_{I/P} = \boldsymbol{C}_X(-i)\boldsymbol{C}_Z(-\Omega)\boldsymbol{C}_Z(-\omega)$

3.4 Asteroid environment

For an Earth-orbiting spacecraft, all perturbations combined are generally less than one part in a thousand compared with the dominant two-body term due to a spherical Earth (Russell, 2012). As a result, Keplerian motion provides a sufficient approximation when high accuracy is unnecessary. In contrast, the environment near irregularly shaped small bodies is far more hostile. Strong gravitational and non-gravitational perturbations make orbital trajectories highly unstable, often leading to impact or escape within hours or days without active control (Scheeres, 2014).

An overview of the sources of acceleration acting on a spacecraft in the proximity of an asteroid is given in Fig. 3.2. It is well established that the main disturbances are generally three, namely the irregularities of the gravity field originating from the non-homogeneous mass distribution, solar radiation pressure, and the solar third-body perturbation. Additionally, other phenomena are worth noting, even if less significant for this study. These include the Yarkovsky and YORP (Yarkovsky–O'Keefe–Radzievskii–Paddack) effects, which lead to semimajor axis drift (e.g., 10^{-4} au in one million years) and spin vector changes over extremely long timescales (Lissauer and de Pater, 2019; Bottke et al., 2006). Additionally, forces from asteroid albedo, infrared radiation pressure, and thermal imbalances across the spacecraft may also become relevant in high-precision applications, such as touchdown or soft-landing maneuvers (Williams et al., 2018). Planetary perturbations from terrestrial planets and Jupiter are generally negligible unless a close planetary flyby occurs, a situation that happens only infrequently (Scheeres, 2012b,c). Evidently, the impact of these phenomena on the short-term dynamics of a nearby spacecraft is too small to warrant consideration in the current scope.

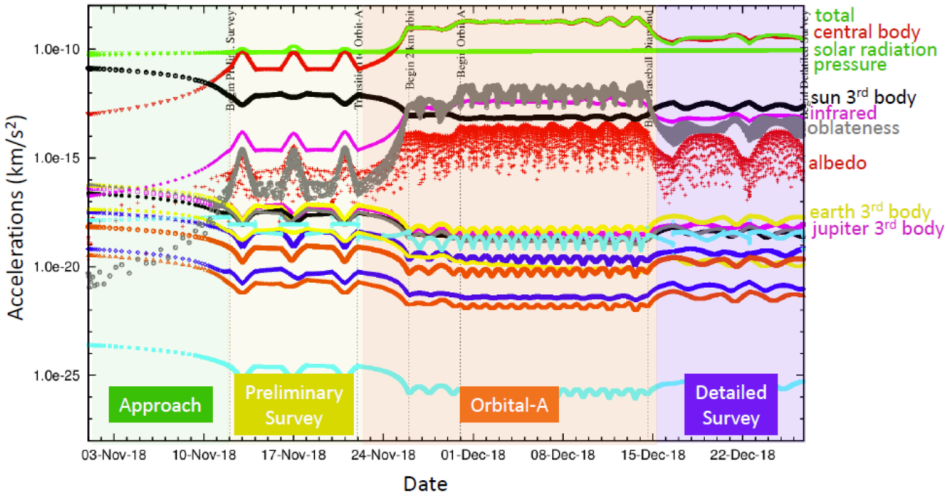

Figure 3.2: Accelerations experienced by OSIRIS-REx at Bennu (Everett et al., 2017).

3.4.1 Gravity field

Gravitational field modeling is the foundation for analyzing orbital motion, particularly for proximity operations around asteroids. The irregular shape and non-homogeneous mass distribution of small bodies result in a highly irregular gravitational field, characterized by rapid variations in intensity and direction which lead to complex, nonlinear dynamics in their proximity. Typically, the gravitational field is described through the gravitational potential:

$$\mathcal{U}(\boldsymbol{r}) = G \int_A \frac{dm(\boldsymbol{\rho})}{|\boldsymbol{r} - \boldsymbol{\rho}|} \tag{3.22}$$

where G is the gravitational constant, $\boldsymbol{r}$ is the position vector of the massless spacecraft, $\boldsymbol{\rho}$ is the position vector of the infinitesimal mass element dm and A is the collection of all mass elements. Gravitational field modeling can be performed using three main approaches, which exhibit a different degree of accuracy and complexity: point mass(es), series approximation, or three-dimensional approximation. Series approximation methods model the gravitational potential energy by an infinite series of specific functions, while three-dimensional methods approximate the geometry of the asteroid as a simple triaxial ellipsoid or as a complex polyhedron (Cui and Qiao, 2014).

Point mass

The most simple formulation that can be used to model the asteroid's gravity field is that of a point mass. Assuming a spherical distribution of mass M and constant density, the gradient of Eq. (3.22) becomes:

$$\boldsymbol{a}_g = \nabla \mathcal{U}(\boldsymbol{r}) = -\frac{GM}{||\boldsymbol{r}||^3}\boldsymbol{r} = -\frac{\mu}{||\boldsymbol{r}||^3}\boldsymbol{r} \tag{3.23}$$

where μ is the gravitational parameter of the body. Despite its attractive simplicity, the point mass formulation does not consider latitudinal or longitudinal variations in the body's mass distribution. In this case, the gravitational potential can be expanded in series, as illustrated in the following paragraph.

Spherical harmonic expansion

The gravitational potential in Eq. (3.22) satisfies Laplace's equation $\nabla^2 \mathcal{U} = 0$ outside of the body (Scheeres, 2012b). This can be exploited by constructing a set of orthogonal solutions to Laplace's equation and choosing the coefficients of these expansions to match with the actual potential function. Multiple harmonic series models exist, each obtained by adopting a particular coordinate system to solve Laplace's equation through separation of variables. This methodology identifies a region of convergence

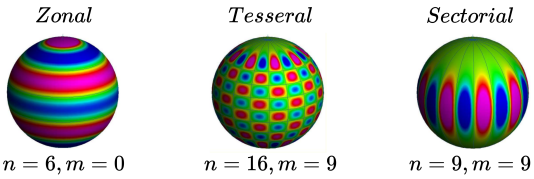

Figure 3.3: Spherical harmonics mapped to the surface of a generic sphere (Barthelmes, 2009).

for the corresponding series where the models are subject only to omission errors representing the residual field variations not accounted for by the finite degree expansions. Outside of these convergence regions, the models are susceptible to amplification of omission errors and possible divergence effects.

The most common series is known as *spherical harmonic* expansion (SHE), which is obtained by solving the equation of Laplace through separation of variables in terms of spherical coordinates. The general form for the spherical harmonic potential of a gravity field is then:

$$\mathcal{U}(r,\delta,\lambda) = \frac{\mu}{r}\left(1 + \sum_{n=1}^{\infty}\sum_{m=0}^{m=n}\left(\frac{R_e}{r}\right)^n P_{nm}(\sin\phi)[C_{nm}\cos m\tilde{\lambda} + S_{nm}\sin m\tilde{\lambda}]\right) \tag{3.24}$$

where R_e is a reference radius of the body, P_{nm} are the Associated Legendre functions of the first kind, and C_{nm} and S_{nm} are referred to as gravity field harmonic coefficients of degree n and order m.

Each combination of n and m represents a distinct kind of gravity field deviation from a perfectly spherical one. For example, when the order m is set to zero, only the coefficients C_{n0} remain. These are referred to as *zonal* terms, as they represent the variations of the gravity field with the latitude, as indicated in Fig. 3.3. Among them, the most relevant is usually C_{20}, which represents the gravitational disturbance caused by the oblateness of a body. The remaining terms, which are not longitudinally symmetric, are referred to as *tesseral*, if $n \neq m$, or *sectorial*, in the opposite case. In particular, second-order tesseral coefficients S_{21} and C_{21} vanish if the body rotation axis is aligned with its principal inertia axis. It is also noted that the terms of degree 1 (C_{10}, C_{11}, S_{11}) describe the location of the center of mass, hence they are also zero when this is assumed to be located at the origin of the reference frame. A slightly different formulation than Eq. (3.24) can be used to reduce numerical errors, since the conventional gravitational coefficients tend to become very small when n, m become large (Melman et al., 2009). Such formulation replaces C_{nm}, S_{nm} and P_{nm} with normalized coefficients and normalized Legendre polynomials, as defined by Kaula (1966):

$$C_{nm} = \bar{C}_{nm}\bar{\mathcal{N}}_{nm} \quad S_{nm} = \bar{S}_{nm}\bar{\mathcal{N}}_{nm} \quad P_{nm} = \frac{\bar{P}_{nm}}{\bar{\mathcal{N}}_{nm}} \tag{3.25}$$

$$\bar{\mathcal{N}}_{nm} = \sqrt{\frac{(2-\delta_{0m})(2n+1)(n-m)!}{(n+m)!}} \tag{3.26}$$

where δ_{0m} is the Kronecker delta. The Cartesian components of the acceleration in the body-fixed frame (ACAF) can then be computed based on the following equations:

$$a_{gx} = \left(\frac{1}{r}\frac{\partial\mathcal{U}}{\partial r} - \frac{z}{r^2\sqrt{x^2+y^2}}\frac{\partial\mathcal{U}}{\partial\phi}\right)x - \left(\frac{1}{x^2+y^2}\frac{\partial\mathcal{U}}{\partial\tilde{\lambda}}\right)y \tag{3.27}$$

$$a_{gy} = \left(\frac{1}{r}\frac{\partial\mathcal{U}}{\partial r} - \frac{z}{r^2\sqrt{x^2+y^2}}\frac{\partial\mathcal{U}}{\partial\phi}\right)y + \left(\frac{1}{x^2+y^2}\frac{\partial\mathcal{U}}{\partial\tilde{\lambda}}\right)x \tag{3.28}$$

$$a_{gz} = \frac{1}{r}\frac{\partial\mathcal{U}}{\partial r}z + \frac{\sqrt{x^2+y^2}}{r^2}\frac{\partial\mathcal{U}}{\partial\phi} \tag{3.29}$$

$$\frac{\partial \mathcal{U}}{\partial r} = -\frac{\mu}{r^2}\left[1 + \sum_{n=1}^{\infty}\sum_{m=0}^{n}\left(\frac{R_e}{r}\right)^n (n+1)\overline{P}_{nm}(\sin\phi)\left(\overline{C}_{nm}\cos m\tilde{\lambda} + \overline{S}_{nm}\sin m\tilde{\lambda}\right)\right] \tag{3.30}$$

$$\frac{\partial \mathcal{U}}{\partial \tilde{\lambda}} = \frac{\mu}{r}\sum_{n=1}^{\infty}\sum_{m=0}^{n}\left(\frac{R_e}{r}\right)^n m\overline{P}_{nm}(\sin\phi)\left(\overline{S}_{nm}\cos m\tilde{\lambda} - \overline{C}_{nm}\sin m\tilde{\lambda}\right) \tag{3.31}$$

$$\frac{\partial \mathcal{U}}{\partial \phi} = \frac{\mu}{r}\sum_{n=1}^{\infty}\sum_{m=0}^{n}\left(\frac{R_e}{r}\right)^n \left[\overline{P}_{n,m+1}(\sin\phi) - m\tan\phi\overline{P}_{nm}(\sin\phi)\right] \left(\overline{C}_{nm}\cos m\tilde{\lambda} + \overline{S}_{nm}\sin m\tilde{\lambda}\right) \tag{3.32}$$

Spherical harmonics can theoretically represent any potential field, even for highly non-spherical asteroids, provided the series is sufficiently long. In practice, the series is truncated to a given degree and order (D/O) to balance accuracy and complexity. For planetary bodies, whose shape is generally quite similar to a sphere, high accuracy can be achieved with relatively few terms. However, for highly irregular bodies like asteroids, the mismatch between the mass-enclosing reference sphere (the *Brillouin* sphere) and the body's actual shape causes the series to diverge within a significant region of *flyable* space, making this formulation unsuitable for landing scenarios.

Alternative formulations address these limitations by using other basis functions to construct a solution to the Laplace equation. The *ellipsoidal harmonic* expansion (EHE) exploits ellipsoidal coordinates defined relative to a triaxial ellipsoid, which better approximates elongated shapes and extends the region of convergence closer to the surface. For a given degree, this approach is more accurate near the Brillouin sphere than the SH model, as illustrated by Fig. 3.4. However, it is computationally intensive due to the absence of recurrence relations for Lamé functions, which are used to construct the potential formulation. For instance, for a reference ellipsoid with semi-axes 3x2x1 km, these functions can reach values on the order of 10^{128}, leading to arithmetic overflow[3] and limiting practical computation to low degrees (Reimond and Baur, 2016). An intermediate solution is the *spheroidal harmonic* expansion, where the asteroid is modeled as a biaxial ellipsoid, either an *oblate spheroid* (for planetary bodies) or a *prolate spheroid* (for elongated bodies such as asteroids). This model is also affected by significant computational burden due to the evaluation of Legendre functions of the second kind (Fukushima, 2014).

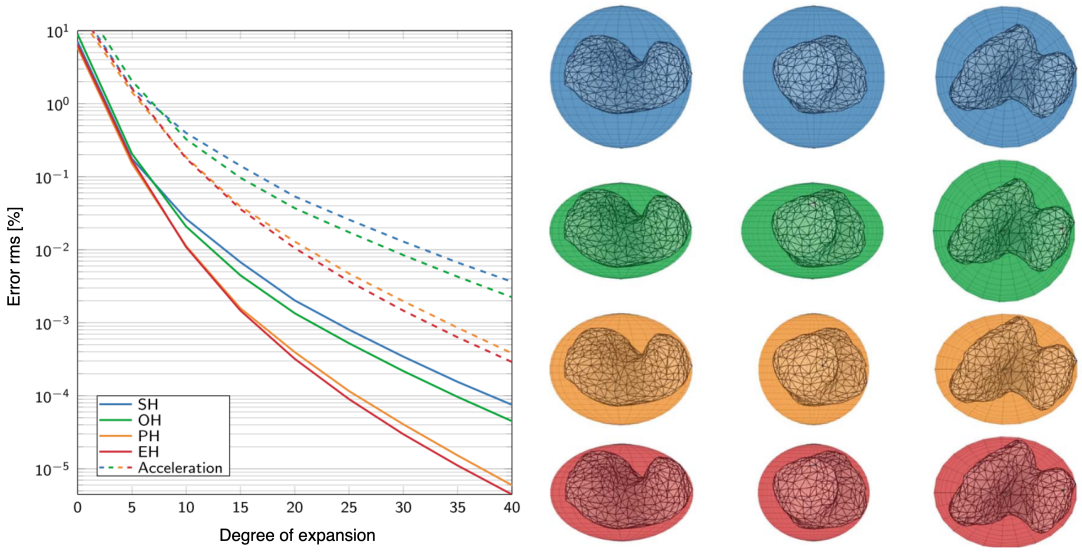

Figure 3.4: Gravity errors when using spherical (SH), spheroidal oblate (OH), spheroidal prolate (PH) and ellipsoidal (EH) harmonics for comet 67P/Churyumov–Gerasimenko (Reimond and Baur, 2016). On the right, the convergence region for each model.

[3]According to Romain and Jean-Pierre (2001), 64-bit arithmetic limits the maximum computable EHE degree to about 15.

Efforts to mitigate the complexity associated with these methods include logarithmic identities (Reimond and Baur, 2016), analytical relations to derive EH from SH coefficients (Dechambre and Scheeres, 2002), and *internal* spherical harmonics (Hesar et al., 2016). However, further investigation of these models was deemed beyond the scope of this research, and thus only the SH expansion was considered.

Triaxial ellipsoid

The most simple method to approximate the three-dimensional figure of an asteroid lies in adopting a constant-density triaxial ellipsoid. Triaxial ellipsoid modeling has three advantages: the small amount of calculation, easy acquisition of data by astronomical observation, and intuitive representation of the gravitational field (Cui and Qiao, 2014). Since the shape of many asteroids resembles that of an ellipsoid, it can represent a significant improvement over the point mass model and often offers a reasonable approximation to small bodies' gravity fields. Given the three semi-axes $c \leq b \leq a$, the closed-form solution of the gravitational potential is:

$$\mathcal{U}(\boldsymbol{r}) = -\frac{3\mu}{4}\int_{\zeta(\boldsymbol{r})}^{\infty}\left(\frac{x^2}{a^2+u}+\frac{y^2}{b^2+u}+\frac{z^2}{c^2+u}-1\right)\frac{du}{\sqrt{(a^2+u)(b^2+u)(c^2+u)}} \tag{3.33}$$

where the position vector $\boldsymbol{r}$ is expressed in a body-fixed frame and $\zeta(\boldsymbol{r})$ is determined by setting the integrand equal to zero. Despite this formulation may appear challenging given that it is formulated as an integral, a relatively simple and robust approach exists based on the computation of Carlson's Elliptic Integrals (Scheeres, 2012b). The detailed implementation of this gravity model combined with the use of elliptic integrals is given in Appendix B.

Polyhedron

An accurate model to describe the gravity of an irregular body is the polyhedron, for which Werner and Scheeres (1997) describe closed-form solutions given an arbitrary constant density. A polyhedron is a three-dimensional body whose surface is approximated by many planar facets (polygons), which allow to model irregular features such as craters. The general formula for the potential of a polyhedron is:

$$U(\boldsymbol{r}) = \frac{G\rho}{2}\left(\sum_{e\in\text{edges}}\boldsymbol{r}_e\cdot\boldsymbol{E}_e\cdot\boldsymbol{r}_e L_e - \sum_{f\in\text{facets}}\boldsymbol{r}_f\cdot\boldsymbol{F}_f\cdot\boldsymbol{r}_f\omega_f\right) \tag{3.34}$$

$$\frac{\partial U}{\partial \boldsymbol{r}} = -G\rho\left(\sum_{e\in\text{edges}}\boldsymbol{E}_e\cdot\boldsymbol{r}_e L_e - \sum_{f\in\text{facets}}\boldsymbol{F}_f\cdot\boldsymbol{r}_f\omega_f\right) \tag{3.35}$$

where $\boldsymbol{r}_e$ represents the vector from any point on the edge to $\boldsymbol{r}$ (the point where the gravity is to be calculated) and $\boldsymbol{r}_f$ denotes the vector from any point on face f to $\boldsymbol{r}$. Also, $\boldsymbol{E}_e$ is the edge dyad, $\boldsymbol{F}_f$ is the face dyad, L_e represents the potential of the edge, and ω_f is the solid angle subtended by face f when viewed from the field point. These quantities are defined as:

$$\boldsymbol{E}_e = \hat{\boldsymbol{n}}_f\hat{\boldsymbol{n}}_e^f + \hat{\boldsymbol{n}}_{f'}\hat{\boldsymbol{n}}_e^{f'} \qquad \boldsymbol{F}_f = \hat{\boldsymbol{n}}_f\hat{\boldsymbol{n}}_f \qquad L_e = \int_e\frac{1}{r}ds = ln\frac{r_i^e+r_j^e+e_{ij}}{r_i^e+r_j^e-e_{ij}} \tag{3.36}$$

$$\omega_f = 2\arctan\frac{\boldsymbol{r}_i\cdot\boldsymbol{r}_j\times\boldsymbol{r}_k}{r_ir_jr_k + r_i\left(\boldsymbol{r}_j\cdot\boldsymbol{r}_k\right) + r_j\left(\boldsymbol{r}_k\cdot\boldsymbol{r}_i\right) + r_k\left(\boldsymbol{r}_i\cdot\boldsymbol{r}_j\right)} \tag{3.37}$$

The terminology introduced in the equations above is clarified by Fig. 3.5a. Specifically, a facet is discretized in l triangular facets, which leads to $2l-4$ facets and $3(l-2)$ edges. Each face is then associated with a set of three vertex vectors $\boldsymbol{r}_i^f, i=1,2,3$, such that the three vertices taken in order are counter-clockwise about the normal face, $\hat{\boldsymbol{n}}_f$. Associated with each edge e are two vertices $\boldsymbol{r}_i^e, i=1,2$, and two facets, f and f', which meet at the edge. Finally, it is necessary to introduce the edge normals $\hat{\boldsymbol{n}}_e^f$ and $\hat{\boldsymbol{n}}_e^{f'}$, which denote the vectors that are normal to the edge, point away from the face, and are normal to $\hat{\boldsymbol{n}}_f$,$\hat{\boldsymbol{n}}_{f'}$, respectively.

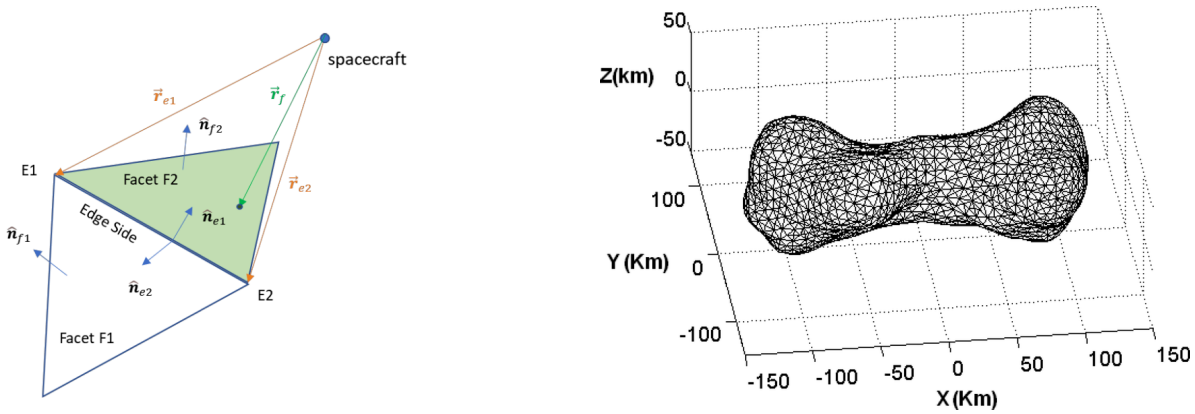

(a) Detail of polyhedron geometry (Xie and Bernelli Zazzera, 2023).

(b) Polyhedron model of asteroid (216) Kleopatra based on shape model with 4092 facets (Chanut et al., 2015).

Figure 3.5: Polyhedron model.

The great advantage of this gravity model is that it allows to compute exactly the gravity field of a body for any given shape on any point of its irregular surface. While the nominal model assumes a constant density, it is possible to include additional potential terms to model density heterogeneity, as done by Spee (2022). The real drawback of this method comes from the computational burden required to evaluate the model, which leads to evaluation times that are slower by one or two orders of magnitudes compared to simpler models and even to spherical harmonics (Melman et al., 2009).

Comparison and discussion

Previous work has already investigated differences in accuracy and computational cost when employing different gravity models. Specifically, Melman et al. (2009) performed a comparative study around asteroid Steins, highlighting that a 32x32 spherical harmonics model requires 1/10 of the computational time that is necessary for a full polyhedron model while attaining similar accuracy. This work also highlighted the relatively good balance between accuracy and computation time that a SH expansion with low D/O can achieve.

A summary of the aspects that characterize the four gravity models considered for this work is reported in Table 3.2. Evidently, the low computational cost and dependency from a few parameters outline the point mass and the triaxial ellipsoid models as ideal candidates for onboard implementations. Additionally, based on the considerations that will be raised in Sec. 3.4.3, also the SH expansion considering only C_{20} and C_{22} will be considered for this purpose. In contrast, the SH expansion with high D/O and the polyhedron model will serve to model real dynamics outside and inside the Brillouin sphere, respectively.

Table 3.2: Comparison of the gravity models considered for this work.

Gravity model	Advantages	Disadvantages
Point mass	- Simplest mathematical model. - Accurate far away from the body.	- Very inaccurate near bodies with non-spherical mass distributions.
Triaxial ellipsoid	- Low computational cost. - Small number of parameters.	- Relies on constant-density assumption. - Loses attractiveness for rounded bodies.
SH expansion	- Models internal density variations. - High accuracy with low order.	- Medium-high computational cost. - Diverges inside the Brillouin sphere. - Requires many parameters.
Polyhedron	- Works inside the Brilluoin sphere. - Allows to detect impacts.	- Highest computational cost. - Relies on constant-density assumption. - Requires a shape model to be available.

Table 3.3: Sphere of influence and Hill radius for Eros.

-	r_{SOI} [km]	r_H [km]
Perihelion	275	1756
Aphelion	433	2760

3.4.2 Solar perturbations

Solar gravitational effects

The third-body perturbation exerted by the Sun acts both on the asteroid and on the orbiter, implying that the net effect is remarkably less pronounced the closer the vehicle is to the asteroid. When computing a third-body acceleration, it is essential to specify the origin of the reference frame:

$$(\boldsymbol{a}_{Ss})_A = \boldsymbol{a}_{Ss} - \boldsymbol{a}_{SA} \tag{3.38}$$

where the notation $(\boldsymbol{a}_{Ss})_A$ indicates the acceleration exerted by the Sun over the spacecraft in an inertial frame centered at the asteroid. The formula above highlights that to predict the motion of the spacecraft relative to the small body, the absolute acceleration that the spacecraft feels because of the Sun ($\boldsymbol{a}_{Ss}$) has to be compensated for the one that the small body also feels due to the Sun attraction ($\boldsymbol{a}_{SA}$). Assuming a point mass gravity model for the Sun, the net acceleration can then be computed as:

$$\boldsymbol{a}_{3BP} = -\mu_\odot \frac{\boldsymbol{r}_\odot}{||\boldsymbol{r}_\odot||^3} - \mu_\odot \frac{\boldsymbol{r} - \boldsymbol{r}_\odot}{||\boldsymbol{r} - \boldsymbol{r}_\odot||^3} \tag{3.39}$$

where $\mu_\odot$ is the gravitational parameter of the Sun, and $\boldsymbol{r}$ and $\boldsymbol{r}_\odot$ are respectively the position vector of the spacecraft and the Sun relative to the asteroid. In the formulation above, the first term represents the acceleration exerted by the Sun on the asteroid (it is assumed that the latter is massless compared to the Sun), while the second is on the spacecraft itself. Notably, $\boldsymbol{a}_{3BP}$ tends to zero as the distance between the asteroid and the spacecraft reduces.

In this paragraph, third-body perturbations are considered under the assumption that the propagation center (i.e., the origin of the reference frame for the equations of motion) is at Eros's center of mass. The region in space where this assumption holds is called the sphere of influence (SOI) of a celestial body. Additionally, it is useful to introduce the concept of the Hill sphere, which, though similar to the SOI, serves a different purpose. In the context of the restricted three-body problem, where the Sun is the primary body and the asteroid is the secondary, the Hill sphere defines the region around Eros within which a spacecraft can orbit without being pulled away by the Sun's gravitational attraction. The radii of the SOI and Hill sphere are given by:

$$r_{SOI} = a \sqrt[3]{\frac{m}{3M}} \qquad r_H = a \left(\frac{m}{M}\right)^{\frac{2}{5}} \tag{3.40}$$

where a is the heliocentric distance between the primary and secondary, m is the mass of the secondary, and M is the mass of the primary. The values of these radii for Eros are provided in Table 3.3, which confirms that all the orbits of interest in this study lie well within the small body's SOI.

Solar radiation pressure

Solar radiation pressure (SRP) arises from photon momentum exchange when electromagnetic radiation impacts a surface with a non-zero projected area in the emission direction. Various methods exist to model SRP, ranging from macro models, such as those used in the Gravity Recovery and Climate Experiment (GRACE) mission (Cheng et al., 2008), which still rely on analytical formulations, to finite element models for the Global Positioning System (GPS) (Ziebart, 2004), which employ Monte Carlo ray-tracing to simulate photon paths. As detailed SRP modeling lies beyond the scope of this work, a simplified first-order approximation, known as the *cannonball model*, is adopted to qualitatively capture the destabilizing effects of SRP (Scheeres, 2014).

The cannonball model assumes that the spacecraft is a homogeneous sphere on which radiation is either absorbed or specularly reflected in a uniform way. It is thus equivalent to a flat plate of area equal to the section of the sphere and always pointed directly at the Sun. According to this model, the acceleration due to SRP does not depend on the attitude of the spacecraft and can be computed as:

$$\boldsymbol{a}_{SRP} = \frac{C_r A}{m} \frac{\psi_0}{c} \frac{1\text{au}^2}{||\boldsymbol{r} - \boldsymbol{r}_\odot||^2} \frac{\boldsymbol{r} - \boldsymbol{r}_\odot}{||\boldsymbol{r} - \boldsymbol{r}_\odot||} = C_{SRP} \frac{\boldsymbol{r} - \boldsymbol{r}_\odot}{||\boldsymbol{r} - \boldsymbol{r}_\odot||^3} \tag{3.41}$$

where $\psi_0 = 1367$ W/m^2 is the solar constant, $\frac{A}{m}$ is the satellite's area-to-mass ratio, C_r is the reflectance of the spacecraft surface, and C_{SRP} is the SRP coefficient. As visible by the term $\boldsymbol{r} - \boldsymbol{r}_\odot$, the force is assumed to always act along the Sun-spacecraft line in the direction away from the Sun.

3.4.3 Proximity dynamics in strongly perturbed environments

In this section, the dynamical environment close to a NEA is described based on previous results from analytical and semi-analytical studies. Although the considerations that arise rely on assumptions that may not fully hold in reality, they still offer critical insights for later analysis, as designing an effective control strategy requires a solid understanding of the uncontrolled motion in the first place.

Included below is a notable example provided by Scheeres (2012a) to emphasize the effects of the highly nonlinear dynamics around an asteroid. As shown in Fig. 3.6, orbits around Eros can exhibit drastically different outcomes when small variations are considered in the initial state: the red orbit remains stable, the green orbit escapes within two revolutions, and the blue orbit impacts the asteroid. The occurrence of such a wide range of behaviors for relatively small initial differences is entirely imputable to the asteroid's gravity field. This pronounced sensitivity to the initial conditions thus highlights the challenges associated with asteroid missions, especially when considering also navigation uncertainties.

Now, the forces acting on the orbiter vary significantly with distance, thereby identifying two main types of motion: the *solar dominated* (far-field) and *gravity-dominated* (near-field) regimes (Scheeres, 2012c, 2014). While the former can be approximated by the Clohessy-Wiltshire equations, the latter is non-integrable and requires numerical methods to be used (the reference mathematical framework is the Hill three-body problem). An overview of these regimes is visible in Fig. 3.7, which compares the magnitudes of SRP and solar gravity to the point mass term for many Solar System bodies. Evidently, SRP is far more significant near asteroids than in any other Solar System environment: for most small bodies, it exceeds the point mass gravity when evaluated near their Hill radius.

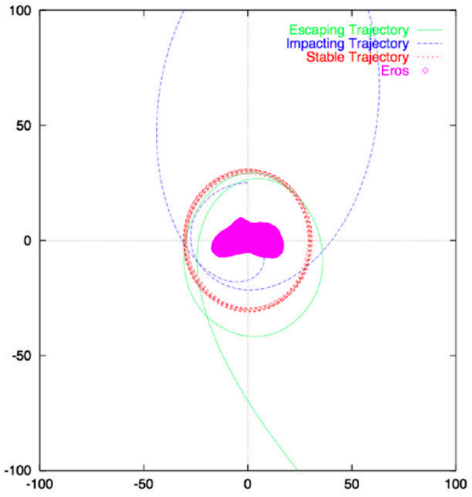

Figure 3.6: Three orbits with different initial conditions around Eros: local circular conditions (red), 45° shift in phase angle (green), lower altitude (blue). Axes are expressed in km (Scheeres, 2012a).

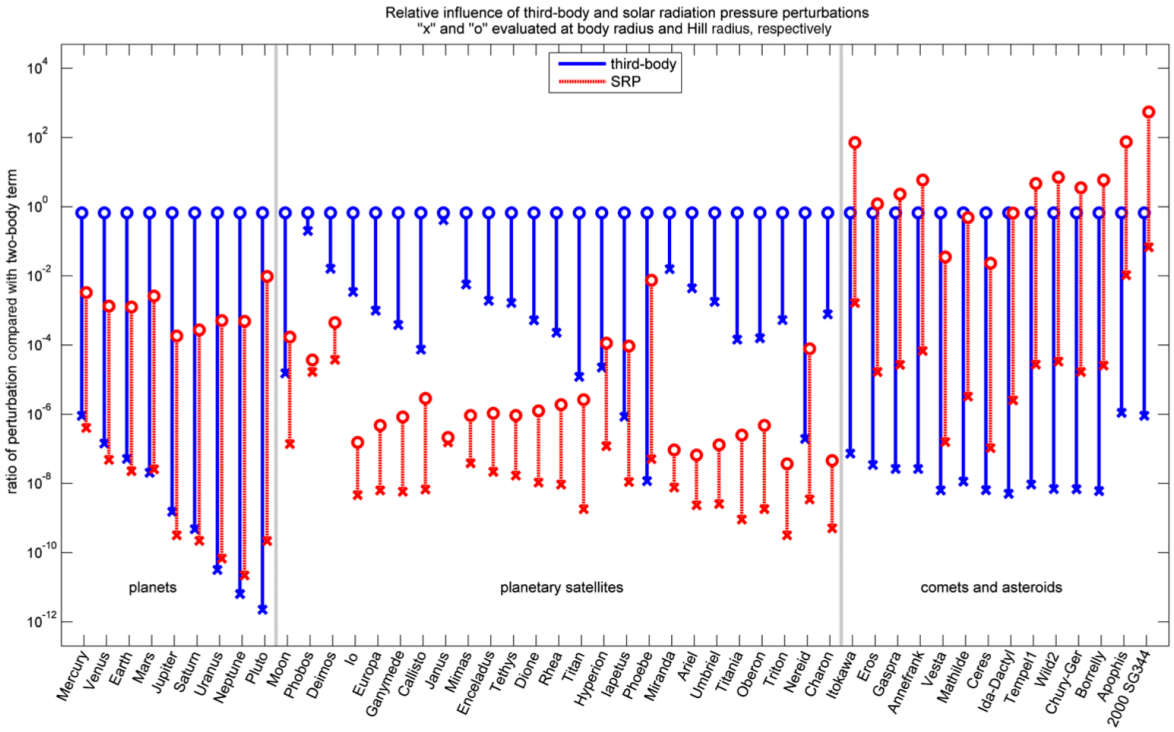

Figure 3.7: Solar pressure and third-body perturbations at bodies of interest in the Solar System (Russell, 2012). The area-to-mass ratio considered for computing SRP is 0.05 kg/m^2.

Table 3.4: Limit semi-major axes for 433 Eros assuming a spacecraft with 0.02 $\frac{A}{m}$ and 0.9 C_r.

-	a_{max} [km]	a_{min} [km]
Perihelion	1159	669
Aphelion	1825	1053

Solar regime

At distances of several tens to hundreds of kilometers from an asteroid, spacecraft motion is dominated by solar perturbations, with SRP typically exceeding tidal effects (Scheeres, 2014). Using averaging techniques, Scheeres (2012c) identified stable orbit classes under SRP perturbations for specific initial conditions. One of these, referred to as *solar plane-of-sky* orbits, lies in the terminator plane, with the orbit's normal aligned to the Sun-asteroid line. These orbits provide stable illumination, remain in sunlight, and become more circular as perturbations increase. Consequently, as noted in Sec. 2.2, asteroid missions typically operate near this plane during their science phases.

By modeling the asteroid's gravity as a point mass term, Dankowicz (1994) established a maximum semi-major axis value (a_{max}) over which an orbiter would escape the small body's attraction, whereas a sufficient condition a_{min} for capture was derived by Scheeres et al. (2013):

$$a_{max} = \frac{\sqrt{3}}{4}\sqrt{\frac{\mu}{C_{SRP}}}r_{\odot} \qquad a_{min} = \frac{1}{4}\sqrt{\frac{\mu}{C_{SRP}}}r_{\odot} \tag{3.42}$$

In other words, while for values above a_{max} it is guaranteed that the orbiter will escape, for values smaller than a_{min} escape is prohibited. It is important to notice that both these terms scale linearly with the distance $r_{\odot}$ between the Sun and the asteroid, showing that an initially bounded orbit may result in escape when close to the perihelion. Because Eros is a relatively massive body, these values are very large, as visible in Table 3.4. Orbits at such a distance from the small body have periods of motion in the order of the asteroid's period around the Sun, thus losing any operational attractiveness.

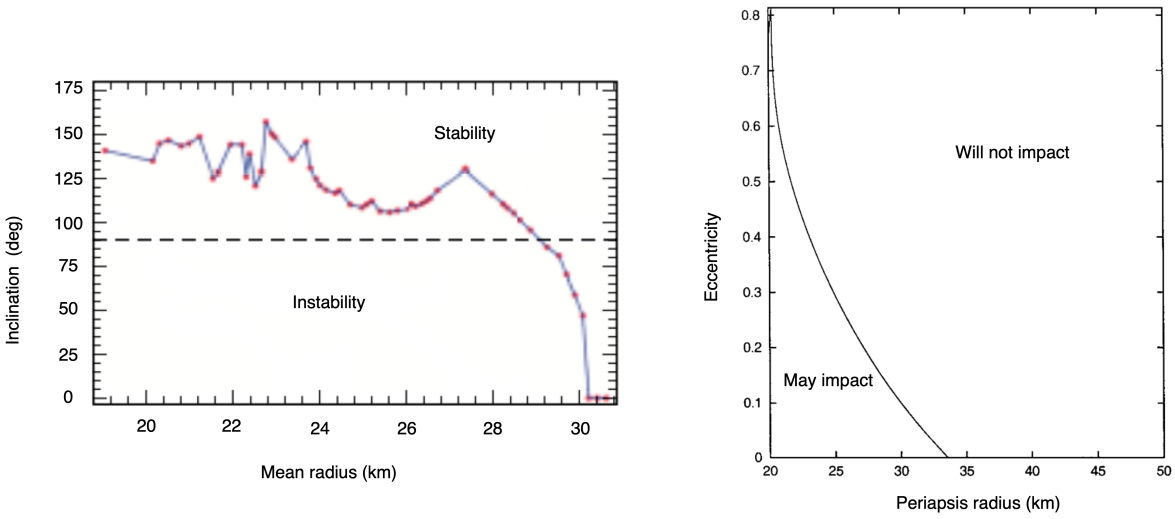

Figure 3.8: Stability regions for three-dimensional motion around asteroid Eros (Scheeres et al., 2002). The plot on the right has been derived for prograde, equatorial orbits.

Gravity regime

When the spacecraft is located closer than a few tens of kilometers to the asteroid (this depends on the mass of the small body), the effect of the rotating, non-spherical gravity is more pronounced and the gravitational attraction of the asteroid becomes the dominant force (Scheeres, 2014).

In this scenario, the major contribution to the strong perturbations from the gravity field is given by the asteroid's oblateness (C_{20}) and ellipticity (C_{22}). The former causes a secular deviation of the orbit's nodes, with a precession rate that can become 200 times faster than for an Earth's orbiter (Scheeres, 2012b). The effect of the oblateness is problematic because it causes the orbital plane to precess, but in itself it does not affect orbital stability. On the contrary, the ellipticity explicitly affects the semi-major axis, eccentricity, and inclination. The changes in orbit energy due to the ellipticity can be severe enough for an initially bound orbit to become hyperbolic, and vice-versa (Scheeres et al., 2000). In regard to this, Scheeres (1999) derived analytical relations which describe the change in the orbital energy and angular momentum caused by C_{22}, proving they depend on a factor $\cos^4 \frac{i}{2}$. As a consequence, the transition from stable to unstable circular orbits occurs at very different radii depending on the inclination. Figure 3.8 shows that for Eros this limit is at 33 km for orbits with inclination close to 0°, but gets down to 20 km for orbits with inclination close to 180° (Scheeres et al., 2002). Based on these results, it is possible to define an effective mission strategy that consists in placing the spacecraft in retrograde motion around the body to achieve low-altitude orbits, which was the approach adopted by NEAR mission (Sec. 2.2.2).

3.5 Equations of motion

In the literature, various frames are used to define and integrate the equations of motion. Ultimately, the choice generally falls between three main options: the orbit-fixed frame, the inertial frame, or the asteroid-fixed frame. The former is needed when dealing with small-sized asteroids whose gravity signature is so small that the heliocentric motion cannot be ignored (i.e., the non-inertial forces associated with the rotation of the asteroid around the Sun are comparable to the gravity force). On the contrary, for larger asteroids, an inertial frame is preferable, or in some cases an asteroid-fixed one. This kind of analysis can be quantified by computing the first and second-time derivatives of Eros's true anomaly, for which analytic formulae exist based on the two-body problem (Takahashi and Scheeres, 2021):

$$\dot{\theta} = (1 + e\cos\theta)^2 \sqrt{\frac{\mu_\odot}{[a(1-e)^2]^3}} \qquad \ddot{\theta} = -2e\sqrt{\frac{\mu_\odot}{[a(1-e)^2]^3}} \sin\theta(1 + e\cos\theta)\dot{\theta} \tag{3.43}$$

According to these equations, the maximum values of $\dot{\theta}$ and $\ddot{\theta}$ for Eros are $1.8{\cdot}10^{-7}$ rad/s and $1.2{\cdot}10^{-14}$ rad/s^2, respectively. This means that at 50 km from the asteroid, the Coriolis acceleration due to the heliocentric motion of Eros is of the order of 10^{-7}, whereas the gravitational acceleration is approximately $1.7{\cdot}10^{-4}$. This justifies the use of an inertially-fixed reference frame at the asteroid.

The translational equations of motion describe the dynamics of the center of mass of the spacecraft in the ACI frame according to Newton's second law:

$$\frac{d^2\boldsymbol{r}}{dt^2} = \frac{\Sigma \boldsymbol{F}}{m} \tag{3.44}$$

In parallel, the equation for the spacecraft's mass m is:

$$\frac{dm}{dt} = -\frac{||\boldsymbol{T}||}{I_{sp} g_0} \tag{3.45}$$

where $||\boldsymbol{T}||$ is the norm of the thrust vector, and g_0 is the Earth's gravitational acceleration on the surface. It is noted that the inertial frame represents the most natural choice for writing the equations of motion, not only for its numerical stability but especially because the target of the orbit control system will be Kepler orbits, which exist only within this frame. Specifically, the trajectory of the spacecraft is a perturbed Kepler orbit, which is represented by the following explicit form of Eq. (3.44):

$$\frac{d^2\boldsymbol{r}}{dt^2} = \boldsymbol{a}^I_{g,pm} + \frac{\Sigma \boldsymbol{F}_{\text{pert}}}{m} = \boldsymbol{a}^I_{g,pm} + \boldsymbol{C}_{I/A}\boldsymbol{a}^A_{g,ns} + \boldsymbol{a}^I_{SRP} + \boldsymbol{a}^I_{3BP} + \boldsymbol{a}^I_T \tag{3.46}$$

where the subscripts pm and ns have been used to indicate the point mass and the non-spherical components of the overall gravitational acceleration, and $\boldsymbol{a}_T$ is the thrust acceleration. Instead, the superscript represents the frame where the acceleration is computed.

Eq. (3.46) is a 2$^{\text{nd}}$ order differential equation based on propagating Cartesian elements, but it is just one possible representation of the dynamics. When it comes to choosing a propagation scheme, many options are available, such as Cartesian elements (Cowell propagator), Kepler elements (Gauss planetary equations), modified equinoctial elements (MEEs), and unified state model (Vittaldev et al., 2012). It has been decided to employ the simplest formulation (Cowell) since it is generally argued that in the presence of highly perturbed motion, the other methods lose their advantages, while Cowell's simplicity and straightforward implementation make it more competitive. Moreover, the disadvantages that are typically associated with it are not particularly valid for the problem at stake. In fact, it is known that the shortcomings of this method lie in the large values and variations characterizing the state derivative, which can lead to large numerical errors and issues with adapting the time step. However, the small size of both the asteroid and the observation orbits (if compared to planets or moons), together with simulation times at most in the order of the weeks, partially mitigate this problem. In addition, as it will be made clear later, GNC design already requires the integrator step size to be very small to deal with the highest frequency of the system.

Finally, a simple model is sufficient to describe the motion of Eros around the Sun, for which a semi-analytical propagator based on the two-body problem is used. Eros orbit is thus assumed to be fully Keplerian, with the only non-constant orbital element being the true anomaly. This can be propagated in time by using Kepler's equation:

$$M = E - e \sin E \tag{3.47}$$

where E is the eccentric anomaly. Starting from the mean anomaly M, which can be computed analytically for any given time, the expression above can be solved numerically for E (a simple Newton's method is more than sufficient), which then yields the true anomaly through the relation:

$$\tan\frac{\theta}{2} = \sqrt{\frac{1+e}{1-e}} \tan\frac{E}{2} \tag{3.48}$$

4

Nonlinear control

This chapter gives an overview of control techniques for nonlinear systems affected by uncertainties and disturbances. Section 4.1 presents a qualitative discussion of the control methods that have been applied for orbit control, raising considerations about their advantages and potential drawbacks. Then, a trade-off analysis is performed to identify adequate control techniques considering the requirements identified for this work. Section 4.2 follows by presenting the theoretical framework of SMC. Finally, the chapter concludes with the mathematical background of the target point approach, presented in Sec. 4.3.

4.1 Nonlinear control in presence of uncertainties

Most physical systems are inherently nonlinear, meaning that they can be described by the use of nonlinear differential equations. While control can sometimes be simplified by approximating the system with a linearized model over a narrow operating range, many control applications involve large operational ranges where nonlinear effects must be explicitly considered to ensure controller performance. Additionally, these systems often face significant uncertainty, which derives from incomplete knowledge of system parameters, partial state measurement, and simplified system modeling. As a consequence, there is a noticeable discrepancy between the mathematical model that is used for the design of the controller and the actual dynamics of the plant. Slotine and Li (1991) identify two main types of uncertainties:

- *structured* uncertainties, which derive from actual uncertainty about the system parameters.
- *unstructured* uncertainties, which arise from the purposeful choice of a simplified representation of the system's dynamics.

Within the topic of this thesis, examples of structured uncertainties include the inaccuracy over the asteroid's gravitational parameter, while unstructured uncertainties may refer to the fact that the control laws are derived by neglecting the presence of high-order gravity terms.

Given these considerations, the purpose of robust control methods is to explicitly consider structured and unstructured uncertainties during the design phase to ensure that they do not prevent the system from satisfying the requirements. In this regard, Sec. 2.3 underscored that previous research on orbit control around asteroids typically evaluated the designed methods against various sources of uncertainties and errors, yet limiting the analysis to a single orbit around a given asteroid. In this work, however, we refer to the *robustness* of a control method as its capacity to satisfy a given set of requirements across a broader class of operational scenarios than those considered during the design process. Based on this definition, the objective of this research is to evaluate the designed control system across the full mission design space of interest, ultimately extending the analysis to additional small bodies.

4.1.1 Overview

This section provides an overview of the control techniques that have been used in the literature for orbit control at asteroids, but also for Earth satellites and libration point orbits.

The most conventional control methods are PID controllers and LQRs, which have been used very frequently for Earth applications. Nevertheless, 2.3.1 highlighted that some authors relied on these techniques also for orbit control around asteroids. Now, PID control is a model-free process that requires the gains to be tuned on a case-by-case approach, thus representing a straightforward effective solution only when the operating condition is one, and the environment is known. In the case of multiple operating scenarios, a gain-scheduling approach is necessary. As for the LQR, it is a state-feedback method where the gain matrix is computed in adherence to optimal control theory, thus representing an ideal approach for linear time-invariant systems. Despite being among the most popular feedback systems, this approach rapidly loses its attractive properties when considered for the investigated problem, since it is inherently not robust and based on linear theory. In the literature, robust adaptations of these methods for orbit control are available, such as nonlinear PIDs (Tiwari et al., 2023) and linear quadratic Gaussian (LQG) controllers (Yang et al., 2014). The former automate the gain-scheduling procedure by adjusting online the gains through nonlinear functions of the control error, while the latter introduce Kalman filtering in combination with an LQR to counteract the uncertainties in the measured state.

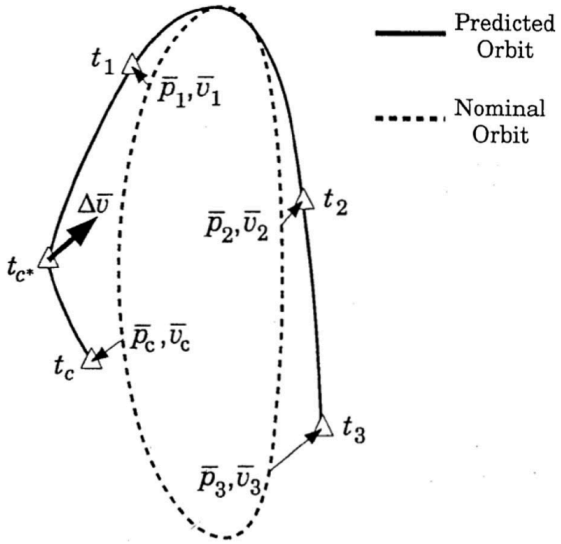

Figure 4.1: Illustration of the target point approach, taken from Howell and Gordon (1994).

Another method that follows from the mission heritage is the target point approach (TPA), a control technique originally developed by Dwivedi (1975) for interplanetary trajectories, then adapted to the problem of station-keeping along libration point orbits by Howell and Pernicka (1993), and finally used for JAXA's Equuleus mission analysis by Oguri et al. (2017). This strategy, illustrated in Fig. 4.1, uses the state transition matrix (STM) to estimate deviations from the reference orbit at discrete future points. Impulsive maneuvers are then calculated to keep the spacecraft within a nominal *torus* around the orbit. While this method has never been applied to the problem of stabilizing an orbit around an asteroid, a similar approach was adopted by Shi et al. (2020), who reported very good results even in spite of the presence of navigation and maneuver errors. Considering the requirements for this study, targeting-based strategies have very attractive properties due to their impulsive nature. However, an explicit feedback mechanism against modeling inaccuracy is absent, since the effectivity of the STM ultimately depends on the accuracy of the dynamical model that is to be linearized. Furthermore, the number and spacing of target points represent unconstrained design parameters that have to be determined by trial and error, thereby requiring that a high-fidelity model of the environment is available a-priori.

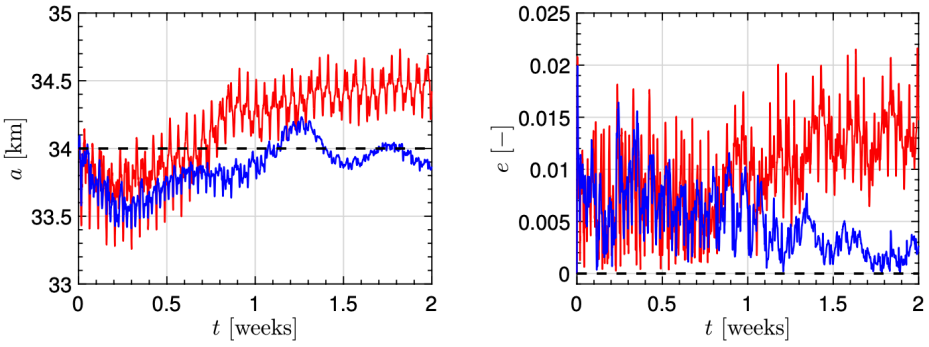

Figure 4.2: Example of an MPC approach for station-keeping around an asteroid (Sanchez et al., 2022). Blue: learning-based MPC; red: non- learning MPC.

More complex control techniques that can be applied to the orbit control problem include model predictive control, a finite-horizon optimization scheme that merges the advantages of constrained optimization and feedback control. Despite its successful application for orbit control around an asteroid by Sanchez et al. (2022), it presents many flaws when considering the specific requirements for this work. Firstly, it is inherently model dependent, which leads its performance to become acceptable only after a parallel estimation process has converged (learning-based MPC, as shown in Fig. 4.2). Secondly, it is optimization-based and requires iteratively solving a quadratic programming (QP) problem. The computational demand of this procedure grows with the size of the control horizon, thereby making it challenging for real-time applications (Sanchez et al. (2022) reports the time required by the MPC algorithm to be two orders of magnitude larger than that required by the UKF). Additionally, the QP problem requires first linearizing the dynamics of the system, making it more sensitive to uncertainties (indeed, the aforementioned authors assumed perfect knowledge of the initial state, thereby making the linearization process more valid).

Another popular control technique that is more suited to deal with model uncertainties is the H_∞ method, which has been successfully applied for the station-keeping in Halo orbits around lagrangian points of the Sun-Earth system (Kulkarni et al., 2006). While being inherently robust, H_∞ employs continuous control and achieves closed-loop robustness by designing for the larger disturbing forces, thereby requiring an initial assumption that may lead to over-conservative performance. Furthermore, it is specifically designed for linear systems, a particularly advantageous feature in the context of libration point orbits, given that they are periodic solutions of a linear time-varying system (LTV). It is also noted that additional shortcomings of H_∞ controllers include the increased number of states required to represent uncertainties (Sagliano et al., 2017), as well as their conservatively robust nature, which can result in sluggish performance during nominal control.

A broad class of controllers that can be used to deal with uncertain environments is that of nonlinear adaptive controllers, which attempt to estimate the uncertain parameters online (during the process) based on the measured system signals. In other words, adaptive controllers can be regarded as control systems with online parameter estimation. This allows them to improve their performance as the adaptation goes on, providing excellent robustness against parametric uncertainties, for which little to no knowledge is required in advance. While being inherently nonlinear, it is important to notice that this control methodology still requires that the structure of the dynamics equations is known, to allow the inclusion of the unknown parameters within the estimation (Zeinali and Notash, 2010). This aspect makes adaptive controllers particularly sensitive to non-parametric uncertainties. As a matter of fact, the authors listed in Sec. 2.3.1 that employed adaptive control schemes (Lee and Singh (2019a),Lee and Singh (2023)) did not test the robustness of their algorithms against navigation errors, but limited their analysis to the uncertainty in the gravity field.

Finally, a popular method that is explicitly designed for nonlinear systems affected by uncertainties and unmodeled dynamics is sliding mode control (Slotine and Li, 1991). This control technique has low sensitivity to parametric uncertainties and can achieve finite time convergence even with greatly reduced-order modeling of the system dynamics. However, the convergence is typically achieved at the cost of a rapidly switching control signal, which inevitably leads to thrust chattering. Moreover, it is generally necessary to have a-priori knowledge of the upper bound of the perturbations acting on the system, which may lead to an overly conservative control design. However, it is noted that a notable advantage of sliding mode control is that it does not necessarily need a reference trajectory, and thus can be used to generate a (non-optimal) trajectory to reach a desired state. In the context of asteroid applications, this control technique has been primarily employed for hovering and landing (Hawkins et al., 2012; Furfaro et al., 2013a; Furfaro, 2015), demonstrating excellent robustness against unmodeled dynamics, as well as navigation and maneuvering errors.

4.1.2 Trade-off analysis

Table 4.1 lists five criteria that have been identified to highlight the advantages and disadvantages of control methods with respect to the mission and system requirements that characterize the specific problem at stake. These criteria will be used to perform a trade-off analysis and steer the decision-making process toward choosing one (or more) method for the development of an orbit control strategy. The identified criteria aim to balance the considerations which would be limited to a purely control analysis with additional factors that have to be taken into consideration for orbit control at asteroids.

Both *model knowledge* and *nonlinearity* have been assigned a high priority given that the particular context of this problem involves uncertain physical parameters and highly perturbed dynamics, thereby requiring that the control system is able to perform well over a broad range of conditions (**MIS-REQ-01**, **MIS-REQ-02**, **MIS-REQ-03**) without requiring accurate knowledge of the system (**OC-REQ-09**). *Tuning* evaluates the complexity of the control method's design procedure and the extent to which a high-fidelity model of the dynamics is required for prior testing. In such a scenario, the attractiveness of the method for the problem at stake would clearly decrease. In parallel, also the nature of the *control law* is an important aspect to consider, especially in light of the fact that scientific observation phases require long times during which thrusters must remain off (**OC-REQ-08**). Eventually, any continuous signal can be transformed into a discrete one, yet some control techniques are inherently impulsive, making them more appealing from this perspective. Finally, it was decided to consider whether a given controller operates exclusively in reference-tracking mode or can also directly target a desired state. While for orbit maintenance purposes this is clearly not relevant, since a reference orbit is available by definition, when changing the orbit geometry and orientation it is important to know whether a parallel procedure within the guidance module needs to generate a transfer trajectory or not.

Except for PIDs and LQRs, which have been excluded a-priori, all the remaining control methods discussed previously have been assessed based on the established criteria, as summarized in Table 4.2. Ultimately, it was decided to employ sliding mode control as the reference theoretical framework for the

Table 4.1: Criteria to evaluate control methods' adequacy to the current problem.

Criterion	Priority	Description
Model knowledge	High	Level of knowledge of the system that is required for the control law to be effective.
Nonlinearity	High	Is the control method explicitly nonlinear or does it require linearization?
Tuning	Medium	How complex is the process required to tune the parameters that govern the control law?
Control law	Medium	Impulsive or continuous nature of the control law.
Reference trajectory	Low	The control method can either track a reference trajectory or target directly a reference state.

Table 4.2: Assessment of control techniques based on established criteria.

Method	Model Knowledge	Nonlinearity	Tuning	Control law	Reference trajectory
TPA	Medium	Linear	Trial-and-error	Impulsive	Yes
MPC	High	Linear	Optimization-based	Continuous	Yes
H_∞	Low	Linear	Worst-case scenario	Continuous	Yes
Adaptive	Medium	Nonlinear	Online adaptation	Continuous	Yes
SMC	Low	Nonlinear	Worst-case scenario	Discontinuous	No

orbit control strategy. This is mainly justified by the fact that its mathematical nature is fully aligned with the criteria established in Table 4.1, especially the high-priority ones. A particular consideration was made regarding the inherent drawback of thrust chattering. In fact, while there are multiple ways in which this problem can mitigated, many argue that the result is often a trade-off between tracking performance and chattering, which may be unacceptable for high-accuracy applications. However, this limitation is not critical for the problem at hand, as spacecraft operating around asteroids do not face stringent position constraints. Another commonly cited drawback of SMC is the need for conservative control gains, which can result in over-conservative design and loss of performance. However, robustness and operational safety are deemed to outweigh the need for optimality within this work. Additionally, the low-gravity environment ensures that OCMs and OMMs remain small, greatly reducing their impact on fuel margins. Lastly, it is noted that SMC provides a straightforward approach for determining control gains, as they are explicitly linked to the system's dynamics, thus simplifying the design process.

The TPA exhibits some deficiencies when considering the trade-off criteria, namely its linearized nature and the extensive trial-and-error procedure required to design it. However, its authors state that the motivating factor behind the development of this station-keeping approach was an explicit interest in maximizing the time between maneuvers (Howell and Gordon, 1994). Given the same interest that characterizes this study, the impulsive nature of the method, and the fact that it has never been applied before to the orbit control problem around an asteroid, it was decided to consider also the TPA.

It is recognized that the other control methods that have been mentioned and classified as inadequate can be modified in specific ways that would make them more suited to this problem, but it is not within the scope of this thesis to take into consideration also these formulations, especially because the trade-off analysis that has been performed in this section was entirely based on the first-order version of each control technique.

4.2 Sliding mode control

Sliding mode control is considered by many sources as one of the most effective techniques for controlling dynamical systems in the presence of bounded uncertainties while guaranteeing finite-time convergence (Yu et al., 2021; Gambhire et al., 2021). Specifically, algorithms based on SMC theory are suited for missions employing a high level of autonomy, where the spacecraft is able to apply real-time control thanks to the onboard state estimation. Moreover, its discontinuous nature genuinely accommodates operating thrusters in an on-off fashion (dead-band control) (Furfaro, 2015).

4.2.1 Overview

Sliding mode control is based on the intuition that it is significantly easier to control first-order systems (described by first-order differential equations) rather than n^{th}-order systems (described by n^{th}-order differential equations). The working principle behind this method lies in the use of a time-varying variable, referred to as *sliding surface*, to drive the system to the desired state. Briefly, when the system state is locked on the sliding surface, the dynamical system tracks the desired reference signal with zero error.

SMC is based on a two-step procedure: first, a switching function has to be designed so that when the system moves along the sliding surface, design specifications are met; secondly, a control law has to be determined such that under the presence of disturbances and uncertainties, the system state is naturally attracted to the surface. As visible in Fig. 4.3, the control law is responsible for steering the trajectory of the system to the sliding surface (*reaching* phase), and then maintaining motion along it (*sliding* phase).

Ideally, this approach allows to achieve perfect tracking performance in the presence of arbitrary parameter uncertainties. In practice, three main drawbacks characterize first-order sliding mode control:

- Tracking is obtained through a high-frequency control activity, which leads to the undesirable chattering effect.
- The sliding variables converge in finite time, but the state variables converge only asymptotically.
- The sliding surface design is constrained by the requirement that it must have a relative degree of one in relation to the control input (i.e., the first derivative of the sliding surface needs to contain the control term).

Therefore, with time many different versions of sliding mode control have been designed to improve its performance and reduce its drawbacks. The most immediate approach to reduce the chattering effect consists of introducing a boundary layer about the sliding surface to which the system is allowed to converge, thus replacing the signum function with a smoother operator. While this is a practical approach, it guarantees convergence only to the proximity of the sliding surface, hence neither the sliding surface nor the state variables converge to the desired variable. In other words, the price to obtain a smooth control function is a loss of accuracy.

To mitigate these problems, high-order sliding mode control techniques are available, starting from second-order ones (SOSC). These methods *hide* the high-frequency switching in the high-order derivatives of the system's state, notably mitigating the chattering effect. Various SOSCs exist, but most of them can be traced back to a generic formulation, as illustrated by Levant (2007). Depending on how the gains of the controller are chosen, there can be two main types of behavior: terminal mode and twisting mode, shown in Fig. 4.4. In the former, the trajectories of the system reach the sliding surface and then remain on it for future time; in the latter, the sliding phase never occurs, and the system reaches the origin of the state space in a twisting-like manner. An alternative declination of second-order sliding

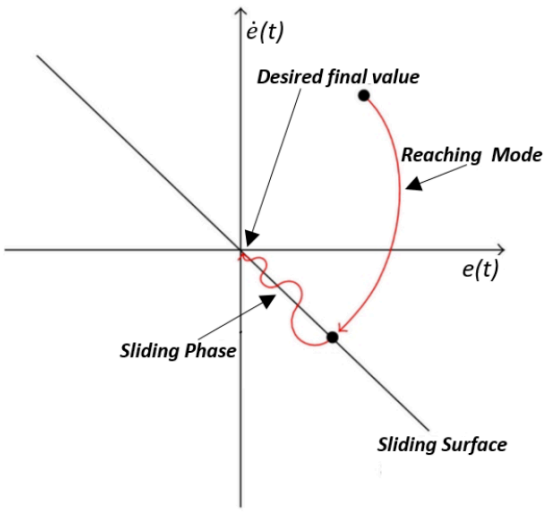

Figure 4.3: Overview of sliding mode dynamics (Holkar and Waghmare, 2013). The oscillations about the sliding surface represent the chattering effect.

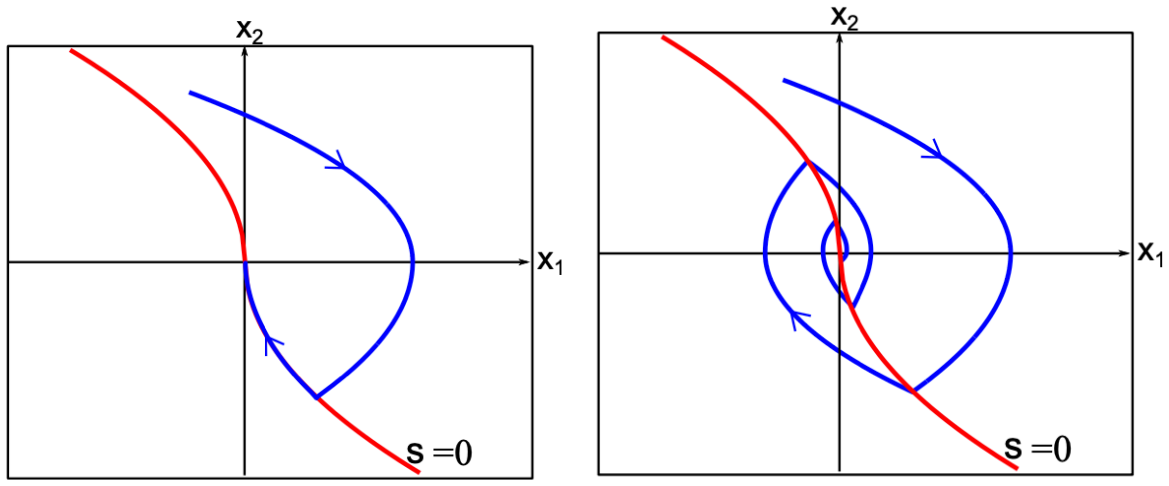

Figure 4.4: Terminal (left) and twisting (right) mode of second-order sliding mode controllers (Fridman et al., 2015).

mode control treats the input of the system, namely the control variable, as a new state variable, and uses its derivative as a virtual controller (Furfaro et al., 2013a). In this way, chattering can be attenuated by means of SOSC in systems with a relative degree of one.

High-order sliding mode controllers have gradually evolved into increasingly complex formulations aimed at improving their finite-time convergence and robustness (Fridman et al., 2015). However, after a careful review, further investigation into these advanced methods was deemed unnecessary for the specific objectives of this work. In fact, first-order methods were identified as particularly attractive due to their alignment with **OC-REQ-07** and **OC-REQ-08**. Specifically, the use of a boundary layer provides a mechanism to explicitly include a design feature that should allow the spacecraft to periodically cease thruster operation. As previously discussed, this negatively affects the tracking performance; however, Sec. 6.5.1 will clarify why this does not represent a problem for the given station-keeping scenario. It is also highlighted that first-order methods retain a key advantage over higher-order sliding mode controllers in the simplicity of the tuning procedure for the control gains.

4.2.2 Mathematical background

Consider a generic single-input single-output (SISO) nth-order dynamic system:

$$x^{(n)} = f(\boldsymbol{x}, t) + b(\boldsymbol{x}, t)u \tag{4.1}$$

where t is time, u is the control input, $\boldsymbol{x} = (x\ \dot{x}\ ...\ x^{(n-1)})^T$ is the state vector, and the notation $(\cdot)^{(n)}$ identifies the derivative of order n. In general, the nonlinear function f and the control gain b are not exactly known, but these inaccuracies are upper bounded by a known continuous function of $\boldsymbol{x}$. Furthermore, unstructured uncertainties are present in the form of a disturbance term d acting on the system. As a consequence, Eq. (4.1) can be rewritten as:

$$x^{(n)} = \hat{f}(\boldsymbol{x}, t) + \Delta f(\boldsymbol{x}, t) + \hat{b}(\boldsymbol{x}, t)u + \Delta b(\boldsymbol{x}, t)u + d(t) \tag{4.2}$$

where $\hat{f}, \hat{b}$ and $\Delta f, \Delta b$ are respectively the known and unknown parts of the dynamics and control gain, and d represents a bounded external disturbance. Specifically, some known functions F=$F(\boldsymbol{x})$, B=$B(\boldsymbol{x})$ and D=$D(\boldsymbol{x})$ exist such that $|\Delta f| \leq F$, $|\Delta b| \leq B$ and $|d| \leq D$. The control problem then can be stated as tracking a given time-varying state $\boldsymbol{x}_d = (x_d\ \dot{x}_d\ ...\ x_d^{(n-1)})^T$ in the presence of model imprecision on $f(\boldsymbol{x})$ and $b(\boldsymbol{x})$. Hence, the tracking error $\tilde{\boldsymbol{x}}$ can be defined as:

$$\tilde{\boldsymbol{x}} = \boldsymbol{x} - \boldsymbol{x}_d = \begin{pmatrix} \tilde{x} & \dot{\tilde{x}} & ... & \tilde{x}^{(n-1)} \end{pmatrix}^T \tag{4.3}$$

In parallel, the time-varying surface $\mathcal{S}(t)$ is defined by the following scalar equation:

$$s(\boldsymbol{x}, t) = \left(\frac{d}{dt} + \lambda\right)^{n-1} \tilde{x} = 0 \tag{4.4}$$

with λ being a strictly positive constant, and s representing a measure of the algebraic distance to the surface. As visible in Fig. 4.6, in a second order system s is a linear combination of the position and velocity errors, thus Eq. (4.4) identifies a line in the phase plane of slope $-\lambda$ containing the time-varying point $\boldsymbol{x}_d = (x_d\ \dot{x}_d)^T$. Now, the problem of tracking $\boldsymbol{x} = \boldsymbol{x}_d$ is equivalent to that of remaining on the surface $\mathcal{S}(t)$ for all $t > 0$, therefore it can be solved by imposing Eq. (4.4), which is a linear differential equation admitting as unique solution that of $\tilde{\boldsymbol{x}} = 0$. In this way, the original problem of tracking an n-dimensional vector is reduced to keeping a scalar quantity at zero, which shows how SMC is able to replace an n$^{\text{th}}$-order tracking problem with a first-order stabilization problem. Indeed, the expression of s contains already the n$^{\text{th}}$-derivative of $\tilde{\boldsymbol{x}}$, therefore it is sufficient to differentiate s only once for the input u to appear.

It is also important to observe that the bounds on s can be directly translated into the bounds on the tracking error vector, such that s represents a true measure of the control performance. In fact, from Eq. (4.4) it follows that every term of the tracking error vector is obtained from s through a sequence of first-order lowpass filters, as shown in Fig. 4.5. As a consequence, it can be demonstrated that:

$$\forall t \geq 0\ |s(t)| \leq \Phi \Rightarrow \forall t \geq 0\ |\tilde{x}^{(i)}| \leq (2\lambda)^i \epsilon \tag{4.5}$$

where $\epsilon = \frac{\Phi}{\lambda^{n-1}}$. After having identified a suitable sliding surface, the actual control law that will drive the system to $\mathcal{S}(t)$ has to be designed such that outside of $\mathcal{S}(t)$, the following expression is satisfied:

$$\frac{1}{2}\frac{d}{dt}s^2 \leq -\eta|s| \tag{4.6}$$

where η is a strictly positive constant. Equation (4.6) is referred to as *sliding condition*, and when $\mathcal{S}(t)$ verifies this condition, it takes the name of *sliding surface* (the system's behavior on the surface is called *sliding mode*). When the system is in sliding mode it benefits from the invariance property, meaning that it is insensitive to matched disturbances entering the system through the control channel. Conceptually, the sliding condition states that the squared distance to the surface decreases along all system trajectories, which are forced to point towards $\mathcal{S}(t)$ and remain on it once they reach it. This is equivalent to saying that the control law needs to be selected to guarantee that s^2 remains a Lyapunov-like function of the closed-loop system, despite the presence of model imprecision and disturbances. In fact, consider a candidate Lyapunov function of the form:

$$V = \frac{1}{2}s^T s \tag{4.7}$$

which satisfies $V(0) = 0$ and $V(s) > s$ for $s > 0$. It is possible to verify that if Eq. (4.6) is substituted in the derivative of the Lyapunov function, then $\dot{V}(s)$ is negative everywhere, which guarantees that the dynamic system is globally stable according to Lyapunov stability theory. Furthermore, it can be proven that even if at the initial time the tracking error is non-zero, satisfying the sliding condition ensures that the surface $\mathcal{S}(t)$ will be reached in a finite time smaller than $|s(t = 0)|/\eta$. Finally, Eq. (4.4) implies

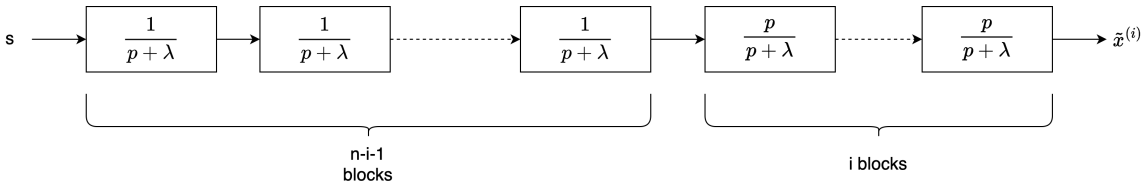

Figure 4.5: Visual representation of SMC as a series of lowpass filters. The variable p is the Laplace operator.

that once on the surface, the tracking error tends exponentially to zero, with a time constant $(n-1)/\lambda$ (which comes from the sequence of $(n-1)$ filters, each with a time constant equal to $1/\lambda$).

The SMC design will now be derived for the specific case where the system is of order two, in which case the sliding surface is defined by the following expression:

$$s = \dot{\tilde{x}} + \lambda\tilde{x} = 0 \tag{4.8}$$

Ideally, a feedback control law that satisfies the sliding condition could be built by exploiting the fact that when the system is in sliding mode, then both s and $\dot{s}$ are equal to zero. Therefore, by solving $\dot{s} = 0$ for the control input, it is possible to obtain an expression for u referred to as *equivalent control*, and denoted as $\hat{u}$:

$$\dot{s} = \ddot{x} - \ddot{x}_d + \lambda\dot{\tilde{x}} = f + bu - \ddot{x}_d + \lambda\dot{\tilde{x}} \tag{4.9}$$

$$\hat{u} = b^{-1}(-f + \ddot{x}_d - \lambda\dot{\tilde{x}}) \tag{4.10}$$

This control would indeed maintain the system on the sliding surface with zero tracking error if the dynamics were exactly known. In practice, the presence of uncertainties implies that $\hat{u}$ is only an approximation of the equivalent control term, thereby requiring an additional mechanism to actually satisfy the sliding condition and achieve $\dot{s} = 0$. Hence, the control law has to be modified to consider only the known part of the dynamics and control gains, and a discontinuous term across the surface needs to be added:

$$\hat{u} = -\hat{f} + \ddot{x}_d - \lambda\dot{\tilde{x}} \tag{4.11}$$

$$u = \hat{b}^{-1}(\hat{u} - k\,\mathrm{sgn}\,(s)) \tag{4.12}$$

$$\mathrm{sgn}\,(s) = \begin{cases} 1 & s > 0 \\ -1 & s < 0 \end{cases} \tag{4.13}$$

To simplify the remaining formulations, and given that it is not relevant for this work, from now on the uncertainties on the control gain will be neglected ($b = \hat{b} = 1$). Following this assumption, it can be proven that the sliding condition is verified by the above control law provided that $k \geq (F + D + \eta)$. Specifically, the switching term, $k\,\mathrm{sgn}\,(s)$, enables the sliding surface $s = 0$ to become a terminal attractor for the system and is thus responsible for closed-loop performance. Once the system has been driven to the surface, the equivalent control term (which has been derived for $\dot{s} = 0$) maintains the system along it (in sliding motion). Within the equivalent control, the quantity $\ddot{x}_d - \lambda\dot{\tilde{x}}$ is a reference acceleration that shifts the desired acceleration profile according to the velocity error. Clearly, a control law that satisfies the sliding condition will be discontinuous across $\mathcal{S}(t)$. In particular, the larger the parametric uncertainty that affects the dynamics $(F + D)$, the larger the discontinuity in the control (k) will be.

4.2.3 Boundary layer method

The most relevant aspect to notice about Eq. (4.13) is that the magnitude of the switching control is entirely dependent on k: the larger this gain, the faster the rise time, but also the chattering effect. Specifically, it is the combination of the signum operator and finite-time control action that leads to control chattering. While many methods exist to mitigate this problem, the most simple one consists of introducing a *boundary layer* about the sliding surface to which the system is allowed to converge (Slotine and Li, 1991):

$$\mathcal{B}(t) = \{\boldsymbol{x}, s(\boldsymbol{x}, t) \leq \Phi\} \qquad \Phi > 0 \tag{4.14}$$

where Φ identifies the boundary layer thickness. Control smoothing can then be achieved by leaving the control in Eq. (4.13) unvaried outside of Φ, which guarantees that the boundary layer is still attractive

for the system, while interpolating u inside $\mathcal{B}(t)$ by means of the saturation operator, as illustrated in Fig. 4.6.

$$u = \hat{u} - k\,\mathrm{sat}\,(s, \Phi) \tag{4.15}$$

$$\mathrm{sat}\,(s, \Phi) = \begin{cases} 1 & s > \Phi \\ s/\Phi & |s| \leq \Phi \\ -1 & s < -\Phi \end{cases} \tag{4.16}$$

The price to pay naturally falls on the tracking performance, which remains guaranteed to within an accuracy ϵ, as defined in Eq. (4.5).

Importantly, the thickness of the boundary layer can be made time-varying to maximize the use of the available control *bandwidth*. Considering a system with no gain margin ($b = \hat{b} = 1$), but without losing generality, the sliding condition has to be modified as follows to account for the presence of a boundary layer:

$$\frac{1}{2}\frac{d}{dt}s^2 \leq (\dot{\Phi} - \eta)|s| \tag{4.17}$$

The condition above ensures that the distance to the boundary layer always decreases, thus maintaining its attractiveness regardless of its temporal variations. In particular, the new term $\dot{\Phi}|s|$ highlights that the attraction condition is more stringent during boundary layer contraction ($\dot{\Phi} < 0$) and less stringent during boundary layer expansion ($\dot{\Phi} > 0$). To satisfy this new sliding condition, the quantity $-\dot{\Phi}$ needs to be added to the control gain, which takes the following form:

$$\overline{k} = k - \dot{\Phi} \tag{4.18}$$

Accordingly, the new control law becomes:

$$u = \hat{u} - \overline{k}(\boldsymbol{x})\,\mathrm{sat}\,(s, \Phi) \tag{4.19}$$

where it has been explicitly shown that gain k needs not to be constant. Now, based on the definition of s and on Eq. (4.19), the s-trajectories (the temporal evolution of s) inside the boundary layer can be expressed as:

$$\dot{s} = -\overline{k}(\boldsymbol{x})\frac{s}{\Phi} + \Delta f(\boldsymbol{x}) \xrightarrow{Eq.(4.5)} -\overline{k}(\boldsymbol{x}_d)\frac{s}{\Phi} + \Delta f(\boldsymbol{x}_d) + \mathcal{O}(\epsilon) \tag{4.20}$$

Again, the above equation has the structure of a first-order filter, whose inputs are the uncertainties in the system:

$$\left(\frac{d}{dt} + \frac{\overline{k}}{\Phi}\right) s = \Delta f \tag{4.21}$$

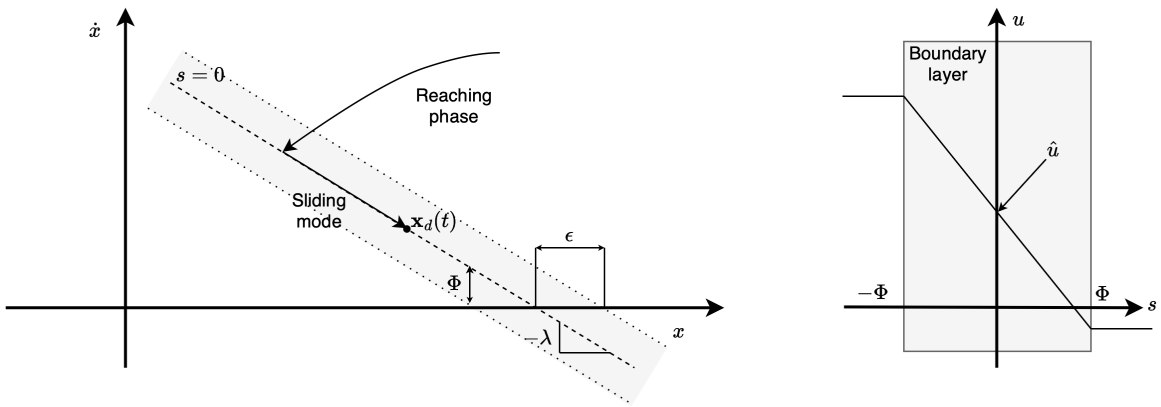

Figure 4.6: Overview of sliding mode dynamics for n=2 (left) and control interpolation in the boundary layer (right). Adapted from Slotine and Li (1991).

In summary, perturbations are first filtered according to Eq. (4.20) to give s, which then is lowpass filtered to yield the tracking error vector, as seen before from Eq. (4.4). Recognizing the filter-like structure of SMC is essential for an efficient design of its gains, particularly of λ, which determines the cut-off frequency and the amplitude of the passband. Moreover, the boundary layer thickness Φ can now be tuned such that also Eq. (4.20) represents a first-order filter of bandwidth λ:

$$\frac{\overline{k}(\boldsymbol{x}_d)}{\Phi} = \lambda \rightarrow \dot{\Phi} + \lambda\Phi = k(\boldsymbol{x}_d) \tag{4.22}$$

Equation (4.22) represents the desired time history of the boundary layer thickness, and allows to design the gain k to account for the temporal evolution of the boundary layer. Specifically, Eq. (4.18) can be rearranged as:

$$\overline{k}(\boldsymbol{x}) = k(\boldsymbol{x}) - k(\boldsymbol{x}_d) + \lambda\Phi \tag{4.23}$$

Conceptually, Eq. (4.22) has a precise physical meaning, which is more evident by reformulating it in terms of the tracking accuracy ϵ:

$$\lambda^n \epsilon = \overline{k}(\boldsymbol{x}_d) \tag{4.24}$$

The expression above, referred to also as *balance condition*, allows to relate the tracking performance (ϵ) to the desired control bandwidth (λ) and the extent of the parametric uncertainty (k), thereby summarizing the overall trade-off process that is at the base of SMC design.

4.3 Target point approach

The target point approach is an orbit control method that computes correction maneuvers by minimizing a weighted cost function that is defined in terms of impulsive $\boldsymbol{\Delta v}$, position deviations $\boldsymbol{\delta r}$, and velocity deviations $\boldsymbol{\delta v}$ from a nominal orbit at n distinct times in the future. The points at which future deviations are calculated are referred to as *target points*. The TPA seeks to find a corrective maneuver $\boldsymbol{\Delta v}_c$ at a given time t_c which minimizes the weighted cost function:

$$J = \boldsymbol{\Delta v_c}^T \boldsymbol{Q} \boldsymbol{\Delta v_c} + \sum_{k=1}^{n} (\boldsymbol{\delta r}_k^T \boldsymbol{R}_k \boldsymbol{\delta r}_k + \boldsymbol{\delta v}_k^T \boldsymbol{T}_k \boldsymbol{\delta v}_k) \tag{4.25}$$

where n is the number of target points along the orbit, while $\boldsymbol{Q}$, $\boldsymbol{R}$ and $\boldsymbol{T}$ are weight matrices to be selected by trial and error ($\boldsymbol{Q}$ needs to be symmetric positive definite, while $\boldsymbol{R}$ and $\boldsymbol{T}$ are positive semidefinite). The deviations from the nominal orbit $\boldsymbol{\delta r}$ and $\boldsymbol{\delta v}$ are predicted by using the state transition matrix $\boldsymbol{\Psi}$:

$$\boldsymbol{\Psi}(t_2, t_1) = \begin{bmatrix} \boldsymbol{\Psi}_{rr}(t_2, t_1) & \boldsymbol{\Psi}_{rv}(t_2, t_1) \\ \boldsymbol{\Psi}_{vr}(t_2, t_1) & \boldsymbol{\Psi}_{vv}(t_2, t_1) \end{bmatrix} \tag{4.26}$$

where $\boldsymbol{\Psi}_{rr}$, $\boldsymbol{\Psi}_{rv}$, $\boldsymbol{\Psi}_{vr}$, and $\boldsymbol{\Psi}_{vv}$ are the three-by-three blocks of the STM from time t_1 to time t_2 associated with the nominal trajectory. The state transition matrix is defined according to the following relationship:

$$\boldsymbol{\Psi}(t, t_0) = \frac{\partial \boldsymbol{x}(t)}{\partial \boldsymbol{x}_0} \tag{4.27}$$

To obtain the STM, the so-called variational equations need to be propagated:

$$\frac{d}{dt}(\boldsymbol{\Psi}(t, t_0)) = \left(\frac{\partial \dot{\boldsymbol{x}}}{\partial \boldsymbol{x}} \right) \boldsymbol{\Psi}(t, t_0) \tag{4.28}$$

$$\boldsymbol{\Psi}(t_0, t_0) = \boldsymbol{I}_{6\times 6} \tag{4.29}$$

Once the STM with respect to the nominal trajectory is available, it can be used to compute the linearized change in the state $\boldsymbol{x}$ of a dynamical system at time t due to a change in the initial state $\boldsymbol{x}_0$. In particular,

for a given velocity perturbation $\boldsymbol{\delta v}_0$ at time t_0, a position perturbation $\boldsymbol{\delta r}_0$ at time t_0, and a corrective maneuver $\boldsymbol{\Delta v}_c$ performed at some time $t_c \geq t_0$, the state deviation $\boldsymbol{\delta x}_k$ at time t_k can be computed as:

$$\delta \boldsymbol{x}_k = \begin{bmatrix} \boldsymbol{\delta r}_k \\ \boldsymbol{\delta v}_k \end{bmatrix} = \boldsymbol{\Psi}(t_k, t_0)\delta \boldsymbol{x}_0 = \boldsymbol{\Psi}(t_k, t_0) \begin{bmatrix} \boldsymbol{\delta r}_0 \\ \boldsymbol{\delta v}_0 + \boldsymbol{\Delta v_c} \end{bmatrix} \tag{4.30}$$

Based on these equations, the TPA derives an optimal expression for the maneuver as a solution to an LQR problem. Specifically, the solution is obtained by the minimization of the performance index J, which can be obtained analytically by solving the vector equality:

$$\frac{\partial J}{\partial \boldsymbol{\Delta v}} = 0 \tag{4.31}$$

The general form of the solution to this problem reads (Cipriano et al., 2018):

$$\boldsymbol{\Delta v} = -\boldsymbol{A}^{-1} \sum_{k=1}^{n} (\alpha_k \boldsymbol{\delta r}_0 + \beta_k \boldsymbol{\delta v}_0) \tag{4.32}$$

where $\boldsymbol{A}$, α_i and β_i are defined as:

$$\boldsymbol{A} = (\boldsymbol{Q}^T + \boldsymbol{Q}) + \sum_{k=1}^{n} \boldsymbol{\Psi}_{rv}^T(t_k, t_0)(\boldsymbol{R}_k^T + \boldsymbol{R}_k)\boldsymbol{\Psi}_{rv}(t_k, t_0) + \tag{4.33}$$

$$+ \boldsymbol{\Psi}_{vv}^T(t_k, t_0)(\boldsymbol{T}_k^T + \boldsymbol{T}_k)\boldsymbol{\Psi}_{vv}(t_k, t_0) \tag{4.34}$$

$$\alpha_k = \boldsymbol{\Psi}_{rv}^T(t_k, t_c)(\boldsymbol{R}_k^T + \boldsymbol{R}_k)\boldsymbol{\Psi}_{rr}(t_k, t_0) + \boldsymbol{\Psi}_{vv}^T(t_k, t_c)(\boldsymbol{T}_k^T + \boldsymbol{T}_k)\boldsymbol{\Psi}_{vr}(t_k, t_0) \tag{4.35}$$

$$\beta_k = \boldsymbol{\Psi}_{rv}^T(t_k, t_c)(\boldsymbol{R}_k^T + \boldsymbol{R}_k)\boldsymbol{\Psi}_{rv}(t_k, t_0) + \boldsymbol{\Psi}_{vv}^T(t_k, t_c)(\boldsymbol{T}_k^T + \boldsymbol{T}_k)\boldsymbol{\Psi}_{vv}(t_k, t_0) \tag{4.36}$$

5

Simulator design and verification

This chapter illustrates the design of the software used to simulate the asteroid environment and the orbit control system. First, Sec. 5.1 describes the high-level architecture of the simulator, highlighting the main components and functionalities. Consequently, Sec. 5.2 presents the list of tests that have been planned to verify the simulator. Specifically, a low-level description of the environment module, along with the corresponding verification results, is reported in Sec. 5.3. Subsequently, Sec. 5.4 illustrates the verification tests regarding the onboard computer module. Section 5.5 briefly describes the modeled sensors and actuators, whereas Sec. 5.6.1 illustrates the high-fidelity dynamical model employed.

5.1 Software top-level architecture

The software is based on GRADS (Generic Rendezvous and Docking Simulator), a library developed in Matlab®/Simulink® for *software-in-the-loop* simulations of GNC systems applied to rendezvous and docking scenarios around Earth (Mooij, 2021). GRADS draws part of its functionalities from the existing ESA SpaceLAB and GAST (GNC and AOCS Simulations Toolbox) toolboxes while providing additional routines that augment the overall flexibility of the software. Despite the orientation towards Earth-orbiting applications, the modularity of GRADS architecture, combined with the flexible implementation of the environment blocks, makes it suitable for general-purpose GNC testing not necessarily limited to the Earth environment. By substituting Earth with the body of interest, many of the blocks available in GRADS can be adapted to design the simulator used in this thesis.

When considering the high-level architecture of a space dynamics software, certain modeling blocks emerge which are common to most scenarios. In short, a generic, multi-purpose simulator for designing and testing the GNC system of a space vehicle will include the following high-level blocks:

- *Environment*, which includes the models to compute the physical effects acting on the system (e.g., gravity acceleration).
- *Flight dynamics*, which contains the equations that describe the evolution of the system's state.
- *Mission manager*, which is responsible for providing the reference trajectory/attitude, target, and eventually mission constraints.
- *Guidance*, whose purpose is to determine the commands required for the spacecraft to follow the reference trajectory and attitude profile.
- *Control*, which converts the actions commanded by the guidance into actions that can be executed directly by the actuators.
- *Actuators*, which models the real hardware performance of the spacecraft actuators.
- *Navigation*, which reproduces the onboard estimation process, and sometimes includes also the mathematical model for instruments (e.g., Sun sensors, star trackers, accelerometers...), so as to reproduce the onboard knowledge of the spacecraft during the mission.

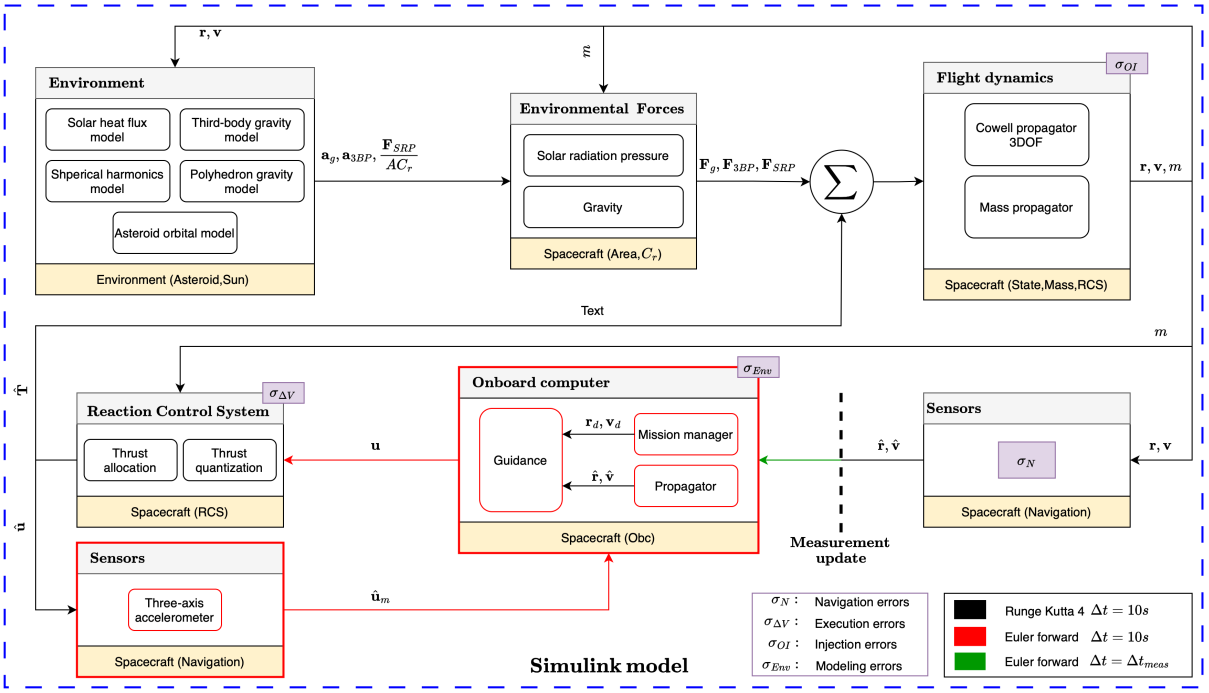

Figure 5.1: Top-level overview of the software architecture. The circumflex (hat) symbol marks those signals that are altered by the errors described in the purple boxes.

The software architecture developed for this work, illustrated in Fig. 5.1, closely follows this high-level structure to ensure a robust and versatile framework for GNC system development and testing. It should be noted that since this study is focused on guidance and control, navigation is the simulator's component which has been developed the least. In fact, in agreement with **BC4**, the capacity of the spacecraft to measure its state through optical sensors has been modeled by simply perturbing the real state with Gaussian noise, with no estimator included in the design. In place of an actual filter, a simple propagator has been incorporated, which, together with a three-axis accelerometer (this is the only sensor that has been modeled), forms an IMU for the translational motion of the spacecraft.

As discussed in Chapter 2, numerous sources of errors degrade the performance of a GNC system, especially in the asteroid environment: the *locations* where each one enters the simulator have been highlighted by a small, purple box. These limitations in the spacecraft's knowledge about its own state and the surrounding environment explicitly affect the computation and execution of the guidance commands. Furthermore, the limited computational capacity of onboard processors in deep space missions adds another layer of complexity, as it requires the onboard dynamics propagation to be computationally light, thus affecting both the choice of the integration scheme and the environment model.

A faithful and realistic model of a GNC system must reproduce these limitations, which is why the software is designed such that simulations occur on two distinct layers. Specifically, two dynamical models are integrated in parallel during a simulation: a high-fidelity environment model, designed to closely represent reality, is integrated using a Runge-Kutta 4 (RK4) integration scheme (the choice of this specific numerical method is explained later in Sec. 5.6); simultaneously, the spacecraft's onboard computer uses a simplified model, integrated with a basic Euler forward scheme, to predict its trajectory and compute the guidance law accordingly. This dual-layered approach ensures that the system's performance can be assessed under realistic operational constraints, and its robustness evaluated against limited knowledge. In relation to this, two features of the simulator should be highlighted:

- The environment structure used inside the onboard computer module is different from the one used within real dynamics. The former belongs to the *Spacecraft* class, whereas the latter to the *Environment* class. This allows to investigate how modeling uncertainties affect the system.

- A measurement update time Δt_{meas} defines the frequency at which the onboard computer is assumed to receive information on the spacecraft state. During the time interval between two consecutive measurements, the knowledge of the spacecraft's position and velocity depends exclusively on the onboard propagation process and the inputs from the accelerometer. This phase is referred to as *dead reckoning*[1].

Finally, it should be noted that all the variables involved in the simulations are grouped in a limited number of data structures that represent the input to the high-level blocks of the model (as indicated by the yellow boxes in Fig. 5.1). Figure 5.2 shows that these data structures have sub-groups of data, which represent the input to lower-level simulator blocks. For example, the *Mission* class, which belongs to *Obc*, is a direct input to the *Mission manager* block. While allowing for an intuitive use of the simulator, this modularity also enables the use of the Matlab Parallel Computing toolbox[2] and the Rapid Acceleration mode from Simulink[3] to reduce drastically the time required to run heavy Monte Carlo simulations. Furthermore, it allows to change the simulation scenario (i.e., the asteroid) in a user-friendly and efficient way, since all the parameters of the simulation depending on the small body are included in one unique data structure (*Environment.Asteroid*). It should be noted that global variables also include the seeds that are used to generate random errors within the Simulink model (a random generator block is present in correspondence of each purple box of Fig. 5.1). These seeds are fixed by the user to ensure reproducibility of the results, and they are sequentially updated when running the simulator in parallel mode to perform Monte Carlo simulations.

Finally, the workflow of the simulator can be described as follows. As highlighted by the colors in Fig. 5.1, black blocks are integrated by an RK4 scheme, which is used to propagate the dynamics of the spacecraft according to a high-fidelity environment model and the thrust commands generated by the reaction control system. These latter are adequately perturbed with respect to the nominal commanded values to reproduce execution errors. The spacecraft state that results from this propagation is corrupted in all its components by the addition of Gaussian noise, which attempts to reproduce the measurements

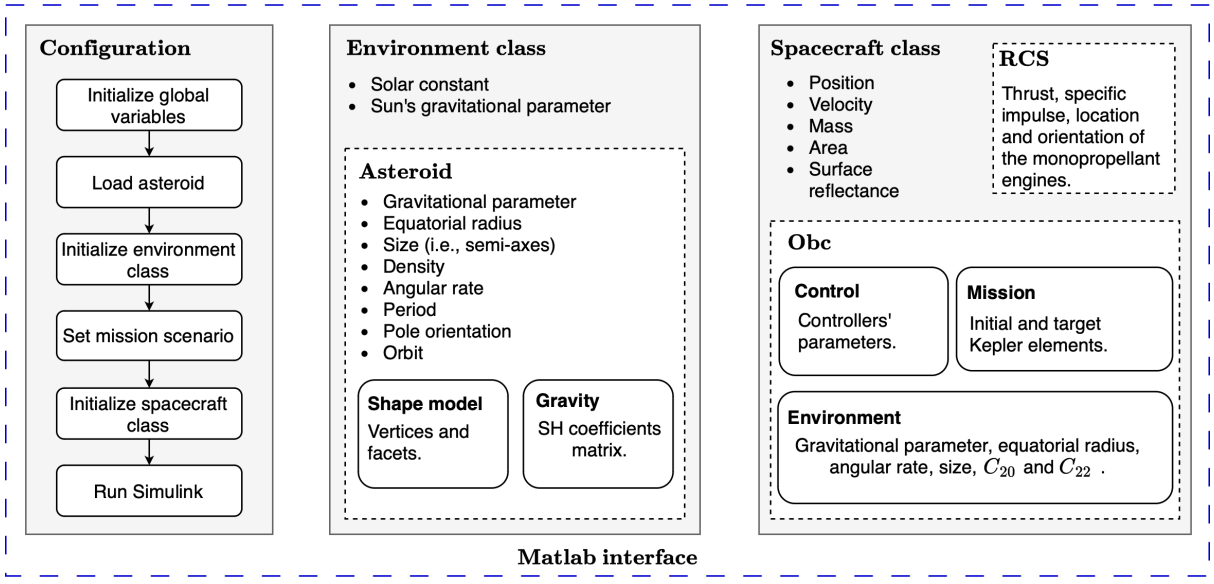

Figure 5.2: Matlab interface of the simulator.

[1] It is noted that in a realistic GNC system there are several sensors, each with a different operational frequency. Having a single value for Δt_{meas} is an approximation used here to model the lack of real-time knowledge.

[2] `https://nl.mathworks.com/products/parallel-computing.html`, accessed on 02/10/2024.

[3] `https://nl.mathworks.com/help/simulink/ug/how-the-acceleration-modes-work.html`, accessed on 02/10/2024.

that would be provided by the onboard sensor suite. These simulated measurements are then fed to the onboard computer once every Δt_{meas}, which represents the frequency at which the onboard knowledge of the system is updated with the values coming from the real dynamics. To simulate the discrete nature of the onboard computer, the propagator unit integrates the spacecraft dynamics until the following measurement update with a Euler forward integrator. In parallel, the mission manager generates a time-varying reference, and the guidance module uses both signals to compute a control law. The latter is then transmitted to the actuator block, where first a quantization logic and then an allocation algorithm determine which thrusters shall be turned on. Here, the discrete control signals from the onboard computer are multiplied for the mass, which is continuous, such that the real thrust force is also integrated through RK4 (the discrete domain ends, and the continuous one begins again). Whenever a maneuver is executed, the accelerometer measures the real components of the thrust acceleration vector, which are then considered by the onboard computer to propagate the dynamics during the following step.

5.2 Verification

The verification of the simulation environment was done through unit and subsystem testing. Although the verification of GRADS is still an ongoing process, the specific functionalities inherited for this work have been reported as already verified, if not at a unit level, at least at a sub-system level, thus not requiring further action.

5.2.1 Verification plan

Table 5.1 gives an overview of the tests executed to verify the software blocks and overall architecture. Tests are categorized as either *unit tests*, for those involving an individual low-level block, or *subsystem tests*, for those involving combinations of multiple blocks. Although formally part of subsystem verification, the tests performed on the spherical harmonics and polyhedron modules have been classified as *acceptance tests*. This emphasizes that these functionalities were already available prior to this work, hence they had already undergone verification. Nonetheless, a set of acceptance tests has been conducted to familiarize with their use. It is also noted that among the highlighted blocks, all gravity models and certain transformation routines were implemented exclusively in MATLAB and subsequently integrated into the Simulink model via Matlab function blocks.

Table 5.1: Verification plan.

Module	Test ID	Test type	Description
Mathematical utilities	MATH1	Unit test	Check orthogonality property of implemented rotation matrices.
	MATH2	Unit test	Check that rotation matrix from RTN frame to ACI frame is the same whether computed with orbital elements (Eq. (3.18)) or with Cartesian elements (Eq. 3.20).
	MATH3	Unit test	Evaluate and compare rotation matrix from J2000 to ACI with TUDAT.
	MATH4	Unit test	Compare the results obtained from the computation of elliptic integrals using the implemented Carlson's algorithms with those obtained by using Matlab built-in functions.
	MATH5	Subsystem test	Ensure that the compound element transformation Kepler-Cartesian-Kepler yields the same initial state when including Kepler singularities (e.g., zero eccentricity and inclination).
	MATH6	Subsystem test	Verify that the Sun position vector rotated from the ACI frame to the ACOF frame has only the radial component that is not zero.
Spherical harmonics	SH1	Acceptance test	Compare the gravity field computed by the spherical harmonics function with the results obtained using Matlab built-in *gravityssphericalharmonic*[4] function.

[4] `https://nl.mathworks.com/help/aerotbx/ug/gravityssphericalharmonic.html`, accessed on 14/11/2024.

Module	Test ID	Test type	Description
	SH2	Acceptance test	Compute the gravity acceleration over a sphere of radius 16 km around Eros, and compare the results with those obtained by Miller et al. (2002).
Triaxial ellipsoid	TRIX1	Subsystem test	Compute gravity acceleration on a sphere around Eros, and compare the results with those obtained by using the spherical harmonics function with the ellipsoid's SH coefficients.
	TRIX2	Subsystem test	Calculate the gravity for a uniform sphere modeled as an ellipsoid, and compare the results with the point mass gravity model.
Polyhedron	PH1	Unit test	Load and visualize shape models to verify that they have been imported correctly.
	PH2	Acceptance test	Compute the gravity field at specific positions of Eros using the shape model with 1708 facets, then compare the results with those presented by D'Urso (2014).
	PH3	Acceptance test	Reproduce the gravity field of Eros up to the surface, and compare results with those obtained by Spee (2022).
Sun-Eros propagator	ORB1	Subsystem test	Propagate the dynamics for one full heliocentric revolution of Eros and observe heliocentric distance and Sun's latitude to ensure that the asteroid motion and attitude is correct.
	ORB2	Subsystem test	Check that solar radiation pressure is maximum at perihelion and minimum at aphelion. Compare results with known values from the literature.
Onboard computer	OBC1	Unit test	Apply the sliding mode controller to a simple problem taken from Slotine and Li (1991) to verify its implementation.
	OBC2	Subsystem test	Verify that the onboard computer state is updated from the real dynamics according to the value of Δt_{meas}.
	OBC3	Subsystem test	Compare the position difference obtained by numerical integration with that obtained by applying the state transition matrix.
Termination settings	TERM1	Subsystem test	Visual inspection of impact and escape trajectories.

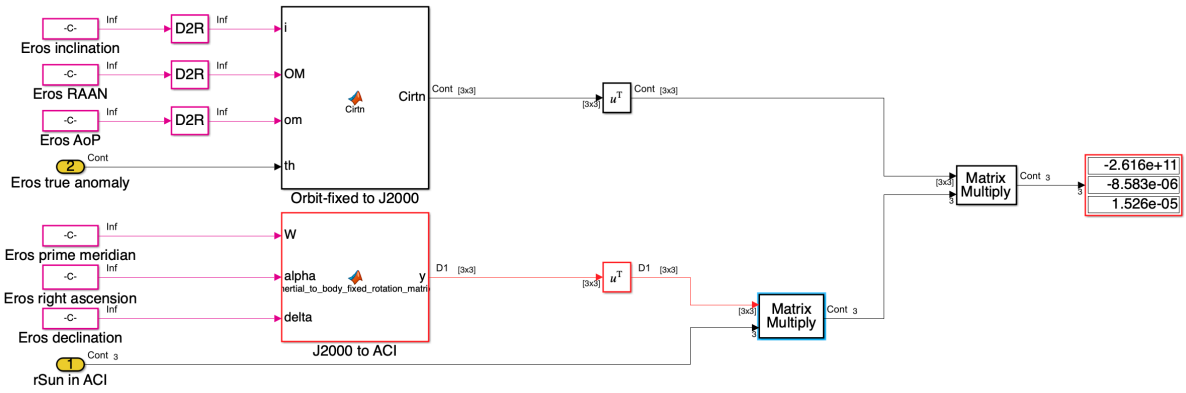

Figure 5.3: Example of verification test for rotation matrices and coordinate transformations.

5.2.2 Mathematical utilities

For brevity, the results of the verification tests for the mathematical utilities have been reported within this section. These software components had to be tested at a unit level because not all the frame and coordinate transformations described in Sec. 3.3 were originally available in GRADS, therefore some had to be implemented from scratch and then verified thoroughly. While a version of the Kepler-to-Cartesian conversion routine was already present in the original software, its formulation could not handle hyperbolic osculating elements or Kepler singularities. Therefore, the routine was implemented a second time by using the equations outlined in Sec. 3.3.1.

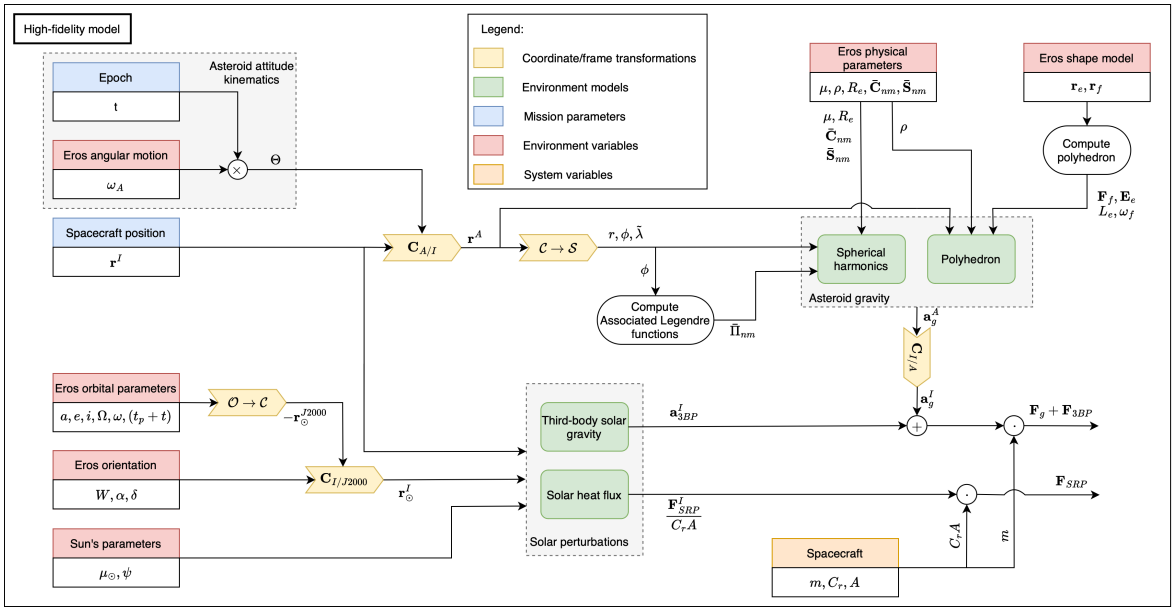

Figure 5.4: Low-level visualization of the environment module.

As for the rotation matrices that were added to the model, these were compared with a known and verified software: TUDAT[5] (TU Delft Astrodynamics Toolbox). Moreover, some matrices, such as $\boldsymbol{C}_{I/R}$, allowed for specific tests since they can be formulated in different ways (orbital elements and inertial components). As a consequence, it was verified that the results obtained from different implementations matched. Finally, a number of tests involving compound transformations were executed, an example of which is reported in Fig. 5.3. Here, it was ensured that transforming the position vector of the Sun from the ACI frame to the orbit-fixed frame would result in a vector with only the first (radial) component being not zero.

5.3 Environment block

This section presents some of the results obtained during the verification campaign of the environment module, whose low-level representation is provided in Fig. 5.4. This visualization has been reduced to the level of verification, such that the visible blocks are those that have been verified by unit/subsystem testing. In addition to environment models and system variables, the inputs for this part of the simulator are the spacecraft position in the ACI frame and the simulation epoch. It is also possible to specify a value for t_p, the time since periapsis passage of Eros, to locate the simulation at the desired position along the heliocentric orbit. Since the asteroid is assumed to be uniformly rotating around its maximum moment of inertia, the attitude kinematics is very simple and obtained by the law $\Theta = \omega_A t$. It should be noted that the *asteroid gravity* unit computes the real acceleration exerted by Eros by relying on either the SH model, the polyhedron model, or, as will be discussed, a combination of both, depending on the user's input.

5.3.1 Spherical harmonics gravity

One of the acceptance tests for the spherical harmonics gravity function consisted of comparing the norm of the gravity acceleration on a sphere of 25 km radius around Eros with the one computed by using the *gravityspericalharmonic* function that is available in the Aerospace toolbox of Matlab. The errors between the two implementations are visible in the top-left plot in Fig. 5.6, where they appear to be in the order of computer precision. Furthermore, Fig. 5.5 displays the radial component of the gravity acceleration on a sphere of 16 km around Eros, with contour lines at intervals of 50 mGals. This

[5] `https://docs.tudat.space/en/latest/`, accessed on 06/06/2024.

figure has been compared with the same one by Miller et al. (2002), where very similar patterns and values can be observed. Specifically, the two lobes of Eros, located at approximately 180° and -10° in longitude, represent the most notable gravitational feature of the asteroid. For these particular results, the SH model used was the one obtained during NEAR mission through radiometric tracking. Additionally, smaller tests for the verification of the SH module included simple routine checks, such as ensuring that the contributions for given single harmonic terms would match theoretical expectations. As an example, the three plots in Fig. 5.6 show the zonal, tesseral, and sectorial components of the third-degree gravity field. In accordance with the theory presented in Sec. 3.4.1, the former is symmetric about the equator, the second forms a grid pattern, and the latter is longitudinally symmetric.

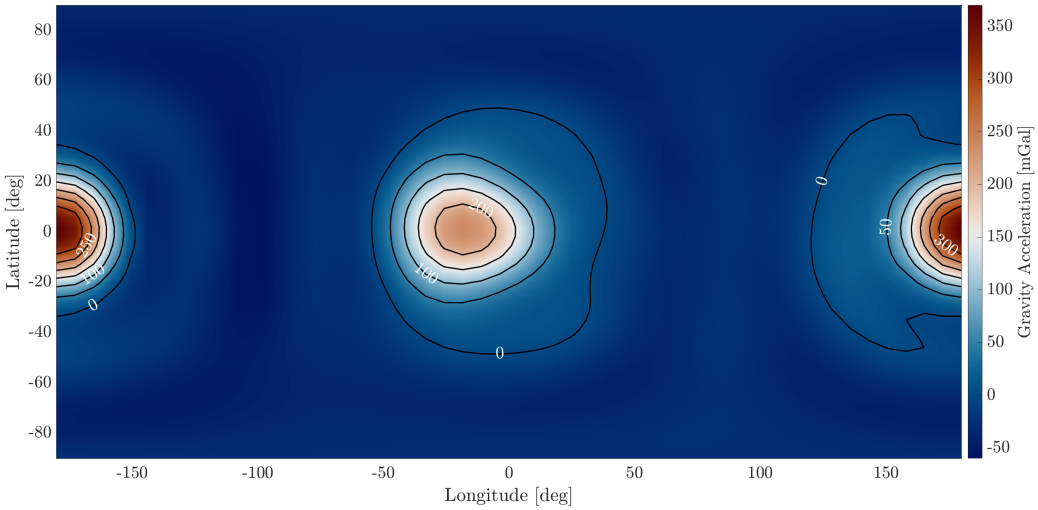

Figure 5.5: The radial acceleration of Eros's gravity field on a sphere of 16 km radius for coefficients through degree 8.

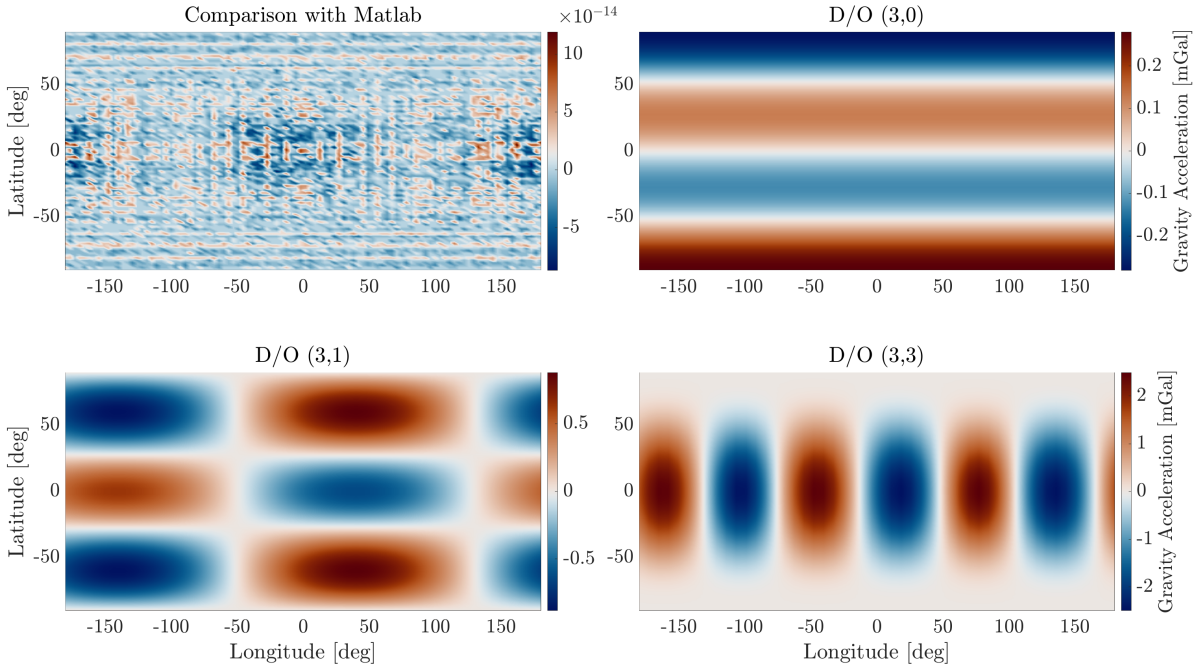

Figure 5.6: Acceptance tests for SH gravity function.

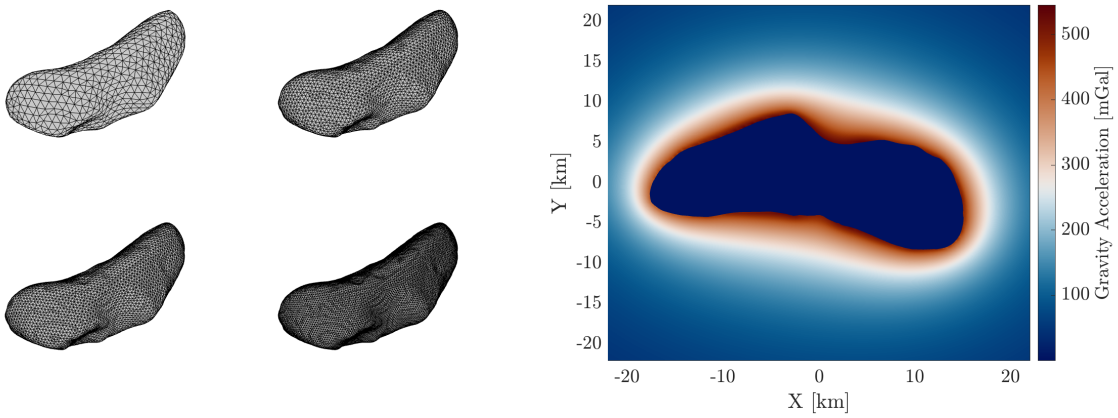

Figure 5.7: On the left, imported shape models of Eros with different resolutions. On the right, the gravity acceleration norm on Eros equatorial plane, computed using a shape model with 22,540 facets).

5.3.2 Polyhedron gravity

Before performing the acceptance tests for the polyhedron gravity model, a Matlab routine to read shape files and translate them into adequate data structures had to be implemented and tested. This was done by visual inspection of the loaded 3D shapes, as reported in Fig. 5.7 on the left. Furthermore, some of the verification tests reported by Razgus (2016) were repeated. In particular, the gravitational potential and the acceleration due to the polyhedron were computed at different points of a rectangular prism (which is modeled without errors by a polyhedron). This also allowed to verify the capacity of the function to correctly compute the volume of a solid, since that of the prism is known analytically. Since Razgus had not focused on Eros, an additional test consisted of repeating the same calculations reported by D'Urso (2014), thus computing the gravity acceleration components for specific points in space and for different shape models of Eros. Finally, the gravity acceleration up to the surface of Eros was computed on the equatorial plane and compared to the results reported by Spee (2022).

5.3.3 Triaxial ellipsoid gravity field

The complete formulation of the triaxial gravity field model is described in Appendix B. Specifically, an integral part of the adopted methodology relies on the implementation of Carlson's algorithms for the evaluation of elliptic integrals, which provide a fast and robust numerical approach that could be suited to onboard applications. Therefore, these algorithms were implemented and tested at a unit level by comparing them to the slower built-in Matlab functions *EllipticE* and *EllipticF*. Over a batch of 1000 simulations with randomly generated elliptic integrals, the solutions provided by the two classes of algorithms were always the same up to computer precision, with observed differences below 10^{-15}.

To verify the implementation of this gravity model, two main tests were conducted. First of all, it should be clarified that due to the symmetry in an ellipsoid's shape, the gravitational coefficients of its spherical harmonic expansion taken about its center of mass can be computed uniquely. In fact, all S_{nm} coefficients are identically equal to zero, whereas all coefficients C_{nm} such that either n or m are odd are equal to zero as well (Scheeres, 2012b). Thus, the only non-zero gravity coefficients are those of the form C_{2n2m}. As shown by Balmino (1994), these (un-normalized) coefficients can be derived exactly:

$$C_{2n2m} = \frac{3}{R_e^{2n}} \frac{n!(2m)!}{2^{2n}(2n+3)(2n+1)!} (2-\delta_{0m}) \frac{(2n-2m)!}{(2n+2m)!} \sum_{k=0}^{n-m} \frac{(-1)^k(4n-2k)!}{(2n-k)!(2n-2m-2k)!} \sum_{s=0}^{m} \frac{(-1)^s}{(2s)!(2m-2s)!} \sum_{p=0}^{k} \frac{(2n-2m-2p)!}{(n-m-p)!(k-p)!} \sum_{q=0}^{p} \frac{(2s+2p-2q)!(2m-2s+2q)!}{q!(p-q)!(s+p-q)!(m-s+q)!} a^{2(m-s+q)} b^{2(s+p-q)} c^{2(n-m-p)} \tag{5.1}$$

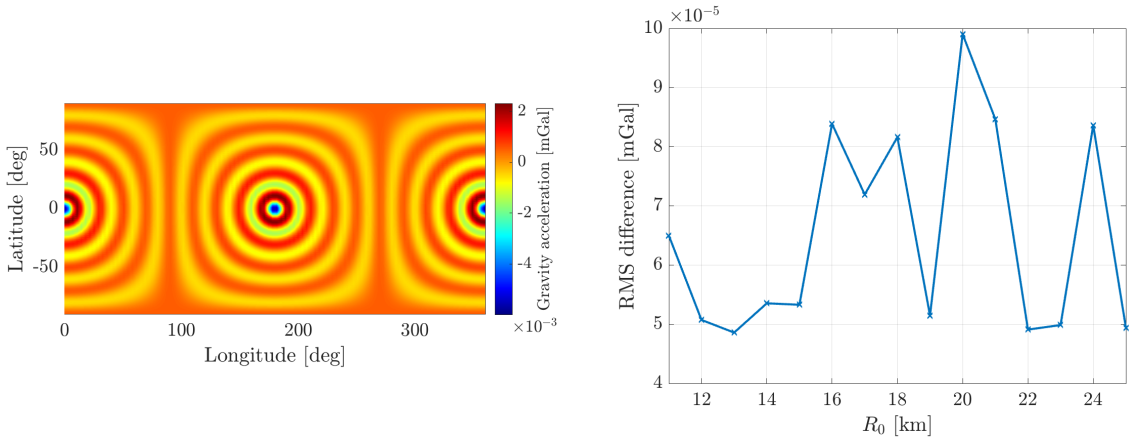

(a) Gravity differences between triaxial ellipsoid gravity model and spherical harmonics with triaxial ellipsoid coefficients over a sphere of radius 25 km around Eros.

(b) RMS gravity differences between the point mass term and the triaxial ellipsoid approximation of a uniform-density sphere.

Figure 5.8: Verification results of the triaxial ellipsoid gravity model.

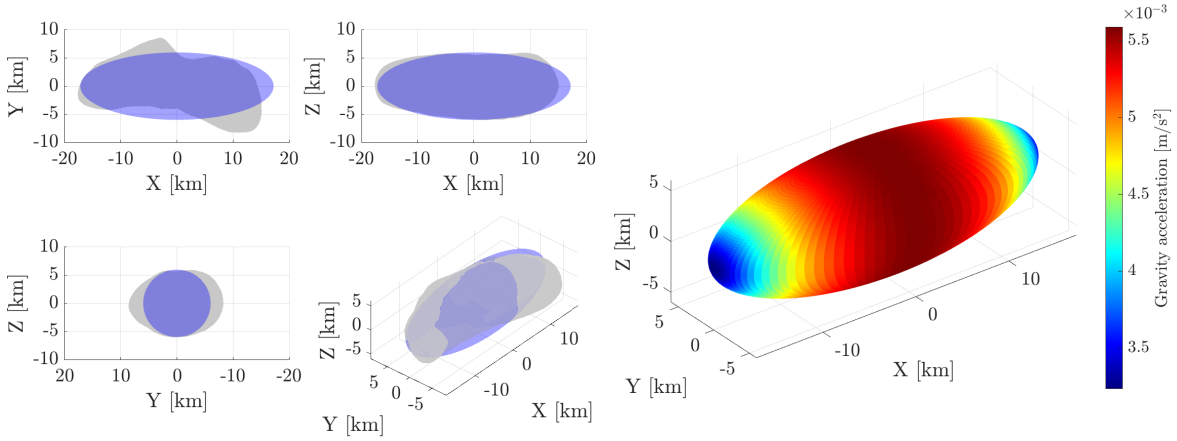

Figure 5.9: Triaxial ellipsoid shape and gravity model for Eros.

The correct implementation of the formula above was verified by assessing the first five terms of the expansion, for which an explicit expression is given by the author. Following this, the coefficients up to order and degree 16 were computed and then normalized using Eq. (3.25). The actual verification test consisted of computing the gravity field acceleration over a sphere of 25 km around Eros by using the spherical harmonics block (verified previously) with the coefficients computed analytically. Then, the results were compared with the implemented triaxial gravity field model. As visible in Fig. 5.8a, the differences are extremely small (more than eight orders of magnitude smaller than the nominal acceleration values). As a second test, the gravity field generated by a sphere of size 10 km and density 1000 kg/m^3 was taken as reference and approximated using the triaxial ellipsoid model. In Fig. 5.8b, the root mean square (RMS) gravity difference between the point mass and the triaxial ellipsoid models has been reported at various distances from the sphere. The differences are very small and exhibit an erratic behavior due to numerical errors, thus proving the correct implementation of this gravity model.

As a final note, it is specified that Eros's shape as a triaxial ellipsoid was modeled by using the *real* dimensions of the small body, reported in Table 2.5. As visible in Fig. 5.9, these values approximate quite well the actual shape of the asteroid. The use of a triaxial ellipsoid model for onboard purposes needs to be distinguished from scientific studies that aim to fit the values of the semi-axes to a given gravity model. In the latter scenario, an optimization procedure is typically required, and results can potentially lead to values of the semi-axes that are pretty distant from reality due to irregularities in the

mass distribution of the celestial body. Throughout this work, the triaxial ellipsoid gravity model will be always used by relying on the physical appearance of the object. The purpose is to reproduce a realistic mission scenario where the small body's size is determined onboard from a rough shape model.

5.3.4 Eros-Sun propagator

Given the relatively short time scale of the simulations compared to Eros's orbital period around the Sun, a first-order approximation could treat the Sun's position as constant. However, due to the mission requirement to maintain a specific solar phase angle (**MIS-REQ-04**), it is important to also model Eros's motion around the Sun. Although the Sun-asteroid vector orientation will remain nearly constant over each controlled trajectory, this approach enables testing the orbit control system's performance at different points along Eros's orbit. As discussed in Sec. 2.2.2, the inclination of the terminator plane relative to Eros's equator can vary by nearly 180 degrees along its heliocentric path. Consequently, modeling the asteroid's orbit will allow to assess the robustness of the system against different types of instabilities, which depend on the inclination and RAAN required to keep the orbit aligned with the terminator plane at a given point along Eros's orbit.

Given these considerations, it follows that modeling Eros's heliocentric trajectory as a Kepler orbit is sufficiently accurate, as stated in **BC3**. This can be implemented quite straightforwardly using a semi-analytical propagator: at each time instant, the true anomaly of Eros is computed by solving numerically Kepler's equation (3.47), and the set of six orbital elements is converted into inertial Cartesian coordinates. The position vector of Eros with respect to the Sun in the J2000 frame is then inverted and rotated using the rotation matrix $\boldsymbol{C}_{I/J2000}$, thus obtaining the position vector of the Sun in the ACI frame. All the blocks involved within this model have already been verified at a unit level, therefore the overall sub-system has been tested by simulating one full revolution of Eros (roughly 643 days) to ensure that the implemented model works correctly. The results, reported in Fig. 5.10, show that the maximum and minimum distances from the Sun match the known perihelion (1.13 au) and aphelion (1.78 au). Most importantly, the evolution of Eros orientation with respect to the Sun is verified, as visible on the right. In fact, the angle under which the Sun is seen from Eros's equator closely matches the plot shown Fig. 2.2b, proving that the poles of Eros experience long periods of darkness as a consequence of the large obliquity of the asteroid. Specifically, a view of Eros as seen from the Sun has been plotted for two particular points: the first one corresponds to where the Sun's latitude is maximum, which, being close to 90 degrees, implies that the Sun is located almost above the north pole; the second one identifies the location where the Sun lies on Eros equator. In both cases, the illuminated view of the asteroid's shape model corresponds to these expectations, thus concluding the verification of this subsystem.

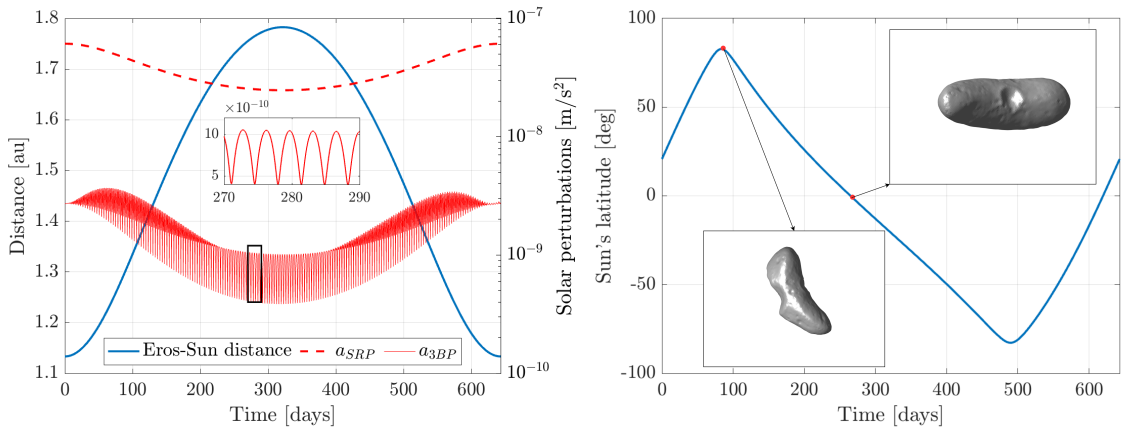

Figure 5.10: On the left, the distance between Eros and the Sun, as well as the magnitude of the solar perturbations, for one heliocentric revolution. On the right, the simulated angle under which the Sun is seen from Eros's equator, together with two views of the asteroid's attitude as seen from the Sun.

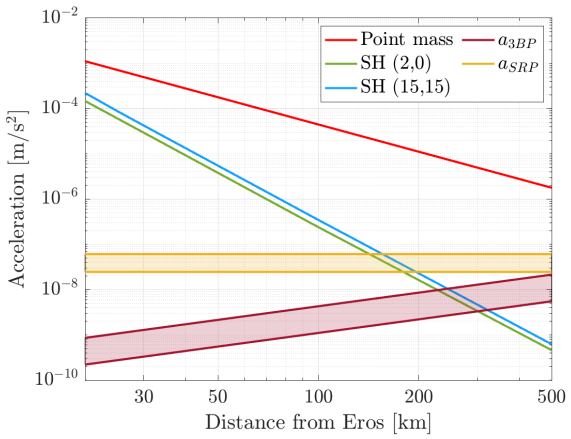

Figure 5.11: Dynamical environment at Eros as a function of the distance to the asteroid's center of mass. The boundary values for solar perturbations correspond to the perihelion and aphelion.

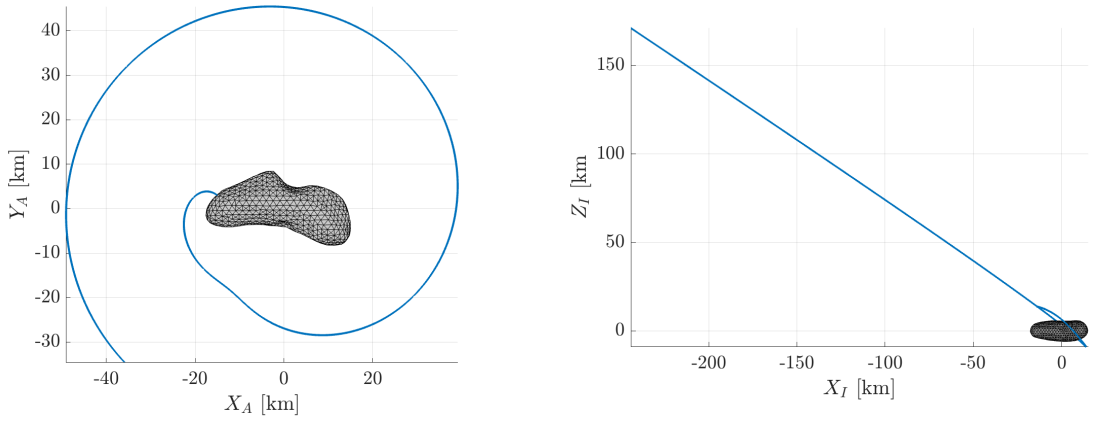

Figure 5.12: Examples of trajectories interrupted due to violation of termination conditions. On the left, an impact trajectory, plotted in the asteroid-fixed frame; on the right, an escape trajectory in the inertial frame.

This test was used also to verify the correct implementation of the solar perturbations. As visible on the left of Fig. 5.10, both the SRP and the three-body accelerations agree with the values that have been reported from other sources in Sec. 3 (Figs. 3.2, 3.7), with solar radiation pressure being dominant over solar tides. As expected, the SRP exhibits a behavior that is inversely proportional to the heliocentric distance, whereas the three-body solar gravity has a periodic pattern that is associated with the time scale of the associated orbit around Eros. As a final verification test for the overall environment module, Fig. 5.11 was generated. The values present in the plot are exactly aligned with those present in the literature, thus concluding the verification of the environment module. Furthermore, this plot confirms that the orbits of interest for this study (semi-major axis lower than 50 km) are all located within the gravity regime (Sec. 3.4.3), where the disturbances generated by the irregular gravity field are several orders of magnitude larger than the solar perturbations.

5.3.5 Termination conditions

A series of termination criteria has been identified to prematurely interrupt the simulator in case the trajectory escapes the asteroid or impacts on its surface. In part, this is done to avoid the waste of computational resources; however, it is also a powerful tool that can provide valuable insights, especially during open-loop simulations. The implementation of these termination criteria has been verified manually by visually inspecting specific trajectories, and an example is shown in Fig. 5.12.

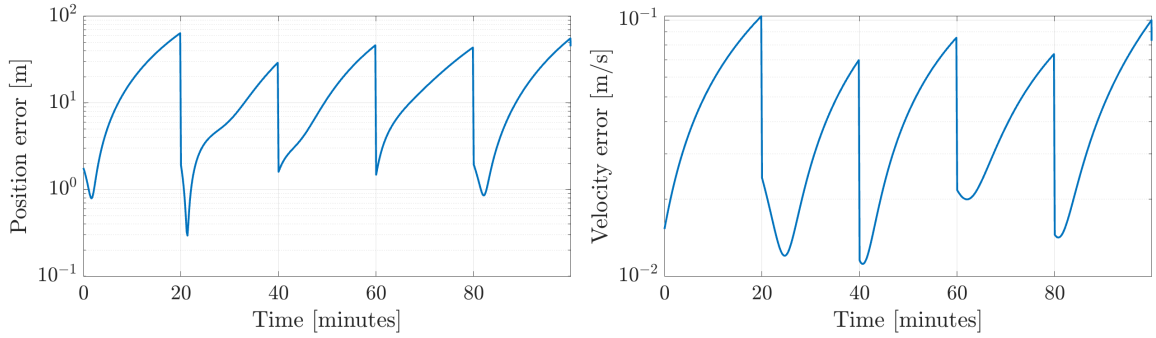

Figure 5.13: Position and velocity errors within the onboard computer for $\Delta t_{meas} = 20$ minutes.

The escape condition is checked in a twofold way: if the semi-major axis becomes negative, meaning the spacecraft has entered a hyperbolic escape trajectory, or if the distance from the asteroid exceeds the value of 5000 km. It is noted that this implementation is affected by a certain bias: since the motion is strongly perturbed, the semi-major axis of a low-altitude trajectory could likely become momentarily negative, without necessarily implying that the trajectory is escaping the system. For this reason, it has been chosen to terminate the simulations only if the condition on the semi-major axis is verified at a distance from the asteroid that is larger than 300 km, where the Keplerian model holds sufficiently well.

Conversely, the impact condition is verified by assessing the value of the solid angle ω_f. Since this angle requires the evaluation of the polyhedron model, it is not generally available during a simulation time step. However, as it will be explained in the next section, it is expected that before an impact occurs the simulator will have automatically switched to the polyhedron model for gravity field computation, thus allowing for this variable to be readily available.

5.4 Onboard computer

The onboard computer block contains the mission manager, the controller, and the propagator modules. All these units are affected by an inaccurate knowledge of the spacecraft state due to navigation errors, which are generated according to a normal distribution with zero mean:

$$\hat{\boldsymbol{r}} = \boldsymbol{r} + \mathcal{N}(0, \sigma_{N,r}^2 \boldsymbol{I}_{3\times3}) \qquad \hat{\boldsymbol{v}} = \boldsymbol{v} + \mathcal{N}(0, \sigma_{N,v}^2 \boldsymbol{I}_{3\times3}) \tag{5.2}$$

To verify the correct implementation of this aspect, a simple test was performed by assuming a value for Δt_{meas} of 20 minutes. The results, reported in Fig. 5.13, show that the errors in position and velocity between the real and the onboard state grow steadily within the 20-minute window, to then decrease instantaneously when the updated state is fed into the onboard computer module. Since they are part of the onboard computer, the verification results for the two controllers are reported hereafter.

Sliding-mode controller

The implemented first-order sliding mode controller was verified by reproducing the results for an example provided by Slotine and Li (1991). The one-dimensional problem given by the authors is described by the following dynamics:

$$\ddot{x} + a(t)\dot{x}^2 \cos 3x = u \qquad a(t) = |sin(t)| + 1 \tag{5.3}$$

$$\hat{f} = -1.5\dot{x}^2 \cos 3x \qquad F = 0.5\dot{x}^2 |\cos 3x| \tag{5.4}$$

with $1 \leq a(t) \leq 2$. Given the reference trajectory $x_d(t) = \sin \pi t/2$, the control law can be designed:

$$u = 1.5\dot{x}^2 \cos 3x + \ddot{x}_d - \lambda\dot{\tilde{x}} - (0.5\dot{x}^2 |\cos 3x| + \eta) \operatorname{sgn}(\dot{\tilde{x}} + \lambda\tilde{x}) \tag{5.5}$$

To replicate the example, η and λ are set at 0.1 and 20, respectively, whereas the control frequency is kept at 1 kHz.

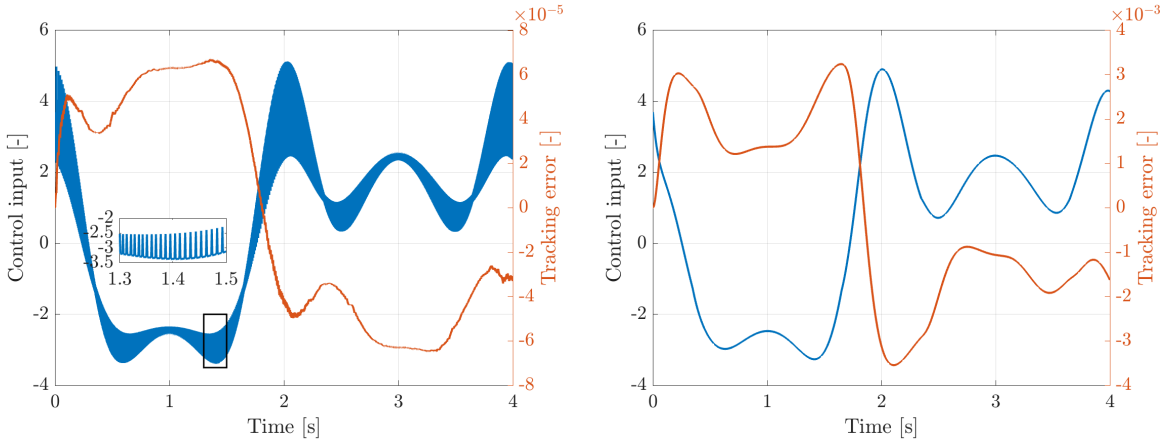

Figure 5.14: Verification results for sliding mode controller in its nominal version (left) and with a boundary layer (right).

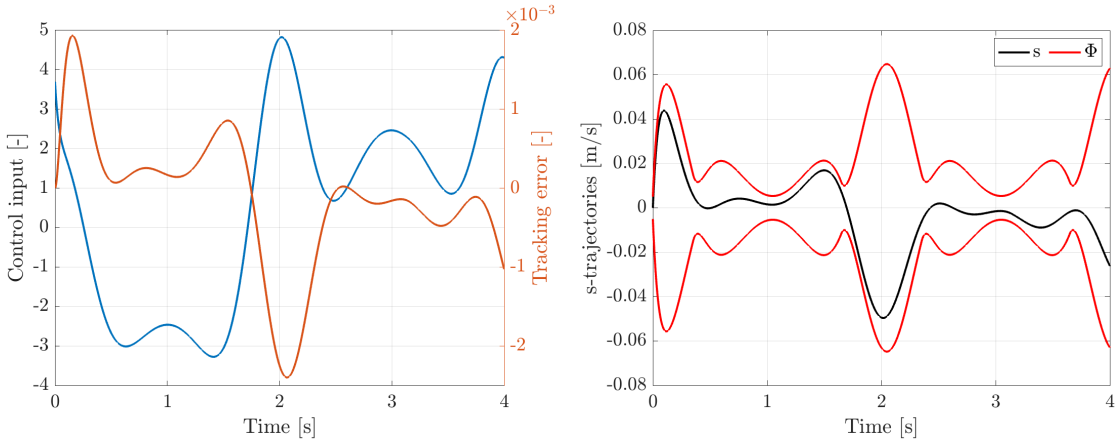

Figure 5.15: Verification results for sliding mode controller with time-varying boundary layer.

The results obtained are reported in Fig. 5.14, where the control input on the left shows the chattering effect caused by the switching term of law, whereas on the right it becomes continuous by introducing a boundary layer of width $\Phi = 0.1$. However, the consequence is that the tracking accuracy decreases by two orders of magnitude. Additionally, also the time-varying boundary layer method has been tested and verified. To do this, the control law was modified to exploit the knowledge about the parametric uncertainty structure:

$$u = 1.5\dot{x}^2 \cos 3x + \ddot{x}_d - \lambda\dot{\tilde{x}} - (0.5\dot{x}^2|\cos 3x| + \eta - \dot{\Phi})\,\mathrm{sat}\,(\dot{\tilde{x}} + \lambda\tilde{x}, \Phi) \tag{5.6}$$

$$\dot{\Phi} = -\lambda\Phi + (0.5\dot{x}_d^2|\cos 3x_d| + \eta) \tag{5.7}$$

In this way, the tracking error decreases by a factor of four compared to a constant boundary layer thickness, as visible in Fig. 5.15. The results presented for both cases are precisely aligned with those reported by the author, thus confirming the correct implementation of the controller.

Variational equations propagator

To verify the correct implementation of the propagator for the variational equations and the state transition matrix (essential for the target point approach), an open-loop simulation of a 50 km equatorial orbit was executed. The orbit was propagated first with initial circular conditions and then with an added small perturbation vector. Simultaneously, the variational equations were propagated, and the state transition matrix history was recorded. Figure 5.16 shows the error between the perturbed and unperturbed trajectories, calculated using both the state transition matrix and the numerical results. As the linearized approximation holds well at the beginning of the simulation, the routine is considered verified.

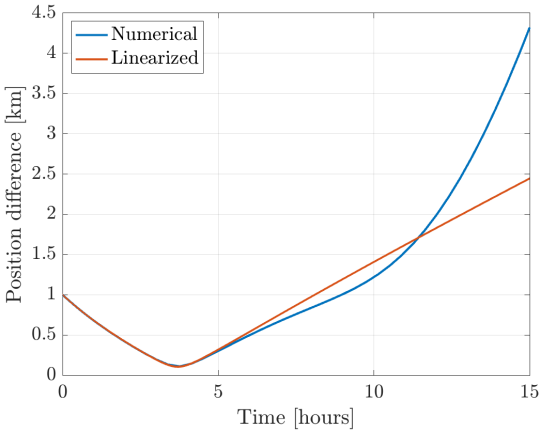

Figure 5.16: Verification test for the variational equations propagator.

Table 5.2: Parameters for the three-axis accelerometer.

Parameter	Symbol	Value
Bias [m/s^2]	b	10^{-8}
Scale factor [-]	s	10^{-3}
Misalignment [-]	m	10^{-5}
Noise density [m/s^2/$\sqrt{Hz}$]	w	10^{-10}

5.5 Sensors and actuators

Although GRADS makes available a large set of Simulink blocks for spacecraft hardware components, the simulator used for this work employs only a three-axis accelerometer and a reaction control system.

5.5.1 Three-axis accelerometer

The three-axis accelerometer is the only sensor that has been included in the simulator. The corresponding Simulink block was already available and verified in GRADS, with a simplified mathematical model that accounts for the scale factors s, the bias b, and the misalignments m of the instrument:

$$\boldsymbol{u}_m = \boldsymbol{u} + \begin{pmatrix} b_x \\ b_y \\ b_z \end{pmatrix} + \begin{bmatrix} s_x & m_{xy} & m_{xz} \\ m_{yx} & s_y & m_{yz} \\ m_{zx} & m_{zy} & s_z \end{bmatrix} \boldsymbol{u} \tag{5.8}$$

where $\boldsymbol{u}$ is the real, non-gravitational acceleration acting on the spacecraft, whereas $\boldsymbol{u}_m$ is the measured one. In the simulator, the only accelerations that can be physically measured are the one due to the solar radiation pressure and the one due to the thrusters of the spacecraft. All the remaining sources of acceleration are gravitational, and therefore cannot be detected by the accelerometer. However, it is assumed that only the thrust acceleration is estimated by the instrument, since the one due to the solar radiation pressure is several orders of magnitude smaller, thereby its signature could not be distinguished. Additionally, measurement noise is also included within the sensor block by defining a noise spectral density w, which is modeled as normally distributed white noise. The values used for the accelerometer parameters have been reported in Table 5.2.

5.5.2 Reaction control system

The spacecraft RCS is assumed to be equipped with 24 monopropellant thrusters of 3N each, for a total available thrust of 12N per side of the spacecraft. To simulate a realistic performance, these thrusters are assumed to work according to an on-off operation mode. A graphical sketch of the propulsion system with respect to the body reference frame is provided in Fig. 5.17.

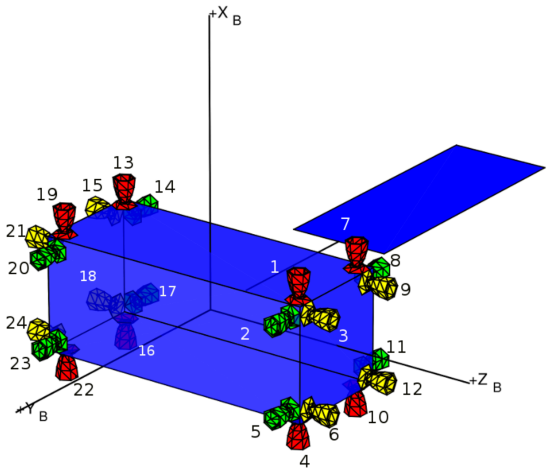

Figure 5.17: Disposition of the RCS thrusters. Source: Habets (2015).

Although GRADS makes available optimization routines to solve the control allocation problem, this has been greatly simplified by the approach described later in Sec. 6.5.2.

To model the presence of maneuvering errors, the discrepancy between the executed and commanded thrust vector is modeled also in this case with a normal distribution. In particular, if the thrust vector is decomposed into spherical components, then:

$$\hat{\boldsymbol{T}} = \begin{pmatrix} T \\ \epsilon \\ \psi \end{pmatrix} + \begin{pmatrix} \mathcal{N}(0, \sigma^2_{\Delta V,mag}) \\ \mathcal{N}(0, \sigma^2_{\Delta V,dir}) \\ \mathcal{N}(0, \sigma^2_{\Delta V,dir}) \end{pmatrix} \tag{5.9}$$

where T is the thrust magnitude, ϵ is the elevation angle, and ψ is the azimuth angle. Uncertainties are considered both on the magnitude ($\sigma_{\Delta V,mag}$) and on the direction ($\sigma_{\Delta V,dir}$) of the thrust vector.

The response of the thrusters to guidance commands is typically modeled using first-order dynamics with a known time constant. However, these time constants are generally on the order of fractions of a second (Furfaro et al. (2013b), Sanchez et al. (2022)). Given that their characteristic time scale is much smaller than that of the problem at hand, these effects are neglected. Additionally, accounting for them would require reducing the integrator time step to unacceptable values considering that station-keeping is to be tested for time windows in the order of days/weeks.

5.6 Dynamical modeling

This section discusses the selection of numerical and modeling settings for the given astrodynamics simulation problem, focusing on the relation between models of the physical environment and the propagated dynamical behavior. Establishing a realistic environment model and selecting appropriate integration settings are essential for accurately evaluating the performance of any GNC system, especially given the diverse dynamical conditions under which the orbit control system is to be tested.

5.6.1 High-fidelity model

In the literature, there can be found a variety of different approaches when designing the high-fidelity scenario for asteroids' proximity operations. Some formulations, as discussed in Sec. 2.3, exclude solar perturbations (Lee and Singh, 2019a), while others simulate a realistic gravity field by superimposing white noise onto a simpler gravity model (Furfaro, 2015). Additionally, other studies employ Sh models and/or polyhedron representations (Winkler et al., 2012; Negri and de Almeida Prado, 2022). Despite

some authors may have opted for more direct approaches due to constraints in time or resources, this project benefited from the availability of both the SH model and the polyhedron, thanks to previous work. For this reason, a portion of the initial research was dedicated to comparing these models to ensure that an inattentive choice of the environment model would not influence the results.

Since Eros is a relatively massive asteroid, solar perturbations affect the dynamics in the proximity of the small body to a minimal extent. As a consequence, the simple formulations described in Sec. 3.4.2 are more than sufficient, and the entire discussion thus falls on the choice of the gravity model. As thoroughly discussed in Sec. 3.4.1, there are mainly two options when it comes to reproducing the gravitational field of an irregularly shaped asteroid to a high degree of accuracy: using a SH expansion or a constant-density polyhedron. Thanks to the data collected by NEAR, which are available on the Small Bodies Node (SBN) of the NASA Planetary Data System (PDS)[6], it is possible to employ and compare various gravity models. Specifically, there are three main possible approaches:

1. Employ a SH gravity model with the coefficients that have been determined through radiometric tracking. A full set up to D/O 15 is available.
2. Employ a SH gravity model with the coefficients that have been determined by integrating a shape model of the asteroid. A 16 D/O set is available for the shape model constructed using NLR measurements.
3. Use the polyhedron gravity model for a given shape directly. In addition to the one created from NLR data, several other models with varying resolutions were obtained from MSI data. For this work, four models were considered (comprising 1708, 7790, 10,152, and 22,540 facets), all derived from MSI measurements. Higher-resolution models, such as those with 89,389 and 200,700 facets, were not included due to their computational and management demands.

A comparison study was performed by computing the gravity acceleration norm over a reference sphere at various distances from the asteroid. For each model, the values were compared to those obtained by using the highest-resolution polyhedron and then displayed in Fig. 5.18. Additionally, the method described by Root et al. (2016) was applied to the shape model with 1708 facets to generate the corresponding SH expansion (referred to as SH D/O 15 MSI in Fig. 5.18). Now, given the differences between the radiometric solution and the polyhedron model, there is no unique solution for the mass distribution of Eros (Miller et al., 2002).

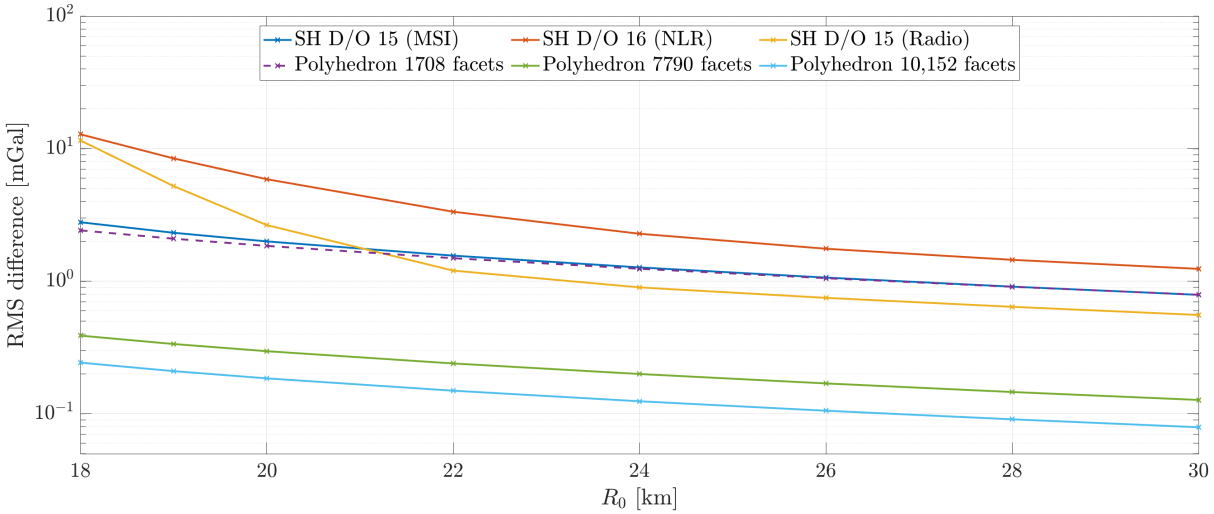

Figure 5.18: RMS gravity difference with respect to the high-resolution polyhedron (22,540 facets) for different gravity models.

[6] `https://sbn.psi.edu/pds/resource/nearbrowse.html`, accessed on 17/05/2024.

Indeed, both models include sources of errors:

- The SH expansion which uses the coefficients obtained from radiometric tracking is generally considered to represent reality to the highest accuracy since it has been derived from real navigation data. However, it is affected by a limited degree and order.
- The polyhedron and the SH expansion based on the coefficients from a shape model are both limited by the constant-density assumption and the resolution of the shape model.

In the figure, it can be recognized that the discrepancy between the polyhedra models and the SH expansion with the radio-science coefficients increases notably as the distance from Eros is reduced. This has to be attributed mainly to the fact that the closer to the asteroid, the stronger the effect of internal density variations on the gravity field. Such density variations are captured by the SH coefficients, but not by the polyhedra models, thus justifying the observable behavior. Instead, away from the small body, the offsets between the models can be imputed to the different values of the gravitational parameter. In fact, for a given density, a different gravitational parameter is associated with each shape model based on its volume.

Interestingly, the polyhedron model which agrees more with the radiometric solution is the lowest-resolution one. However, for this research, it is not of particular interest to model the environment in the proximity of the asteroid as accurately as possible, as long as comparable dynamics are obtained. Based on this consideration only, it is clear from Fig. 5.18 that any of the models considered would be adequate. However, a major consideration arises from the necessity to reproduce impact trajectories, which are to be investigated within open-loop analysis. Since impact trajectories can only be computed using the polyhedron due to the divergence of the SH model below the Brillouin sphere (R_e = 16 km), it was decided to model the real dynamics around Eros with a hybrid approach. The simulator uses the SH model with the coefficients computed from the integration of the shape model above 20 km and transitions to the polyhedron formulation below this threshold to handle the dynamics accurately near the asteroid. In this way, the selected approach balances accuracy with computational cost, ensuring that the dynamical model remains consistent during the transition, and avoiding the high computational cost associated with the polyhedron model when not strictly necessary.

5.6.2 Integrator analysis

For the current problem, the choice of an adequate integration scheme is driven mainly by two considerations:

1. The time step Δt is inherently constrained by the operating frequency of the onboard computer ($\Delta t \leq T_s^{-1}$). Since the designed software approximates a GNC system, a single frequency value governs all discrete components.
2. The weak gravitational field that characterizes the asteroid environment results in relatively low orbital velocities compared to planetary or interplanetary scenarios. Consequently, the dynamics, though locally variable due to the gravity field's irregularity, remain slow in absolute terms. This permits the use of a relatively large time step to accurately capture relevant phenomena.

Based on these considerations, an RK4 integrator with a fixed time step was selected. The numerical scheme was preferred over higher-order methods for its proven reliability and simplicity. Furthermore, the small time step dictated by the GNC system's operating frequency implies that such methods would increase computational cost through additional function evaluations while offering negligible accuracy improvements. Variable-step integrators were also discarded, given the absence of rapidly changing dynamics and the necessity to simulate the discrete operation of onboard components.

Finally, a brief analysis of the time step was performed. The candidate trajectory is an uncontrolled elliptical orbit with an apoapsis of 50 km that ultimately impacts the surface of the small body. By using a benchmark time step of 0.1 seconds, the position error for other values of Δt was computed and

reported in Fig. 5.19. The results indicate that for the three time steps considered, the position error remains well within acceptable values for most of the simulation time. However, a discontinuity near the end arises due to the transition from the SH gravity model to the polyhedron model. Although this behavior is inevitable, the position error still remains acceptable for both $\Delta t = 1$ s and $\Delta t = 10$ s (lower than 10 m), whereas it exceeds 100 m for $\Delta t = 60$ s. For uncontrolled motion, the latter time step would be more than sufficient, as the ultimate purpose of this analysis is to detect the presence of an impact, and not to compute with high accuracy its location. Nonetheless, this value was deemed too large to be used for the orbit control module. In conclusion, a time step of 10 seconds was chosen as the optimal compromise between the computational cost associated with running week-long simulations and the necessity of simulating the operating frequency of an onboard computer.

This choice establishes a minimum maneuver duration of 10 seconds, which is relatively long compared to the valve opening times of conventional monopropellant engines (in the order of ms). However, this should not be seen as a limitation, as these engines are capable of operating also for extended periods. For example, Rosetta conducted interplanetary correction maneuvers relying solely on its RCS, with the engines remaining active for durations of up to three hours[7].

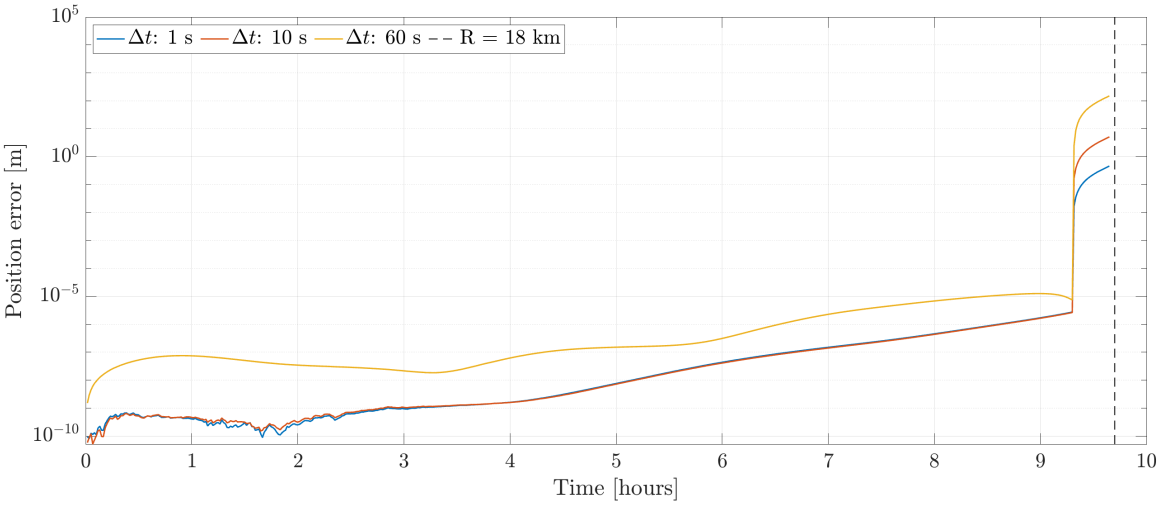

Figure 5.19: Position error for an impact trajectory using different time steps.

[7] `https://en.wikipedia.org/wiki/Timeline_of_Rosetta_(spacecraft)`, accessed on 28/11/2024.

6

Orbit control

This chapter illustrates the orbit control system. First, Sec. 6.1 clarifies how orbit control is collocated among the spacecraft subsystems. Subsequently, Sec. 6.2 presents the mathematical formulation of the controllers implemented for this work, while also describing how the reference trajectory is generated and which performance indicators are used to evaluate the system performance. Section 6.3 describes the three orbits used within this chapter to assess the designed system. A parametric analysis of the sliding mode controller is then presented in Sec. 6.4, whereas Sec. 6.5 illustrates the thrust quantization logic employed to achieve control through impulsive maneuvers. Finally, Sec. 6.6 presents the results of the Monte Carlo closed-loop simulations conducted for the previously introduced scenarios.

6.1 GNC fundamentals

In general, different conceptions are present regarding the terminology for the spacecraft subsystems in charge of orbit and attitude control. The Guidance, Navigation, and Control subsystem is generally responsible for various tasks, including attitude-orbit control and estimation. However, its function-

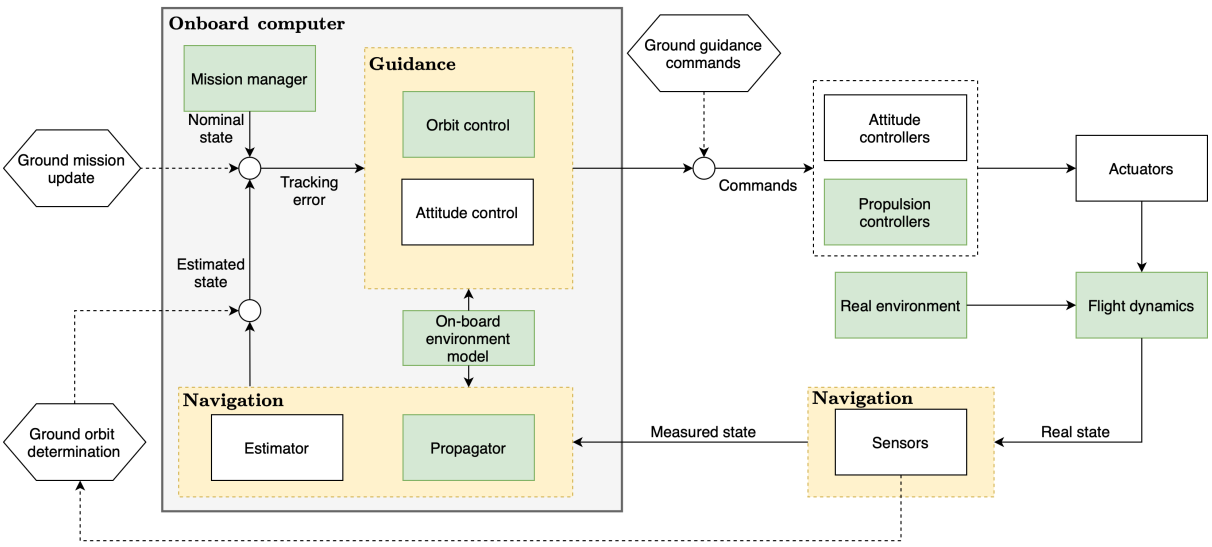

Figure 6.1: Schematic overview of an autonomous GNC system for orbit-attitude control, with modeled components colored in green. Dashed lines represent the ground components (absent in an autonomous system).

alities often overlap with those of the Attitude and Orbit Control System (AOCS)[1], which, however, is commonly used when the orbit guidance is not executed onboard, but via the ground segment. In some cases, either GNC or AOCS can also refer to the whole function, distributed between onboard and ground systems, with some authors considering GNC a part itself of AOCS (Pugliatti et al., 2023). To this regard, Fig. 6.1 illustrates the three most relevant interfaces between a GNC system and the ground segment: mission updates, which adjust the reference trajectory; guidance commands, which override onboard computations; and orbit determination, which refines the onboard navigation solution. Within this thesis, GNC will be deemed as the sole subsystem responsible for onboard orbit control. Since full autonomy of the spacecraft is assumed, the AOCS is not present.

Additionally, it has to be clarified what Guidance, Control, and Navigation refer to, since also these terms have been interpreted in slightly different ways depending on the context of application. Specifically, with guidance we intend the system in charge of generating the steering commands (an attitude and/or a thrust) for the vehicle in relation to a reference state and trajectory constraints. Therefore, despite the name may be misleading, orbit control falls within the guidance module, as clarified by Fig. 6.1. Instead, the control system is responsible for converting the actions commanded by the guidance into actions that can be executed directly by the actuators. Finally, the navigation module uses onboard models and data from the sensors to provide the guidance system with an estimate of the vehicle state and other physical parameters. It should be noted that in Fig. 6.1, the *propagator* unit has been explicitly separated from the *estimator*, despite the former is often considered as a sub-unit of the latter.

6.2 Control architecture

6.2.1 Sliding mode controller

Following the theory presented in Chapter 4, the equations for the translational motion (in the ACI frame) from Sec. 3.5 can be rewritten as follows:

$$\frac{d\boldsymbol{v}}{dt} = \underbrace{-\frac{\mu}{\boldsymbol{r}^3}\boldsymbol{r}}_{\hat{\boldsymbol{f}}} + \underbrace{\boldsymbol{C}_{I/A}\boldsymbol{a}_{g,ns}}_{\Delta\boldsymbol{f}} + \underbrace{\hat{\beta}\frac{\boldsymbol{r}-\boldsymbol{r}_\odot}{||\boldsymbol{r}-\boldsymbol{r}_\odot||^3}}_{\hat{\boldsymbol{f}}} + \underbrace{(\beta-\hat{\beta})\frac{\boldsymbol{r}-\boldsymbol{r}_\odot}{||\boldsymbol{r}-\boldsymbol{r}_\odot||^3}}_{\Delta\boldsymbol{f}} + \underbrace{\boldsymbol{a}_{3BP}}_{\hat{\boldsymbol{f}}} + \underbrace{\boldsymbol{a}_T}_{\boldsymbol{u}} \tag{6.1}$$

where the known and unknown terms of the dynamics have been highlighted. Specifically, the lack of knowledge about the SH coefficients results in unknown gravitational forces, while inaccuracies in the spacecraft SRP coefficient imply that this force is also not exactly known. In contrast, the three-body solar perturbation can be assumed to be accurately determined. However, all these forces notably depend on the precise knowledge of the spacecraft's position, which is known to be affected by navigation errors. Additionally, the commanded thrust acceleration tends to differ from the executed one due to errors within the RCS. Consequently, these factors introduce additional perturbing dynamics not accounted for in Eq. (6.1). For the design of the controller, these can be all lumped in a disturbance vector $\boldsymbol{d}$.

Although part of the SRP could be considered to be known and thus included within the equivalent control term, it has been omitted due to its relative magnitude with respect to the gravitational perturbations. As a consequence, the known and unknown dynamics terms considered for the controller design are:

$$\hat{\boldsymbol{f}} = -\frac{\mu}{\boldsymbol{r}^3}\boldsymbol{r} \tag{6.2}$$

$$\Delta\boldsymbol{f} = \boldsymbol{C}_{I/A}\boldsymbol{a}_{g,ns} + \boldsymbol{a}_{SRP} + \boldsymbol{a}_{3BP} \tag{6.3}$$

In this way, the control law computed by the sliding mode controller relies exclusively on the point mass gravity acceleration of the asteroid, in compliance with **OC-REQ-09**. At this point, it is possible

[1]AOCS has also to be distinguished from the Attitude Determination Control System (ADCS), which alludes to those satellites that do not have any orbit control capabilities (without thrusters), and thus can only control their attitude.

to define the sliding surface. Clearly, the system is of order two, therefore the sliding variable can be defined as the linear combination of the position and velocity errors:

$$\boldsymbol{s} = (\boldsymbol{v} - \boldsymbol{v}_d) + \boldsymbol{\Lambda}(\boldsymbol{r} - \boldsymbol{r}_d) \tag{6.4}$$

Applying Eq. (4.12) component-wise to the given problem results in:

$$\boldsymbol{u} = \frac{\mu}{||\boldsymbol{r}||^3}\boldsymbol{r} - \frac{\mu}{||\boldsymbol{r}_d||^3}\boldsymbol{r}_d - \boldsymbol{\Lambda}(\boldsymbol{v} - \boldsymbol{v}_d) - \boldsymbol{K}\,\mathrm{sgn}\,\boldsymbol{s} \tag{6.5}$$

where $\boldsymbol{\Lambda}$ and $\boldsymbol{K}$ are diagonal gain matrices corresponding respectively to the scalar gains λ and k in the equations presented in Sec. 4.2. Hereafter, proof is given about the stability of the designed control law. In particular, the sliding condition in Eq. (4.6) takes the following explicit form:

$$\begin{aligned}
&\frac{1}{2}\frac{d}{dt}s_i^2 = \dot{s}_i s_i = \\
&[(a_i - a_{i,d}) + \Lambda_{ii}(v_i - v_{i,d})]s = \\
&[f_i + d_i + u_i - a_{i,d} + \Lambda_{ii}(v_i - v_{i,d})]s = \\
&[f_i + d_i - \hat{f}_i + \cancel{a_{i,d}} - \cancel{\Lambda_{ii}(v_i - v_{i,d})} - K_{ii}\,\mathrm{sgn}\,(s_i) - \cancel{a_{i,d}} + \cancel{\Lambda_{ii}(v_i - v_{i,d})}]s = \\
&(f_i + d_i - \hat{f}_i)s - K_{ii}|s| < -\eta|s|
\end{aligned} \tag{6.6}$$

As already anticipated, the design choice of the gain matrix $\boldsymbol{K}$ determines the effectivity of the control law. For the problem at stake, global stability is guaranteed provided that:

$$K_{ii} > (f_i - \hat{f}_i) + d_i + \eta \tag{6.7}$$

which requires an assumption on the upper bounds for $f_i - \hat{f}_i$ and d_i. Since this control will be highly discontinuous, a boundary layer vector $\boldsymbol{\Phi}$ can be introduced such that:

$$\boldsymbol{u} = \frac{\mu}{||\boldsymbol{r}||^3}\boldsymbol{r} - \frac{\mu}{||\boldsymbol{r}_d||^3}\boldsymbol{r}_d - \boldsymbol{\Lambda}(\boldsymbol{v} - \boldsymbol{v}_d) - \boldsymbol{K}\,\mathrm{sat}\,(\boldsymbol{s}, \boldsymbol{\Phi}) \tag{6.8}$$

where the saturation operator is applied component-wise to $\boldsymbol{s}$ and $\boldsymbol{\Phi}$. According to the theory presented in Sec. 4.2.3, it is possible to exploit the mathematical form of the gravitational perturbations to design a boundary layer that varies in time according to the available control bandwidth. Because the perturbations from the gravity field overshadow the solar radiation pressure and the third-body gravity, the sliding mode controller can be modified as follows:

$$\begin{cases}
\boldsymbol{u} = \frac{\mu}{||\boldsymbol{r}||^3}\boldsymbol{r} - \frac{\mu}{||\boldsymbol{r}_d||^3}\boldsymbol{r}_d - \boldsymbol{\Lambda}(\boldsymbol{v} - \boldsymbol{v}_d) - (\boldsymbol{K}(\boldsymbol{r}) - \dot{\boldsymbol{\Phi}})\,\mathrm{sat}\,(\boldsymbol{s}, \boldsymbol{\Phi}) \\
\dot{\boldsymbol{\Phi}} = \boldsymbol{K}(\boldsymbol{r}_d) - \boldsymbol{\Lambda}\boldsymbol{\Phi} \\
\boldsymbol{\Phi}_0 = \boldsymbol{\Lambda}^{-1}(\boldsymbol{\eta}_0 + \boldsymbol{\eta})
\end{cases} \tag{6.9}$$

where the diagonal gain matrix $\boldsymbol{K}$ is adaptively changed based on the state of the system according to:

$$\boldsymbol{K}(\boldsymbol{r}) = |\boldsymbol{a}_{g,pm}(\boldsymbol{r}) - \boldsymbol{C}_{I/A}\hat{\boldsymbol{a}}_{g,ns}(\boldsymbol{r})| + \boldsymbol{\eta} \tag{6.10}$$

In the equation above, $\hat{\boldsymbol{a}}_{g,ns}$ highlights that the non-spherical components of the gravitational acceleration are estimated and not exactly known. One should also notice that this controller formulation may be affected by uncertainties in the attitude kinematics of the asteroid due to matrix $\boldsymbol{C}_{I/A}$. However, the boundary conditions listed in Sec. 2.4.3 specify that such uncertainties have not been considered for this work. Additionally, it is noted that from now on the vector symbol for the boundary layer will be dropped, and replaced by Φ, which indicates its width in all three Cartesian directions.

6.2.2 Target points controller

The first step to designing a controller based on the TPA is to compute the Jacobian of the reference dynamics, as it is needed to propagate the variational equations. Although this can be quite cumbersome for highly complex dynamical systems, it is not the case for the current study, where the reference trajectory is a Keplerian orbit. Therefore, the only dynamics term to consider is that due to the point mass gravity acceleration, which makes it possible to calculate the Jacobian analytically without the need for numerical differentiation programs. In particular, one obtains:

$$\frac{\partial \dot{\boldsymbol{x}}}{\partial \boldsymbol{x}} = \begin{bmatrix} \frac{\partial \boldsymbol{v}}{\partial \boldsymbol{r}} & \frac{\partial \boldsymbol{v}}{\partial \boldsymbol{v}} \\ \frac{\partial \boldsymbol{a}}{\partial \boldsymbol{r}} & \frac{\partial \boldsymbol{a}}{\partial \boldsymbol{v}} \end{bmatrix} = \begin{bmatrix} \boldsymbol{0}_{3\times3} & \boldsymbol{I}_{3\times3} \\ \frac{\partial \boldsymbol{a}}{\partial \boldsymbol{r}} & \boldsymbol{0}_{3\times3} \end{bmatrix} \tag{6.11}$$

$$\frac{\partial \boldsymbol{a}}{\partial \boldsymbol{r}} = -\mu \left(\frac{\boldsymbol{I}_{3\times3}}{r^3} - \frac{3\boldsymbol{r}\cdot\boldsymbol{r}^T}{r^5} \right) \tag{6.12}$$

The TPA is characterized by a relatively large set of design parameters. To reduce the time required to tune the controller, some of these have been fixed a-priori based on results from previous studies (Keeter, 1994; Gomez et al., 1998). Specifically, the controller implemented within this work includes three target points and does not consider velocity deviations when computing the correction maneuvers. To make the notation more compact, we refer to the submatrices of the STM as:

$$\boldsymbol{\Psi}(t_1,t_0) = \begin{bmatrix} \boldsymbol{\Psi}_{rr}(t_1,t_0) & \boldsymbol{\Psi}_{rv}(t_1,t_0) \\ \boldsymbol{\Psi}_{vr}(t_1,t_0) & \boldsymbol{\Psi}_{vv}(t_1,t_0) \end{bmatrix} = \begin{bmatrix} \boldsymbol{A}_{t_1t_0} & \boldsymbol{B}_{t_1t_0} \\ \boldsymbol{C}_{t_1t_0} & \boldsymbol{D}_{t_1t_0} \end{bmatrix} \tag{6.13}$$

With this notation, Eq. (4.32) can now be made explicit as:

$$\begin{aligned} \boldsymbol{\Delta v}^* = &- \left[\boldsymbol{Q} + \boldsymbol{B}_{t_1t_c}^T \boldsymbol{R}_1 \boldsymbol{B}_{t_1t_c} + \boldsymbol{B}_{t_2t_c}^T \boldsymbol{R}_2 \boldsymbol{B}_{t_2t_c} + \boldsymbol{B}_{t_3t_c}^T \boldsymbol{R}_3 \boldsymbol{B}_{t_3t_c}\right]^{-1} \cdot \\ &\cdot \left[(\boldsymbol{B}_{t_1t_c}^T \boldsymbol{R}_1 \boldsymbol{B}_{t_1t_0} + \boldsymbol{B}_{t_2t_c}^T \boldsymbol{R}_2 \boldsymbol{B}_{t_2t_0} + \boldsymbol{B}_{t_3t_c}^T \boldsymbol{R}_3 \boldsymbol{B}_{t_3t_0})\boldsymbol{\delta v}_0 + \right. \\ &\left. + (\boldsymbol{B}_{t_1t_c}^T \boldsymbol{R}_1 \boldsymbol{A}_{t_1t_0} + \boldsymbol{B}_{t_2t_c}^T \boldsymbol{R}_2 \boldsymbol{A}_{t_2t_0} + \boldsymbol{B}_{t_3t_c}^T \boldsymbol{R}_3 \boldsymbol{A}_{t_3t_0})\boldsymbol{\delta r}_0\right] \end{aligned} \tag{6.14}$$

where it has been specified that the maneuvers may not be necessarily performed at time t_0, but at a potential optimal time $t_0 \leq t_c < t_1$. However, since this controller does not represent the primary focus of this study, $t_c = t_0$ has been assumed. Moreover, asteroid applications, with their short-term dynamics, require much shorter intervals between maneuvers compared to those that characterize libration point orbits, reducing the practicality of finding an optimal t_c.

6.2.3 Reference trajectory

Employing an adequate reference, be this a constant state or a time-varying profile, is essential to guarantee a good performance of the controller. In the orbit control literature, some authors generate the reference numerically by including the most relevant perturbations in the equations of motion. For example, Garulli et al. (2011) consider gravitational perturbations in the reference dynamics by incorporating the Earth gravity model EGM96 up to degree and order 9. In this way, the controller does not compensate for the oscillatory perturbations arising from the gravity field, but only the secular effects generated by the drag, thereby reducing the overall station-keeping cost. For asteroid applications, Sanchez et al. (2022) proposed an approach referred to as *nullifying out-of-plane control*. With this method, the guidance generates the reference by integrating the onboard dynamical model with a predefined control policy that cancels the cross-track gravitational perturbations. As a result, the reference is not a Keplerian orbit but a trajectory that evolves as if uncontrolled, with its osculating semi-major axis and eccentricity remaining fixed. As these elements are mainly (in some cases, entirely) governed by the cross-track component of the forces acting on the vehicle, the result is that the controller never commands cross-track thrusting, thus reducing the control effort.

This approach is effective because the authors circumscribe their interest to tracking only the orbit's semi-major axis and eccentricity, which can be decoupled from the other orbital elements if the equations of motions are written in terms of MEEs. For this study, this is not sufficient because the orientation of the orbits in space needs to be controlled as well (**MIS-REQ-04**). Unfortunately, when introducing additional elements to track, the aforementioned method loses attractiveness. For example, one could think of generating the reference trajectory by propagating in time only the true longitude, while maintaining all the other MEEs constant. However, this would not lead to a comparable result, as this method is founded on the assumption that the in-plane motion is decoupled from cross-track perturbations when using Gauss variational equations. If the inclination and the RAAN have to be maintained, cross-track control becomes inevitable. Furthermore, the effectiveness of this approach heavily depends on the accuracy of the onboard navigation solution, which must be used to estimate the cross-track component of the gravitational perturbations. It is also impractical to attempt a similar strategy using Cartesian coordinates, as this coordinate set does not support explicit tracking of a subset of orbital elements (e.g., only the semi-major axis, eccentricity, and inclination). Each Kepler element contributes to every component of the osculating position and velocity vectors, making it impossible to isolate specific orbital elements for targeted control.

Since conventional sliding mode controllers need a time-varying profile for the target state, as well as a reference acceleration, the most simple approach to generate the desired orbital trajectory relies on the conversion of the target orbital elements into inertial Cartesian coordinates according to the procedure outlined in Algorithm 1. Specifically, Kepler's equation (3.47) allows to propagate in time the true anomaly according to the two-body motion, thereby generating a time-varying profile for the desired position $\boldsymbol{r}_d(t)$, velocity $\boldsymbol{v}_d(t)$ and acceleration $\boldsymbol{a}_d(t)$. Using this approach, the control problem can be framed as a two-satellite formation-flying scenario, where the spacecraft *chases* a virtual point moving along a Keplerian orbit. This tracking mode, which is widely adopted in orbit control for Earth applications, will henceforth be referred to as the *chaser-target* mode.

Algorithm 1 Chaser-target tracking mode.

1: Retrieve current time t
2: Retrieve rotation matrix from PWQ to ACI frame for target orbit: $\boldsymbol{C}_{I/P}(i_d, \Omega_d, \omega_d)$
3: Compute target mean anomaly: $M = \sqrt{\frac{\mu}{a_d^3}} t$
4: Solve Kepler's equation for E: $M = E - e_d \sin E$
5: Compute target true anomaly: $\theta_d = 2 \arctan\left(\sqrt{\frac{1+e_d}{1-e_d}} \tan\frac{E}{2}\right)$
6: Apply Eq. (3.13): $(a_d, e_d, i_d, \Omega_d, \omega_d, \theta_d) \rightarrow (\boldsymbol{r}_d^P, \boldsymbol{v}_d^P)$
7: Rotate position and velocity vectors back to the inertial frame: $\boldsymbol{r}_d^I = \boldsymbol{C}_{I/P}\boldsymbol{r}_d^P$, $\boldsymbol{v}_d^I = \boldsymbol{C}_{I/P}\boldsymbol{v}_d^P$
8: Compute reference acceleration: $\boldsymbol{a}_d = -\frac{\mu}{||\boldsymbol{r}_d||^3}\boldsymbol{r}_d$

Formulating the controller in this way can be inefficient, as it requires unnecessary control effort to follow a virtual satellite unaffected by gravitational perturbations. Since tracking of the true anomaly is not a requirement for this study, a novel approach is proposed under the term *line-of-sight* (LOS) guidance. With this method, the target state is adaptively adjusted based on the spacecraft's current state estimate. At each control time step, the mission manager unit computes the reference state and acceleration corresponding to the point on the target orbit that is closest to the estimated spacecraft position at that moment. For circular orbits, this can be found by solving an easy geometric problem:

$$\boldsymbol{r}^P = \boldsymbol{C}_{P/I}\boldsymbol{r}^I \tag{6.15}$$

$$\boldsymbol{r}_d^I = \boldsymbol{C}_{I/P} R_d \hat{\boldsymbol{r}}^P \tag{6.16}$$

$$\boldsymbol{v}_d^I = \boldsymbol{C}_{I/P}\left(\sqrt{\frac{\mu}{R_d}}\frac{\hat{\boldsymbol{q}} \times \hat{\boldsymbol{r}}^P}{||\hat{\boldsymbol{q}} \times \hat{\boldsymbol{r}}^P||}\right) \tag{6.17}$$

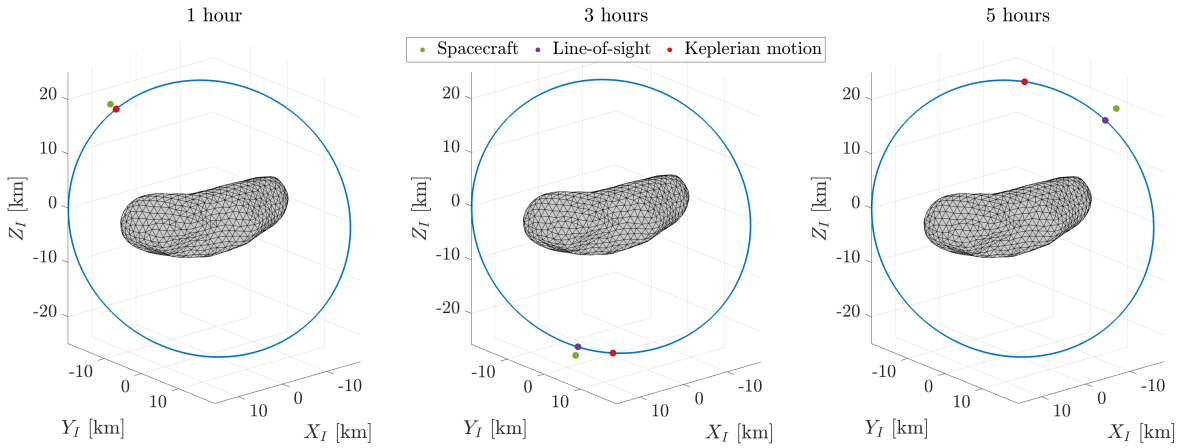

Figure 6.2: Comparison of the references provided by the chaser-target and line-of-sight tracking mode at different times for a 25 km polar orbit.

where R_d is the desired radius of the target orbit. For elliptical orbits, the process is more complex, as the minimum distance between a point and an ellipse cannot be found analytically. However, simple numerical methods can be employed such that the target position vector is first determined, and then the corresponding reference velocity is assigned using Eq. (3.13) and the osculating orbital elements. The steps required by the line-of-sight approach are summarized in Algorithm 2.

Algorithm 2 Line-of-sight tracking mode.

1: Retrieve current position vector $\boldsymbol{r}$
2: Retrieve rotation matrix from PWQ to ACI frame: $\boldsymbol{C}_{I/P}(i_d, \Omega_d, \omega_d)$
3: Project the current position vector on the plane of the target orbit: $\boldsymbol{r}^P = \boldsymbol{C}_{P/I}\boldsymbol{r}^I$
4: Find closest point on target orbit to obtain $\boldsymbol{r}_d^P$
5: Assign velocity to the closest point $\boldsymbol{v}_d^P$
6: Rotate position and velocity vectors back to the inertial frame: $\boldsymbol{r}_d^I = \boldsymbol{C}_{I/P}\boldsymbol{r}_d^P$, $\boldsymbol{v}_d^I = \boldsymbol{C}_{I/P}\boldsymbol{v}_d^P$
7: Compute reference acceleration: $\boldsymbol{a}_d = -\frac{\mu}{||\boldsymbol{r}_d||^3}\boldsymbol{r}_d$

An example of the line-of-sight tracking mode is shown in Fig. 6.2, which illustrates the locations of the target points commanded by both the chaser-target and line-of-sight methods at three different times during the uncontrolled propagation of a low-altitude polar orbit. Over time, the distance along the orbit between the virtual point (moving according to Keplerian dynamics) and the real point (following the perturbed motion) increases significantly, underscoring the additional control effort required to chase the moving target.

6.2.4 Performance indicators

The physical quantities which will be used to assess the performance of the orbit control system are now defined. The efficiency of the algorithm is evaluated in terms of ΔV, which is computed as:

$$\Delta V = \int_{t_0}^{t_f} ||\boldsymbol{u}(t)||dt \tag{6.18}$$

Consequently, the accuracy of the overall GNC system is evaluated by inspecting the evolution of the orbit radius (which is equivalent to the distance from the asteroid) and the solar phase angle. In fact, since tracking the true anomaly is not of interest, observing these two quantities allows to efficiently capture the tracking performance with a lower number of indicators. The solar phase angle results unambiguously from the combination of the inclination, RAAN, and time since Eros periapsis passage. Once this latter

is defined, maintaining a given value of the solar phase angle also implies that the orientation of the orbit with respect to the asteroid remains fixed. Similarly, the distance from the asteroid ensures that the semi-major axis and eccentricity remain within the desired values. Thus, both the root mean square and the maximum errors for these metrics are considered:

$$\Delta R = \sqrt{\frac{1}{t_f - t_0}\int_{t_0}^{t_f} (||\boldsymbol{r}(t)|| - R(t))^2 dt} \quad \Delta R_{max} = \max_{t\in[t_0,t_f]} |||\boldsymbol{r}(t)|| - R(t)| \tag{6.19}$$

$$\Delta \beta = \sqrt{\frac{1}{t_f - t_0}\int_{t_0}^{t_f} (\beta(t) - \beta_0(t))^2 dt} \quad \Delta \beta_{max} = \max_{t\in[t_0,t_f]} |\beta(t) - \beta_0(t)| \tag{6.20}$$

where $R(t)$ and $\beta_0(t)$ are the commanded orbital radius and solar phase angle at a given time instant t. It should be noted that during Monte Carlo simulations, injection errors may generate an initial position deviation such that ΔR_{max} is larger than the required tracking accuracy. In these situations, ΔR_{max} is computed only after the controlled trajectory is brought back within the desired control space.

Finally, attention is also given to the available observation time T_{obs}, defined as the total time during which the spacecraft does not perform orbit correction maneuvers. A 30-minute window between thrust firings is considered the minimum interval for counting time as actually available. This metric aims to qualitatively assess the amount of time that could be dedicated to scientific activities, such as gravity estimation, without interference from thruster operations.

6.3 Test scenarios

Three significant scenarios have been identified to analyze the performance of the orbit control system:

- **Orbit A**: a 25 km polar orbit which, given its inclination and low altitude, guarantees an optimal platform for surface mapping, identification of landmarks, and gravity estimation. However, the proximity to the asteroid makes it highly unstable and leads it to escape the system within one week.
- **Orbit B**: an elliptical orbit (20x50 km) nearly lying on Eros equator and suited to achieve frequent low-altitude flyovers of Eros's western lobe (similarly to what NEAR achieved at the very end of its mission, see Table 2.3). Due to the strong gravitational perturbation caused by the asteroid's lobe, the orbit deviates and leads to an impact on the surface in less than one revolution.
- **Orbit C**: a 35 km orbit with a relatively high inclination, such that the ground coverage is good, while avoiding the instabilities which affect orbits at lower altitudes. In this case, however, the problem is dictated by the fact that the gravitational perturbations (especially C_{20}) lead to a very fast precession of the nodes, which in turn implies that the orbit rotates by more than 40 degrees around the Sun-asteroid line in less than one week, thus entering shadow and lying almost perpendicular to the terminator plane.

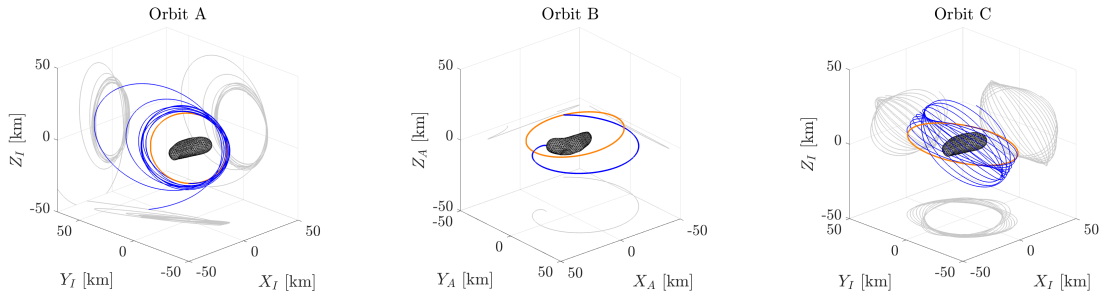

Figure 6.3: The three orbits considered for this study, in their ideal (orange) and real, uncontrolled (blue) behavior. Orbits A and C are represented in the ACI frame, whereas orbit B is in the ACAF frame.

Table 6.1: Main parameters for the three orbits at study.

Scenario	a [km]	e [-]	i [deg]	Ω [deg]	ω [deg]	T [hours]	β [deg]	$t_p[T_{Eros}]$
A	25	0	87.1	127.8	-	10.3	88-92	0.4
B	35	0.43	7.2	38.6	359.6	13.6	86-94	0.13
C	35	0	43	120	-	13.6	87-93	0.24

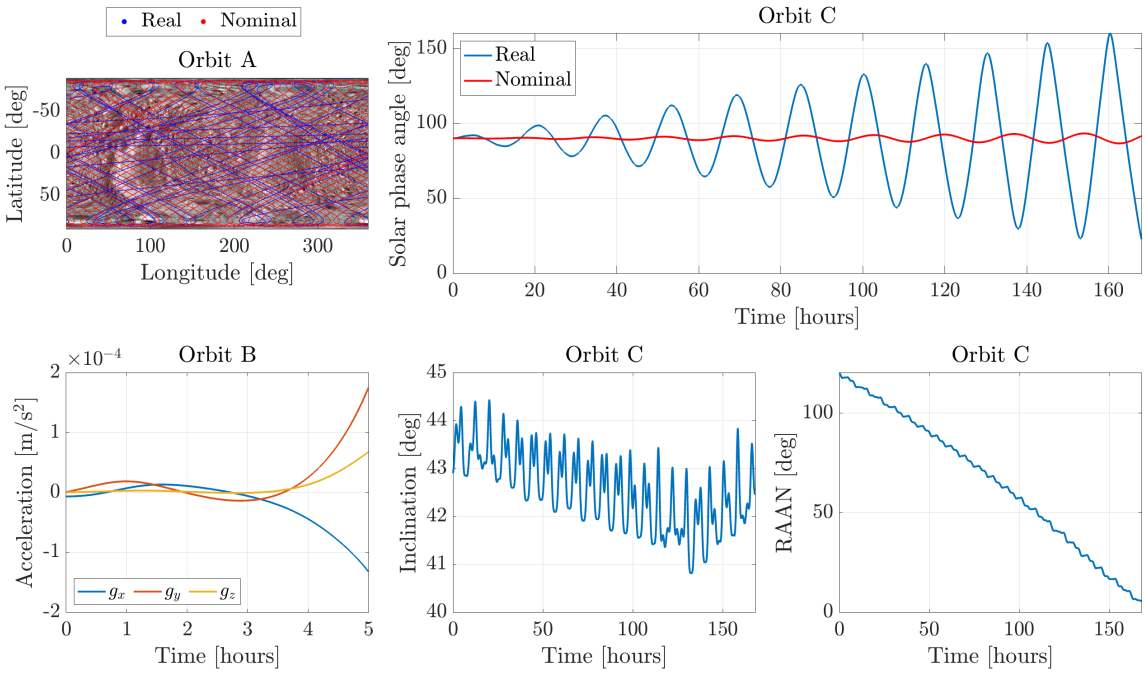

Figure 6.4: Parameters of interest for the three orbits at study.

All three orbits lie on the terminator plane, hence they are simulated at different locations along Eros's heliocentric orbit: Table 6.1 reports the corresponding time since the periapsis passage of the asteroid, together with the orbital parameters, periods, and nominal solar phase angle range. It is also important to mention that the uncontrolled behavior of the orbits shown in Fig. 6.3 has been obtained without considering any uncertainty on the initial state, which has been set to the local circular/elliptical conditions. This highlights even more that these orbits need to be actively controlled.

Figure 6.4 highlights key parameters for the three selected orbits. Notably, it includes the ground track of the polar orbit, illustrating its suitability for gravity field mapping; the magnitude of the disturbances from the gravitational field relative to the point mass term during orbit B; and, for orbit C, the evolution of the solar phase angle, which is caused by the secular drift of the RAAN combined with inclination oscillations.

Finally, since all the orbits considered are on the Sun-terminator plane, the procedure used to generate their initial condition is briefly reported. For a circular orbit of radius R_d, the position and velocity vectors are set in the orbit-fixed frame such that the spacecraft position lies along the Y_O-axis and the velocity lies along the Z_O-axis:

$$\boldsymbol{r} = \begin{pmatrix} 0 \\ R_d \\ 0 \end{pmatrix} \qquad \boldsymbol{v} = \begin{pmatrix} 0 \\ 0 \\ -\sqrt{\frac{\mu}{R_d}} \end{pmatrix} \tag{6.21}$$

Then, the rotation matrix $\boldsymbol{C}_{J2000/O}$ is used to rotate these vectors from the orbit-fixed frame to the J2000 frame, and a second rotation which leverages matrix $\boldsymbol{C}_{I/J2000}$ transforms them to the asteroid inertial frame, where the equations of motion can be integrated.

6.4 Continuous tracking

This section analyzes the performance of the sliding mode controller applied to the orbit control problem in continuous form. The guidance law generated by the controller is applied unfiltered and continuously to the dynamics, without accounting for navigation errors, the vehicle's actual propulsion capabilities, and orbit control requirements. Consequently, the following considerations extend beyond practical station-keeping scenarios, yet they offer valuable insights into the design process. Additionally, the results serve as a baseline for later assessing the impact of real-world constraints on the orbit control problem. The scenario that has been used to perform this study is orbit A, and the control frequency has been set to 0.1 Hz. During these simulations, navigation and execution errors have not been considered, therefore the controller has to counteract only the gravitational and solar disturbances, and the offset in the initial state.

6.4.1 Parametric analysis

A sensitivity study has been carried out to assess the effect of the controller's parameters on the tracking performance. The diagonal elements of matrices $\mathbf{\Lambda}$ and $\boldsymbol{K}$ (respectively referred to as Λ and K) have been assumed to be identical within each matrix, and the boundary layer width Φ has been considered uniform across all directions. In this way, the set of tunable parameters is relatively limited, thus allowing for a thorough investigation of the possible combinations.

The results of the parametric study are reported in Figs. 6.5 and 6.6, which showcase the impact of the control gains on the tracking accuracy in terms of two relevant parameters: the distance from the asteroid and the solar phase angle. It is noted that while the target distance is a constant value, the nominal profile of the solar phase angle gradually oscillates as Eros moves around the Sun. In agreement with the theory presented in Chapter 4, there are four main considerations which arise from this figure:

1. When the gain K is chosen to be smaller than the upper bound of the disturbances (10^{-4}, according to Fig. 6.4), the system never converges to the desired configuration, but maintains an oscillatory behavior, regardless of the value of Λ.

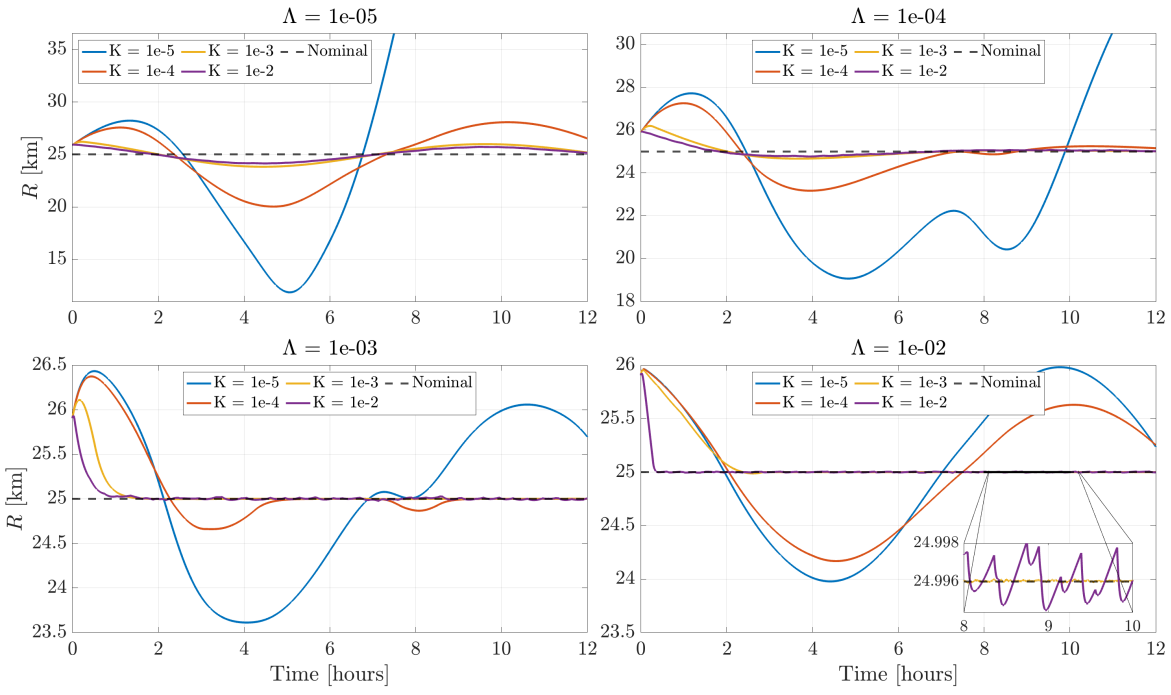

Figure 6.5: Distance from Eros for different combinations of the control gains.

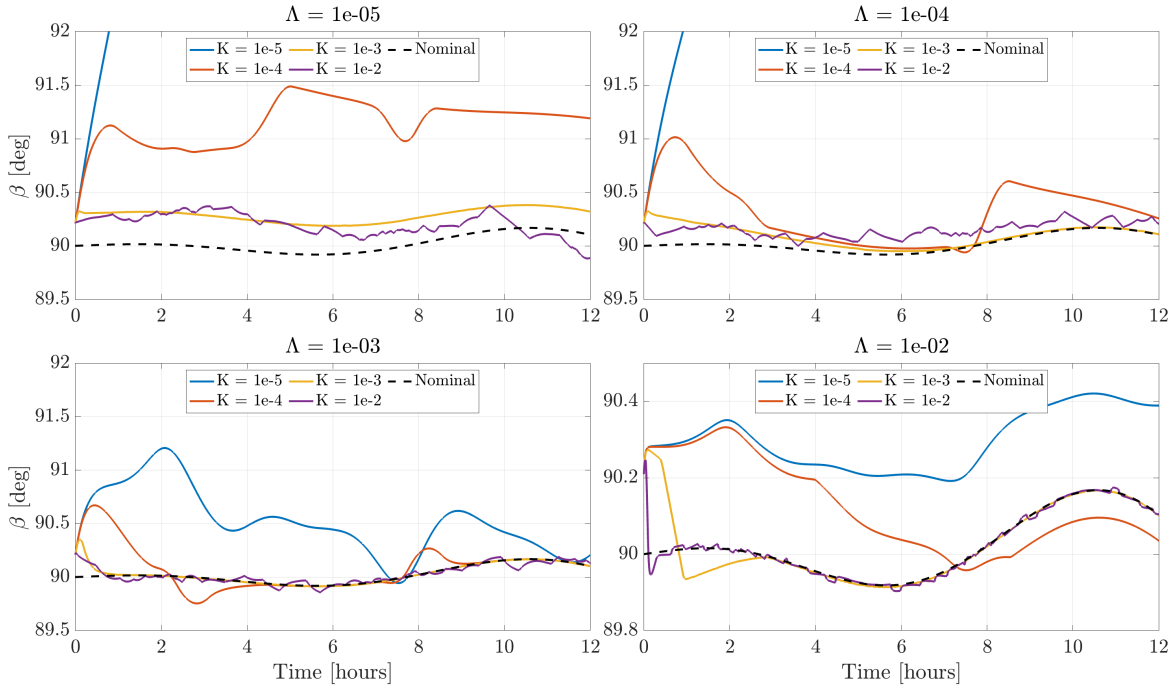

Figure 6.6: Solar phase angle for different combinations of the control gains.

2. Larger values of K increase the rate at which the system trajectory approaches the sliding surface, thereby decreasing the response time of the system. Indeed, Eq. (6.7) states that if K is chosen to precisely match the upper bound on the disturbances, then η is a remaining degree of freedom which determines the duration of the reaching phase (i.e., the time taken by the system to reach the sliding mode). For example, taking the scenario for $\Lambda = 0.01$, it can be observed that the response for $K = 0.01$ reaches the nominal trajectory earlier than for $K = 0.001$.

3. The coefficient of the sliding surface Λ also affects the rate of convergence. It is important to notice that if this parameter is chosen to be too low, then the differences in the responses obtained for different values of K (provided they are larger than the disturbances' upper bounds) are significantly less pronounced. In other words, even if K is chosen to be larger than the known disturbances, the system struggles to converge to the desired configuration.

4. Once the system reaches the sliding surface, chattering occurs. This is particularly evident for the curves associated with the higher gain values, which exhibit an irregular behavior. More specifically, the box highlighted in Fig. 6.5 shows how the magnitude of chattering increases with K. It should be stressed that chattering manifests because the control action happens in finite time; in an ideal scenario where the switching happened instantaneously, then the system would slide along the surface with no error.

The results shown until now were obtained by maintaining the signum operator in the controller formulation, thus leading to a highly chattering control law. Introducing now a boundary layer, the same type of parametric study can be conducted. Figure 6.7 clearly shows that increasing Φ implies loosening the requirement on the tracking accuracy. In parallel, the plot on the right showcases that the improvement in the control law smoothness is significant. A particularly interesting observation arises by comparing the results obtained for $\Phi = 0.1$ and $\Phi = 0.01$. In fact, this latter value describes a boundary layer that is too narrow for the time step used, thereby the corresponding control law preserves its chattering behavior as if the signum operator had been left. However, the tracking accuracy is still worse than that achieved by the control law with a larger boundary layer, and smoother control history. This reinforces the conclusion that larger values of K enhance robustness against disturbances, but they also increase chattering about the sliding surface, thereby leading to a higher tracking error.

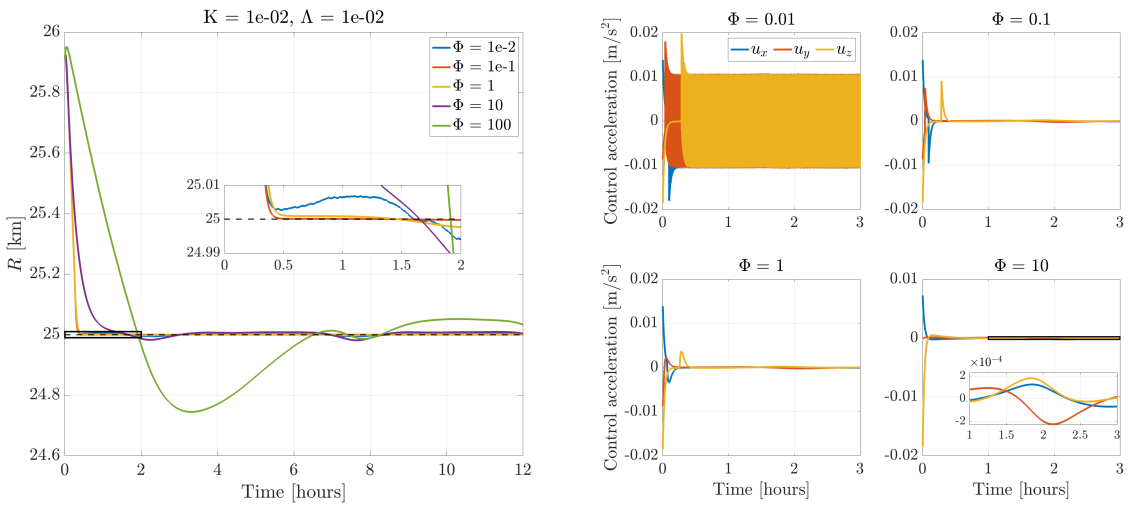

Figure 6.7: Distance from Eros for various boundary layer widths (left) and corresponding control laws (right).

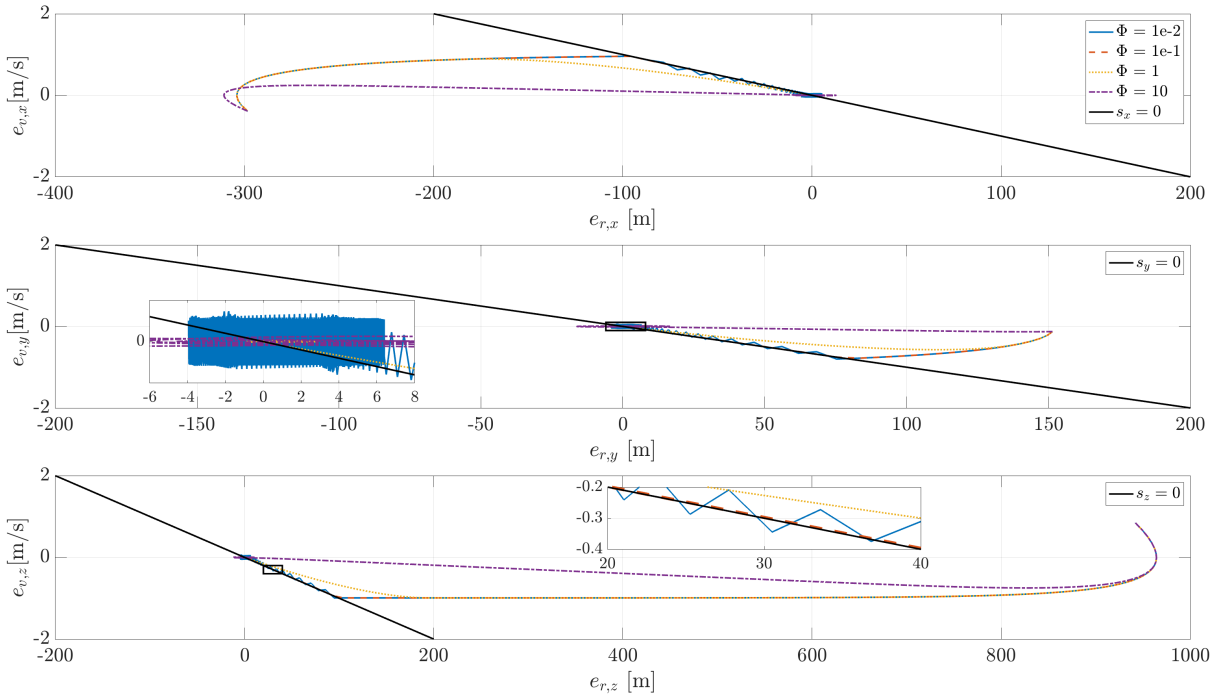

Figure 6.8: Controlled trajectories in the phase plane for various boundary layer widths.

To further visualize and inspect the behavior of the sliding mode controller when introducing a boundary layer, it is interesting to observe the evolution of the system in the phase plane, as displayed by Fig. 6.8. The system trajectories change quite drastically depending on the size of Φ, although they all converge towards the origin of the plane, proving to be stable (in correspondence of the origin, limit cycles can be observed). A reaching phase can be identified for both $\Phi = 0.01$ and $\Phi = 0.1$, with the system first targeting the surface, and then sliding towards the origin. However, the behavior in sliding mode differs greatly: for $\Phi = 0.01$, the trajectories switch from one side to the other of the surface, thus leading to high-frequency control activity; on the contrary, for $\Phi = 0.1$ the trajectory steadily reaches the origin of the plane by remaining very close to the surface. Instead, the curves corresponding to the other two values of Φ do not appear to have a reaching phase because the initial state is already inside the boundary layer, therefore the trajectories move towards the origin but without sliding along the surface.

It is interesting to correlate the system dynamics in the phase plane with the control behavior that is visible in Fig. 6.7 on the right. The control history for $\Phi = 0.1$ exhibits a spike in all control directions (excluding the one at the first instant, which is due to the initial state offset): this is due to the combination of time step and boundary layer width. Since this latter is relatively narrow, the system trajectory rapidly crosses the entire layer within a single time step as it approaches the sliding surface. Consequently, a strong control action is required to bring the system back toward the surface. This sharp corrective action is akin to *braking* the system to prevent it from deviating too much from the target surface, and if maintained in time it leads to chattering. In this case, however, the commands are modulated by the saturation function and control remains smooth after the first correction. This behavior is still partially visible for $\Phi = 1$, and completely disappears for $\Phi = 10$.

6.4.2 Time-varying boundary layer

The approach of choosing K to be a large constant enhances robustness and convergence to the sliding surface but increases imprecision and chattering. The use of a constant-width boundary layer allows to avoid chattering, but the value of Φ requires to be tuned on a case-by-case scenario. The performance of the controller in sliding mode can thus be improved by using a time-varying boundary layer (TVBL).

Despite the gravitational perturbations arising from the asteroid's irregular shape are assumed to be not known, their mathematical structure is fixed. The analysis that follows investigates the performance of the sliding mode controller when the boundary layer is allowed to vary in size depending on the magnitude of the perturbations, and the gain of the switching term is changed accordingly. To implement such an approach, an assumption is necessary over the low-order SH coefficients of the asteroid. As discussed in Sec. 3.4.3, C_{20} and C_{22} are the dominant sources of perturbation for the dynamics around an irregularly shaped asteroid. As a matter of fact, C_{20} represents the oblateness of a body (equatorial bulge), whereas C_{22} identifies the asymmetry in the mass distribution around the equator: for asteroids like Eros, which resemble a triaxial ellipsoid, these coefficients will be inevitably very large compared to planetary bodies. Therefore, a conservative estimate of these two values can be made, and the controller designed according to Eq. (6.9). Specifically, to fully harness the structure of the parametric uncertainty, it is required that the coefficient η is chosen to be smaller than the perturbation, otherwise the results will be the same as with a constant boundary layer. For the following analysis, η has been fixed at 10^{-5}.

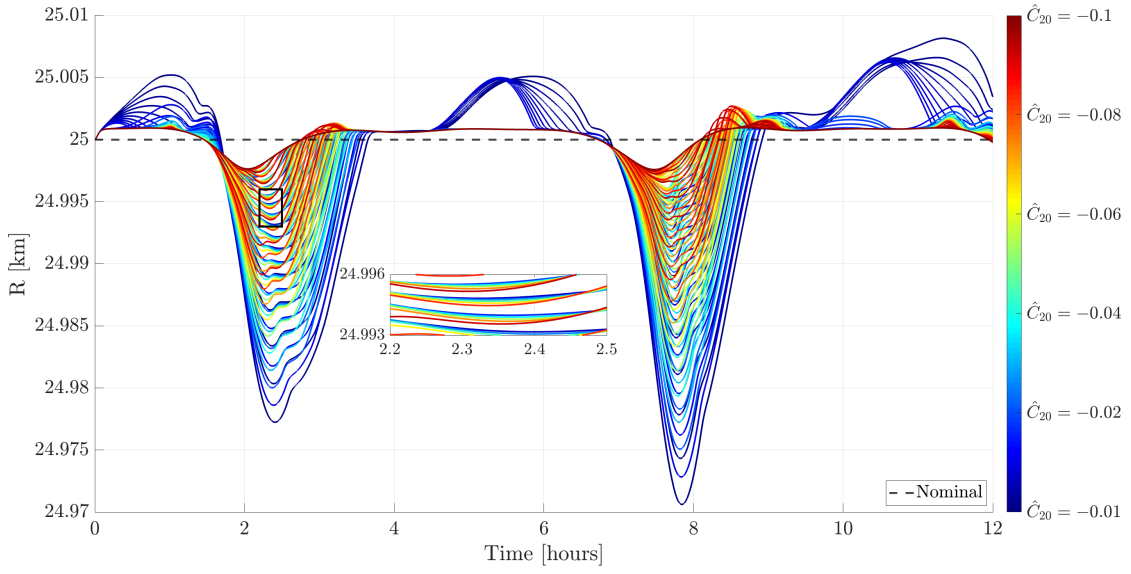

Figure 6.9: Tracking performance of the orbital radius with a time-varying boundary layer as a function of the assumed asteroid's oblateness and ellipticity.

Table 6.2: Assumed upper bounds of C_{20} and C_{22} for the time-varying boundary layer.

Parameter	Tested range	Real value
C_{20}	-[0.01,0.1]	-0.0525
C_{22}	[0.01,0.1]	0.0824

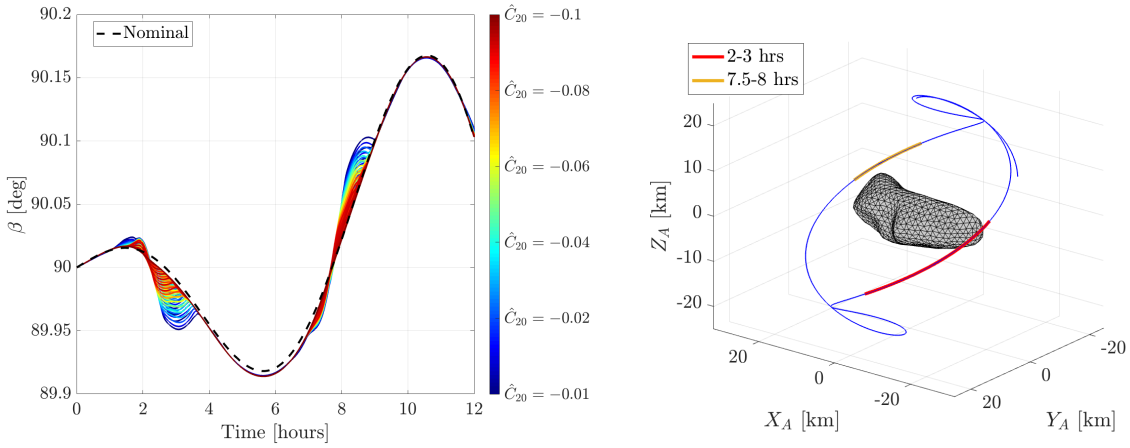

Figure 6.10: On the left, the tracking performance of β with a time-varying boundary layer as a function of the assumed asteroid's oblateness and ellipticity. On the right, the controlled trajectory in the asteroid-fixed frame.

It is known that negative values of C_{20} correspond to oblate bodies, whether positive values of C_{22} reflect if the equatorial asymmetry in the mass distribution is aligned with the X-axis of the body-fixed reference frame, which is indeed the convention used (see Sec. 3.1). For these reasons, these two coefficients have been varied over the 10-by-10 grid shown in Table 6.2. The results of these simulations are shown in Fig. 6.9 and 6.10, where each combination of the two coefficients has been assigned to a color. To better interpret the figures, it should be understood that the coefficients have been varied in ascending order, by fixing C_{20} and then sliding over the range for C_{22}.

The results, which are evidently chattering-free, allow for some considerations. First of all, there are certain intervals during the simulations in which the controllers that underestimate C_{20} (hence, colored in dark blue) lead to a noticeably lower tracking performance than those that do not (e.g., during the first two hours). On the contrary, between 2 and 4 hours, and again at 8 hours, all the trajectories showcase a tendency to deviate from the nominal orbit. In this situation, however, the trend is more complex to interpret. In fact, there appear to be simulations that have been controlled by assuming a larger value for C_{20} which deviate from the reference more than those that have been controlled with lower values. As an example, it suffices to observe that in the highlighted black box, there are some curves with a blue-cyan color (thus assuming smaller C_{20}) which achieve a better tracking performance than some red curves. To explain this behavior, the plot on the right in Fig. 6.10 needs to be inspected in parallel. Here, it can be observed that the spacecraft, which is on a polar orbit, is passing very close to the lobes of Eros during these two time windows. As a consequence, the effect of C_{22} dominates that of C_{20} to the point that overestimating the former, but underestimating the latter, leads to an improved performance. On the contrary, the time windows mentioned at the beginning, where the underestimation of C_{20} reduces the tracking accuracy, correspond to when the spacecraft is located far from the equatorial plane, and thus the gravitational moment associated with the asteroid's oblateness is the dominating perturbation.

A comparison of the control law when using a fixed and a time-varying boundary layer is provided in Fig. 6.11. Clearly, the TVBL controller exploits much more the switching term to remain in sliding mode than the nominal controller, which instead relies in good part also on the equivalent control term, thus being more inaccurate. On the right, it can be observed that the dynamics of the sliding surface fully exploit the available bandwidth for control when the boundary layer is allowed to vary in width.

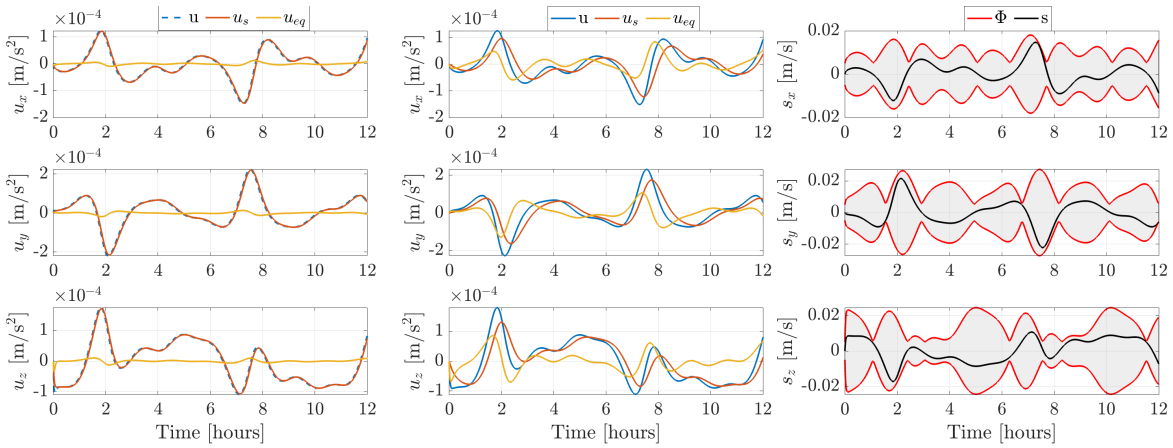

Figure 6.11: Sliding mode control law with time-varying (left) and fixed (middle) boundary layer. On the right, the sliding mode dynamics.

Table 6.3: Tracking performance of the sliding mode controller for different boundary layers during sliding mode (no initial state errors).

Φ [-]	ΔR [m]	ΔR_{max} [m]	$\Delta\beta$ [deg]	$\Delta\beta_{max}$ [deg]
0.01	4.403	7.134	0.007	0.321
1	1.098	3.101	0.001	0.330
100	28.11	50.77	0.021	0.330
Time-varying	1.099	3.126	0.001	0.330

6.4.3 Comparison and discussion

The tracking accuracy achieved with time-varying boundary layer and gain K is generally superior to that with fixed parameters. As shown in Table 6.3, certain values of Φ yield comparable performance between the two approaches. However, the key advantage of the TVBL method described in the previous section is that it removes the need for precise tuning, allowing it to be conservatively set based on the specific dynamics involved. The results obtained prove that the use of a time-varying boundary layer allows to harness the knowledge about the perturbations' mathematical structure to improve the efficacy of the control action.

Now, an essential requirement in this study is that control be applied discretely through rapid, impulsive maneuvers. While the TVBL controller effectively maintains the spacecraft near the target orbit, the study's goal is not strict adherence but rather containment within a permissible deviation range (discussed in the following section). Thus, the primary focus in the design should be on the controller's performance during the reaching phase rather than the sliding phase. In the former, a fixed-gain controller significantly outperforms a TVBL. In fact, the latter adjusts gains based on the estimated gravity perturbations, thus the commanded control acceleration matches gravity in magnitude. Although this enhances performance in sliding mode, it extends the reaching phase duration compared to a constant-gain reaching law, as underscored by Fig. 6.12. The TVBL implementation remains a valuable outcome, as it could benefit different missions or systems where more precise adherence to a continuous control law is feasible and/or needed. Notably, it may be ideal for low-thrust propulsion or attitude control applications. The use of a time-varying boundary layer for orbit-tracking, as applied here, is innovative and, to the author's knowledge, undocumented in the existing literature. It represents a robust control solution that minimizes tuning requirements, making it applicable to a wide array of scenarios. Ultimately, the choice of the control strategy depends on the requirements for the envisioned mission. For this reason, for the remaining of this report the sliding mode controller will be considered with constant gains and boundary layer.

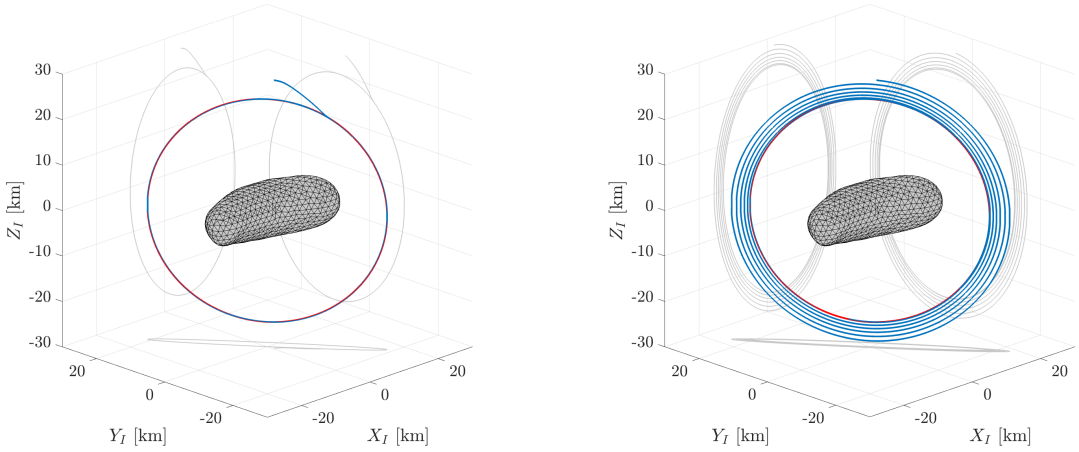

Figure 6.12: 3D trajectory controlled with fixed (left) and time-varying (right) boundary layer.

6.5 Impulsive tracking

6.5.1 Definition of the station-keeping problem

The results presented until now have been obtained by applying a continuous control signal. However, it is necessary to shift the perspective from that of an exclusive control problem to an actual mission scenario, where operational and scientific constraints demand for minimization of fuel consumption and maximization of observation time. In parallel, this introduces margins on the required tracking accuracy. In other words, the increase in the problem complexity generated by additional practical constraints is compensated by a relaxation of the performance requirements for the orbit control system.

In agreement with the performance indicators outlined in Sec. 6.2.4, the accuracy requirements are set on distance from the asteroid and the solar phase angle. Together, they contribute to identifying the volume in space where the spacecraft is allowed to navigate, and where control is thus not strictly necessary. Unlike other typical scenarios, where it is desired to maintain the spacecraft within some torus centered about the reference trajectory (Howell and Pernicka, 1993), in the case at stake the flyable space has a slightly different shape, as explained in the following paragraph.

To improve the understanding of how these two conditions combine, it is helpful to visualize them individually first. The required accuracy on the distance from the asteroid simply identifies a spherical shell of thickness equal to twice the maximum allowed deviation ($2\Delta R_{max}$). Instead, the requirement on the solar phase angle is a bit more complex to visualize. For a given location along Eros orbit, the normal vector to the terminator plane can trace a cone around the Sun-asteroid line, with an angle at the apex equal to twice the maximum allowed deviation from the terminator plane ($2\Delta\beta_{max}$). The cone in turn

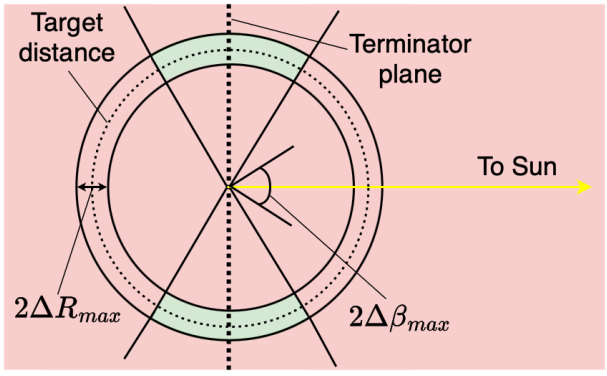

Figure 6.13: Graphical representation of the flyable zone after introducing operational requirements.

can be used to infer the presence in 3D space of four planes within which the spacecraft needs to remain. The intersection of these two regions of space is a volume, whose cross-section is colored in green in Fig. 6.13. This volume tends to resemble a circular torus with a squared cross-section only if ΔR_{max} and $\Delta\beta_{max}$ are sufficiently small.

Given these considerations, the station-keeping problem consists of maintaining the spacecraft within this region of space. In other words, the specific trajectory of the spacecraft is not of interest, as long as it remains confined within the allowable space. In this sense, one may notice that the presence of a target orbit is not strictly necessary anymore. Nonetheless, it is still a precious reference as it defines the trajectory that is further away from violating the constraints. Given the indicators for the tracking accuracy introduced in Sec. 6.2.4, $\Delta R(t)$ and $\Delta\beta(t)$ are not considered anymore, and only ΔR_{max} and $\Delta\beta_{max}$ remain.

6.5.2 Thrust quantization logic

One of the main objectives of this work is to demonstrate that a reference control law, designed using sliding mode control, can be effectively implemented to execute impulsive control commands in an on/off mode. These commands are intended to keep the spacecraft within a designated region of space while ensuring that thrusters remain inactive for a sufficient amount of time. Given the highly nonlinear dynamics of the environment, achieving this balance is a significant challenge. After several efforts, three quantization mechanisms have been identified to obtain the desired outcome:

1. **Activation and deactivation thresholds**: two parameters, r^{on} and β^{on}, activate control only when tracking requirements — either for distance to the target orbit or deviation from the terminator plane — are not met. Correspondingly, two other parameters, r^{off} and β^{off}, create a hysteresis effect, ensuring that control remains active until tighter conditions are met, thereby preventing rapid on-off switching. It should be noted that these parameters offer a noticeable advantage as they can be directly measured with specific sensors (e.g., laser altimeter and Sun sensor).

2. **Thrust level threshold**: An additional parameter, T^{on}, sets the thrust level required to activate the thrusters. Only when the commanded thrust exceeds this threshold will the thrusters engage.

3. **Non-intervention logic** When $r^{off} < r^{on}$, a specific check within the algorithm prevents the spacecraft from executing a maneuver when the distance to the target orbit is naturally decreasing. In other words, if gravitational forces are already directing the spacecraft back toward the desired trajectory, active control is paused to conserve fuel, allowing gravity to perform the correction passively.

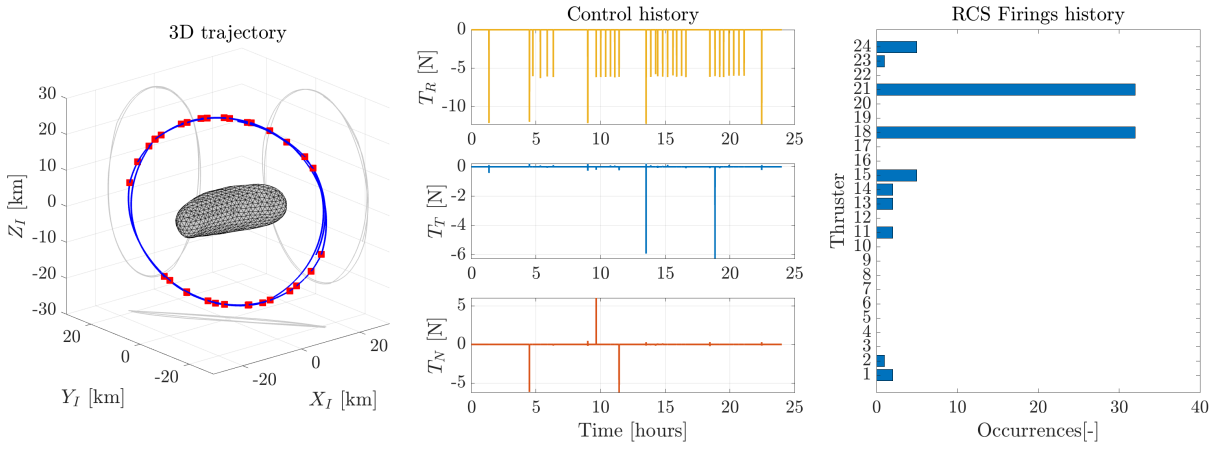

Figure 6.14: Orbit A controlled with impulsive burns. On the left, the 3D trajectory with maneuvers highlighted in red; in the middle, the thrust history; on the right, the history of the RCS activations.

Two main operational constraints related to the propulsion system were also considered. The first one arises from the controller operating via Cartesian elements, where the commanded thrust is always expressed in the asteroid's inertial frame. However, since the spacecraft's RCS thrusters are fixed in orientation, each maneuver would normally require an attitude adjustment to align the spacecraft with the thrust direction. Such a design flaw would be impractical, as corrections need to be executed immediately upon computation. To address this, the spacecraft is assumed to always maintain a nadir-pointing attitude mode (**BC2**), thus aligning its body axes with the RTN frame and keeping the science deck pointed toward the asteroid. In this configuration, the commanded thrust is rotated into the RTN frame before applying the quantization logic.

The second constraint considers the spacecraft's propulsion capabilities. The RCS thrusters are monopropellant engines with a fixed thrust of 3 N each. The spacecraft is equipped with 24 thrusters, allowing four potential thrust levels along each body axis. However, to avoid inducing torque on the spacecraft, only two net thrust levels are permitted: 6 N and 12 N. Therefore, the T^{on} parameter determines, for each side of the spacecraft, whether all four thrusters remain off, two thrusters are activated, or all four are engaged. An example that showcases the firings history of the RCS during a station-keeping simulation is provided in Fig. 6.14. For this simulation, the thrusters which are activated more frequently are numbers 18 and 21. According to Fig. 5.17, these engines are those responsible for providing thrust along the Z_B-axis, thus agreeing with the control history, which shows that most maneuvers are commanded in the negative radial direction. Furthermore, also engines 15 and 24 are occasionally engaged to provide the maximum amount of thrust available in the radial direction.

In parallel, Fig. 6.15 illustrates how the quantization logic affects the station-keeping of orbit A. For this simulation, the values of r^{on} and r^{off} were fixed at 2 km and 1 km, respectively. The combined action of all quantization mechanisms successfully reduces the number of required maneuvers, but their interaction can affect greatly the outcome, and even lead to failure. In particular, it is important to remark that the boundary layer preserves its theoretical meaning. As a consequence, its use is highly functional to the proper working of the algorithm because it modulates the required control based on the distance to the sliding surface. When this reduces, the commanded thrust diminishes, and the value of T^{on} ensures that no additional burns are executed. Decreasing the boundary layer makes the control system more responsive and prone to execute maneuvers, thus resulting in more expensive station-keeping simulations.

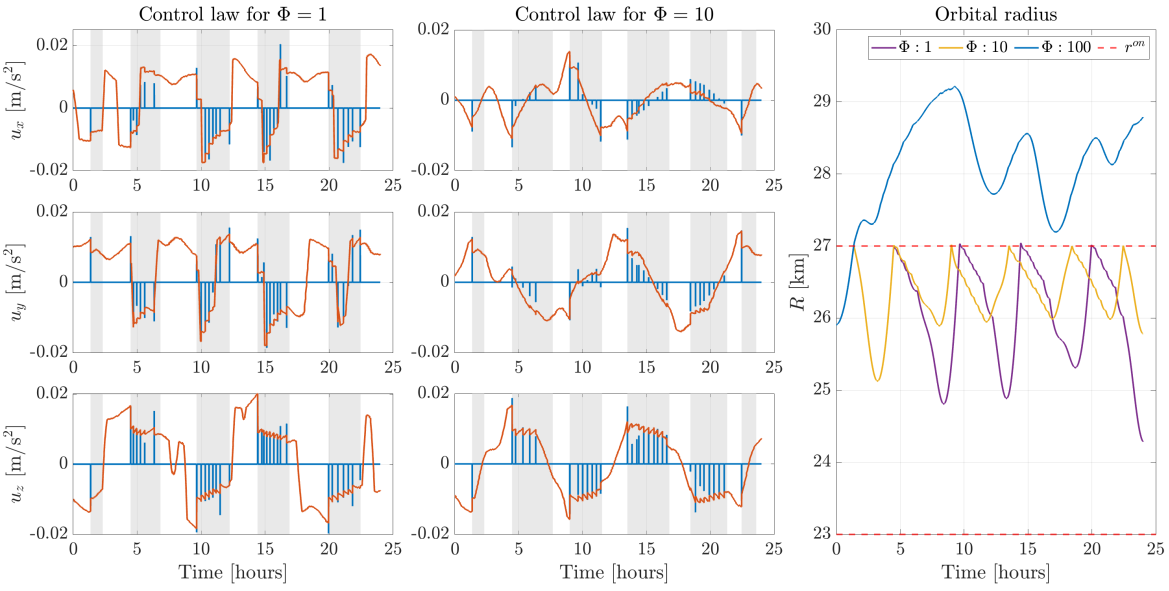

Figure 6.15: Orbit A controlled with different quantization parameters. The continuous control laws and the impulsive burns are represented per thrust acceleration component for different values of Φ. The bands in gray highlight the time windows during which the activation threshold for the distance to the target orbit is on.

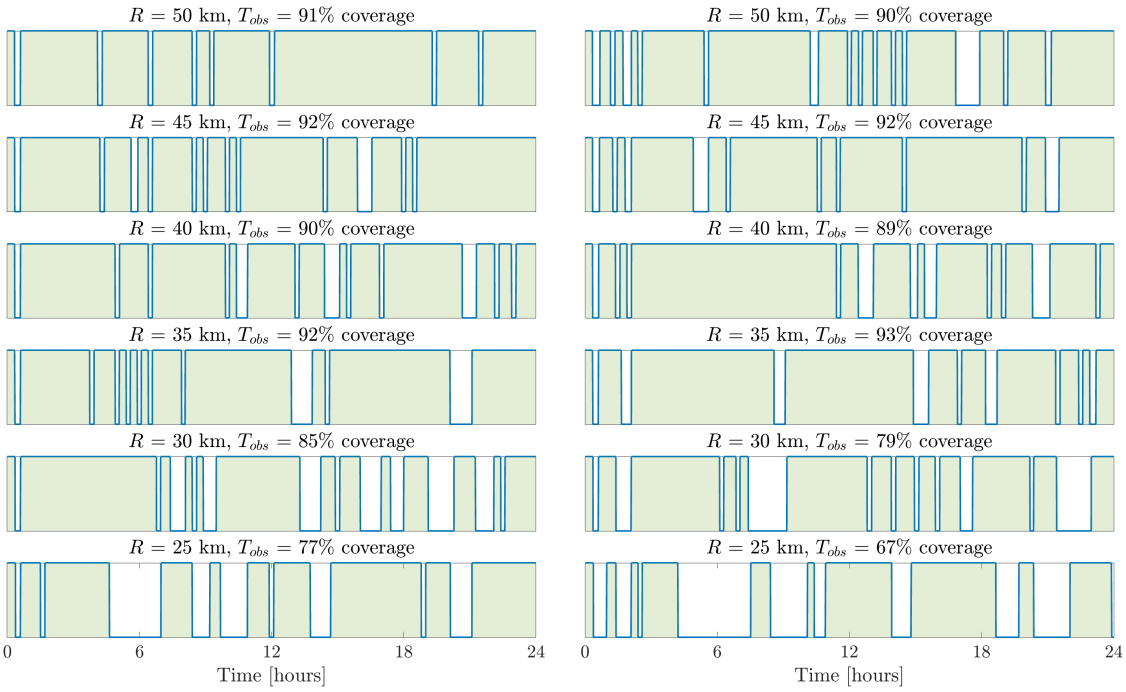

Figure 6.16: Effect of the intervention logic (active on the left, deactivated on the right) on polar orbits for r^{on}= 2 km and r^{off}= 100 m. Areas in green correspond to available time for scientific operations.

Finally, Fig. 6.16 highlights the effect of the non-intervention logic for Sun-terminator, polar, circular orbits with different radii. Notably, the effect of this mechanism becomes more evident as the altitude is reduced and perturbations grow stronger. The efficiency of the orbit control algorithm is clearly improved below 30 km, with an increase in the available coasting time by 10%.

6.6 Closed-loop simulations

To test the robustness of the designed orbit control scheme, closed-loop Monte Carlo simulations were performed for station-keeping and orbit transfer scenarios. According to the considerations raised in Sec. 2.2.7, injection, navigation, and execution errors were generated to reproduce a realistic scenario, while a sufficient number of simulations was chosen to ensure statistical confidence in the results. These errors were generated randomly by assuming a Gaussian probability distribution with zero mean and the standard deviations reported in Table 6.4 (the same distribution is used for all three components of the position/velocity/thrust vector). Specifically, the uncertainty value chosen for the execution error is fully in line with the real values that affected the orbit control maneuvers performed by NEAR spacecraft, as reported by Dunham et al. (2002b).

Table 6.4: Uncertainties affecting the simulations compared with the values taken from similar studies.

	Orbit injection		**Navigation**		**Maneuvers**	
	$\sigma_{OI,r}$ [m]	$\sigma_{OI,v}$ [m/s]	$\sigma_{N,r}$ [m]	$\sigma_{N,v}$ [m/s]	$\sigma_{\Delta V,mag}$ [-]	$\sigma_{\Delta V,dir}$ [-]
This work	1000	0.1	10	0.1	3%	0.5 deg
Negri and de Almeida Prado (2022)	35	0.02	0.8	10^{-4}	3%	-
Furfaro (2015)	100	0.02	0.5	0.1	10%	-
Williams (2002)	-	-	100	10^{-4}	1-5%	1-5%
Shi et al. (2020)	100	0.01	5	10^{-3}	2%	-

Table 6.5: Simulation settings for closed-loop Monte Carlo simulations. Activation thresholds for orbit B are tighter than for the other two due to the very low altitude reached by this orbit.

Setting	Value
T_s [Hz]	0.1
Δt_{meas}[min]	5
r^{on} [km]	2 (A,C), 0.5 (C)
r^{off} [km]	1 (A,C), 0.25(C)
β^{on} [deg]	10
β^{off} [deg]	5
Φ [m/s]	1
T^{on}	[3,9]

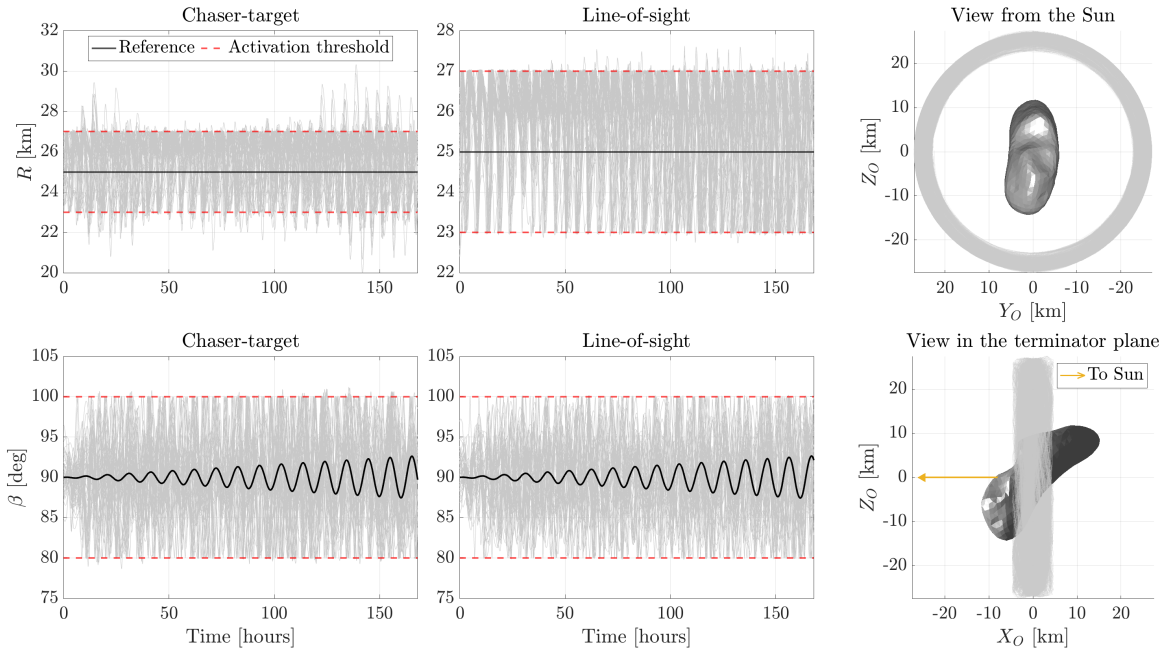

Figure 6.17: A representative sample (50) of trajectories among the Monte Carlo simulations for orbit A.

6.6.1 Station-keeping

For station-keeping analysis, a batch of Monte Carlo simulations was run for orbits A, B, and C. The number of samples was fixed at 300, and the propagation time to a week, which is similar to the amount of time spent by NEAR on low-altitude orbits in between OCMs. The simulations were done by using both the chaser-target and line-of-sight guidance modes, and a summary of the settings used has been reported in Table 6.5.

Figure 6.17 showcases the results for orbit A in terms of orbital radius and solar phase angle, together with a view of the orbits projected in the orbit-fixed frame (limited to those controlled with line-of-sight tracking). Evidently, the line-of-sight guidance yields a more accurate tracking performance than the chaser-target mode, which exceeds the activation threshold by more than 3 km in some cases. On the contrary, the line-of-sight trajectories remain well within 2.5 km from the reference, thus exceeding r^{on} by 500 meters at most. It should be stressed that the values of r^{on} and β^{on} do not represent hard constraints. Since they are activation thresholds for the orbit control module, the interest lies in observing how much they are violated, as this is direct proof of the time that the orbit control system requires to redirect the vehicle within the desired region of space. Therefore, results will highlight the 3σ value for the distribution of ΔR_{max} and $\Delta\beta_{max}$, identified by the symbols $\Delta R_{3\sigma}$ and $\Delta\beta_{3\sigma}$, respectively.

In parallel, the solar phase angle remains within the imposed margins for both guidance modes, although very small violations can still be seen when employing the chaser-target mode. In general, it can be concluded that controlling the 3D orientation of this orbit is significantly less demanding than maintaining the desired size and shape. An insight into the other performance parameters is given by Fig. 6.20, which provides the distribution of the orbit control cost and the coasting time, together with an overview of $\Delta R_{3\sigma}$ and $\Delta\beta_{3\sigma}$. Here, it is possible to observe that line-of-sight tracking not only allows for higher tracking accuracy but also notably reduces the station-keeping cost and increases the coasting time, thereby improving the overall efficiency of the algorithm.

In the analysis of orbit B, the impact of line-of-sight tracking becomes particularly evident. In fact, with the nominal chaser-target approach all the orbits maintain approximately the same period, since for each orbit the controller tracks a point moving with the same speed. On the contrary, line-of-sight tracking is not affected by how the orbital perturbations change the local speed of the spacecraft. As a consequence, all the orbits tend to change their period over time, and the curves associated with the orbital radius shift with respect to each other. However, the desired orbital geometry is maintained, and the save in terms of orbit control cost is very large, with Fig. 6.20 showcasing almost a 50% reduction in station-keeping cost. It should be noted that in Fig. 6.18, the threshold lines identify only the allowed maximum deviation from the periapsis and apoaposis altitudes. In fact, because of line-of-sight tracking, these lines vary for each trajectory, and therefore could not be visualized for all Monte Carlo results.

An example for orbit B is displayed in Fig. 6.19, which presents the trajectory and the control law for one of the Monte Carlo samples (controlled with line-of-sight guidance mode) during the first three days of the simulation. Evidently, the Kepler orbit (which would be the trajectory commanded using the conventional chaser-target approach) and the controlled trajectory diverge in time while remaining bounded between the same periapsis and apoapsis radii. This helps to explain why there is such a large difference in the orbit maintenance cost between the two approaches: the line-of-sight mode does not chase the Kepler solution in time, thereby saving a significant amount of fuel. Furthermore, it is highlighted that the designed orbit control system is successfully able to achieve a minimum altitude of approximately 2 km over the pole of Eros. Such a close passage is extremely risky and likely to impact with the asteroid, thereby proving the robustness of the implemented approach.

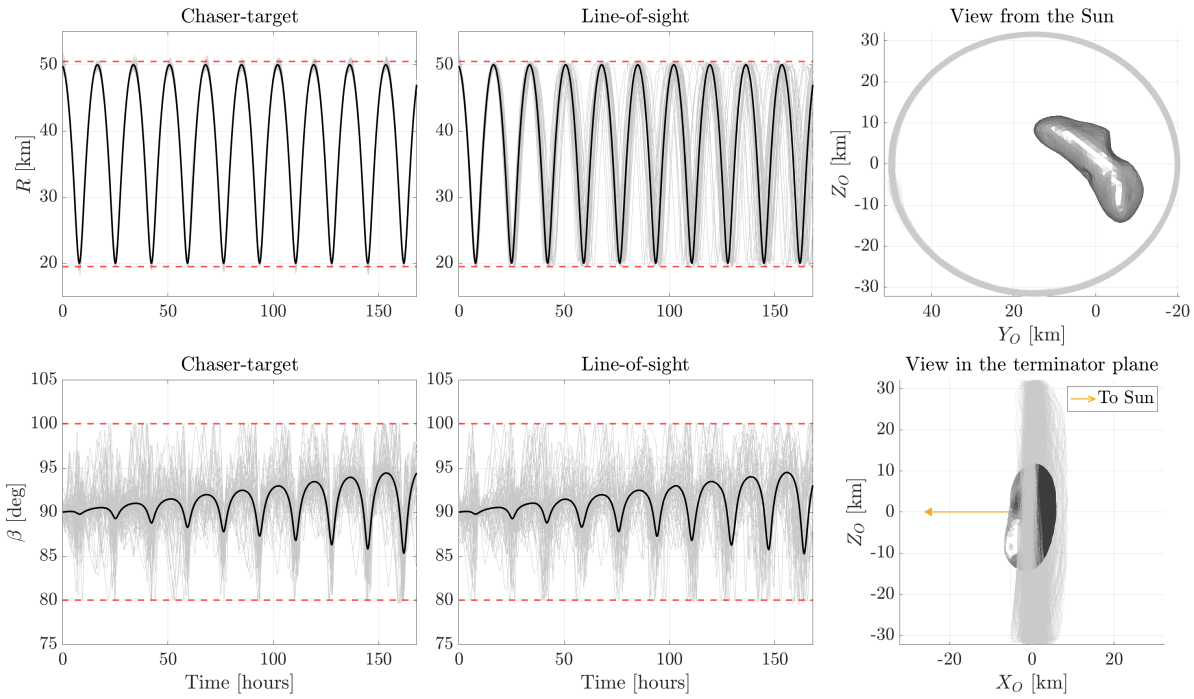

Figure 6.18: A representative sample (50) of trajectories among the Monte Carlo simulations for orbit B.

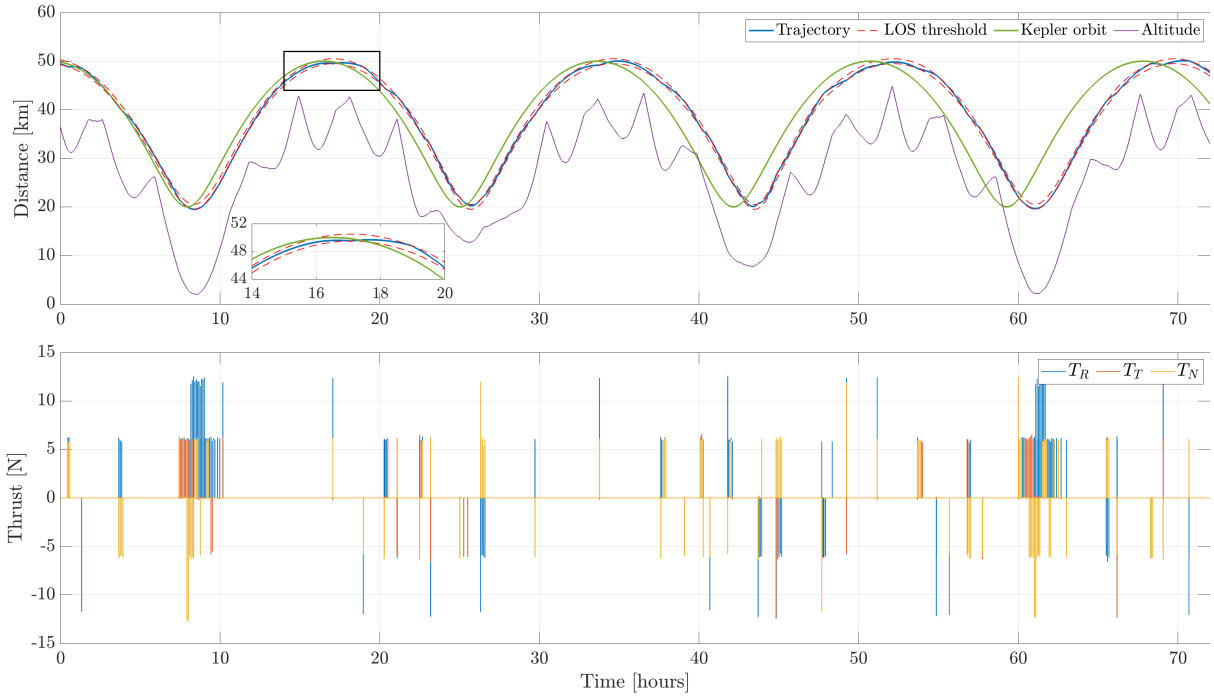

Figure 6.19: Above, the trajectory of one sample from the Monte Carlo simulations of orbit B. Below, the corresponding control law.

Table 6.6: Statistics of Monte Carlo simulations for the three orbits at study. The overline represents the mean, whereas the σ subscript indicates the standard deviation.

Orbit	Tracking mode	$\overline{\Delta V}$ [m/s]	ΔV_σ [m/s]	$\overline{T}_{obs}$ [hours]	$T_{obs,\sigma}$ [hours]	$\Delta R_{3\sigma}$ [km]	$\Delta\beta_{3\sigma}$ [deg]
A	Chaser-target	13.9	1.3	96.8	5.4	6.5	11.8
	Line-of-sight	9.5	1.5	109.3	8.3	2.7	10.4
B	Chaser-target	19.4	1.3	78.5	4.7	3.1	11.5
	Line-of-sight	11.7	0.8	92.7	3.7	1.0	11.2
C	Chaser-target	10.7	1.8	121.5	5.9	4.2	10.7
	Line-of-sight	11.1	1.8	122.3	6.9	3.6	10.1

For brevity, the figures for orbit C are not included. However, results can still be inferred from Fig. 6.20 and Table 6.6, where the two tracking modes appear to produce nearly identical results for this orbit. Indeed, it is expected that as the altitude of the orbit is increased, the differences between the two approaches tend to disappear. In fact, the perturbations from the gravity field of Eros lose strength, implying that the natural motion of the spacecraft resembles more that of a fictitious point moving accordingly to the two-body problem.

Additionally, it is noted that the activation thresholds are exceeded far more than for A and B. Due to the design of the orbit control algorithm, which triggers a control maneuver only when the limit is breached, simulations will always exceed the specified tracking accuracy. Navigation errors and the onboard measurement update frequency also play a role, as these factors often mean the spacecraft begins returning within the control volume only after it has exceeded the constraint by a fair amount. This should not be viewed as an explicit flaw; rather, it underscores the importance of conservatively setting r^{on} to meet tracking accuracy requirements. The following chapter will explore adjustments to the control algorithm parameters to enhance its overall performance.

In conclusion, line-of-sight tracking generally provides superior performance to the nominal two-satellite formation control approach that is found in the literature. The improvement affects all performance parameters: station-keeping cost, coasting time, and tracking accuracy. While the geometrical path fol-

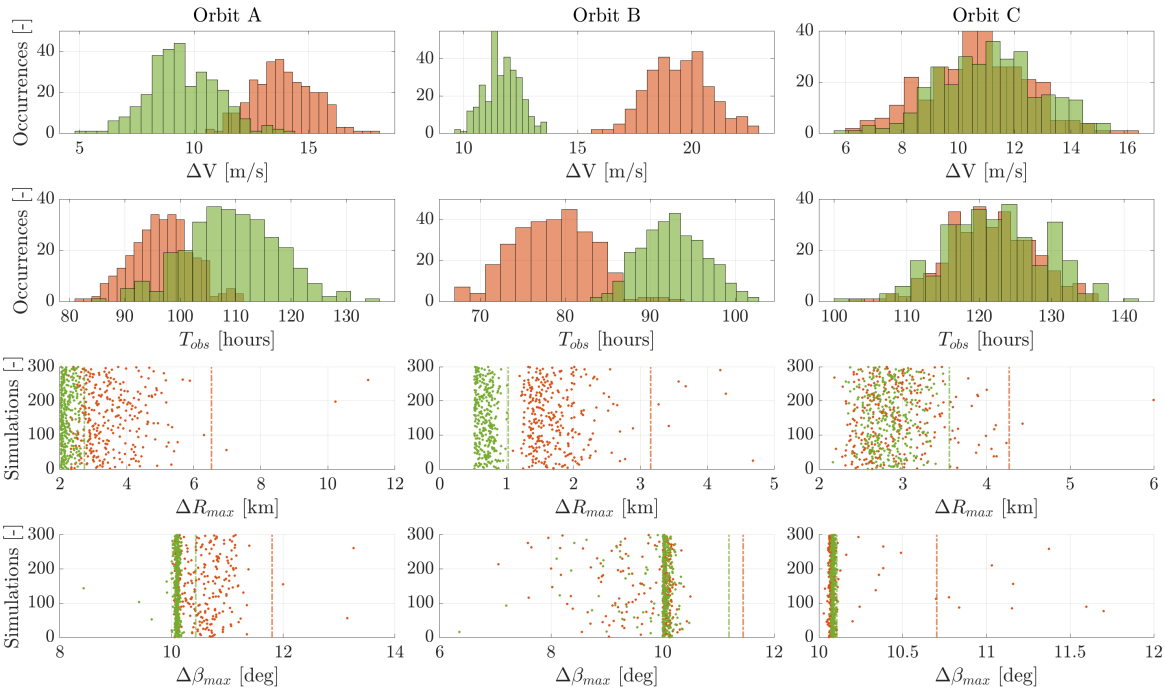

Figure 6.20: Distribution of the performance parameters among the Monte Carlo simulations. Orange and green identify the chaser-target and the line-of-sight tracking mode, respectively. The dashed lines show the 3σ confidence level with respect to ΔR_{max} and $\Delta\beta_{max}$.

lowed by the spacecraft matches the desired one, the time required to do one full revolution changes depending on the perturbations. For the type of mission envisioned within this study, this does not represent an issue. However, specific scientific experiments may require the spacecraft to be at a certain location at a given time, in which case the current approach would lose its advantages.

Unfortunately, there are no direct sources available to compare these results, as active station-keeping for the NEAR mission is largely unaddressed in publicly available documentation. This omission is likely due to NEAR's cautious mission design, which relied extensively on frequent communication with ground control. Through precise environmental characterization, NEAR achieved highly accurate maneuvers with precise injection conditions, resulting in stable orbits that required minimal intervention. Additionally, NEAR's operational constraints - specifically, its avoidance of prolonged stays in low orbits (typically limited to one to two weeks) and its relatively relaxed tracking requirements — meant that active orbit control was unnecessary.

6.6.2 Orbit transfers

Although the main focus of this work is to design a robust algorithm for maintaining an orbit in the perturbed environment of an asteroid, it is interesting to investigate how the designed system adapts to an orbit transfer scenario. In fact, the low-gravity environment of an asteroid makes it possible for a spacecraft to use the RCS to perform proper trajectory correction maneuvers in addition to nominal maintenance operations. For this purpose, two types of maneuvers have been considered, as they are deemed as the most relevant for the envisioned mission:

- A planar transfer from a 50 km circular, polar orbit to a 25 km circular, polar orbit.
- A change in the orbital plane to correct a large deviation from the terminator plane.

Table 6.7: Reference orbits for planar transfer.

-	a [km]	e [-]	i [deg]	Ω [deg]	ω [deg]	Condition
Orbit 1	50	0	87.1	127.8	-	Maintain for 30 hours
Transfer leg	37.5	0.33	87.1	127.8	277.2	Maintain until $R < 28$ km
Orbit 2	25	0	87.1	127.8	-	Maintain until end

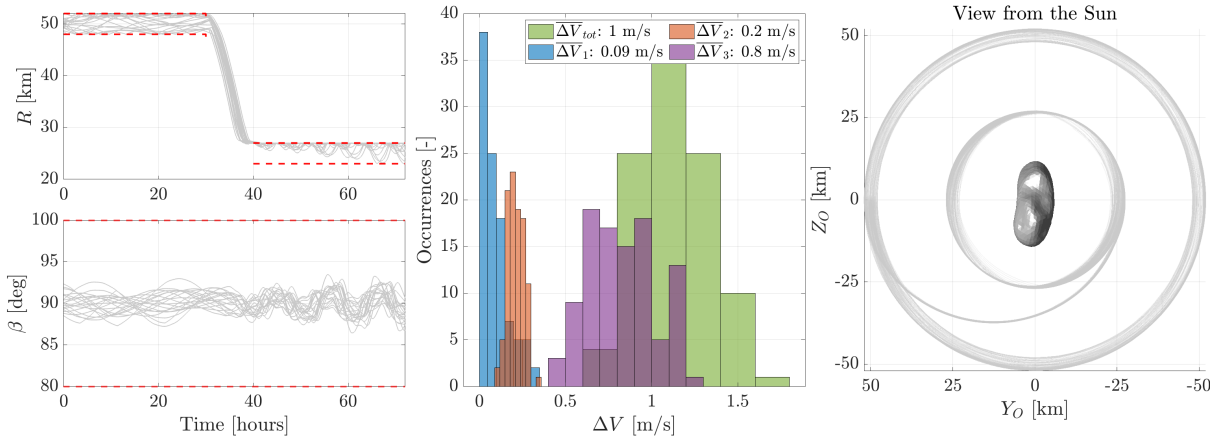

Figure 6.21: Results from Monte Carlo simulations of a planar transfer around Eros.

Planar transfer

To implement the transfer, the mission manager uses three reference orbits, as detailed in Table 6.7. It should be noted that the nature of the sliding mode controller is such that it would be theoretically able to bring the spacecraft from any initial state to any desired state. This means that one could set the target orbit directly at 25 km and fix the initial position in the simulator at 50 km. Although this approach is feasible, it results in a trajectory that takes multiple revolutions to reach the target orbit, making it less efficient. Therefore, a transfer approach involving an intermediate elliptical leg was preferred. This orbit, whose semi-major axis and eccentricity can be quickly computed from the departure and target radii, is used as the reference during the transition. Once the spacecraft reaches a distance from the asteroid below 28 km, the reference orbit is changed to the final one, and the orbit control guidance computes the commands required to perform proper station-keeping as already analyzed in the previous section.

Figure 6.21 shows the results obtained from Monte Carlo simulations of the transfer. The orbit control module works effectively while respecting the desired conditions set by r^{on} and β^{on} also during the transfer. It should be highlighted that especially for this type of scenario, the line-of-sight tracking mode works particularly well, making the designed control system very versatile. Additionally, it is interesting to notice that the average ΔV for the transfer itself (0.2 m/s) is quite reduced if compared to the station-keeping cost at 25 km (0.8 m/s). Although this may not be the optimal approach to execute this orbit transfer, the results highlight the robustness and versatility of the designed control framework. Furthermore, a reference value for the cost of a similar maneuver is provided by Williams (2002), where it is reported that a planar transfer from a 50 km circular orbit to an elliptical 50×20 km×km orbit cost approximately 0.76 m/s, thus further validating the quality of the results obtained.

Change of plane

For this scenario, the spacecraft is originally placed in a circular 35 km orbit which lies 60° from the terminator plane. The initial orbit is maintained for 24 hours, and then the reference from the mission manager is switched to an orbit with the same size and shape, but different inclination and RAAN. Also for this case, Monte Carlo simulations were run, with the results reported in Fig. 6.22.

After 24 hours spent on the initial orbit, the controller is able to bring back the spacecraft within the desired limit from the terminator plane, while guaranteeing that the distance from the asteroid remains

within the desired margins. In this case, the maneuver appears more expensive, with an average cost of 1 m/s. Still, the comparison with the values reported by Williams (2002) has a positive outcome also in this case. Specifically, it is reported that a change of 15 degrees in inclination for a 50 km orbit cost NEAR 1.01 m/s.

It is relevant to underscore that for this maneuver, the property of SMC to operate without requiring a reference trajectory was explicitly utilized. In fact, the target state was set directly on the final orbit, with no intermediate trajectory being tracked. This aligns with the considerations discussed in Chapter 4, which guided the selection of the control method.

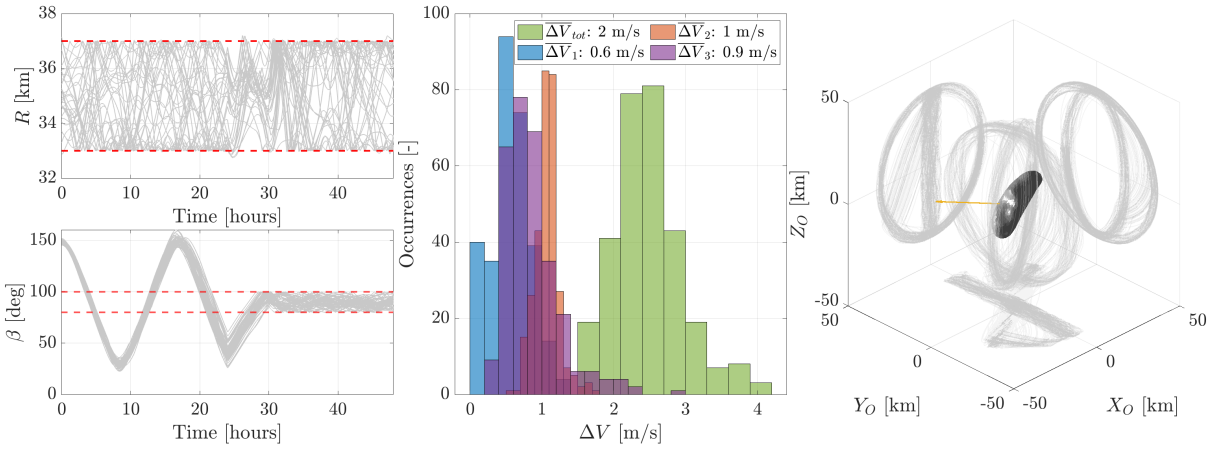

Figure 6.22: Results from Monte Carlo simulations of plane change maneuver around Eros.

7

Robust analysis and design

In this chapter, robust design principles are applied to the designed orbit control system to improve its performance and assess how it is affected by the asteroid environment. Section 7.1 presents the principles of robust design in engineering, introducing fundamental concepts such as orthogonal experiments and factor levels optimization. Section 7.2 gives an overview of the design space, followed by the estimation and choice of the optimal factor levels. Subsequently, Sec. 7.3 applies the refined orbit control over the full mission design space of interest, focusing on the effects that the periapsis radius, inclination, and eccentricity have on the system performance. This is followed by a study of how the onboard environment model affects the robustness of the system against navigation errors, presented in Sec. 7.4. Furthermore, Sec. 7.5 showcases the results obtained by applying the designed orbit control scheme to two new asteroids: Bennu and Kleopatra. The chapter is concluded by Sec. 7.6, which presents a comparison between the implemented method and the target point approach.

7.1 Methodology

In its broader meaning, *Robust Design* can be defined as the *engineering methodology for improving productivity during research and development so that high-quality products can be produced quickly and at low cost* (Phadke, 1989). The fundamental techniques and tools of Robust Design are applied within this chapter to improve the performance of the designed orbit control algorithm while reducing the computational cost required with such an analysis.

Before delving into the details of the process, it is important to first introduce some key concepts. We refer to *factors* as the design parameters which can be controlled by the engineer and which affect the output of the process, whereas the *levels* describe the range of values at which each factor can be set. Together, factors and levels define the *experimental region*, or *design space*, of the design process. In this context, a *matrix experiment* consists of a set of experiments where the factors are varied over different levels to study how they affect the system. Matrix experiments belong to the broader field of *design of experiments* (DOE).

7.1.1 Taguchi experiments

Professor Genichi Taguchi was an engineer and statistician who developed practical methods relying on statistics aimed at improving the quality of the design process for a product. The methodology he developed relies on the use of specific experiment matrices whose purpose is to detect the main effects of the factors involved in the design process while minimizing the number of experiments required to gather the data. Taguchi experiments represent an example of *fractional factorial design* (FFD): the matrices used to design such experiments include only a limited subset of all the possible factor-level combinations, thereby reducing notably the number of simulations compared to a *full factorial design* (FD) experiment,

where all the combinations are explored. Despite the exploration of the design space being significantly reduced, the statistical quality of the results is preserved thanks to the so-called *balancing* property of the experiment arrays, which allows to increase significantly the overall efficiency of the design exploration. In fact, the matrices used to design such experiments are *orthogonal*, where the orthogonality is to be intended in the combinatorial sense: for any pair of columns, all combinations of factor levels occur and they occur an equal number of times. As a consequence, the number of experiments at each level of every factor is the same. This property is maintained by the array even if one or more of its columns is removed; on the contrary, removing even one row will make the matrix not orthogonal anymore. The mathematical definition of an orthogonal matrix experiment is not included for conciseness, but the interested reader can refer to Appendix A in the book by Phadke (1989).

7.1.2 Signal-to-noise ratio

The purpose of Robust Design is to identify the levels of the control factors which make the design less sensitive to noise while maximizing one, or more, performance indexes of interest. In particular, the identification of an objective function to be maximized is a crucial step, as an inadequate choice may compromise the interpretation of results and thus lead to wrong conclusions about the optimum levels for the control factors. The *signal-to-noise* (S/N) ratio is a commonly used figure of merit in robustness analysis to highlight, and subsequently minimize, the sensitivity to noise of a process. Depending on the type of problem at stake, there exist different ways in which the S/N ratio can be defined. Specifically, for a continuous and non-negative quality characteristic, the most common design problems fall into either three of the following categories:

- *Smaller-the-better* problems, whose quality characteristic needs to be minimized. For this scenario, the S/N ratio is defined as:

$$\eta = -10 \log_{10} \left(\frac{1}{n} \sum_{i=1}^{n} y_i^2 \right) \tag{7.1}$$

  where y_i is the quality characteristic for the i^{th} sample (i.e., simulation, for the context of this work) out of n total samples.

- *Nominal-the-best* problems, where the objective is to stabilize the mean of the response at a desired value, and then minimize the variance with respect to it. For these situations, the S/N ratio is defined as:

$$\eta = 10 \log_{10} \left(\frac{\mu^2}{\sigma^2} \right) \tag{7.2}$$

  where μ is the mean of the response, whereas σ is the standard deviation, respectively defined as:

$$\mu = \frac{1}{n} \sum_{i=1}^{n} y_i \qquad \sigma^2 = \frac{1}{n-1} \sum_{i=1}^{n} (y_i - \mu)^2 \tag{7.3}$$

- *Larger-the-better* problems, where the quality characteristic is desired to be as large as possible. The S/N ratio is defined as:

$$\eta = -10 \log_{10} \left(\frac{1}{n} \sum_{i=1}^{n} \frac{1}{y_i^2} \right) \tag{7.4}$$

  It should be noted that for this problem the definition of the S/N ratio explicitly avoids maximizing the mean square quality characteristic because it would lead to maximizing both μ and σ^2, which is not desirable.

Finally, it should be remarked that the purpose of using the log in constructing the S/N ratio is to avoid the predicted quality characteristic under optimum conditions becoming negative. Regardless of the problem, the S/N ratio needs always to be maximized.

7.1.3 Analysis of variance

The decomposition of variance, also called analysis of variance (ANOVA), is a powerful tool to gain insight into the relative effect that the different factors and their interactions have on the response of the system. In theory, ANOVA can accommodate for an infinite number of factors, and be able to estimate their primary effects as well as the effects of their interactions. In practice, however, the increase in the number of simulations makes it highly impractical to consider interactions of order higher than one when the number of factors is high. To simplify the discussion, the following definitions and equations are based on the two-way ANOVA, whose general model is:

$$\eta_{ijr} = \mu + \alpha_i + \beta_j + (\alpha\beta)_{ij} + \epsilon_{ijr} \tag{7.5}$$

where η_{ijr} is one observation of the response variable. In particular, i=1, 2, ...I is the level of factor A, j=1, 2, ...J is the level of factor B, and r represents the replication number, which defines the number of times the same experiment has been carried out, such that the total number of experiments is $N = IJR$. Moreover, α_i, β_j, and $\alpha\beta_{ij}$ represent the deviations from the overall mean μ caused by factors A, B, and the first-order interaction AB, respectively. In particular, the following *sum-to-zero* constraints ensure statistical identifiability of the parameters :

$$\sum_{i=1}^{I} = \alpha_i = 0 \quad \sum_{j=1}^{J} \beta_j = 0 \quad \sum_{i=1}^{I} (\alpha\beta)_{ij} = \sum_{j=1}^{J} (\alpha\beta)_{ij} = 0 \tag{7.6}$$

Finally, ϵ_{ijr} is the error that is made by the model, which is assumed to be independent, normally distributed, and with constant variance.

ANOVA is performed by first computing the total sum of squares, which derives from the following equation:

$$\sum_{k=1}^{N} \eta_k^2 = Nm^2 + \sum_{k=1}^{N} (\eta_k - m)^2 \tag{7.7}$$

where m is the mean of the S/N ratio for all the experiments ($\sum_{k=1}^{N} \eta_k$). The term on the left is the *grand total sum of squares*, whereas the two on the right are the *sum of squares due to mean* and the *total sum of squares*, respectively. It is then possible to partition the total sum of squares SS_T into the sum of squares due to factor A (SS_A), the sum of squares due to factor B (SS_B), the sum of squares due to the first-order (and only) interaction between A and B (SS_{AB}), and the sum of squares due to the error (SS_E):

$$\begin{aligned} \underbrace{\sum_{i=1}^{I}\sum_{j=1}^{J}\sum_{r=1}^{R}(\eta_{ijr} - m)^2}_{SS_T} = \underbrace{JR\sum_{i=1}^{I}(\bar{\eta}_i - m)^2}_{SS_A} + \underbrace{IR\sum_{j=1}^{J}(\bar{\eta}_j - m)^2)}_{SS_B} + \\ \underbrace{R\sum_{i=1}^{I}\sum_{j=1}^{J}(\bar{\eta}_{ij} - \bar{\eta}_i - \bar{\eta}_j + m^2)}_{SS_{AB}} + \underbrace{\sum_{i=1}^{I}\sum_{j=1}^{J}\sum_{r=1}^{R}(\eta_{ijr} - \bar{\eta}_{ij})^2}_{SS_E} \end{aligned} \tag{7.8}$$

where $\bar{\eta}_i$ is the mean of the observations at level i of factor A, and similar for factor B and the interaction AB.

To conclude this synthesis of the ANOVA theoretical background, it is also necessary to define the *degrees of freedom*, the *mean square*, the *F-statistic*, and the *p-value*. These terms are typically collected in specific tables (e.g., Table 7.1) to help visualize the results in a compact form.

Table 7.1: Example of ANOVA table for an experiment with two factors.

-	Sum of squares (SS)	Degrees of freedom	Mean squares (MS)	F-statistic
Factor A	SS_A	I-1	SS_A/I-1	MS_A/MS_E
Factor B	SS_B	J-1	SS_B/J-1	MS_B/MS_E
Interaction AB	SS_{AB}	(I-1)(J-1)	SS_{AB}/((I-1)(J-1))	MS_{AB}/MS_E
Error	SS_E	$IJ(R$-1)	$SS_E/IJ(R$-1)	-
Total	SS_T	IJR-1	-	

Degrees of freedom
The degrees of freedom indicate the number of independent parameters associated with the overall design experiment. More generally, one degree of freedom is spent to estimate the overall mean, which means that SS_T has always N-1 degrees of freedom. The degrees of freedom associated with a factor are one less than the number of levels over which that factor is varied, whereas the degrees of freedom for a generic n^{th}-order interaction are given by the product of the degrees of freedom of each factor appearing in the interaction term. If present, the degrees of freedom not used by the mean, the factors, and their interactions are used to estimate the error.

Mean square
The mean square is defined as the ratio between the total sum of squares and the degrees of freedom corresponding to a given factor or interaction.

F-statistic
The F-statistic, or *variance ratio*, is the ratio between the mean square due to a factor/interaction and the error mean square. In general, this indicator shows whether the effect of a factor is large compared to the error variance. Therefore, not only does it provide a qualitative measure of how influential that factor is on the process response, but it also showcases how *confident* one can be about such result.

p-value
The p-value is a probability computed through the variance ratio which measures the evidence against the null hypothesis. In other words, it allows to determine whether the association between the response and a given term in the model is statistically significant. A common significance level is 0.05, which indicates a 5% risk of inferring that the coefficient is not 0 when it is. If the p-value is lower than 0.05, then the association can be considered to be statistically significant.

Finally, it should be noted that the ratio between the sum of squares due to a given factor i and the total sum of squares can be used to estimate the percentage contribution to the variance according to the following formula:

$$P_i = \frac{SS_i}{SS_T} * 100 \tag{7.9}$$

7.2 Control parameters refinement

7.2.1 Experiment set-up

Before running simulations, it is crucial to invest a considerable amount of time in establishing a matrix experiment that satisfies the user's needs, so as to gather meaningful data and reduce the number of experiment iterations to a minimum. Specifically, the design space needs to be carefully analyzed in advance, and a reasoned choice made regarding the factors and the corresponding levels to be investigated. At first glance, the number of variables involved in the problem at stake may appear quite large. In particular, we can identify four main categories of variables which affect the results:

1. **Mission design parameters**: these include both the orbital elements of the target orbit and the accuracy requirements on the tracking performance (i.e., the activation thresholds). Furthermore, the asteroid itself may be considered a mission design variable.

2. **Control parameters**: these are the parameters used to design the control law, and thus include the control gains and the variables introduced within the thrust quantization scheme.
3. **onboard environment models**: these represent the considered options to model gravity within the onboard computer. The measurement update frequency is also included in this group.
4. **Uncertainties**: the distributions used to generate the uncertainties which affect the simulations. More generally, the purpose of Robust Design is to minimize the sensitivity of the process to uncertainties, which can be referred to as *noise factors*.

Exploring the design space by considering all these parameters together would be very complicated and likely inconclusive since the method exposed by Phadke (1989) is based on the assumption that the control factors do not interact with each other. On the contrary, it is expected that there will be strong interactions among the listed factors, in particular with the orbital parameters of the target orbit. These are likely to dominate the response of the orbit control system, and their signature would then overshadow the effects of the other parameters. For this reason, it has been decided to perform a first robustness analysis by considering exclusively the control parameters, which represent the core of the orbit control scheme. In a second moment, robust design principles will also be used to explore the mission design space and the onboard environment models. However, one has to realize that for these purposes, it is much easier to explain the results based on the knowledge of the physical problem at stake; on the contrary, it is significantly more cumbersome to gain insight into the control parameters, which are typically tuned with trial-and-error procedures, at the expense of the experimentation cost. Regarding uncertainties, it was not considered meaningful to evaluate the system's performance as a function of their magnitude, therefore they are taken as fixed noise inputs.

Now, having fixed the focus of this analysis on the control parameters, the experiment can be designed. First of all, the factors ought to be explicitly listed, these being K, Λ, Φ, r^{off}, β^{off} and T^{on}. It should be noted that while r^{on} and β^{on} are chosen based on the tracking accuracy requirements, r^{off} and β^{off} define the hysteresis mechanism used to quantize the thrust, and thus are to be considered in a different category of decision variables. Furthermore, K and Λ can be excluded from the analysis because the parametric study that has been conducted in Sec. 6.4.1 has already identified adequate values for these gains (indeed, one of the advantages of SMC is that these two parameters can be selected straightforwardly based on the dynamics at stake). This reduces the analysis to four factors only, thereby lowering the computational cost required by a considerable amount.

The levels chosen for each factor are reported in Table 7.2, which highlights the starting (baseline) values by an underscore. The number of levels has been fixed at three because this allows to reproduce *curvature* effects while exploring the design region on either side of the initial operating condition. Furthermore, it is essential to select the levels to be sufficiently apart to detect the nonlinear nature of the relationship between the control factors and the noise factors. In fact, one may be tempted to choose the levels to be relatively close to the baseline to reduce the probability of obtaining bad results; on the contrary, this

Table 7.2: Control factors and their levels.

Factor	Levels		
	-1	0	1
Φ [m/s]	0.01	1	100
T^{on} [N]	[1,7]	[3,9]	[6,12]
r^{off} [m]	100	1000	2000
β^{off} [deg]	1	5	10

Table 7.3: L_9 orthogonal array (Phadke, 1989).

Factors → / Experiment ↓	A	B	C	D
1	-1	-1	-1	-1
2	-1	0	0	0
3	-1	1	1	1
4	0	-1	0	1
5	0	0	1	-1
6	0	1	-1	0
7	1	-1	1	0
8	1	0	-1	1
9	1	1	0	-1

allows to identify which region of the design space should be avoided. Additionally, levels that are wide apart imply that the factor effects are large compared to the experimental errors, thereby enhancing the capacity of the designer to infer meaningful considerations.

The next step requires choosing an experiment array. A suitable orthogonal matrix for this study would be the L_9, where the notation L_k identifies an experiment with a total of k runs. As visible in Table 7.3, his array accommodates four three-level factors and requires only nine experiments to be conducted. However, it does not allow to identify interactions between the control factors, thus leading to potentially misleading results. Because of this phenomenon, referred to as *confounding*, it may become impossible to distinguish the effect of a given factor A from that of an interaction B×C. Given the nature of the factors involved, some interactions are expected, making the L_9 array less suitable for this experiment.

Generally, Taguchi arrays are designed to emphasize main effects, requiring engineers to carefully select control factors and S/N ratios so that the effects of interactions are minimized. However, specific arrays can be configured to explicitly distinguish them from the main effects. This is done by leaving specific columns empty, which isolates interactions and prevents confounding. The columns that need to be left empty are chosen based on an interaction table, which indicates which factors' interactions overlap in each array pairing. In particular, the L_{27} array, which accommodates up to 13 factors at three levels, is particularly appealing for the current scenario. Although not all Taguchi arrays admit an *interaction table*, the L_{27} does: with four control factors, it allows all six first-order interactions to be entirely separated from the main effects, while still requiring one-third of the experiments of a full factorial design (3^4=81). To achieve this, it is sufficient to assign the four factors to columns 1, 2, 5, and 12, leaving the remaining columns empty. The L_{27} array and its interaction table are provided in Appendix C.

In compliance with robust design methodology, the overall analysis requires simulations to be run in two nested loops, the outer one being the fractional factorial design identified by the L_{27} array, and the inner one being Monte Carlo simulations, where injection, navigation, and execution errors are generated with different seeds per each run. In other words, for each combination of the control factors identified by the L_{27} array, a number of Monte Carlo simulations has to be run to make the results statistically significant in light of the presence of random uncertainties. For computational reasons, this number was set to 100, whereas the total propagation time of each controlled orbit was fixed at one day.

7.2.2 Estimation of factor effects

The optimum level for a factor is intended as the one that maximizes the value of η over the experimental region. To determine the optimum level for each factor, the estimated main effects can be used, provided the variation of η as a function of the factor levels follows the *additive model*. For the problem at stake, the additive model would imply that the following relationship approximates well the response:

$$\eta_{ijst} = m + r_i^{off} + \beta_j^{off} + \Phi_s + T_t^{on} + \epsilon \tag{7.10}$$

where m is the mean value of η over the experimental region, while ϵ is the error. The results presented in the following sections have been obtained for a Sun-terminator, circular orbit with a 25 km semi-major axis and 45° of inclination. This orbit is particularly challenging to control due to difficulties in maintaining both the distance from the asteroid and alignment with the terminator plane. As such, it serves as an adequate worst-case scenario to perform the robustness analysis of the orbit control system.

For the problem at stake, there are two main figures of merit that evaluate the response obtained for a given combination of factors, namely the total control effort (ΔV) and the available observation time (T_{obs}). Since the former is to be minimized, while the latter is to be maximized, the corresponding S/N ratios are defined according to Eq. (7.1) and Eq. (7.4), respectively:

$$\eta^{\Delta V} = -10\log_{10}\left(\frac{1}{n}\sum_{i=1}^{n}\Delta V_i^2\right) \qquad \eta^{T} = -10\log_{10}\left(\frac{1}{n}\sum_{i=1}^{n}T_{obs,i}^{-2}\right) \tag{7.11}$$

where n is the number of Monte Carlo simulations executed for a given experiment (100 for this analysis). There are two additional indicators that have to be taken into consideration to evaluate the results: the maximum error on the distance from the target orbit (ΔR_{max}) and the maximum deviation from the terminator plane ($\Delta\beta_{max}$). In this case, the choice of the S/N ratio is more critical, since such deviations are not necessarily to be minimized, but rather should be on target (if they were minimized, it would imply that unnecessary control effort is being spent). As noted by Phadke (1989), this is similar to a constrained optimization problem, where the objective is to minimize variance while keeping the mean on target. In these cases, a *scaling factor* should be identified. A scaling factor is a parameter that can be varied linearly to obtain a proportional response, such that the mean can be adjusted on target. For the problem at stake, it is relatively easy to find the scaling factor for both $\eta^{\Delta R}$ and $\eta^{\Delta\beta}$, as these are simply r^{on} and β^{on}. Given these considerations, the most suited form for the S/N ratio according to Eq. (7.2) is:

$$\eta^{\Delta R} = 10\log_{10}\left(\frac{\mu^2_{\Delta R}}{\sigma^2_{\Delta R}}\right) \qquad \eta^{\Delta\beta} = 10\log_{10}\left(\frac{\mu^2_{\Delta\beta}}{\sigma^2_{\Delta\beta}}\right) \tag{7.12}$$

Now, the effect of a factor level, referred to as *main effect*, is defined as the deviation it causes from the overall mean. As an example, the effect of T^{on} (placed in the 12$^{\text{th}}$ column of the L_{27} array) at level 3 over the ΔV is calculated as:

$$m^{\Delta V}_{T^{on}_3} = \frac{1}{9}(\eta^{\Delta V}_3 + \eta^{\Delta V}_5 + \eta^{\Delta V}_7 + \eta^{\Delta V}_{12} + \eta^{\Delta V}_{15} + \eta^{\Delta V}_{17} + \eta^{\Delta V}_{20} + \eta^{\Delta V}_{22} + \eta^{\Delta V}_{27}) \tag{7.13}$$

In other words, the mean effect is taken by averaging the values of $\eta^{\Delta V}$ for all the experiments in which the factor at stake has taken the investigated level. The average S/N ratio for the other factors and levels can be obtained similarly, and because the matrix experiment is based on an orthogonal array, all the level averages possess the same balancing property. A graphical representation of this decomposition is given in Fig. 7.1. If the additive model is correct, the overall value of η observed in such figure should be equal to the sum between the overall mean and the deviations from the mean caused by the levels of the four factors. Furthermore, it is possible to obtain a qualitative impression of the relative importance of each factor on the quality characteristics.

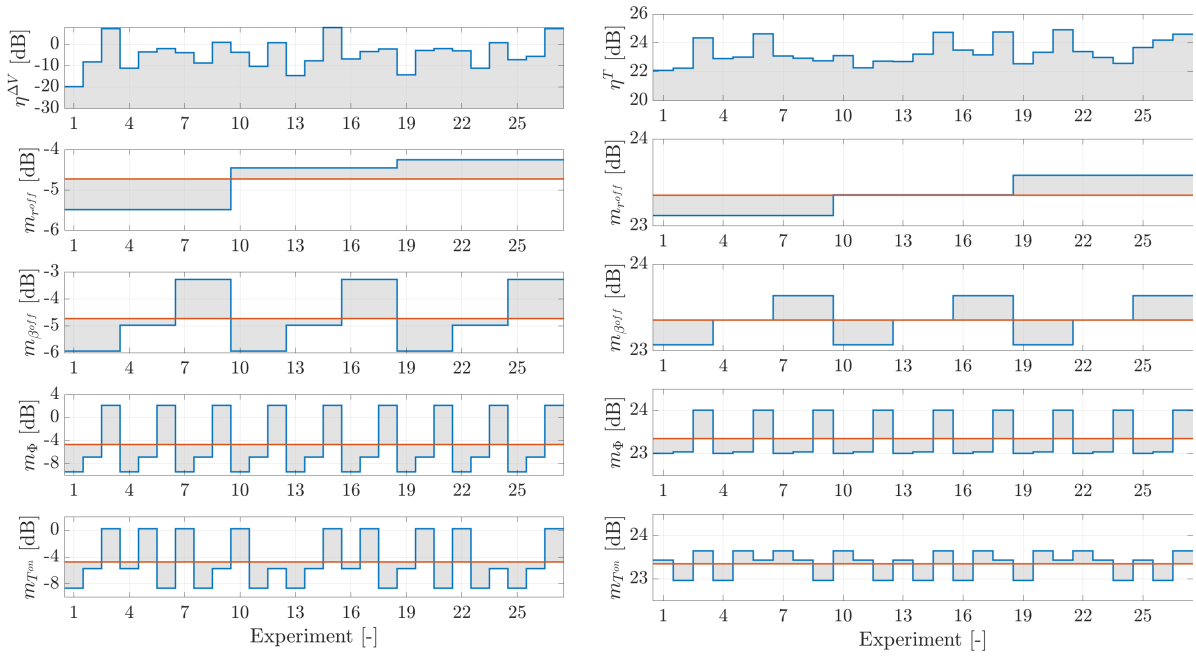

Figure 7.1: S/N orthogonal decomposition. The orange line represents the overall mean of η over the entire experimental region.

At this point, should the additive model hold, the optimum levels of the factors could be chosen directly by plotting the estimated main effects. However, although the main effects that can be computed are not confounded with first-order interactions thanks to the use of the L_{27} array, they do not allow to infer the relative weight that they have on the response of the system compared to that of the interactions. As a consequence, it is first needed to observe the ANOVA results, which have been reported in Tables 7.4, 7.5, 7.6, and 7.7.

In these tables, the terms labeled with an asterisk indicate those whose mean square has been included in the error term. This process is referred to as *pooling* and it can be used to provide an estimate of the error in situations where the number of degrees of freedom would not allow it. Thus, the pooled error is obtained by summing the sums of squares due to the error and the chosen factor(s), and the corresponding mean square takes the name of *error variance*, identified by the symbol σ_e^2. As a rule of thumb, the sum of squares corresponding to the bottom half of the factors (as defined by the lower mean square) and

Table 7.4: ANOVA results for $\eta^{\Delta V}$.

Factors	Sum of squares	Degrees of freedom	Mean square	F	p
r^{off}	7.94*	2	3.969	-	-
β^{off}	32.3*	2	16.149	-	-
Φ	662.07	2	331.03	55.58	$2.5{\cdot}10^{-9}$
T^{on}	367.38	2	183.69	30.84	$4.1{\cdot}10^{-7}$
Error	90.79	18	5.044	-	-
Total	1160.47	26	-	-	-
Pooled error	131.02	22	5.956	-	-

Table 7.5: ANOVA results for η^{T}.

Factors	Sum of squares	Degrees of freedom	Mean square	F	p
r^{off}	0.98*	2	0.49	-	-
β^{off}	1.46*	2	0.73	-	-
Φ	5.77	2	2.89	6	$8.3{\cdot}10^{-3}$
T^{on}	2.20	2	1.10	2.28	$1.3{\cdot}10^{-1}$
Error	8.15	18	0.45	-	-
Total	18.55	26	-	-	-
Pooled error	10.58	22	0.48	-	-

Table 7.6: ANOVA results for $\eta^{\Delta R}$.

Factors	Sum of squares	Degrees of freedom	Mean square	F	p
r^{off}	0.63*	2	0.32	-	-
β^{off}	1.09*	2	0.55	-	-
Φ	0.63*	2	0.32	-	-
T^{on}	1473.90	2	737	26.93	$7.37{\cdot}10^{-7}$
Error	654.53	18	36.36	-	-
Total	2130.78	26	-	-	-
Pooled error	656.89	24	27.37	-	-

Table 7.7: ANOVA results for $\eta^{\Delta \beta}$.

Factors	Sum of squares	Degrees of freedom	Mean square	F	p
r^{off}	1.47*	2	0.74	-	-
β^{off}	4.69*	2	0.35	-	-
Φ	122.27	2	61.13	0.73	$4.93{\cdot}10^{-1}$
T^{on}	9.3*	2	4.65	-	-
Error	1999.89	18	111.11	-	-
Total	2137.63	26	-	-	-
Pooled error	2015.36	24	83.97	-	-

corresponding to about half of the degrees of freedom can be used for pooling (Phadke, 1989). The error variance obtained from the pooled error is used to compute the F-index, which then allows to establish the relative importance of the factors.

Since the error term includes all the contributions to the model response given by first-order (or higher) interactions, the F-indicator is useful to assess whether the main effect of a given control factor is large enough to neglect its interactions with the other factors, or not. If the interaction between two variables is comparable, if not larger, than the main effect of one of the factors involved, then the choice of an optimum level for that factor becomes very complex, and leaving the nominal value may represent the most reasonable choice. Based on the ANOVA results, the percentage contributions to the variance given by the main effects of the control factors have been reported in Fig. 7.2. Evidently, the main effects due to Φ and T^{on} on the ΔV are dominant, as they can explain approximately 90% of the response. On the contrary, the observation time appears to be severely affected by the interactions of the control factors, because the main effects account only for 56% of the response. Instead, the only main effect to consider for $\eta_{\Delta R}$ is the one due to the thrust quantization parameter T^{on}, whereas for $\eta_{\Delta\beta}$ the error variance is larger than the mean square for any of the control factors, thereby denying the possibility of making meaningful conclusions on the factor levels. As a result, the choice of the optimum levels based on the main effects should be made by considering only $\eta^{\Delta V}$ and $\eta^{\Delta R}$. The factor effects for these two figures of merit are reported in Fig. 7.3, from which the following observations can be made:

- Intuitively, for each factor the third (and higher) level maximizes the S/N ratio for the ΔV, thereby reducing the control effort for the orbit-keeping. In fact, setting the three quantization parameters at their highest levels implies that the criteria for activating the thrust are met less frequently. In parallel, increasing the boundary layer width yields a smoother and less aggressive control law.
- The thrust quantization parameter T^{on} has a major impact on the tracking accuracy. Lower values guarantee a safer approach since thrust is activated more frequently.
- No curvature effects are present, thus implying that the explored range for the factor levels could be extended for later analysis.

Because of the conflicting nature of these quality indicators, choosing the optimum level for each factor requires a trade-off logic to be employed. While minimizing the orbit-keeping cost is desirable, priority is given to the tracking accuracy of the system. Having these considerations in mind, T^{on} needs to be set at level one to guarantee that the distance from the target orbit is maintained within the desired range. Instead, Φ can be set at the third level to maximize $\eta^{\Delta V}$. Although this choice is based only on two out of the four quality indicators, this is not a particular issue because both $\Delta\beta_{max}$ and T_{obs} are arguably less relevant compared to ΔV and ΔR_{max}.

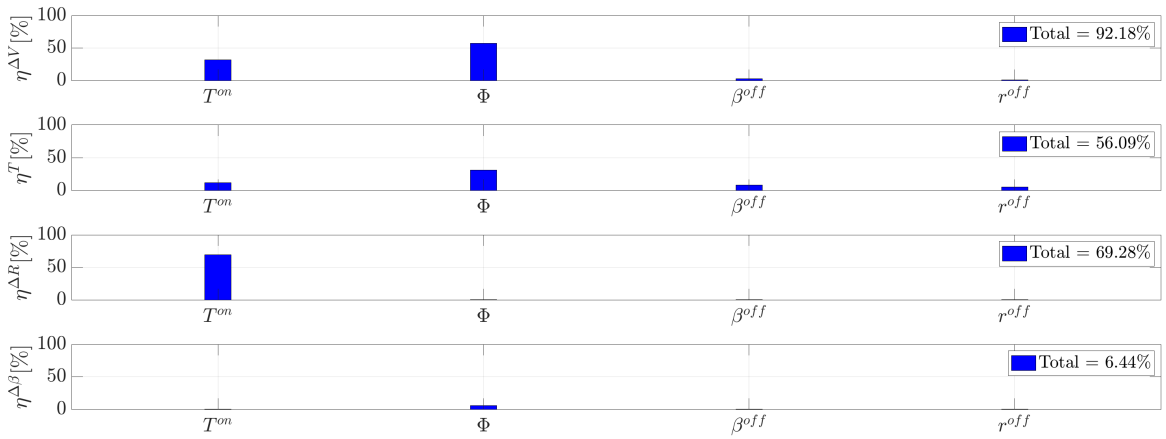

Figure 7.2: Contributions of the control factors' main effects to the S/N ratios. In the top-right corner it is reported how much of the total response can be explained using only the main effects.

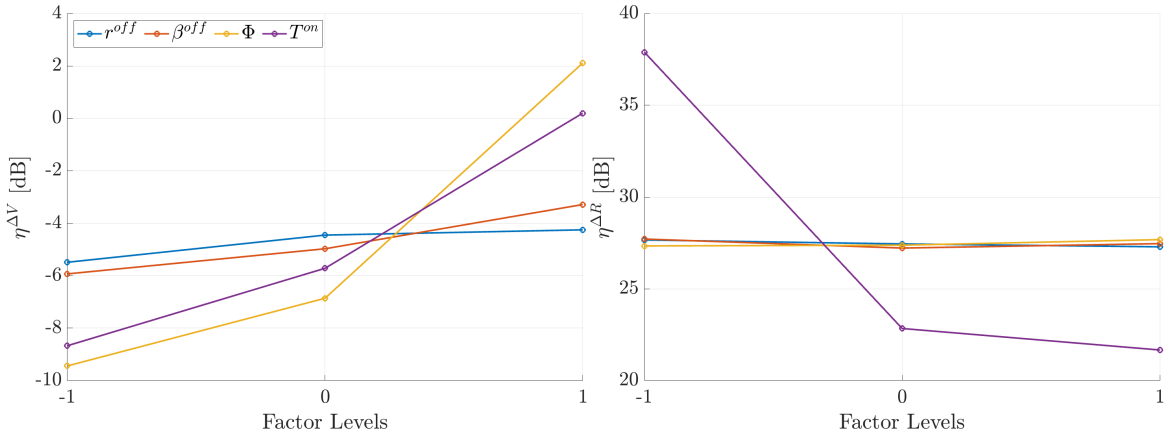

Figure 7.3: Factor effects for $\eta^{\Delta V}$ and $\eta^{\Delta R}$.

In parallel, also the choice of r^{off} and β^{off} remains not fully possible through this analysis, as they tend to interact with the other variables and have less predictable effects. A small full factorial design was run, for a total of only 3^2=9 runs, by fixing Φ and T^{on} at the desired values. The results were not reported because they show a negligible impact of the main effects and interactions on all four S/N ratios. The reason why these two hysteresis parameters do not affect the performance of the system likely depends on the orbit at stake, therefore the next section will investigate if this remains true over the whole mission design space or not.

7.2.3 Prediction and verification

As a final step in Robust Design, a test that verifies whether the additive model holds or not needs to be conducted. Starting from the error variance, one can compute a predicted value for the optimal S/N ratio under the chosen combination of factor levels. Employing the additive model results in:

$$\eta_{opt}^{\Delta V} = m^{\Delta V} + (m_{\Phi_3}^{\Delta V} - m) + (m_{T_1^{on}}^{\Delta V} - m) \tag{7.14}$$

$$\eta_{opt}^{\Delta R} = m^{\Delta R} + (m_{T_1^{on}}^{\Delta V} - m) \tag{7.15}$$

In predicting the optimal values for the S/N ratio, the terms that have been used to obtain the pooled error were not included. In fact, should these contributions be added to the model, the predicted improvement in η would likely exceed the actual realized improvement. Instead, by ignoring the contribution from factors with small sums of squares, it is possible to reduce this bias.

The last step consists of running an experiment with the optimum parameter settings and comparing the observed S/N ratios with the predicted ones. In case these are close enough, it is possible to conclude that the additive model is sufficient to describe the dependence of η on the investigated parameters. Should this not be the case, then the interaction between the control factors is likely to be significant, or the S/N ratio formulation is inadequate. To assess how close η_{opt} is to the experimental value, the variance of the prediction error has to be computed. This error has two independent components: one is caused by the approximation of the additive model (i.e., the errors contained within the estimates of the factor effects), whereas the second is the repetition error of an experiment. Since these two components are independent, the variance of the prediction error is the sum of their respective variances. Having estimated σ_e^2 thanks to ANOVA, the predicted error variance σ_{pred}^2 for $\eta^{\Delta V}$ and $\eta^{\Delta R}$ follows:

$$\frac{1}{n_0^{\Delta V}} = \frac{1}{N} + \left(\frac{1}{n_{\Phi_3}} - \frac{1}{N}\right) + \left(\frac{1}{n_{T_1^{on}}} - \frac{1}{N}\right) \qquad \frac{1}{n_0^{\Delta R}} = \frac{1}{N} + \left(\frac{1}{n_{T_1^{on}}} - \frac{1}{N}\right) \tag{7.16}$$

$$\sigma_{pred}^2 = \left(\frac{1}{n_0}\right)\sigma_e^2 + \left(\frac{1}{n_r}\right)\sigma_e^2 \tag{7.17}$$

Table 7.8: Results of verification experiment.

Parameter	Experiment result	Predicted optimum	2σ confidence level
$\eta^{\Delta V}$ [dB]	-2.04	-1.83	5.31
$\eta^{\Delta R}$ [dB]	18.83	27.68	11.03

where n_r is the number of times the experiment has been run with optimal settings, while n_{A_i} is the number of experiments in which factor A was set at level i. The results from this verification experiment are reported in Table 7.8, which shows that the experimental values for both S/N ratios fall within the 2σ confidence limit of the corresponding prediction error. This proves that for the two quality characteristics at stake, the additive model holds sufficiently well to justify the choice of the factor levels based on their main effects. In the next section, the orbit control with baseline (nominal) and optimal control levels will be compared.

7.3 Robust mission design

The purpose of this paragraph is to evaluate how the performance of the orbit control system is affected by the type of orbit that needs to be maintained. This study has a twofold purpose: on one hand, it investigates the relationship between the particular dynamics regimes that exist around the asteroid (Sec. 3.4.3) and the control performance; on the other, it verifies the robustness of the designed algorithm to the mission design parameters. In fact, from the considerations made at the beginning of this chapter, it follows that the performance of the control system with the chosen settings may not be particularly adequate over the entire mission design space.

All the reference orbits considered for this study lie on the terminator plane, which means that the inclination and the RAAN are constrained. In compliance with robust design methodology, the mission design space has been investigated by running 100 Monte Carlo simulations for each type of orbit under study. To reduce the computational cost associated with such a large-scale study, the propagation time has been reduced from one week to one day. However, it was noted that both station-keeping cost and observation time tend to increase linearly over time. Consequently, the results obtained here can be reliably scaled to provide a quantitative assessment of the system's performance over a full week.

7.3.1 Open-loop analysis

An initial open-loop analysis of orbits around Eros was conducted through 1,000 uncontrolled simulations with a one-week duration, where the initial orbital parameters were uniformly sampled within the mission's design space of interest, except for the eccentricity which was constrained to zero (i.e., only

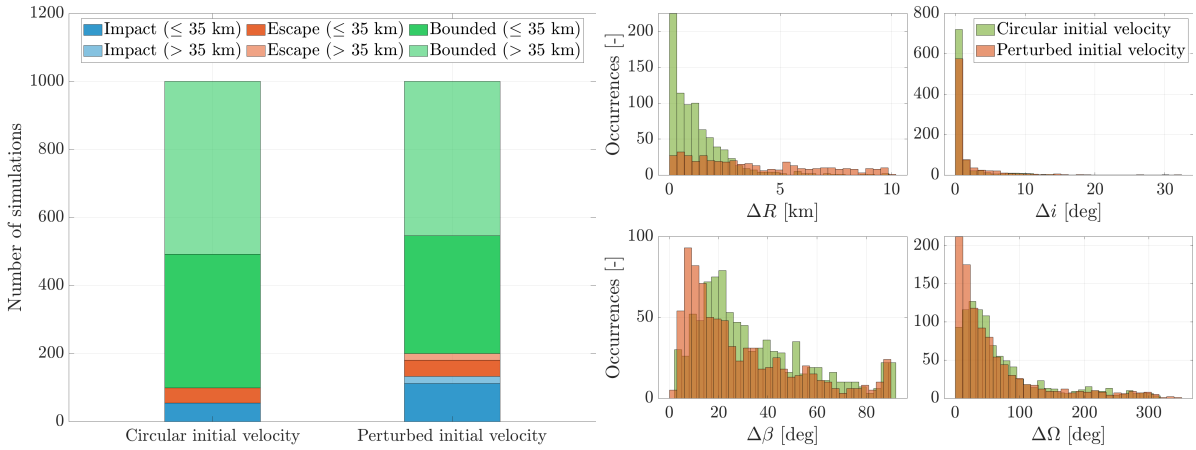

Figure 7.4: Results of the open-loop analysis for circular, Sun-terminator orbits around Eros.

circular orbits were investigated). To simulate all the orbits on the terminator plane, the time since Eros periapsis passage was generated from a uniform distribution, and the inclination and the RAAN computed accordingly (this allows to span uniformly the range of inclinations from 0° to 180°). This batch was run twice: once with initial conditions precisely matching the local circular velocity, and once with a 1σ random error of 0.5 m/s in the initial velocity. Though large, this sample size helps capture uncertainties also in the initial position and in Eros's gravitational parameter, which are effectively modeled as an uncertain velocity term. The goal of this analysis is to examine how initial state uncertainties, representing injection maneuver errors, affect orbital behavior within a highly irregular gravitational field.

Figure 7.4 illustrates that under the ideal assumption of perfect environmental knowledge and error-free maneuvers, circular orbits with an initial radius greater than 35 km avoid escape or impact risk with the small body, aligning closely with the findings from Scheeres et al. (2002) presented in Sec. 3.4.3. Interestingly, when orbit propagation includes initial velocity uncertainty, a subset of trajectories with departure radii nominally expected to ensure stable motion also results in asteroid impacts or escapes. This occurs because initial velocity perturbations alter the osculating semi-major axis and eccentricity, reducing the initial periapsis radius below the planned departure radius. This is proven by Fig. 7.5, where it can be observed that the threshold value on the initial periapsis radius for impact/escape actually remains largely stable despite these uncertainties.

In parallel, the plot on the right in Fig. 7.4 displays variations in key parameters, namely the orbit radius, inclination, RAAN, and solar phase angle, for orbits that remained bounded according to the termination criteria in Sec. 5.3.5 (with the deviations always computed with respect to the initial value, being it perturbed or ideal). Unlike ΔR, whose distribution changes significantly with initial velocity perturbations, both the inclination and the RAAN appear to be less affected, thereby proving that the orientation of the orbit in space is more robust to initial state perturbations than the orbit radius. In particular, it is important to underscore that the inclination appears to be stable regardless of the initial condition, with more than 90% of the simulations remaining well below a 5° variation. Instead, the RAAN undergoes wide variations, even up to 300° within one week. Therefore, as Fig. 7.6 highlights, the solar phase angle exhibits a large variation as well, provided the orbits are sufficiently far from the equatorial plane of Eros. In other words, the irregularity of Eros's gravitational field (mainly C_{20}) is responsible for a very strong drift effect on the nodes, regardless of the type of orbit. Consequently, depending on the inclination of the orbit, this effect can lead to strong deviations from the terminator plane.

In summary, this analysis underscores that in the context of autonomous operations, orbit control is essential around an asteroid like Eros, not only at low altitudes where stable motion is unattainable, but also at higher altitudes where uncertainties and environmental errors can affect long-term stability.

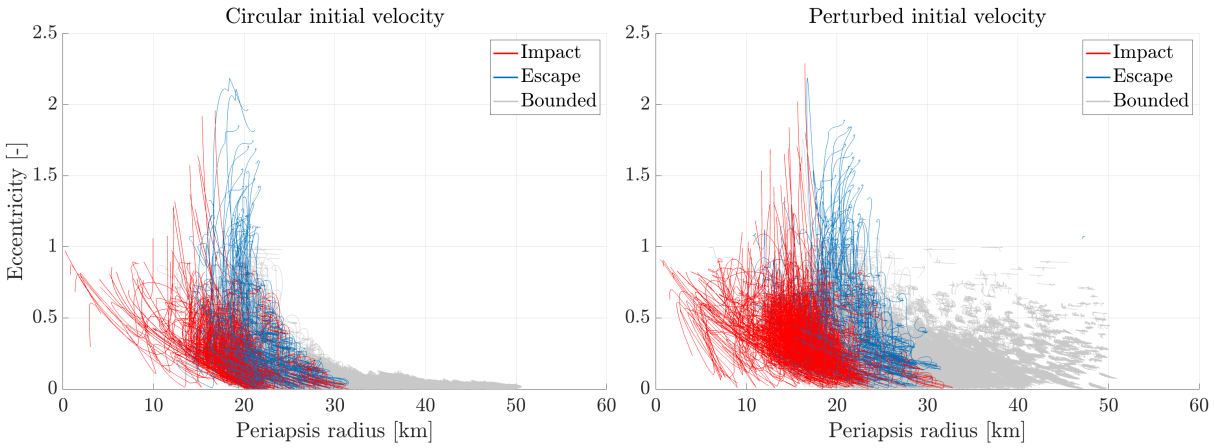

Figure 7.5: Periapsis radius-eccentricity plots for uncontrolled orbits.

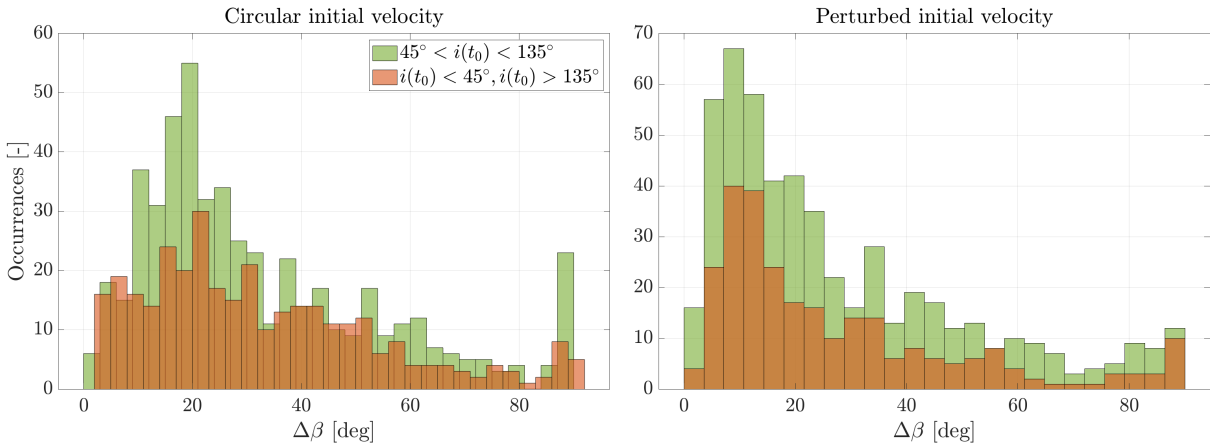

Figure 7.6: Distribution of the variation in solar phase angle for different initial inclinations.

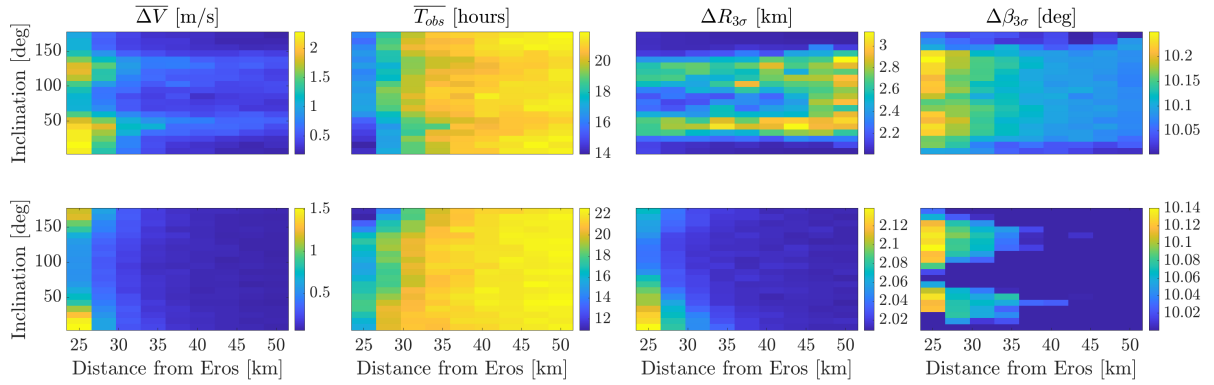

Figure 7.7: Performance comparison between baseline (above) and refined (below) orbit control system.

Furthermore, it is proven that despite the orbit's inclination is a relatively stable parameter, cross-track control is essential if one wants to maintain the spacecraft close to the terminator plane. This reinforces the approach taken to design the orbit control system, in opposition to other approaches found in the literature (e.g., Sanchez et al. (2022)) which focus exclusively on in-track control.

7.3.2 Comparison between baseline and refined parameters

To evaluate the orbit control system's performance under both the baseline parameters and those refined in the previous section, the space around the asteroid was discretized into a 9x20 grid, defined by radius and inclination, with the analysis restricted to circular orbits only. The results, shown in Fig. 7.7, showcase that the updated parameters have significantly improved system performance. Specifically, three main observations arise:

1. The station-keeping cost has been substantially reduced across the entire space, in some areas by as much as 50%. Additionally, it can be noticed that with the baseline parameters the control algorithm was particularly struggling for orbits with inclinations between 40°– 60° and 120°– 140°, where node drift is particularly pronounced and complicates orbit maintenance on the terminator plane. As a consequence, $\Delta R_{3\sigma}$ exceeded the activation threshold (2 km) by more than 1 km within this range of latitudes.
2. The 3σ confidence interval with respect to ΔR_{max} now remains below 200 meters, at most, from the value of r^{on}. This occurs for low-inclination orbits at 25 km, whereas for higher orbits the value reduces to the order of the meters. Additionally, the distribution of $\Delta\beta_{3\sigma}$ proves that the solar phase angle is successfully maintained within the desired value of 10 degrees for all orbits.

3. Improvements in coasting time are evident only for semi-major axes above 35 km, where up to 90% of the total simulation time sees the spacecraft idle. However, for low-altitude retrograde orbits near the equatorial plane, the coasting time drops to 50%, indicating sub-optimal algorithm parameters in these cases — a matter to be explored further in the following sections.

A more in-depth analysis of the orbit control performance can be done by observing Fig. 7.8, where also the variance and the S/N ratio have been reported. Overall, results closely match theoretical expectations, since the orbits which are more expensive to maintain are those at low altitudes, and with prograde motion. In particular, the inclination affects the station-keeping cost only below 35 km, whereas for higher altitudes its effect on the stability, thus on the orbit-keeping cost, is negligible. These considerations are important for two reasons: firstly, they prove that the conclusions inferred from the semi-analytical astrodynamics models presented in Sec. 3.4.3 are still valid when considering actively controlled motion in the presence of uncertainties; secondly, they confirm that the designed orbit control algorithm is not overly aggressive, despite having being tuned for a highly perturbed scenario.

Another important observation is the absence of a proportional relationship between station-keeping cost and coasting time. For instance, orbits at a radius of 25 km exhibit a maximum station-keeping cost at minimum inclination but achieve the lowest coasting time at maximum inclination. This happens because both metrics are influenced by a combination of the frequency and magnitude of maneuvers (the spacecraft can command burns independently on three axes, and with two available values). As a

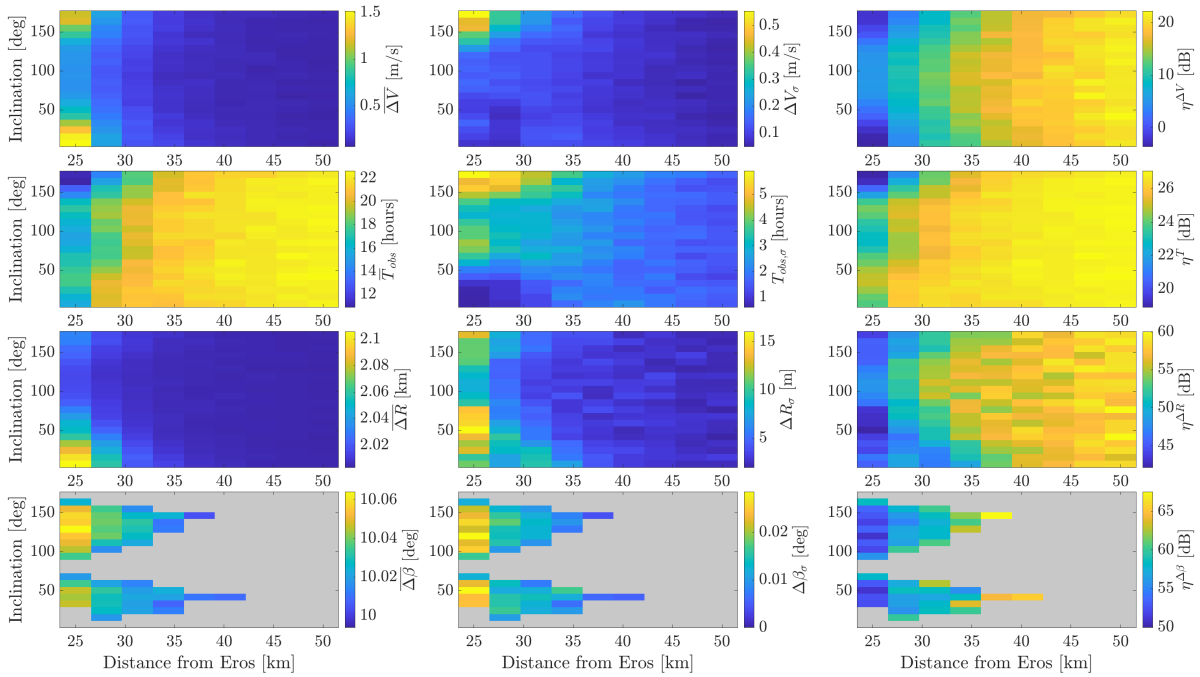

Figure 7.8: Performance parameters over the explored mission design space for the refined control system. In gray, the simulations that did not deviate from the terminator plane by more than 10°.

Table 7.9: Performance comparison for orbits A, B, and C between baseline and refined control system.

Orbit	Parameters	$\overline{\Delta V}$ [m/s]	ΔV_σ [m/s]	$\overline{T}_{obs}$ [hours]	$T_{obs,\sigma}$ [hours]	$\Delta R_{3\sigma}$ [km]	$\Delta\beta_{3\sigma}$ [deg]
A	Baseline	9.5	1.5	109.2	8.4	2.4	10.2
	Refined	3.6	0.5	114.4	17.9	2.1	10.1
B	Baseline	11.7	0.7	93.1	3.7	1.3	10.3
	Refined	5.4	0.3	105.4	3.2	0.8	7.7
C	Baseline	11.2	1.9	122.1	7.1	3.1	10.1
	Refined	1.5	0.4	143.8	8.8	2.0	10.2

result, prograde equatorial orbits generally demand more frequent activation of the spacecraft's thrusters, whereas retrograde equatorial orbits require smaller but more frequent maneuvers. Interestingly, this latter class of orbits emerges as the only one where the orbit control system appears to perform in a sub-optimal way. In theory, these orbits should be the cheapest to control; yet, Fig. 7.8 highlights that the station-keeping cost does not monotonically decrease with the inclination for R=25 km. Instead, it reaches a minimum at an inclination of 130°, only to increase again at higher inclinations. In parallel, a peculiar feature is observed in the ΔV variance, which shows a pronounced increase in the dispersion of the orbit maintenance cost. These phenomena will be addressed in the next section.

Finally, one-week Monte Carlo simulations were run again for orbits A, B, and C to compare the results in the long term with those obtained at the end of Chapter 6. As visible in Table 7.9, the changes adopted have improved significantly all the performance metrics for all three orbits.

7.3.3 Effects of inclination on low-altitude orbits

To investigate the results obtained for low-altitude retrograde orbits, it is useful to first analyze how the trajectories with radius of 25 km evolve differently depending on the target inclination. As Fig. 7.9 highlights, the behavior of the controlled trajectories varies quite significantly as the target orbit changes from prograde to retrograde. For direct orbits, gravitational perturbations intermittently push the spacecraft toward and away from the asteroid. As a result, the spacecraft oscillates between the upper and

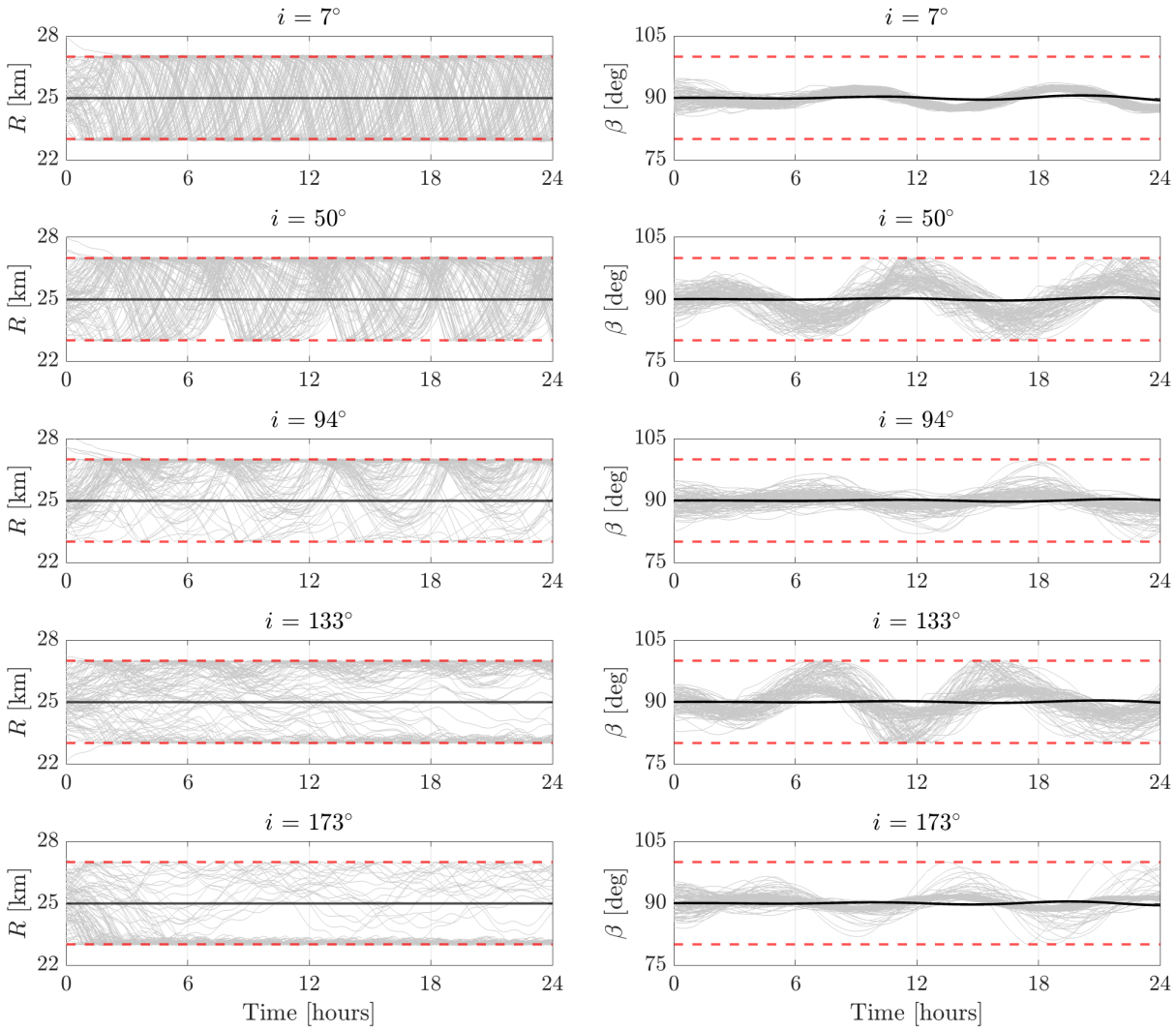

Figure 7.9: Monte Carlo results for circular, Sun-terminator orbits with 25 km radius and various inclinations.

lower bounds of the allowed deviation from the target radius, with no control impulses executed during the transitions between these bounds. In parallel, it can be observed that active control of the orbital plane is required only when far from the asteroid equator, thus confirming the previous open-loop results shown in Sec. 7.3.1, where it had been highlighted that these orbits tend to undergo larger variations in the solar phase angle.

As discussed in Sec. 3.4.3, orbital instabilities generally decrease with increasing inclination of the target orbit. This can lead to a situation where, with sufficiently loose tracking requirements, trajectories tend to stay closer to the reference orbit naturally, thus reducing the need for control actions. However, this stability effect seems to hold only within a certain range of inclinations. Specifically, for an orbit with an inclination of 173°, a significant portion of the trajectories are consistently drawn toward lower altitudes. Because the hysteresis parameter r^{off} has been set equal to r^{on}, the orbit control simply maintains the trajectory within the desired bounds, but does not actively take back the vehicle to the reference orbit. Due to gravity perturbations, this behavior is effective for prograde orbits but loses efficacy in retrograde motion. In this latter case, the frequency of correction maneuvers rises substantially, resulting in a ΔV expenditure that surpasses that of orbits with lower inclinations, and an average observation time that is the lowest across the entire mission design space, as shown in Fig. 7.8.

It is important to emphasize that these results do not contradict the fact that retrograde motion generally provides greater stability than prograde one. As highlighted by Fig. 7.10, retrograde orbits are less prone to escape/impact than prograde orbits. However, this graph also shows that among retrograde orbits, equatorial ones are the most unstable. In fact, an orbit with an inclination close to 180° is more exposed to perturbations from Eros's poles than orbits further away from the equatorial plane. Therefore, two main conclusions can be drawn:

- There is an explicit correlation between the orbits that are more prone to escape/impact and those that require more control effort to be maintained.
- For the given values of r^{off} and r^{on}, equatorial orbits are generally less advantageous than retrograde orbits that are further away from the equatorial plane.

Still, Table 7.10 shows that it is possible to improve the results for these orbits by adjusting the hysteresis parameter r^{off} to lower values. In this way, the orbital trajectories are brought back towards the reference orbit, which not only extends the coasting time but also reduces the overall maintenance cost.

Table 7.10: Monte Carlo results for an equatorial, retrograde 25-km orbit for different values of r^{off}.

r^{off} [km]	$\overline{\Delta V}$ [m/s]	ΔV_σ [m/s]	$\overline{T}_{obs}$ [hours]	$T_{obs,\sigma}$ [hours]
1.9	1.14	0.54	10.65	6.30
1.0	0.79	0.50	12.23	7.39
0.1	1.03	0.37	14.53	3.44

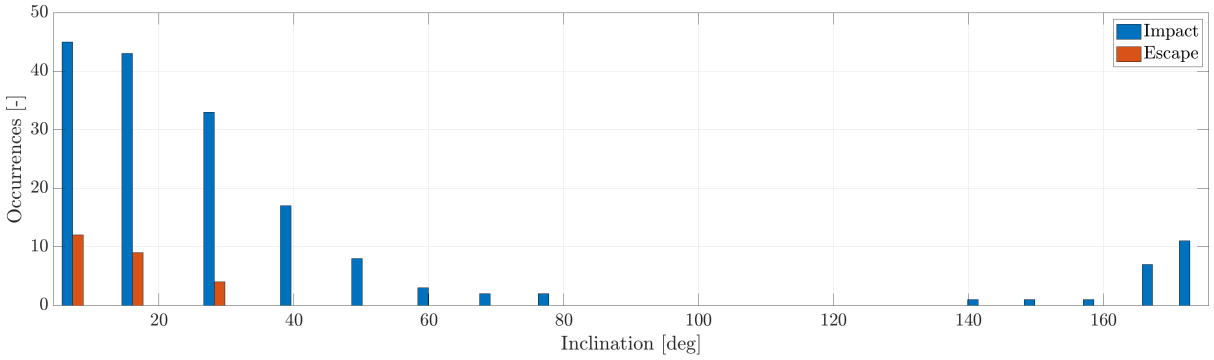

Figure 7.10: Escape and impact rate for uncontrolled 25 km circular orbits with varying inclinations.

Figure 7.11 compares prograde and retrograde equatorial orbits using two Monte Carlo samples for $i = 7°$ and $i = 173°$. In both cases, control impulses occur at regular intervals, driven by Eros's rotation rate: for a 25 km orbit, the orbital period is approximately twice that of the asteroid's rotation. As a result, a spacecraft in prograde motion on the equator passes over one of Eros's poles about once every 2.5 hours. In contrast, in a retrograde equatorial orbit the vehicle encounters Eros's poles twice as frequently per orbit, effectively doubling the number of correction maneuvers required.

The considerations made until now on retrograde equatorial orbits hold for the considered activation threshold r^{on} of 2 km. If this value is progressively reduced, these orbits may eventually become the cheapest to maintain while guaranteeing the maximum coasting time, as displayed in Fig. 7.12. In fact, such a small threshold makes it challenging to satisfy the constraint on the distance and that on the solar phase angle simultaneously. As a consequence, the orbits with intermediate inclinations not only lose their previous attractiveness but also become the most expensive to maintain.

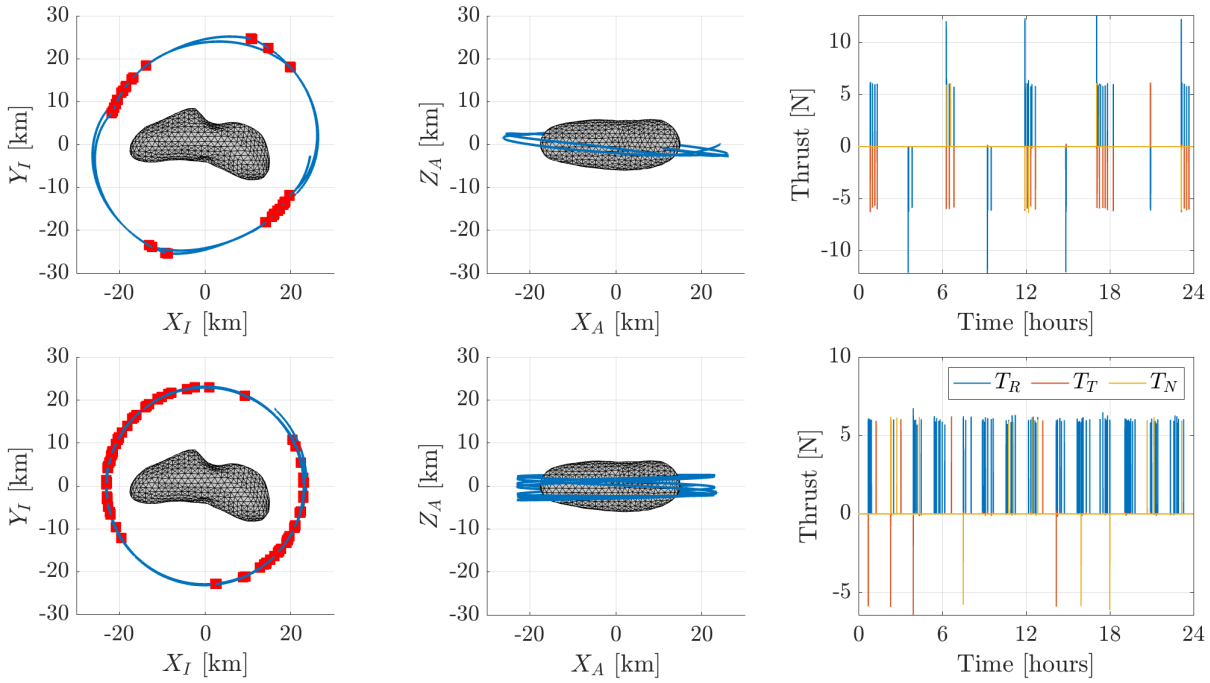

Figure 7.11: Comparison of two controlled nearly-equatorial orbits: prograde (top row) and retrograde (bottom row). From left to right: (1) polar view of the orbit in the inertial frame, with maneuver locations marked in red; (2) equatorial view of the orbit in the body-fixed frame; (3) control history.

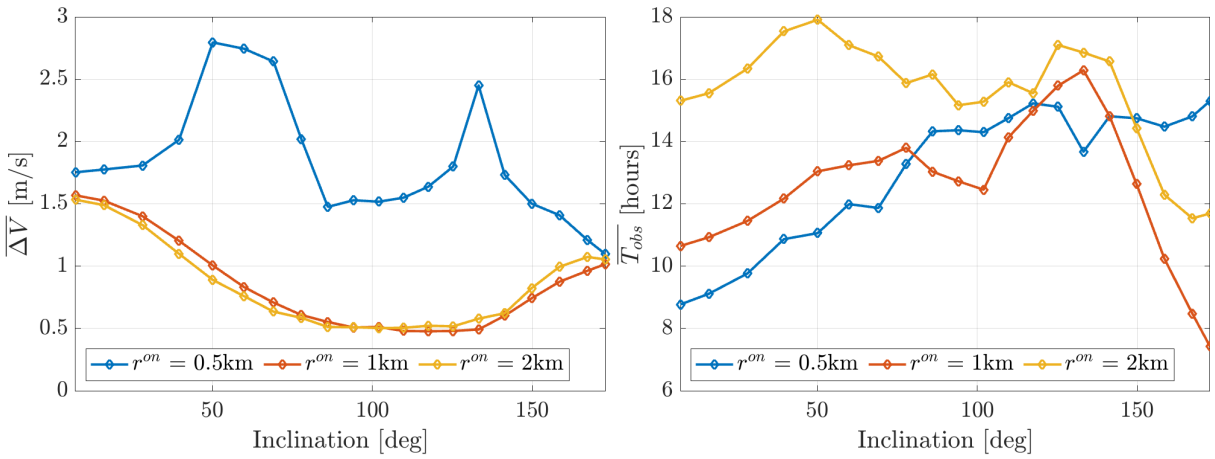

Figure 7.12: Average station-keeping cost and coasting time for different tracking requirements.

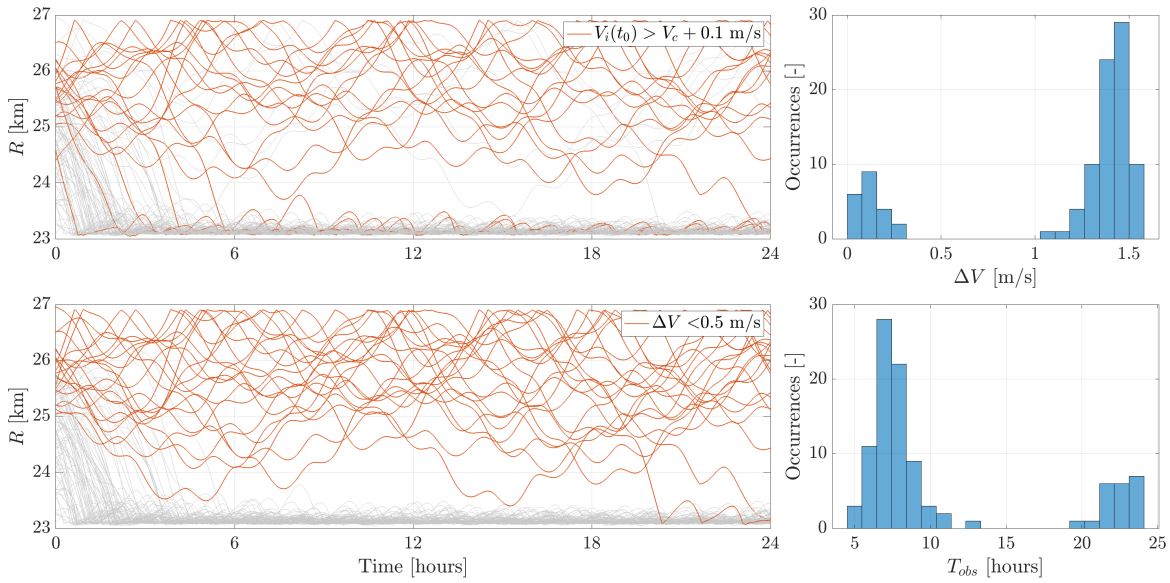

Figure 7.13: Monte Carlo results for retrograde, equatorial orbits with radius of 25 km.

A final relevant observation arises from the observation of Fig. 7.13. A significant, though smaller fraction of trajectories does not follow the main behavior and remains stable by requiring little to no corrections. While this explains the large variance observed in the previous section for low-altitude retrograde orbits, it is relevant to further investigate its causes. It was found that there is a clear correspondence between the trajectories propagated with an initial velocity that is larger than the corresponding circular velocity V_c, and those that require a smaller maintenance cost. In other words, when the randomly generated initial velocity error is such that the injection velocity is sufficiently larger than the local circular velocity, the orbit can be controlled at almost zero cost. This results in two distinct groups of orbits: one with high control cost and limited available observation time, and another with the opposite characteristics. Thus, one could argue that a viable strategy would be to command tangential burns that increase the spacecraft's velocity above the local circular speed, attempting to replicate the trajectories shown in Fig. 7.13. However, this is clearly not a robust approach and should not be implemented without a thorough understanding of the asteroid environment and extensive ground-based simulations.

7.3.4 Effects of eccentricity

As a final study of the mission design space, the effects of the eccentricity were investigated. In this case, a full factorial design was run according to the levels shown in Table 7.11. The ANOVA results from the full factorial design provide insight into the relative contributions of orbital parameters and their interactions on the orbit control cost and available observation time.

As illustrated in Fig. 7.14, the ΔV is primarily influenced by the periapsis radius, accounting for over 60% of the response. Eccentricity proves more influential than inclination, while interactions among parameters have minimal effect overall. In contrast, the coasting time is affected more by interactions, with R_p remaining the dominant factor but contributing less than before, eccentricity maintaining its influence, and inclination playing an increasingly substantial role.

Table 7.11: Design space explored for the periapsis radius, inclination, and eccentricity of the target orbit.

Factor	Range	Number of levels
R_p [km]	25-35	3
i [deg]	0-180	20
e [-]	0-0.3	4

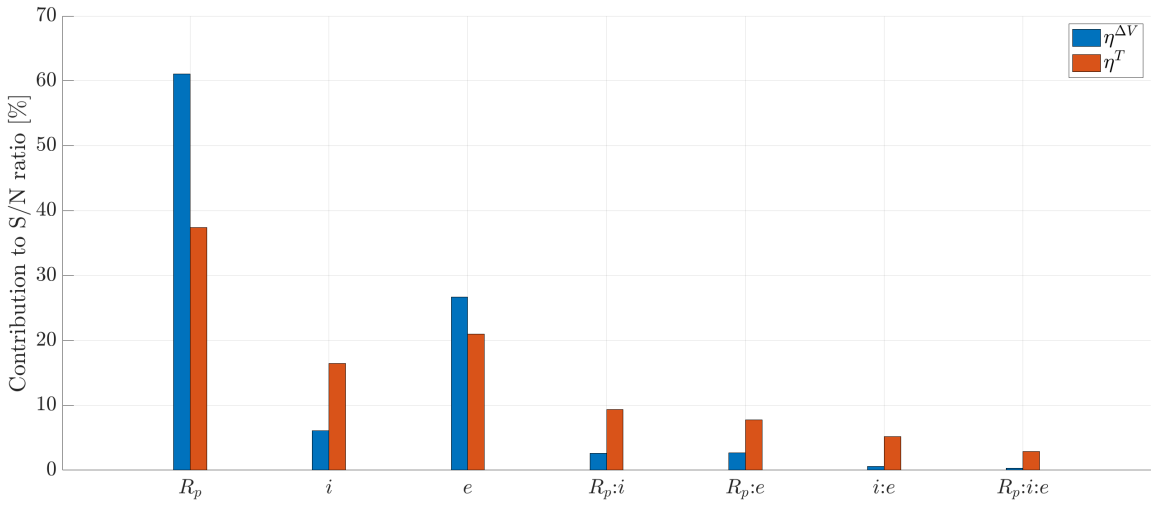

Figure 7.14: Contributions of the periapsis radius, inclination, and eccentricity of the target orbit to the station-keeping cost and the coasting time.

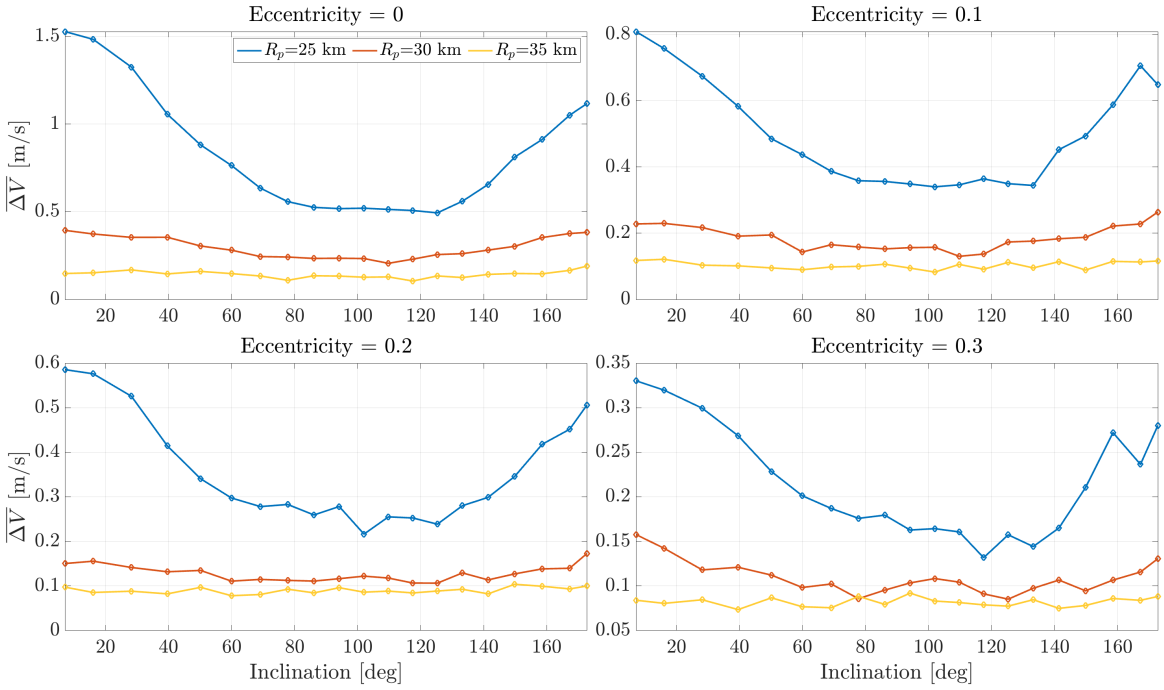

Figure 7.15: Mean ΔV as a function of the periapsis radius, inclination, and eccentricity of the target orbit.

To further examine these interactions, Figs. 7.15 and 7.16 display the mean values of ΔV and T_{obs} as functions of the three parameters. These graphs reveal two key points:

1. As anticipated by the ANOVA analysis, the interactions have little impact on the orbit control cost. Consequently, the previously noted behavior of retrograde orbits holds across different eccentricities, with ΔV curves displaying a nearly parabolic trend that reaches a minimum for orbits with an inclination of 100°-120°.

2. Eccentricity enhances significantly both performance metrics, reducing the station-keeping cost and increasing the coasting time. The former exhibits a 75% decrease compared to the circular case when the eccentricity of the orbit is fixed at 0.3. For T_{obs}, interactions complicate the ability to make broad generalizations. However, it appears that observation time typically peaks around inclinations of 45° and 135°.

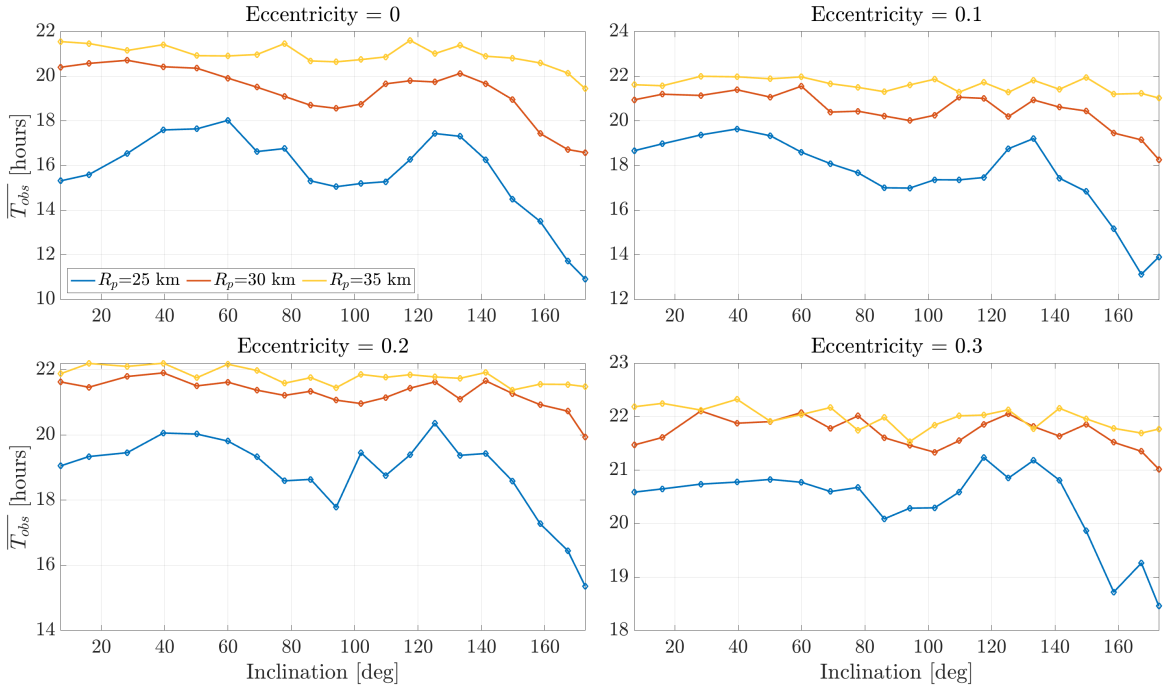

Figure 7.16: Mean observation time as a function of the periapsis radius, inclination, and eccentricity of the target orbit.

In conclusion, combining a low periapsis radius with a relatively high eccentricity can generate an orbit that allows the spacecraft to approach the asteroid closely, enhancing surface detail capture and enabling estimation of high-order gravity coefficients, all while minimizing station-keeping costs. However, additional analysis is needed to determine whether, for a given degree and order of gravity coefficients to be estimated, the total orbit control cost is more favorable on low-altitude circular orbits or elliptical orbits with a low periapsis altitude. In fact, when the eccentricity exceeds 0.1 (assuming R_p=25 km), the average value of T_{obs}, considering only intervals where the spacecraft altitude is below 35 km, decreases by more than 70%. This significantly reduces the available time windows for estimating high-order spherical harmonic coefficients.

7.4 Onboard environment modeling

The designed orbit control system has demonstrated its capability to safely maintain the spacecraft in orbit by relying solely on the asteroid's gravitational parameter. However, it is also valuable to assess how incorporating more complex environmental models onboard could impact the overall performance. This evaluation is especially relevant when paired with an analysis of how the measurement update frequency influences system robustness. The current value, 5 minutes, is relatively conservative compared to similar studies (e.g., Munuera Vilalta (2024)), yet in cases of potential onboard sensor failure or other constraints, maintaining this frequency might not always be feasible. For this reason, testing the system with longer update intervals is necessary.

7.4.1 Monte Carlo simulations

As discussed in Sec. 3.4.1, two additional gravity models beyond the point mass were identified for potential onboard implementation due to their balance of accuracy and computational efficiency. These are the triaxial ellipsoid gravity model and the spherical harmonics expansion, considering only C_{20} and C_{22}. The use of these models, however, requires estimating more parameters, namely the asteroid's semi-axes for the ellipsoid and the asteroid's oblateness and ellipticity for the SH expansion. Therefore, to ensure realistic results, simulations incorporate uniformly distributed errors on each parameter as

specified in Table 7.12. Before analyzing the results, it should be noted that the gravity model affects the guidance logic mainly through two channels. On one hand, the model is used to propagate the dynamics onboard between two measurement updates, which means that the estimated state of the spacecraft used to compute the control law depends on the accuracy of the implemented model. On the other hand, the model is also used within the guidance module to compute the equivalent control term of the control law ($\hat{\boldsymbol{f}}$).

Figure 7.17 shows the results obtained for orbit A by using different environment models and measurement update frequencies, for a value of r^{on}=2 km. Intuitively, the effect of the environment model on the tracking accuracy becomes more evident as Δt_{meas} increases. In fact, longer propagation times amplify the effects of nonlinear dynamics, causing simpler models to lose accuracy more rapidly. The results show that despite the presence of uncertainties in the two enhanced onboard models, the control system delivers a better tracking performance in every considered scenario than when using the point mass gravity model. The 3σ confidence value for ΔR_{max} achieved with these models is always lower than that of the point mass model, even at a minimum update interval of 5 minutes. At a 30-minute update interval, the differences between models become even more significant: with $\Delta R_{3\sigma}$ for the point mass model exceeds 300 meters from the activation threshold, while the other models maintain errors within 200 meters. Furthermore, it should also be highlighted that the triaxial ellipsoid consistently performs as well as the SH model, validating the use of this type of model for asteroids similar to Eros. This represents a valuable result because the three parameters required by this model can be easily estimated with a navigation camera, unlike SH coefficients which need a filtering process.

Table 7.12: Uncertainties considered for onboard environment models.

Parameter	1σ
C_{20} [-]	5%
C_{22} [-]	5%
a [m]	1000
b [m]	300
c [m]	300

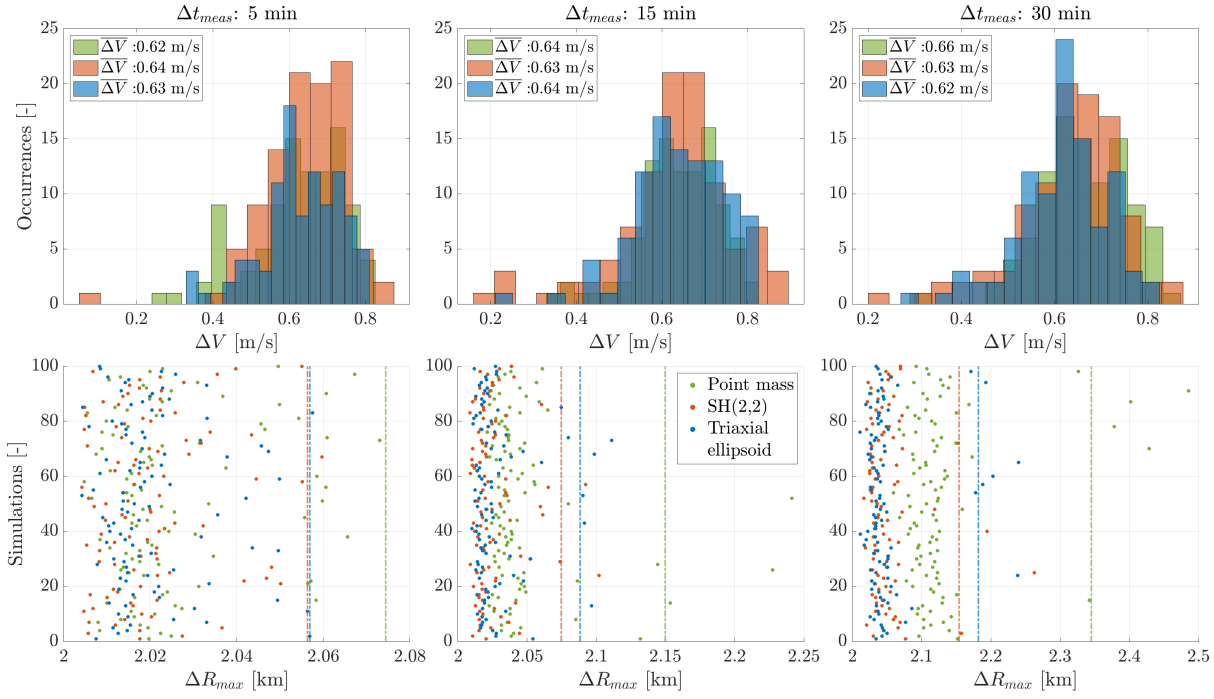

Figure 7.17: Monte Carlo results for station-keeping of orbit A using different onboard environment models. The dashed lines represent the 3σ confidence value for ΔR_{max}.

In parallel, the station-keeping cost varies by a negligible amount among the simulations performed. While this may sound inconclusive, one should consider that the spacecraft's propulsive capacity has been constrained severely to consider a realistic RCS. As a consequence, the limited availability of options for thrust values likely overshadows any potential benefit that may come from the use of a more accurate onboard model within the control law itself.

7.4.2 Knowledge Analysis

Three levels of knowledge can be identified during any simulation: the real dynamics, the estimated dynamics (in this case, simply propagated onboard), and the reference dynamics. A powerful method to assess how the system is affected by navigation errors and environment uncertainties is the so-called *Knowledge Analysis*, as proposed by Bottiglieri et al. (2023). A synthesis of this framework is illustrated in Fig. 7.18, which illustrates how the three levels of knowledge interact with each other. In particular, we

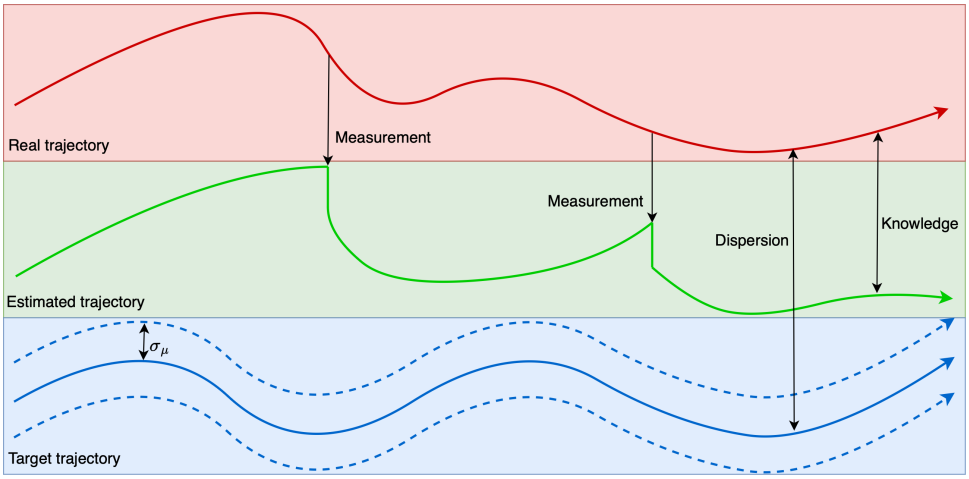

Figure 7.18: Knowledge levels during simulations.

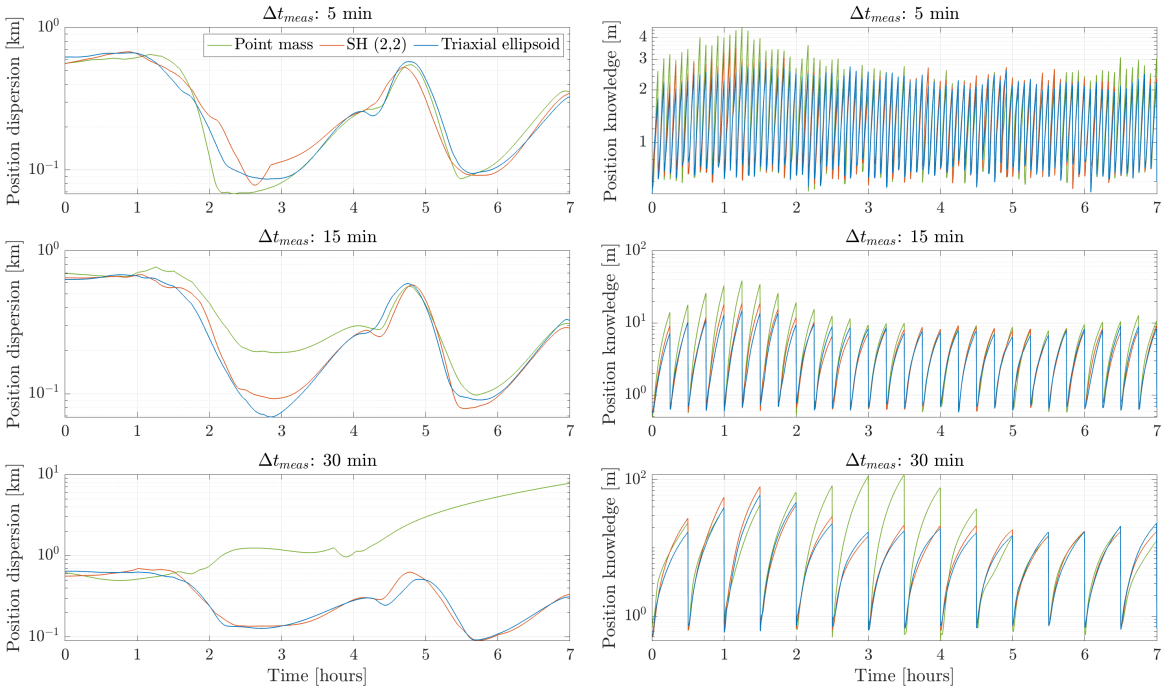

Figure 7.19: Standard deviation in position knowledge and dispersion for a 25 km, equatorial, prograde orbit considering different onboard environment models.

refer to the *distance* between the real trajectory and the target trajectory as *dispersion*, and to the distance between the real trajectory and the estimated one as *knowledge*. In this case, the distance is to be intended as a stochastic distance, which can be computed from Monte Carlo simulations. Since the current study uses Kepler orbits as reference trajectories, it has also been highlighted that any possible uncertainty in the value of the asteroid's gravitational parameter could affect the reference trajectory itself, thereby introducing a fourth level of knowledge. In this study, however, the asteroid's gravitational parameter has been assumed to be fully known (**BC1**), therefore this aspect can be discarded.

Knowledge Analysis can be applied to highlight how the onboard environment model affects the robustness of the system performance against navigation errors. Figure 7.19 illustrates the standard deviation in position dispersion and knowledge as a function of different measurement update intervals and onboard models. The results indicate that when Δt_{meas} is set at 5 minutes, position knowledge remains similar across all onboard models. Specifically, the triaxial ellipsoid and SH models may exhibit slightly less robustness compared to the point mass model due to uncertainties in the SH parameters and ellipsoid semi-axes. As a consequence, the dispersion of the trajectory with respect to the target orbit remains approximately the same for every model used. In contrast, when the duration of dead reckoning phases extends, the distinction between models becomes more evident. In these cases, the triaxial ellipsoid and SH models consistently demonstrate improved position knowledge compared to the point mass model.

It needs to be stressed that the results from Fig. 7.19 allow to evaluate the robustness of the system knowledge, not its accuracy. In other words, from the figure above one could only infer that the triaxial ellipsoid and SH models produce results that are more robust against uncertainties, thus leading to smaller standard deviations. However, one cannot actually say which model is more accurate. To do so, we turn to Figure 7.20, which displays the average position error relative to both the target trajectory and the estimated state. From this data, it becomes clear that using the triaxial ellipsoid and SH models improves both accuracy and robustness in tracking performance. Consequently, the spacecraft is able to respect more consistently the activation threshold of 2 km for deviations from the target orbit, demonstrating the enhancement that these models can bring to autonomous orbit control.

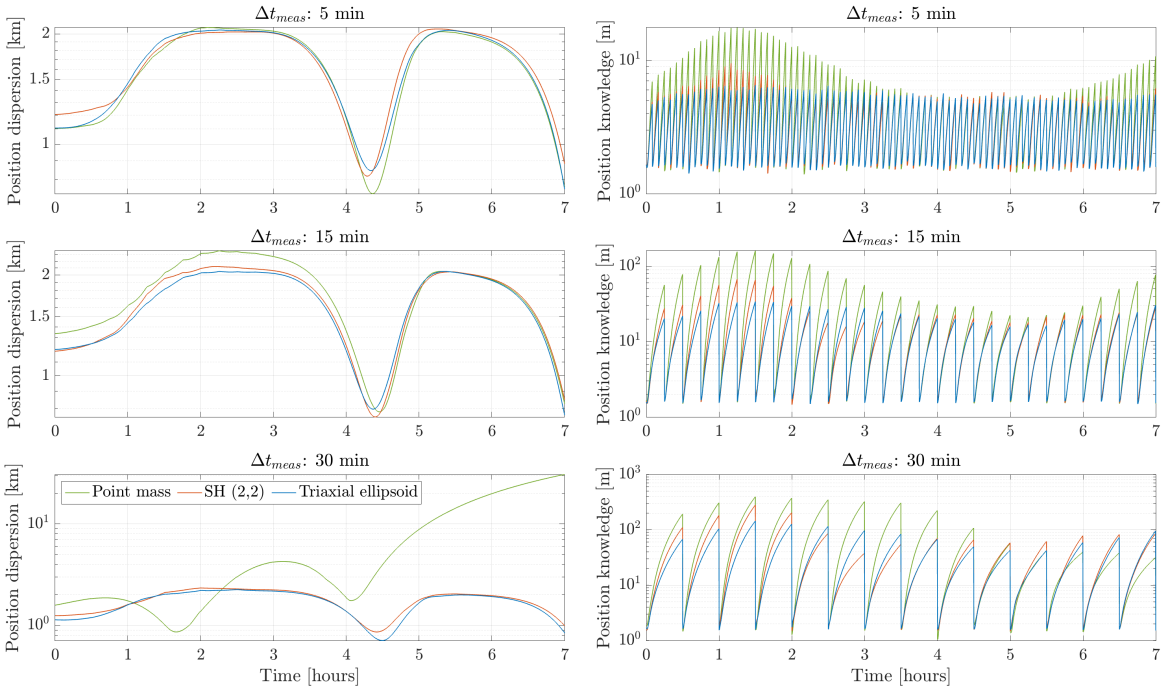

Figure 7.20: Mean position knowledge and dispersion for a 25 km, equatorial, prograde orbit considering different onboard environment models.

7.5 Applications to other asteroids

The small body itself represents a mission design parameter that can be taken into consideration when testing the robustness of the orbit control scheme. Now, this may be viewed as a rather extreme consideration, as very different bodies will generally require entirely different approaches due to their specific properties. For example, Itokawa is so small that the cost of orbiting it overcomes that of a hovering approach by too much to make the first option worth consideration. Nonetheless, assessing the capacity of the designed orbit control system to work effectively in different asteroid environments represents valuable proof in support of the quality of this work. For these reasons, this section investigates the application of the designed system to two new asteroids: (216) Kleopatra and (101955) Bennu.

Kleopatra is a large M-type asteroid with a remarkably irregular shape due to its dumbbell shape. Although it has never been explored by any spacecraft, orbiting it would likely present a significant challenge due to its irregular shape and a mass three orders of magnitude greater than that of Eros. This makes the intensity of the gravitational perturbations very strong, and would require the spacecraft to be equipped with more powerful engines than those which have been considered for this study. Conversely, Bennu represents the opposite case: it is relatively rounded and with a mass five orders of magnitude smaller than Eros. A summary of the main physical parameters of the two asteroids is given in Tables 7.21 and 7.22. Relevant data has been taken from the Small-Body Database[1] of the Jet Propulsion Laboratory (JPL). The gravity field of the two asteroids was modeled using a SH expansion of D/O 15 whose coefficients were calculated by applying the model developed by Root et al. (2016) to the constant-density polyhedra of the small bodies. The shape models used to generate the SH expansion were the preliminary version of Bennu by OSIRIS-REx [2] and the one described by Chanut et al. (2015) for Kleopatra.

Table 7.21: Parameters for Bennu.

Parameter	Value	Unit
μ	4.8904	m^3/s^2
ρ	1.194	g/cm^3
V	$6.17 \cdot 10^{-2}$	km^3
$a \times b \times c$	252x246x228	m
ω_A	2014.0	deg/day
T	4.29	hrs
W	135.82	deg
α	85.65	deg
δ	-60.17	deg

Table 7.22: Parameters for Kleopatra.

Parameter	Value	Unit
μ	$3.097 \cdot 10^8$	m^3/s^2
ρ	4.881	g/cm^3
V	$7.089 \cdot 10^5$	km^3
$a \times b \times c$	139.5x47x39	km
ω_A	1604.5	deg/day
T	5.39	hrs
W	0	deg
α	74	deg
δ	20	deg

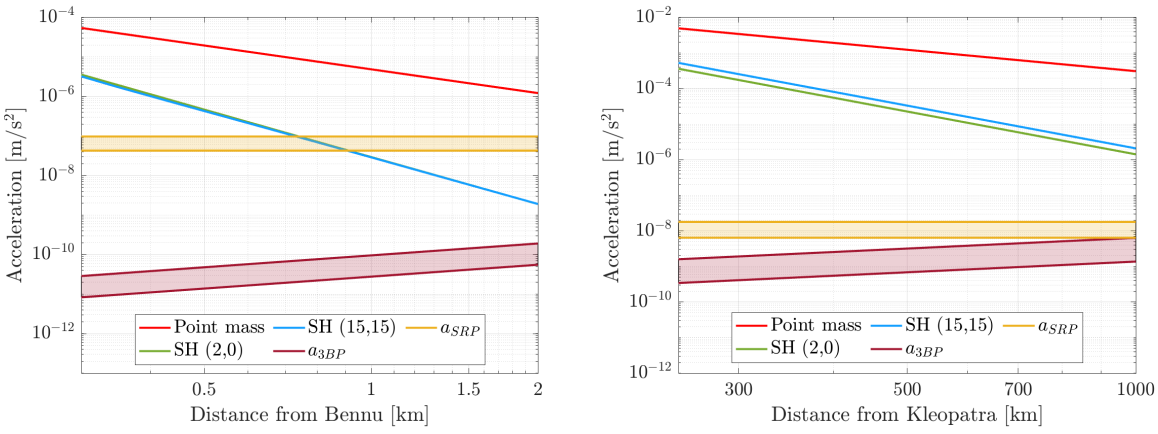

Figure 7.23: Dynamical environment at Bennu and Kleopatra.

[1] https://ssd.jpl.nasa.gov/tools/sbdb_lookup.html#/?sstr=bennu&view=VPD, accessed on 10/11/2024
[2] https://www.asteroidmission.org/updated-bennu-shape-model-3d-files/, accessed on 10/11/2024

Since there is no time to explore the full mission design space around the asteroid as it was done for Eros, Fig. 7.23 provides an overview of the main forces acting in the proximity environment of each asteroid as a function of the distance to the small body, thus helping to qualitatively understand which areas are of interest for orbital operations. As was the case for Eros, the interest for this research lies in those orbits lying particularly close to the body, such that the high-order SH coefficients could be estimated using a navigation filter. As a consequence, we consider for both asteroids a Sun-terminator, circular orbit, of radius 500 m and 300 km respectively, with specific parameters reported in Table 7.13. It should be noted that for Bennu the SRP is significantly more important than for Eros and Kleopatra, but at the altitude of interest the effect is still smaller than that due to the small body's oblateness alone.

Figure 7.24 shows the reference orbits propagated for one week, both in the open-loop and in the continuously controlled cases. For Bennu, the uncontrolled target orbit would remain bounded, but undergo a significant deviation from the terminator plane, while for Kleopatra it would escape the asteroid's system. Both orbits were successfully controlled without the need to tune any parameter by using the time-varying boundary layer sliding mode controller developed previously, proving that the intuition about using a conservative estimate for C_{20} and C_{22} remains beneficial even for other bodies than Eros and removes the need to tune control gains while providing an effective reference control law.

Table 7.13: Main parameters for the reference orbits at Bennu and Kleopatra.

Asteroid	a [km]	e [-]	i [deg]	Ω [deg]	ω [deg]	T [hours]	β [deg]	$t_p[T_{Ast}]$
Bennu	0.5	0	70.19	81.26	-	8.8	86-94	0.43
Kleopatra	300	0	90.5	258.18	-	12.4	89-91	0.13

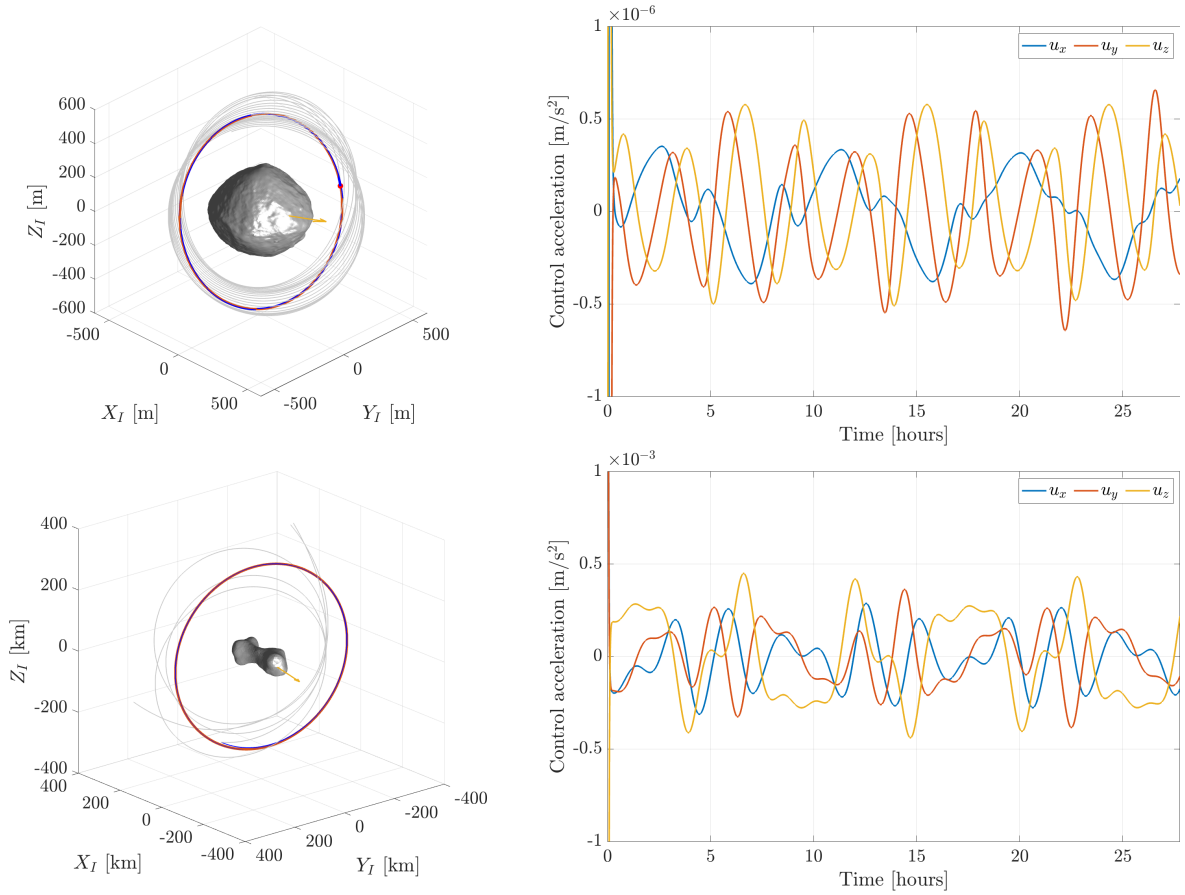

Figure 7.24: Reference orbits around Bennu and Kleopatra: the uncontrolled trajectory is shown in gray, the trajectory controlled with TVBL SMC in blue, and the reference orbit in orange.

Subsequently, uncertainties and operational constraints were introduced, and some environment and system values were adjusted according to the new scenario (as reported in Table 7.14). Also, the thrust provided by a single engine of the RCS was fixed at 6 N for the mission to Kleopatra, and at 0.5 N for the mission to Bennu, thus remaining within the operational range of monopropellant engines. All the remaining system and control parameters were left the same as for Eros, and 100 Monte Carlo simulations were run for each of the two orbits, with a propagation time of one week. The results, which are reported in Fig. 7.25, highlight an excellent performance of the designed system for both asteroids.

For Bennu, the 3σ confidence interval with respect to ΔR_{max} is below 10 meters from the activation threshold, highlighting that the slow dynamics of the small asteroid, combined with a weak gravitational field, allow the onboard system to maneuver the spacecraft with great accuracy. The average ΔV for one week is remarkably low, which is due to the small size of the asteroid, although there appears to be a significant variation in the obtained data. This is likely caused by the relatively large injection error considered for the initial position ($\sigma_{OI,r}$ is 20% of the target radius; for Eros and Kleopatra it is 4% and 3%, respectively). For Kleopatra, the 3σ dispersion of ΔR_{max} is naturally larger, but still within 250 meters from the activation threshold of 5 km. Considering the size of the orbit, this arguably represents a good performance. The station-keeping cost is very high, with 10 m/s on average for a week, thus highlighting the extreme challenge that this asteroid poses in terms of mission design. In both scenarios, more than 75% of the propagation time sees the spacecraft idle, thus allowing a considerable amount of time for a navigation filter to estimate the gravity field undisturbed.

Table 7.14: Uncertainties and control settings for Monte Carlo simulations around Bennu and Kleopatra.

	$\sigma_{OI,r}$ [m]	$\sigma_{OI,v}$ [m/s]	$\sigma_{N,r}$ [m]	$\sigma_{N,v}$ [m/s]	r^{on} [m]	r^{off} [m]	T^{on} [N]
Bennu	100	0.01	0.1	0.001	50	20	[0.05,1.05]
Kleopatra	10000	1	10	0.1	5000	5000	[1,13]

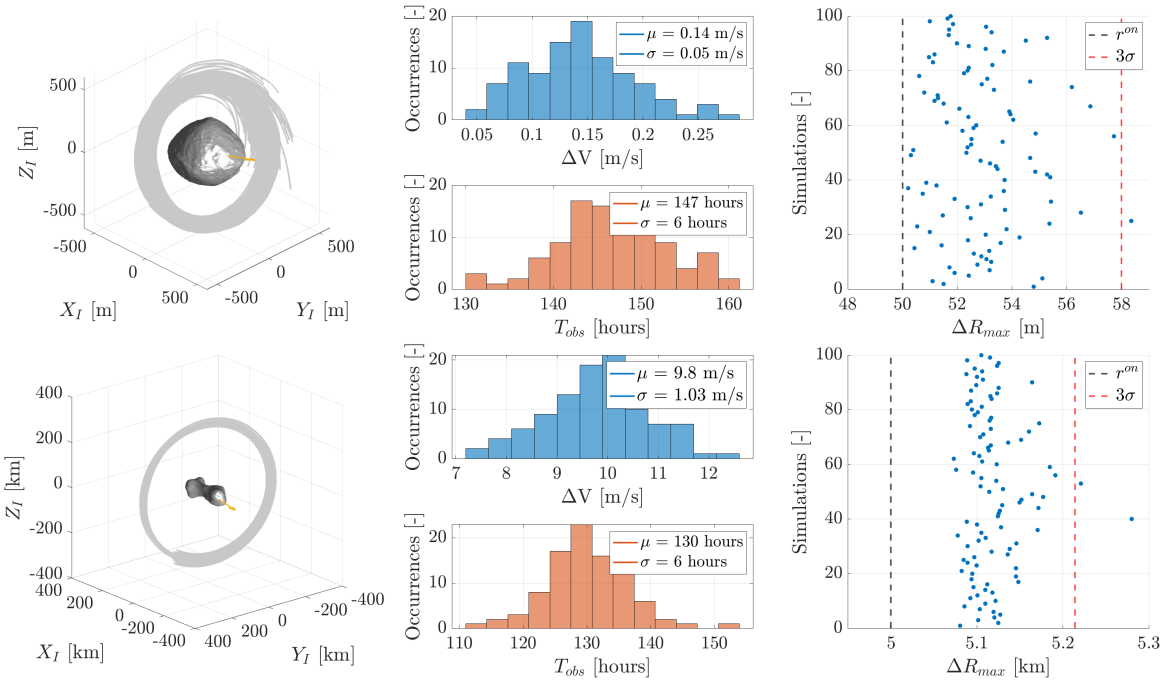

Figure 7.25: Results of the Monte Carlo simulations for the two orbits at Bennu and Kleopatra.

Table 7.15: Uncertainties (1σ) considered for onboard environment models at Bennu and Kleopatra.

Parameter	Bennu	Kleopatra
C_{20} [-]	5%	5%
C_{22} [-]	-	5%
a [m]	13	7000
b [m]	12	2500
c [m]	12	2000

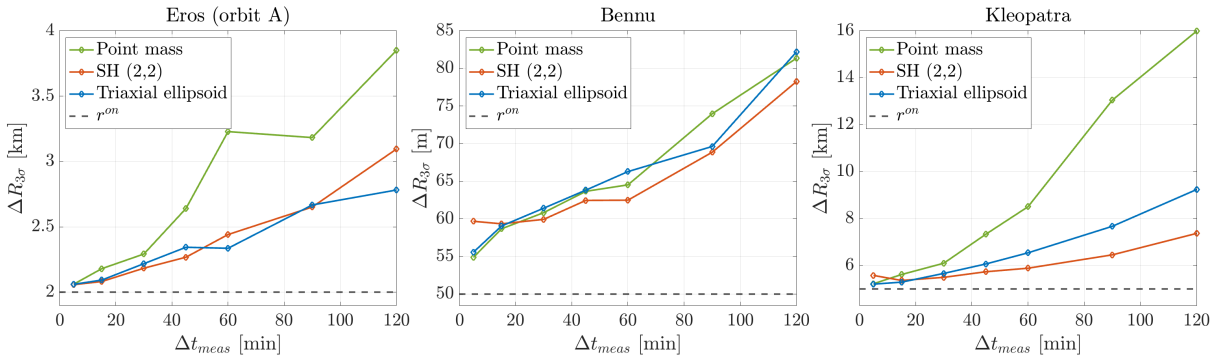

Figure 7.26: 3σ confidence value for ΔR_{max} as a function of the measurement update time, onboard model, and asteroid.

The study of onboard environment models was extended to Bennu and Kleopatra, incorporating the uncertainties listed in Table 7.15. Results from a one-day propagation time and 100 Monte Carlo samples confirm that the conclusions of the previous section hold when applied to other small bodies. Specifically, tracking accuracy shows little dependence on the onboard model for Bennu, likely due to its relatively rounded shape. Conversely, significant improvements are observed for Kleopatra when using the triaxial ellipsoid and SH models, greater even than for Eros, owing to Kleopatra's more irregular shape. Finally, it should be noted that even with the measurement update interval extended to two hours, no simulations resulted in an impact or escape from either asteroid.

7.6 Target point approach

The results presented until now have shown that a sliding mode controller with a boundary layer can be used as a reference to generate impulsive burns that successfully maintain the spacecraft within the desired region of space despite the presence of uncertainties and perturbations. However, it is acknowledged that this approach prioritizes robustness over optimality. Specifically, it relies on the intuition that the continuous control law will generally indicate the correct direction to execute a maneuver. Yet, since these commands are derived for continuous applications, they may be accurate only locally, and thus not achieve the desired effect in the moments after the maneuver.

On the contrary, the target point approach is explicitly designed to provide impulsive control maneuvers by propagating their linearized effect over time. However, this method is less robust than SMC because it relies on the linearization of the dynamics and requires numerous parameters to be tuned through trial and error. As it remains yet to be applied to the orbit control problem around an asteroid, it falls within the interest of this work to assess its performance and compare it to the designed system. Now, there are four main groups of parameters for the TPA:

- The number and spacing of future target times.
- The weighting matrices $\boldsymbol{Q}$, $\boldsymbol{R}$ and $\boldsymbol{T}$.
- The minimum time t_{min} required between consecutive maneuvers.
- The determination of some *optimal* time t_c for a station-keeping maneuver.

As anticipated in Chapter 4, the last parameter, t_c, was not included in the following analysis, as it remains a potential area for future development according to the authors of the method themselves. Also, the number of future target times was fixed a-priori at three. For the remaining parameters, trial runs quickly revealed that the spacing of downstream target times has a far greater impact on results than the weighting matrices. When target points are too widely spaced, linearization errors grow significantly, rendering maneuvers ineffective, regardless of the gain matrix values. Therefore, the approach adopted followed these steps:

- A set of initial input values for all parameters was found by trial and error to obtain successful control of the spacecraft along the target orbit, regardless of the total station-keeping cost. In particular, the spacing between the target points was selected to achieve reasonable values for ΔR_{max}.
- The initial set of parameters was adjusted to reduce the station-keeping cost while maintaining the position deviation from the target orbit within reasonable values. This allowed to define a baseline set of parameters.
- A small batch of 10 one-week Monte Carlo simulations was run with the baseline parameters, followed by adjustments to the weight matrices. These influence the performance index J: increasing $\boldsymbol{Q}$ emphasizes control effort minimization, while $\boldsymbol{R}$ prioritizes tracking accuracy.
- Once the results from the small Monte Carlo campaign proved to be sufficiently satisfactory, a larger batch of 100 simulations was processed to obtain more statistical confidence. If issues arose with the larger sample, adjustments would revert to step 3 for further refinement.

To provide a realistic comparison with the designed approach, the ΔV has not been modeled as impulsive; instead, the maximum available thrust is maintained until the desired change in velocity is achieved, resulting in burns that last from ten seconds to a few minutes.

Application of the TPA to the current problem appeared immediately very problematic due to the non-intuitive choice of the control parameters. The primary issue arises from the fact that at such low altitudes above Eros, Keplerian orbits quickly lose significance and effectively become uncontrolled trajectories. In contrast, the TPA was designed to maintain libration point orbits, whose mathematical model generally holds well. As a consequence, the outcome of a station-keeping simulation is highly sensitive to the choice of the control parameters, especially the targeting times, and several efforts are required before a given combination of gains allows to achieve an acceptable result.

To draw conclusions, we refer again to the nominal test scenarios introduced in Chapter 6. Table 7.16 reports the final values of the control gains which were obtained through the procedure illustrated before. In particular, it can be observed that because orbit C is at a higher altitude, and therefore less affected by the asteroid's gravitational perturbations, the algorithm's performance was improved by increasing the spacing of the target points. Orbit B has not been reported because it was not possible to find a combination of control parameters that would successfully avoid impact with the asteroid.

Table 7.16: Tuned parameters for the TPA.

Parameter	Orbit A	Orbit C
t_{min} [min]	5	5
t_1 [hours]	0.5	2.5
t_2 [hours]	1	5
t_3 [hours]	2	8
$\boldsymbol{Q}$	diag$\{10^6,10^6,10^6\}$	diag$\{10^8,10^8,10^8\}$
$\boldsymbol{R}_1$	diag$\{10^{-3},10^{-3},10^{-3}\}$	diag$\{10^{-4},10^{-4},10^{-4}\}$
$\boldsymbol{R}_2$	diag$\{10^{-3},10^{-3},10^{-3}\}$	diag$\{10^{-2},10^{-2},10^{-2}\}$
$\boldsymbol{R}_3$	diag$\{10^{-2},10^{-2},10^{-2}\}$	diag$\{10^{-3},10^{-3},10^{-3}\}$

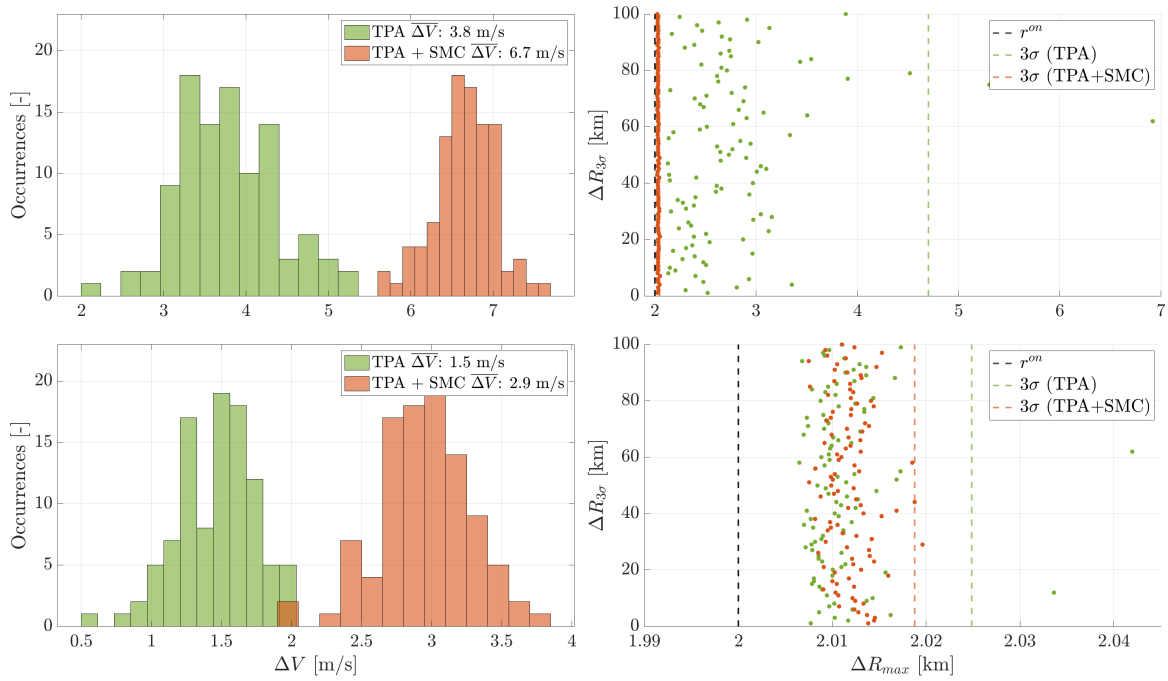

Figure 7.27: Results from Monte Carlo simulations using the TPA to control orbit A (above) and orbit C (below).

The results from the Monte Carlo simulations for both orbits are reported in Fig. 7.27. For orbit A, several simulations exceed r^{on} by more than one km, leading to a large 3σ confidence interval. As the inherent nature of the method lies in limiting the number of maneuvers, there is the absence of an explicit real-time feedback system that can correct the trajectory when one of the computed maneuvers has an undesired outcome. For this reason, a hybrid framework consisting of TPA and SMC combined has also been tested. In this case, the former method provides maneuvers that aim to have an effect in the long term, whereas the second method corrects local deviations from the desired control space. With this approach, results show that it is possible to achieve very good control in terms of tracking accuracy, but the average station-keeping cost nearly doubles. In contrast, the more stable nature of orbit C is such that the TPA alone is able to maintain almost all trajectories to within 30 meters from r^{on}.

Now, it is acknowledged that there might be additional combinations of gains through which the performance obtained with the TPA can surpass that achieved with SMC. However, the purpose of this section is to highlight that the effort required to achieve such performance makes this approach rather impractical and inefficient. Furthermore, it was found that if the gains obtained for orbit A or C were applied to an orbit with the corresponding altitude but different inclination, a significant fraction of the simulations would largely exceed the values of r^{on} and β^{on}, and a smaller group would even fail by crashing on the asteroid or leaving the system.

In conclusion, the relatively large number of parameters and the high sensitivity to them make this method not adequate for a scenario where the orbits to be controlled can vary greatly in shape and size. In parallel, the values obtained for the average station-keeping cost by using only the TPA are closely aligned with those shown in Table 7.9 for the designed orbit control system, thereby proving that the impulsive strategy established for this work is effective despite it relies on a continuous control law. These results are in contrast to those exposed by Howell and Gordon (1994) for liberation point orbits, as the authors mention that the TPA was developed following the disappointing performance obtained with a feedback controller operating in an on/off mode (although the specific controller type was not specified). Clearly, the different application contexts necessitate distinct approaches, as the dynamics and uncertainties that characterize libration point orbits and proximity operations around asteroids are fundamentally different.

8

Conclusions and recommendations

This chapter provides a concise overview of the key findings from this study together with possible directions for future research. Section 8.1 explicitly addresses the research questions that were established in Chapter 1, while also highlighting compliance of the designed system with the requirements outlined in Sec. 2.4.3. Subsequently, Sec. 8.2 contains a list of ideas for improvement and further investigation.

8.1 Conclusions

This research project has investigated the design of an autonomous orbit control system to maintain a spacecraft in orbit around an irregularly shaped asteroid. Sliding mode control was identified as the reference theoretical framework to produce a control law that is robust against the unmodeled perturbations coming from the gravity field of the small body. Subsequently, a quantization logic was developed to ensure that the spacecraft performs station-keeping maneuvers through a series of impulsive burns while remaining within a desired region of space around the nominal orbit. Robust Design principles were applied to improve the control system performance and study how it is affected by key factors, such as the target orbit parameters and the onboard environment model. Based on the results collected, the research sub-questions which were formulated at the beginning of the report can now be answered.

RSQ-1: ***What is a robust control scheme that can maintain a spacecraft close to a reference orbit through impulsive commands?***

The designed orbit control system leverages a sliding mode controller based on a linear sliding surface and a constant-rate reaching law. With minimal gain tuning, the continuous control law obtained by employing a fixed-width boundary layer allows tracking of any reference orbit despite the presence of gravitational perturbations. The results have shown that coupling this control law with a thrust quantization logic successfully accommodates the on-off operating mode of standard RCS thrusters (**OC-REQ-07**) while allowing for a considerable amount of time during which the spacecraft is coasting (**OC-REQ-08**). The system was tested for tracking requirements varying between 100 m to a maximum of 2 km from the target orbit, and 10° from the terminator plane.

Monte Carlo simulations showed that the station-keeping scheme is consistently able to maintain the spacecraft at the desired distance from the asteroid and close to the Sun-terminator plane, proving to be robust against unmodeled perturbations from the asteroid's gravity field (**OC-REQ-06)** and injection, navigation, and execution errors (**OC-REQ-03**, **OC-REQ-04**, **OC-REQ-05**). Additionally, the control system was successfully applied to two asteroids with markedly different characteristics from Eros, namely Bennu and Kleopatra, thus extending its applicability beyond the operational scenario where it was designed. Overall, the system displayed a high level of versatility, providing the designer with the flexibility to set tracking requirements without requiring further adjustments. This versatility was also

particularly evident in its successful application to orbit transfer scenarios, namely a planar transfer to lower the altitude and a plane change maneuver.

As the system developed in this study assumes an autonomous mission, it is designed to function without real-time environment characterization. In particular, the control scheme proved capable of maintaining the spacecraft within the desired region of space by relying exclusively on the knowledge of the asteroid's point mass gravity acceleration (**OC-REQ-09**). Nominal results showed that with an update on the spacecraft's state once every 5 minutes, station-keeping is successfully performed on orbits with varying semi-major axes between 25 and 50 km, reaching a minimum distance from Eros's surface of just 2 km, thus replicating the operations that were executed by NEAR with continuous ground support.

Compared to the target point approach, the designed system could achieve better tracking performance by requiring nearly identical station-keeping costs. In parallel, results highlighted the unsuitability of the TPA to the current problem due to the complexity of its tuning procedure, thus restricting its applicability to the original context for which it was developed (liberation point orbits).

How is the orbit control performance affected by the orbital parameters of the target orbit?
The available mission design space around asteroid Eros was explored through the combined use of full factorial design and ANOVA to quantitatively assess the impact that each orbital parameter has on the station-keeping problem. The main conclusions regarding this aspect are summarized in three points:

1. The orbital radius (or periapsis radius, when considering eccentric orbits) is by far the most influential parameter on all the figures of merit identified to assess the orbit control performance. As the orbit altitude is lowered, the unstable motion associated with gravitational perturbations from the asteroid requires increasingly higher station-keeping costs due to the difficulty of maintaining the spacecraft within the desired control volume.
2. Inclination has a significant impact on the performance of the station-keeping algorithm provided the orbit radius is below 30 km. In this case, the known instabilities associated with prograde orbits lead to a fast oscillating motion that requires many correction maneuvers. However, it was found that also retrograde equatorial orbits are particularly difficult to control, despite being generally recognized in the literature as those guaranteeing more stability. Due to the repeated encounters with Eros's poles, this class of orbits appears to be more expensive to maintain than retrograde orbits that are further away from the equator.
3. Increasing the eccentricity while maintaining a low periapsis radius enables access to very low altitudes with a reduction in control costs of up to 50% compared to circular orbits. However, the available coasting below 35 km decreases by up to 70% for eccentricities above 0.1, thus limiting the time windows during which it is possible to estimate high-order gravity terms.

Ultimately, the results demonstrated that with sufficiently loose tracking requirements (2 km), employing retrograde orbits with inclinations between 100° and 130° enables a significant reduction in achievable orbital radius while maintaining station-keeping costs at approximately 0.5 m/s per day and coasting times of up to 18 hours per day. These orbits provide a near-polar view of the asteroid, making them ideal observation platforms for gravity science. Additionally, they minimize encounters with Eros's poles and leverage the inherent stability of retrograde motion.

The results of this specific study should serve as preliminary considerations for future mission design of hypothetical autonomous missions around asteroids. To the author's knowledge, this represents the first analysis of its kind, as prior studies typically focused on a single orbit. Specifically, results have highlighted that many of the considerations that can be drawn from astrodynamics theory about the uncontrolled motion in the proximity of an asteroid remain applicable when considering a controlled system in the presence of uncertainties. For instance, a sharp increase in the station-keeping cost for Eros was observed below 35 km, which agrees with the open-loop analysis done in the literature that identifies this as the limit value below which orbits risk impacting and/or escaping the asteroid system.

RSQ-3: ***How can we generate a reference trajectory which improves the efficiency of the orbit control system?***
When considering a continuous control law, tracking the Keplerian motion of a virtual satellite along the target orbit works very well, and the system is able to follow this reference by employing a smooth, continuous control signal. However, when navigation errors and realistic operational constraints are considered, the chaser-target approach exhibits noticeable limits.

It was established that for orbits with semi-major axis lower than 35 km, gravitational perturbations not only cause the spacecraft to deviate from the target orbit but also affect significantly the speed of the vehicle around the asteroid, ultimately changing the orbital period. By commanding a specific position at a specific time, the chaser-target tracking mode thus requires more fuel to follow the virtual satellite. In contrast, line-of-sight tracking explicitly removes time parametrization from the target orbit because the reference is continuously updated according to the current estimated position of the spacecraft. Furthermore, it was found that the chaser-target approach not only increases the station-keeping cost but also decreases the tracking performance: for a 25 km circular polar orbit, some simulations exceeded the activation threshold on the distance from the target orbit by more than 3 km, against the 500 m obtained with line-of-sight. This happens because as the virtual point gets further away from the satellite, the commands for the spacecraft become increasingly inaccurate compared to the current position of the vehicle.

Using line-of-sight tracking has shown to overcome efficiently the limitations that affect the chaser-target approach for low-altitude orbits, enabling to reduce the station-keeping cost while increasing the tracking accuracy and the total coasting time. Specifically, for a polar, circular orbit with a 25 km orbital radius, employing the line-of-sight approach allowed to decrease the maintenance cost by 31% and the 3σ confidence interval in ΔR from 6.5 km to 2.7 km (for a given activation threshold of 2 km). For low-altitude flyovers, the improvements in performance reached 40% for the ΔV and a reduction of 2 km in ΔR_{max} for an activation threshold of 500 m.

Additionally, it is argued that line-of-sight tracking is easy to implement as it relies on simple geometrical considerations. In these terms, it is more advantageous than other approaches present in the literature where the reference trajectory is generated by integrating in time a set of equations of motion that try to include also the main perturbation terms. It is also stressed that line-of-sight tracking is robust not only to navigation errors but also against environmental uncertainties since the reference position is assigned independently from the gravitational parameter of the asteroid. As a final remark, it is noted that this guidance mode allows to employ the designed orbit control system also for performing orbit transfers, in addition to nominal station-keeping, thereby notably increasing its versatility.

RSQ-4: ***How do navigation errors and onboard environment modeling affect the performance of the orbit control system?***
The knowledge of the onboard computer about the spacecraft state is inaccurate due to navigation errors and modeling errors, which affect both the timing of correction maneuvers and their effectiveness. As a result, there is typically a delay between the moment in which the spacecraft escapes the region of space where it needs to be maintained and the moment in which the corrective maneuvers are initiated. Additionally, some of these maneuvers may also have undesired effects, thus requiring further corrections and leading to an increased station-keeping cost.

To address this, activation thresholds for the orbit control module need to be set with a conservative approach, such that any real constraint on the trajectory is not violated. Specifically, with a 5-minute measurement update, orbits around Eros showed a 3σ dispersion in maximum deviation from the target orbit that ranged from a few meters to 150 meters under a 2 km activation threshold. Extending the update interval to two hours increased this deviation to nearly 2 km. Instead, when employing the triaxial ellipsoid and the SH gravity models, tracking performance remained similar to the point mass model with frequent updates, but improved significantly with extended intervals: at a 2-hour interval, these models achieved around 30% lower $\Delta R_{3\sigma}$ than the point mass model. These results were further confirmed by

considering the orbit control problem around two additional asteroids: Bennu and Kleopatra. For the former, no significant variation in the results was observed as a function of the onboard environment module and measurement update frequency. In contrast, for Kleopatra, the results were even more pronounced than for Eros, with the two more accurate onboard models achieving a value for $\Delta R_{3\sigma}$ 55% and 45% better than the point mass gravity model given a measurement update time of 2 hours.

Using the Knowledge Analysis framework, it was found that adopting the triaxial ellipsoid and the SH expansion limited to C_{20} and C_{22} for onboard dynamics propagation is able to significantly enhance the robustness of the system against navigation errors and measurement update time. Even with a 5% uncertainty (1σ) considered in the asteroid's parameters, these models provided a noticeable improvement in the 3σ confidence level with respect to the maximum distance deviation from the target orbit. These gravity models are computationally light and adequate for onboard implementation, and they guarantee a higher tracking accuracy than the point mass model. This appears to be valid for highly irregular asteroids such as Eros and Kleopatra, while for more uniform bodies such as Bennu, results did not highlight any significant difference between the three models.

Ultimately, it is possible to provide an answer to the overall research question:

Research Question

How can autonomous orbit control guarantee safe station-keeping around an irregularly shaped asteroid in the presence of uncertainties and perturbations?

Autonomous orbit control can guarantee safe station-keeping around an irregularly shaped asteroid by integrating a robust reference control law, line-of-sight tracking, and efficient onboard modeling of the environment. Open-loop analysis has shown that uncertainties can transform otherwise stable regions of space into unstable ones, causing uncontrolled orbital trajectories to risk impact or escape. This makes active orbit control an essential capability for future autonomous asteroid missions. However, the effectiveness of orbit control depends heavily on the orbital parameters. Understanding the dynamics of the asteroid environment is therefore crucial for designing the nominal orbital plan, with altitude, inclination, and eccentricity needing careful selection to balance station-keeping costs and observation opportunities.

Notably, the ability to achieve and maintain low-altitude orbits using only the asteroid's mass highlights the potential for rapid asteroid characterization early in a mission. These low-altitude orbits could provide valuable data to refine the onboard environment models, improving the performance and efficiency of the whole GNC system during subsequent mission phases.

8.2 Recommendations for future work

Two main limitations affecting the designed control system have been identified. The first relates to the availability of coasting time, as its specific timeframe cannot be determined in advance. While this may not pose an issue for certain scientific experiments, such as gravity estimation, other activities may require prior planning and execution within a specific time window. To address this, a potential approach could involve designing the system to stabilize the spacecraft along the reference orbit before the planned science time window, such that more time is available before the spacecraft escapes the desired control volume.

The second limitation concerns the formulation of the control law based on Cartesian elements, which is the only possible approach when using conventional sliding mode control. However, computing correction maneuvers by relying on Gauss variational equations may offer greater efficiency, as the control law would be computed directly into the RTN frame, thus bypassing the current method of calculating it in the inertial frame and subsequently rotating it. Future research should explore the feasibility of formulating a sliding mode control framework based on orbital elements or modified equinoctial elements, which could enhance the precision and efficiency of the control strategy.

Following this, an additional improvement to this work could consider the possibility of decoupling cross-track control from in-track control. As emphasized in the conclusions, the results demonstrated that maintaining the orbit's shape and size demands considerably more effort than preserving its orientation. This indicates that employing distinct control strategies for these two types of motion could enhance overall efficiency and performance.

Additionally, the following areas are suggested for further research into the topic:

6-DOF simulations
An intuitive extension of this work would be that of integrating the onboard control system with attitude control. Although orbit control is not continuous, coupling between rotational and translational motion is particularly relevant during station-keeping correction maneuvers. As this work assumed an ideal spacecraft attitude, further research should aim to investigate how real attitude control impacts the performance of the designed system. Given that continuous control laws are suited to attitude control, the sliding mode controller with a time-varying boundary layer developed within this work could be directly applied to the problem.

Navigation
The simulator could be extended by including a full navigation architecture, comprising a sensor suite and a state estimator in place of the propagator. In fact, many of the considerations raised within this work were based on the heritage left from previous thesis focused on autonomous navigation. Future research should thus prioritize integrating the individually designed systems from these previous efforts, enabling a more realistic representation of a complete GNC system. This could open the way to *hardware-in-the-loop* simulations within the new GNC Robotics laboratory of the TU Delft Aerospace faculty.

Orbit control leveraging SH coefficients
Future research should try to develop specific control strategies that leverage the knowledge of the asteroid's gravity field. This study focused on designing an orbit control system that is robust enough to guarantee safe station-keeping while relying exclusively on the asteroid's point mass gravity model. Although this may represent an effective strategy during the initial phase of a mission, in the long term the spacecraft will have access to the low-order SH coefficients of the asteroid. As a consequence, conventional orbit control methods from Earth applications may become more competitive, and mean orbital elements could be exploited to effectively reduce station-keeping costs.

Machine learning
The method proposed by this study has proven to be effective and reliable. As such, it could be used as a baseline to assess the performance of more recent control methods exploiting neural networks and reinforcement learning.

High-order target point approach
Although the target point approach has proven to be not adequate for the requirements considered within this work, future research could aim at developing an improved version of this method. To achieve this, uncertainty propagation techniques, such as differential algebra, could be incorporated.

Bibliography

Alvarez, L. W., Alvarez, W., Asaro, F., and Michel, H. V. "Extraterrestrial Cause for the Cretaceous-Tertiary Extinction". *Science*, 208, No. 4448, 1095–1108, 6 1980. doi: 10.1126/science.208.4448.1095.

Antreasian, P., Helfrich, C., Miller, J., Owen, W., Williams, B., Yeomans, D., Giorgini, J., Dunham, D., Farquhar, R., and McAdams, J. "Preliminary considerations for NEAR's low-altitude passes and landing operations at 433 Eros". In: *AIAA/AAS Astrodynamics Specialist Conference and Exhibit*, Reston, Virigina, 8 1998. American Institute of Aeronautics and Astronautics. doi: 10.2514/6.1998-4397.

Archinal, B. A., Acton, C. H., A'Hearn, M. F., Conrad, A., Consolmagno, G. J., Duxbury, T., Hestroffer, D., Hilton, J. L., Kirk, R. L., Klioner, S. A., McCarthy, D., Meech, K., Oberst, J., Ping, J., Seidelmann, P. K., Tholen, D. J., Thomas, P. C., and Williams, I. P. "Report of the IAU Working Group on Cartographic Coordinates and Rotational Elements". *Celestial Mechanics and Dynamical Astronomy*, 130, No. 3, 22–46, 3 2018. doi: 10.1007/s10569-017-9805-5.

Balmino, G. "Gravitational potential harmonics from the shape of an homogeneous body". *Celestial Mechanics & Dynamical Astronomy*, 60, No. 3, 331–364, 11 1994. doi: 10.1007/BF00691901.

Barthelmes, F. "Definition of Functionals of the Geopotential and Their Calculation from Spherical Harmonic Models". Technical report, German Research Center for Geosciences, Postdam, 2009.

Berry, K., Antreasian, P., Moreau, M. C., May, A., and Sutter, B. "OSIRIS-REx Touch-And-Go (TAG) Navigation Performance". In: *38th Annual AAS Guidance and Control Conference*, 2015.

Beshore, E., Sutter, B., Mink, R., Lauretta, D., Moreau, M., Boynton, W., Dworkin, J., Everett, D., Shinohara, C., and Gal-Edd, J. "The OSIRIS-REx asteroid sample return mission". In: *2015 IEEE Aerospace Conference*, pp. 1–14. IEEE, 3 2015. doi: 10.1109/AERO.2015.7118989.

Bonaventure, F., Baudry, V., Sandre, T., and Gicquel, A.-H. "Autonomous orbit control for routine station-keeping on a leo mission". In: *International Symposium on Space Flight Dynamics*, Pasadena, California, 2005.

Bottiglieri, C., Piccolo, F., Giordano, C., Ferrari, F., and Topputo, F. "Applied Trajectory Design for CubeSat Close-Proximity Operations around Asteroids: The Milani Case". *Aerospace*, 10, No. 5, 464, 5 2023. doi: 10.3390/aerospace10050464.

Bottke, W. F., Vokrouhlický, D., Rubincam, D. P., and Nesvorný, D. "The Yarkovsky and Yorp effects: Implications for Asteroid Dynamics". *Annual Review of Earth and Planetary Sciences*, 34, No. 1, 157–191, 5 2006. doi: 10.1146/annurev.earth.34.031405.125154.

Bourgeaux, A. "Autonomous estimation of the gravity field for asteroid missions". MSc thesis, Delft University of Technology, 2020.

Broschart, S. B., Lantoine, G., and Grebow, D. J. "Quasi-terminator orbits near primitive bodies". *Celestial Mechanics and Dynamical Astronomy*, 120, No. 2, 195–215, 10 2014. doi: 10.1007/s10569-014-9574-3.

Calla, P., Fries, D., and Welch, C. "Asteroid mining with small spacecraft and its economic feasibility", 2019.

Canale, A. "Autonomous Spacecraft Guidance for Small-Body Proximity Missions". MSc thesis, Delft University of Technology, 2018.

Carlson, B. C. "Computing elliptic integrals by duplication". *Numerische Mathematik*, 33, No. 1, 1–16, 1979. doi: 10.1007/BF01396491.

Chanut, T. G. G., Aljbaae, S., and Carruba, V. "Mascon gravitation model using a shaped polyhedral source". *Monthly Notices of the Royal Astronomical Society*, 450, No. 4, 3742–3749, 7 2015. doi: 10.1093/mnras/stv845.

Cheng, A., Rivkin, A., Michel, P., Lisse, C., Walsh, K., Ragozzine, D., Chapman, C., Merline, W., and Benner, L. "Binary and Multiple Systems". Technical report, Johns Hopkins University Applied Physics Laboratory, 2009.

Cheng, M., Ries, J. C., and Tapley, B. "Assessment of the solar radiation model for grace orbit determination". *Advances in the Astronautical Sciences*, 129 501–510, 3 2008.

Cipriano, A. M., Dei Tos, D. A., and Topputo, F. "Orbit Design for LUMIO: The Lunar Meteoroid Impacts Observer". *Frontiers in Astronomy and Space Sciences*, 5, 9 2018. doi: 10.3389/fspas.2018.00029.

Cui, P. and Qiao, D. "The present status and prospects in the research of orbital dynamics and control near small celestial bodies". *Theoretical and Applied Mechanics Letters*, 4, No. 1, 013013, 2014. doi: 10.1063/2.1401313.

Dankowicz, H. "Some special orbits in the two-body problem with radiation pressure". *Celestial Mechanics & Dynamical Astronomy*, 58, No. 4, 353–370, 4 1994. doi: 10.1007/BF00692010.

De Florio, S. and D'Amico, S. "Optimal Autonomous Orbit Control of Remote Sensing Spacecraft". In: *19th AAS/AIAA Space Flight Mechanics Meeting*, Savannah, USA, 2009.

De Florio, S., D'amico, S., and Radice, G. "Precise Autonomous Orbit Control in Low Earth Orbit". In: *AIAA/AAS Astrodynamics Specialist Conference*, Reston, Virigina, 8 2012. American Institute of Aeronautics and Astronautics. doi: 10.2514/6.2012-4811.

Dechambre, D. and Scheeres, D. J. "Transformation of spherical harmonic coefficients to ellipsoidal harmonic coefficients". *Astronomy & Astrophysics*, 387, No. 3, 1114–1122, 6 2002. doi: 10.1051/0004-6361:20020466.

Dunham, D. W., Farquhar, R. W., McAdams, J. V., Holdridge, M., Nelson, R., Whittenburg, K., Antreasian, P., Chesley, S., Helfrich, C., Owen, W. M., Williams, B., Veverka, J., and Harch, A. "Implementation of the First Asteroid Landing". *Icarus*, 159, No. 2, 433–438, 10 2002a. doi: 10.1006/icar.2002.6911.

Dunham, D. W., Mcadams, J. V., and Farquhar, R. W. "NEAR mission design". *Johns Hopkins APL Technical Digest*, 23, No. 1, 18–33, 2002b.

Dwivedi, N. P. "Deterministic optimal maneuver strategy for multi-target missions". *Journal of Optimization Theory and Applications*, 17, No. 1-2, 133–153, 10 1975. doi: 10.1007/BF00933919.

D'Urso, M. G. "Analytical computation of gravity effects for polyhedral bodies". *Journal of Geodesy*, 88, No. 1, 13–29, 1 2014. doi: 10.1007/s00190-013-0664-x.

Elffers, P. "Autonomous Navigation for Binary Asteroid Landing A vision-based and altimeter-aided navigation filter for small spacecraft". MSc thesis, Delft University of Technology, 2023.

Everett, D., Mink, R., Linn, T., and Wood, J. "Designing to sample the unknown: Lessons from OSIRIS-REx project systems engineering". In: *2017 IEEE Aerospace Conference*, pp. 1–19. IEEE, 3 2017. doi: 10.1109/AERO.2017.7943586.

Feng, Z., Zheng, Y., and Xu, M. "Integrated strategy of stationkeeping, autonomous navigation, and real-time geodetical recovery of gravity fields: application into asteroid Lutetia mission". *Nonlinear Dynamics*, 106, No. 4, 3247–3263, 12 2021. doi: 10.1007/s11071-021-06694-8.

Fridman, L., Moreno, J. A., Bandyopadhyay, B., Kamal, S., and Chalanga, A. *Continuous Nested Algorithms : The Fifth Generation of Sliding Mode Controllers*, pp. 5–35. Springer International Publishing, Cham, 2015. doi: 10.1007/978-3-319-18290-2_2.

Fukushima, T. "Prolate spheroidal harmonic expansion of gravitational field". *The Astronomical Journal*, 147, No. 6, 152, 5 2014. doi: 10.1088/0004-6256/147/6/152.

Furfaro, R. "Hovering in Asteroid Dynamical Environments Using Higher-Order Sliding Control". *Journal of Guidance, Control, and Dynamics*, 38, No. 2, 263–279, 2 2015. doi: 10.2514/1.G000631.

Furfaro, R., Cersosimo, D., and Wibben, D. R. "Asteroid Precision Landing via Multiple Sliding Surfaces Guidance Techniques". *Journal of Guidance, Control, and Dynamics*, 36, No. 4, 1075–1092, 7 2013a. doi: 10.2514/1.58246.

Furfaro, R., Gaudet, B., Wibben, D. R., Kidd, J., and Simo, J. "Development of Non-Linear Guidance Algorithms for Asteroids Close-Proximity Operations". In: *AIAA Guidance, Navigation, and Control (GNC) Conference*, Reston, Virginia, 8 2013b. American Institute of Aeronautics and Astronautics. doi: 10.2514/6.2013-4711.

Gambhire, S. J., Kishore, D. R., Londhe, P. S., and Pawar, S. N. "Review of sliding mode based control techniques for control system applications". *International Journal of Dynamics and Control*, 9, No. 1, 363–378, 3 2021. doi: 10.1007/s40435-020-00638-7.

Garulli, A., Giannitrapani, A., Leomanni, M., and Scortecci, F. "Autonomous Low-Earth-Orbit Station-Keeping with Electric Propulsion". *Journal of Guidance, Control, and Dynamics*, 34, No. 6, 1683–1693, 11 2011. doi: 10.2514/1.52985.

Godard, B., Budnik, F., Muñoz, P. M., Morley, T., and Janarthanan, V. "Orbit determination of Rosetta around comet 67P/Churyumov-Gerasimenko". In: *25th International Symposium on Space Flight Dynamics*, 2015.

Gomez, G., Howell, K., Simò, C., and Masdemont, J. J. "Station-keeping strategies for translunar libration point orbits". In: *AAS/AIAA Spaceflight Mechanics Conference*, 1998.

Guelman, M. "Closed-Loop Control of Close Orbits Around Asteroids". *Journal of Guidance, Control, and Dynamics*, 38, No. 5, 854–860, 5 2015. doi: 10.2514/1.G000158.

Guelman, M. "Closed-loop control for global coverage and equatorial hovering about an asteroid". *Acta Astronautica*, 137 353–361, 8 2017. doi: 10.1016/j.actaastro.2017.04.035.

Habets, J. "Evolving Systems Approach to the Attitude Control of a Large-Space-Debris Removal Spacecraft". MSc thesis, Delft University of Technology, 2015.

Hall, C. D. and Ross, I. M. "Dynamics and Control Problems in the Deflection of Near-Earth Objects". In: *AAS/AIAA Astrodynamics Specialist Conference*, 1997.

Han, D., Smith, J., Kennedy, B., Mastrodemos, N., and Whiffen, G. "Dawn Navigation and Mission Design at Dwarf Planet Ceres". In: *Space Operations: Contributions from the Global Community*, pp. 517–541. Springer International Publishing, Cham, 2017. doi: 10.1007/978-3-319-51941-823.

Hawkins, M., Guo, Y., and Wie, B. "ZEM/ZEV Feedback Guidance Application to Fuel-Efficient Orbital Maneuvers Around an Irregular-Shaped Asteroid". In: *AIAA Guidance, Navigation, and Control Conference*, Reston, Virigina, 8 2012. American Institute of Aeronautics and Astronautics. doi: 10.2514/6.2012-5045.

Hazra, S. "Autonomous Guidance for Asteroid Descent using Successive Convex Optimisation". MSc thesis, Delft University of Technology, 2019.

Hesar, S., Mcmahon, J. W., and Takahashi, Y. "Surface proximity gravitational field analysis of the asteroid 433 Eros". *Advances in the Astronautical Sciences*, 157 643–654, 2016.

Holdridge, M. E. "NEAR Shoemaker Spacecraft Mission Operations". *Johns Hopkins APL Technical Digest*, 23, No. 1, 58–70, 2002.

Holkar, K. and Waghmare, L. "Sliding Mode Control with Predictive PID Sliding Surface for Improved Performance". *International Journal of Computer Applications*, 78, No. 4, 1–5, 9 2013. doi: 10.5120/13474-0992.

Howell, K. and Gordon, S. "Orbit determination error analysis and a station-keeping strategy for sun-earth L1 libration point orbits". *Journal of The Astronautical Sciences*, 42 207–228, 11 1994.

Howell, K. C. and Pernicka, H. J. "Station-keeping method for libration point trajectories". *Journal of Guidance, Control, and Dynamics*, 16, No. 1, 151–159, 1 1993. doi: 10.2514/3.11440.

Ieva, S., Dotto, E., Mazzotta Epifani, E., Perna, D., Fanasca, C., Lazzarin, M., Bertini, I., Petropoulou, V., Rossi, A., Micheli, M., and Perozzi, E. "Extended photometric survey of near-Earth objects". *Astronomy & Astrophysics*, 644 A23, 12 2020. doi: 10.1051/0004-6361/202038968.

Kaula, W. M. *Theory of Satellite Geodesy*. Blaisdell Publishing Company, Waltham, 1966.

Keeter, T. M. "Station–keeping strategies for libration point orbits: Target point and floquet mode approaches". MSc thesis, Purdue University, 1994.

Khoroshylov, S. and Redka, M. "Deep learning for spacecraft guidance, navigation, and control". *Kosmična nauka ì tehnologìâ*, 27, No. 6, 38–52, 2021. doi: 10.15407/knit2021.06.038.

Kikuchi, S., Tsuda, Y., and Kawaguchi, J. "Delta-V Assisted Periodic Orbits Around Small Bodies". *Journal of Guidance, Control, and Dynamics*, 40, No. 1, 150–163, 1 2017. doi: 10.2514/1.G000696.

Kulkarni, J., Campbell, M., and Dullerud, G. "Stabilization of Spacecraft Flight in Halo Orbits: An H-infinity Approach". *IEEE Transactions on Control Systems Technology*, 14, No. 3, 572–578, 5 2006. doi: 10.1109/TCST.2006.872517.

Lara, M. and Scheeres, D. J. "Stability Bounds for Three-Dimensional Motion Close to Asteroids". *The Journal of the Astronautical Sciences*, 50, No. 4, 389–409, 12 2002. doi: 10.1007/BF03546245.

Lee, K. W. and Singh, S. N. "Adaptive and Supertwisting Adaptive Spacecraft Orbit Control Around Asteroids". *Journal of Aerospace Engineering*, 32, No. 4,, 7 2019a. doi: 10.1061/(ASCE)AS.1943-5525.0001043.

Lee, K. W. and Singh, S. N. "Immersion-and Invariance-Based Adaptive Control of Asteroid-Orbiting and - Hovering Spacecraft". *The Journal of the Astronautical Sciences*, 66, No. 4, 537–553, 12 2019b. doi: 10.1007/s40295-019-00163-6.

Lee, K. W. and Singh, S. N. "Composite Adaptive Spacecraft's Orbit Control and Asteroid's Parameter Estimation by Integral Excitation". In: *AIAA SCITECH 2023 Forum*, Reston, Virginia, 1 2023. American Institute of Aeronautics and Astronautics. doi: 10.2514/6.2023-2169.

Levant, A. "Principles of 2-sliding mode design". *Automatica*, 43, No. 4, 576–586, 4 2007. doi: 10.1016/j.automatica.2006.10.008.

Lissauer, J. J. and de Pater, I. *Fundamental Planetary Science*. Cambridge University Press, 7 2019. doi: 10.1017/9781108304061.

MacMillan, W. D. *The Theory of the Potential*, volume 7. American Chemical Society, 10 1930. doi: 10.1021/ed007p2530.

Mastrodemos, N., Rush, B., Vaughan, D., and Owen, B. "Optical Navigation for the Dawn Mission at Vesta". *Advances in the Astronautical Sciences*, 140 1739–1754, 2011.

Melman, J., Mooij, E., and Noomen, R. "Autonomous navigation at asteroids". In: *60th International Astronautical Congress*, 2009.

Miller, J., Konopliv, A., Antreasian, P., Bordi, J., Chesley, S., Helfrich, C., Owen, W., Wang, T., Williams, B., Yeomans, D., and Scheeres, D. "Determination of Shape, Gravity, and Rotational State of Asteroid 433 Eros". *Icarus*, 155, No. 1, 3–17, 1 2002. doi: 10.1006/icar.2001.6753.

Mooij, E. "On-board constrained optimisation of final rendezvous". Technical note, Delft University of Technology, 2021. University Proprietary.

Morrison, D. "The Spaceguard Survey: Report of the NASA International Near- Earth-Object Detection Workshop". Technical report, Jet Propulsion Laboratory, Pasadena, 1992.

Munuera Vilalta, M. "Asteroid Gravity Field Estimation by a Satellite Constellation". MSc thesis, Delft University of Technology, 2024.

National Research Council. *Exploration of Near Earth Objects*. National Academies Press, Washington, D.C., 5 1998. doi: 10.17226/6106.

Negri, R. B. and de Almeida Prado, A. F. B. "Robust path-following for keplerian orbits". *Journal of the Brazilian Society of Mechanical Sciences and Engineering*, 46, No. 8,, July 2020. doi: 10.1007/s40430-024-05031-5.

Negri, R. B. and de Almeida Prado, A. F. B. "Autonomous and Robust Orbit-Keeping for Small-Body Missions". *Journal of Guidance, Control, and Dynamics*, 45, No. 3, 587–598, 3 2022. doi: 10.2514/1.G005863.

Negri, R. B., de Almeida Prado, A. F. B., Chagas, R. A. J., and Moraes, R. V. "Autonomous Rapid Exploration in Close-Proximity of Asteroids". *Journal of Guidance, Control, and Dynamics*, 47, No. 5, 914–933, 5 2024. doi: 10.2514/1.G007186.

Oguri, K. and Mcmahon, J. W. "SRP-based Orbit Control with Application to Orbit Stationkeeping at Small Bodies". *Advances in the Astronautical Sciences*, 168 2077–2093, 2019.

Oguri, K. and McMahon, J. W. "Robust Spacecraft Guidance Around Small Bodies Under Uncertainty: Stochastic Optimal Control Approach". *Journal of Guidance, Control, and Dynamics*, 44, No. 7, 1295–1313, 7 2021. doi: 10.2514/1.G005426.

Oguri, K., Kakihara, K., Campagnola, S., Ozaki, N., Ohima, K., and Yamaguchi, T. "Equuleus mission analysis: design of the science orbit phase". In: *26th International Symposium on Space Flight Dynamics*, 2017.

Ohman, Y. "The asteroids as possible research objects for future ESRO missions". *European Preparatory Commission for Space Research*, 1963.

Ono, G., Terui, F., Ogawa, N., Kikuchi, S., Mimasu, Y., Yoshikawa, K., Ikeda, H., Takei, Y., Yasuda, S., Matsushima, K., Masuda, T., Saiki, T., and Tsuda, Y. "GNC strategies and flight results of Hayabusa2 first touchdown operation". *Acta Astronautica*, 174 131–147, 9 2020. doi: 10.1016/j.actaastro.2020.04.029.

Parcher, D. W. "Low-Thrust Orbit Transfer Design for DAWN Operations at VESTA". *Advances in the Astronautical Sciences*, 140, 2011.

Pasquale, A., Silvestrini, S., Capannolo, A., Lunghi, P., and Lavagna, M. "Small bodies non-uniform gravity field on-board learning through Hopfield Neural Networks". *Planetary and Space Science*, 212, 3 2022. doi: 10.1016/j.pss.2022.105425.

Phadke, M. S. *Quality Engineering Using Robust Design*. Prentice-Hall, 1989.

Press, W., Teukolsky, S., Vetterling, W., and Flannery, B. *Numerical recipes in FORTRAN. The Art of Scientific Computing*. Cambridge: University Press, 1992.

Pugliatti, M., Piccolo, F., Rizza, A., Franzese, V., and Topputo, F. "The vision-based guidance, navigation, and control system of Hera's Milani CubeSat". *Acta Astronautica*, 210 14–28, 9 2023. doi: 10.1016/j.actaastro.2023.04.047.

Razgus, B. "Relative Navigation in Asteroid Missions". MSc thesis, Delft University of Technology, 2016.

Reimond, S. and Baur, O. "Spheroidal and ellipsoidal harmonic expansions of the gravitational potential of small Solar System bodies. Case study: Comet 67P/Churyumov Gerasimenko". *Journal of Geophysical Research: Planets*, 121, No. 3, 497–515, 3 2016. doi: 10.1002/2015JE004965.

Reuilh, A., Bonneau, C., Bonnamy, O., and Ferri, P. "Rosetta AOCS behaviour in the first years of operations". *IFAC Proceedings Volumes*, 40, No. 7, 383–388, 2007. doi: 10.3182/20070625-5-FR-2916.00066.

Reyhanoglu, M., Kamran, N., and Takahiro, K. "Orbital and Attitude Control of a Spacecraft Around an Asteroid". In: *12th International Conference on Control, Automation and Systems*, pp. 1627–1632, 2012.

Romain, G. and Jean-Pierre, B. "Ellipsoidal Harmonic expansions of the gravitational potential: theory and application". *Celestial Mechanics and Dynamical Astronomy*, 79, No. 4, 235–275, 2001. doi: https://doi.org/10.1023/A:1017555515763.

Root, B., Novák, P., Dirkx, D., Kaban, M., van der Wal, W., and Vermeersen, L. "On a spectral method for forward gravity field modelling". *Journal of Geodynamics*, 97 22–30, 7 2016. doi: 10.1016/j.jog.2016.02.008.

Russell, R. P. "Survey of Spacecraft Trajectory Design in Strongly Perturbed Environments". *Journal of Guidance, Control, and Dynamics*, 35, No. 3, 705–720, 5 2012. doi: 10.2514/1.56813.

Sagliano, M., Mooij, E., and Theil, S. "Adaptive Disturbance-Based High-Order Sliding-Mode Control for Hypersonic-Entry Vehicles". *Journal of Guidance, Control, and Dynamics*, 40, No. 3, 521–536, 3 2017. doi: 10.2514/1.G000675.

Sanchez, J. C., Vazquez, R., Biggs, J. D., and Bernelli-Zazzera, F. "Orbit-Attitude Predictive Control in the Vicinity of Asteroids with In Situ Gravity Estimation". *Journal of Guidance, Control, and Dynamics*, 45, No. 2, 262–279, 2 2022. doi: 10.2514/1.G005572.

Santo, A. G., Lee, S. C., and Gold, R. E. "NEAR Spacecraft and Instrumentation". *The Journal of Astronautical Sciences*, 43 373–397, 1995.

Schaub, H., Vadali, S. R., Junkins, J. L., and Alfriend, K. T. "Spacecraft Formation Flying Control Using Mean Orbit Elements". *The Journal of the Astronautical Sciences*, 48, No. 1, 69–87, 3 2000. doi: 10.1007/BF03546219.

Scheeres, D. "Dynamics about Uniformly Rotating Triaxial Ellipsoids: Applications to Asteroids". *Icarus*, 110, No. 2, 225–238, 8 1994. doi: 10.1006/icar.1994.1118.

Scheeres, D. "The Effect of C22 on Orbit Energy and Angular Momentum". *Celestial Mechanics and Dynamical Astronomy*, 73, No. 1/4, 339–348, 1999. doi: 10.1023/A:1008384021964.

Scheeres, D. "Orbital mechanics about small bodies". *Acta Astronautica*, 72 1–14, 3 2012a. doi: 10.1016/j.actaastro.2011.10.021.

Scheeres, D., Ostro, S., Hudson, R., and Werner, R. "Orbits Close to Asteroid 4769 Castalia". *Icarus*, 121, No. 1, 67–87, 5 1996. doi: 10.1006/icar.1996.0072.

Scheeres, D., Miller, J., and Yeomans, D. "The Orbital Dynamics Environment of 433 Eros: A Case Study for Future Asteroid Missions". *Advances in the Astronautical Sciences*, 109, No. 1, 1017–1038, 10 2002.

Scheeres, D. J. *Orbital Motion in Strongly Perturbed Environments*. Springer Berlin Heidelberg, Berlin, Heidelberg, 2012b. doi: 10.1007/978-3-642-03256-1.

Scheeres, D. J. "Orbit Mechanics About Asteroids and Comets". *Journal of Guidance, Control, and Dynamics*, 35, No. 3, 987–997, 5 2012c. doi: 10.2514/1.57247.

Scheeres, D. J. "Close proximity dynamics and control about asteroids". In: *2014 American Control Conference*, pp. 1584–1598. IEEE, 6 2014.

Scheeres, D. J., Williams, B. G., and Miller, J. K. "Evaluation of the Dynamic Environment of an Asteroid: Applications to 433 Eros". *Journal of Guidance, Control, and Dynamics*, 23, No. 3, 466–475, 5 2000. doi: 10.2514/2.4552.

Scheeres, D. J., Rosengren, A. J., Sutter, B. M., and Rosengren, A. J. "Design, dynamics and stability of the OSIRIS-REx sun-terminator orbits". *Advances in the Astronautical Sciences*, 148 3263–3283, 2013.

Shi, Y., Wang, Y., Misra, A. K., and Xu, S. "Station-Keeping for Periodic Orbits near Strongly Perturbed Binary Asteroid Systems". *Journal of Guidance, Control, and Dynamics*, 43, No. 2, 319–326, 2 2020. doi: 10.2514/1.G004638.

Shirobokov, M., Trofimov, S., and Ovchinnikov, M. "Survey of Station-Keeping Techniques for Libration Point Orbits". *Journal of Guidance, Control, and Dynamics*, 40, No. 5, 1085–1105, 5 2017. doi: 10.2514/1.G001850.

Slotine, J.-J. E. and Li, W. *Applied nonlinear Control*. Prentice Hall, 1991.

Spee, S. J. H. "Asteroid gravity field estimation below the Brillouin sphere". MSc thesis, Delft University of Technology, 2022.

Takahashi, S. and Scheeres, D. J. "Autonomous Exploration of a Small Near-Earth Asteroid". *Journal of Guidance, Control, and Dynamics*, 44, No. 4, 701–718, 4 2021. doi: 10.2514/1.G005733.

Takei, Y., Saiki, T., Yamamoto, Y., Mimasu, Y., Takeuchi, H., Ikeda, H., Ogawa, N., Terui, F., Ono, G., Yoshikawa, K., Takahashi, T., Sawada, H., Hirose, C., Kikuchi, S., Fujii, A., Iwata, T., Nakazawa, S., Hayakawa, M., Tsukizaki, R., Tanaka, S., Matsushita, M., Mori, O., Koda, D., Shimada, T., Ozaki, M., Abe, M., Hosoda, S., Okada, T., Yano, H., Kato, T., Yasuda, S., Matsushima, K., Masuda, T., Yoshikawa, M., and Tsuda, Y. "Hayabusa2's station-keeping operation in the proximity of the asteroid Ryugu". *Astrodynamics*, 4, No. 4, 349–375, 12 2020. doi: 10.1007/s42064-020-0083-8.

Tavakoli, M. and Assadian, N. "Model predictive orbit control of a Low Earth Orbit satellite using Gauss's variational equations". *Proceedings of the Institution of Mechanical Engineers, Part G: Journal of Aerospace Engineering*, 228, No. 13, 2385–2398, 11 2014. doi: 10.1177/0954410013516252.

Tiwari, M., Prazenica, R., and Henderson, T. "Direct adaptive control of spacecraft near asteroids". *Acta Astronautica*, 202 197–213, 1 2023. doi: 10.1016/j.actaastro.2022.10.014.

Trullas, M. "Asteroid Mission Guidance and Control using Dual Quaternions". MSc thesis, Delft University of Technology, 2018.

Vittaldev, V., Mooij, E., and Naeije, M. C. "Unified State Model theory and application in Astrodynamics". *Celestial Mechanics and Dynamical Astronomy*, 112, No. 3, 253–282, 3 2012. doi: 10.1007/s10569-011-9396-5.

Werner, R. and Scheeres, D. "Exterior gravitation of a polyhedron derived and compared with harmonic and mascon gravitation representations of asteroid 4769 Castalia". *Celestial Mechanics and Dynamical Astronomy*, 65, No. 3,, 1997. doi: 10.1007/BF00053511.

Wertz, J. "Autonomous Navigation and Autonomous Orbit Control in Planetary Orbits as a Means of Reducing Operations Cost". In: *5th International Symposium on Reducing the Cost of Spacecraft Ground Systems and Operations*, 2003.

Williams, B., Antreasian, P., Carranza, E., Jackman, C., Leonard, J., Nelson, D., Page, B., Stanbridge, D., Wibben, D., Williams, K., Moreau, M., Berry, K., Getzandanner, K., Liounis, A., Mashiku, A., Highsmith, D., Sutter, B., and Lauretta, D. S. "OSIRIS-REx Flight Dynamics and Navigation Design". *Space Science Reviews*, 214, No. 4, 69, 6 2018. doi: 10.1007/s11214-018-0501-x.

Williams, B. G. "Technical Challenges and Results for Navigation of NEAR Shoemaker". *Johns Hopkins APL Technical Digest*, 23, No. 1,, 2002.

Winkler, T., Hawkins, M., Lyzhoft, J., and Wie, B. "Fuel-Efficient Feedback Control of Orbital Motion Around Irregular-Shaped Asteroids". In: *AIAA Guidance, Navigation and Control Conference*, Ames, 2012. Iowa State University, Digital Repository. doi: 10.31274/etd-180810-3208.

Xie, H. and Bernelli Zazzera, F. "6-DOF Orbit-Attitude Stabilization Around an Asteroid by Using Performance-Based Intermittent Event-Triggered Control". In: *Aerospace Europe Conference 2023 - Joint 10th EUCASS - 9th CEAS Conference*, 2023. doi: 10.13009/eucass2023-027.

Yang, W., Li, S., and Li, N. "Station-keeping control method for GEO satellite based on relative orbit dynamics". In: *Proceeding of the 11th World Congress on Intelligent Control and Automation*, pp. 1682–1687. IEEE, 6 2014. doi: 10.1109/WCICA.2014.7052973.

Yoshikawa, M., Ikeda, H., Yano, H., Saito, J., Kubota, T., Hashimoto, T., Fujiwara, A., Kawaguchi, J., Kominato, T., Matsuoka, M., Shirakawa, K., Ohnishi, T., Abe, S., Mukai, T., Gaskell, R., and Scheeres, D. "Astrodynamics Science About Itokawa, Gravity and Ephemeris". In: *AIAA/AAS Astrodynamics Specialist Conference and Exhibit*, Reston, Virigina, 8 2006. American Institute of Aeronautics and Astronautics. doi: 10.2514/6.2006-6658.

Yu, X., Feng, Y., and Man, Z. "Terminal Sliding Mode Control – An Overview". *IEEE Open Journal of the Industrial Electronics Society*, 2 36–52, 2021. doi: 10.1109/OJIES.2020.3040412.

Zeinali, M. and Notash, L. "Adaptive sliding mode control with uncertainty estimator for robot manipulators". *Mechanism and Machine Theory*, 45, No. 1, 80–90, 1 2010. doi: 10.1016/j.mechmachtheory.2009.08.003.

Zhang, B., Cai, Y., and Wang, C. "Adaptive super-twisting control for orbiting around irregular shape small bodies with input saturation". *Aerospace Science and Technology*, 106 106171, 11 2020. doi: 10.1016/j.ast.2020.106171.

Zhang, P., Ma, T., Zhao, B., Dong, B., and Li, Y. "Robust Linear Quadratic Regulator via Sliding Mode Guidance for Spacecraft Orbiting a Tumbling Asteroid". *Mathematical Problems in Engineering*, 2015 1–11, 2015. doi: 10.1155/2015/947843.

Ziebart, M. "Generalized Analytical Solar Radiation Pressure Modeling Algorithm for Spacecraft of Complex Shape". *Journal of Spacecraft and Rockets*, 41, No. 5, 840–848, 9 2004. doi: 10.2514/1.13097.

A

Research plan

This chapter outlines the structured research plan established to guide and schedule the progression of this research study. Section A.1 provides an in-depth overview of each work package (WP), detailing their objectives, required inputs, expected outputs, and associated tasks. Following this, Sec. A.2 offers a personal evaluation of the thesis progress, reflecting on accomplishments and areas for improvement. Lastly, Sec. A.3 showcases the Gantt chart illustrating the timeline and interdependencies of the WPs.

A.1 Work breakdown structure

This master thesis focuses on the development of a robust orbit control scheme. The objective is to ensure orbit maintenance around asteroid 433 Eros in the presence of navigation, maneuvering, and modeling errors. The research work was planned with a work breakdown structure (WBS) approach, through which 7 main work packages were established.

WP1: Simulator set-up and verification

The initial phase of this research focuses on gaining familiarity with the pre-existing software tool, identifying missing features, implementing them, and verifying their functionality, with particular emphasis on gravity models. Adopting a bottom-up approach, implementation and testing are confined to subsystem level or lower. In practical terms, this means that the individual blocks/functions of the simulator are evaluated independently, without conducting full orbit simulations.

Input: Pre-existent open-loop simulator, GRADS (software and technical notes), gravity models identified during literature study, Eros's properties (physical parameters, SH coefficients, and shape models).

Tasks:

1. Read GRADS technical notes. [1 day]
2. Investigate the open-loop simulator and its structure, identifying the features that need to be modified and those that are missing. [2 days]
3. Modify/implement and verify missing mathematical routines (e.g., rotation matrices, coordinate transformations). [1 day]
4. Implement and verify the Sun-asteroid propagator, such that the location of the asteroid along the orbit is a simulation input. [1 day]
5. Implement and verify Carlson's algorithm for elliptic integrals. [2 days]
6. Implement and verify the triaxial ellipsoid gravity model using MacMillan formulation. [2 days]
7. Execute acceptance tests for the SH gravity function. [1 day]

8. Execute acceptance tests for the polyhedron gravity function. [2 days]
9. Write the results from this package on the report. [3 days]

Expected outcome: Verified environment block; verification results reported.
Pauses: None.
Duration: 3 weeks (end date 17 May).

Esa Academy Training Course: 20-24 May, 1 week

WP2: Environment modeling and open-loop testing

This work package entails running open-loop orbit simulations. The main purpose is to determine the settings for the high-fidelity dynamical environment by assessing different gravity models; in second place, open-loop solutions are also useful to infer realistic requirements for the orbit control system.

Input: Simulink blocks for SH and polyhedron gravity models, updated simulator from previous work package.

Tasks:

1. Perform a brief integrator study. [1 day]
2. Choose and implement termination settings. [1 day]
3. Assess different sets of SH coefficients. [1 day]
4. Assess different shape models for the polyhedron gravity. [1 day]
5. Compare the available gravity models (SH and polyhedron) to determine the high-fidelity settings. [3 days]
6. Post-process and analyze open-loop MC simulations for orbits with random initial Kepler elements. [3 days]
7. Write on the report the results of this work package. [2 days]
8. Buffer. [3 days]

Expected outcome: Settings for high-fidelity model and integrator; A first batch of results concerning open-loop trajectories around Eros.
Pauses: None.
Duration: 3 weeks (end date 14 June).

WP3: Onboard computer design

The purpose of this work package is to transform the software architecture from an open-loop to a closed-loop simulator by implementing the onboard computer Simulink block.

Input: Open-loop simulator, Cartesian to Keplerian conversion routines.

Tasks:

1. Define uncertainties and implement them in such a way that they can be easily included or excluded from the simulations while ensuring reproducibility. [2 days]
2. Implement the onboard propagator. [2 days]
3. Implement the mission manager block with chaser-target approach. [2 days]
4. Design a sliding mode controller for a simpler problem. [1 day]
5. Implement SMC within the onboard computer. [3 days]
6. Write results on report. [2 days]

7. Buffer. [3 days]

Expected outcome: Closed-loop simulator, additional part of software chapter written down.
Pauses: None.
Duration: 3 weeks (end date 5 July).

Alpbach Summer School: 8-19 July, 2 weeks.

WP4: Continuous control

This work package aims to perform a parametric study of the SMC to choose adequate control gains. Realistic errors and operational constraints are not considered, and control is applied continuously to the dynamics.

Input: Closed-loop simulator, SMC theory.

Tasks:

1. Define performance parameters and identify adequate scenarios for testing. [1 day]
2. Parametric study of SMC controller. [1 day]
3. Implement a time-varying boundary layer. [2 days]
4. Parametric study of the TVBL controller. [2 days]
5. Comparison and analysis. [2 days]
6. Write results on report. [2 days]
7. **Mid-term review** (01/08/2024)

Expected outcome: Tuned SMC controller; results for continuous control.
Pauses: None.
Duration: 2 weeks (end date 2 August).

Holidays: 5-23 August (3 weeks).

Buffer: 26-30 August (1 week).

WP5: Impulsive control

In this work package, the main objective is to introduce a quantization logic that allows to perform station-keeping with impulsive (on/off) maneuvers. Furthermore, an effort is made to improve the reference trajectory generation approach. Realistic errors and constraints are introduced, and Monte Carlo simulations are run for the identified orbit maintenance scenarios.

Input: SMC controller, onboard environment models.

Tasks:

1. Design an adequate thrust quantization scheme. [5 days]
2. Implement algorithm for minimum distance to an ellipse. [1 day]
3. Implement line-of-sight guidance. [1 day]
4. Implement setup for Monte Carlo simulations. [1 day]
5. Post-process and analyze Monte Carlo results for identified orbit scenarios. [2 days]
6. Write results on report. [2 days]
7. Buffer. [3 days]

Expected outcome: Orbit control scheme with baseline parameters; comparison results between line-of-sight and chaser-target tracking modes.
Pauses: None.
Duration: 3 weeks (end date 20 September).

WP6: Robust analysis and design

This work package employs Robust Design principles to improve the orbit control system performance and study how it is affected by the choice of given design variables. The analysis is extended by considering additional small bodies and comparing the performance of the control system with the target point approach.

Input: Impulsive orbit control scheme with nominal parameters, line-of-sight guidance formulation, theory on TPA, Robust Design principles, and orthogonal arrays.

Tasks:

1. Conduct a preliminary design space study, identifying decision variables of interest and their range. [3 days]
2. Choose and implement an adequate experiment matrix. [1 day]
3. Perform ANOVA for the control variables. [2 days]
4. Identify optimal factor levels. [2 days]
5. Do a comparison between the optimal and the refined control system. [2 days]
6. Investigate the mission design space (target inclination). [3 days]
7. Investigate the mission design space (target eccentricity). [1 day]
8. Do a knowledge analysis for different onboard propagation models. [2 days]
9. Add new asteroids to the simulator. [1 day]
10. Run station-keeping simulations on the new asteroids. [3 days]
11. Implement variational equations propagator. [1 day]
12. Implement targets point controller. [1 day]
13. Compare SMC with TPA. [1 day]
14. Buffer. [2 days]
15. Write results on report. [5 days]

Expected outcome: finalized orbit control scheme; robust analysis results; comparison results with TPA.
Pauses: None.
Duration: 5 weeks (end date 1 November)

WP7: Finalization

This work package concludes the research work. The main purpose is to finalize the structure and content of the report.

Input: Advanced thesis draft and results generated from previous work packages.

Tasks:

1. Write conclusions and recommendations based on results. [3 days]
2. Improve report layout. [2 days]
3. Proofread the report. [3 days]

4. Consistency check bibliography. [2 days]
5. **Green light review** (15/11/2024)
6. Implement feedback. [10 days]
7. Prepare presentation. [10 days]
8. **Thesis defense** (13/12/2024)

Duration: 6 weeks (end date 13 December).

A.2 Reflection

At the end of this research work, it is valuable to reflect on the adequacy of the original research plan, highlighting how the project's nature has evolved over time and the subsequent impact on the planned schedule.

Overall, the research plan formulated at the conclusion of the literature study proved well-designed and effective up to the Mid-term Review. Indeed, the first four work packages were successfully completed by the end of July, which allowed to stop the work for the summer break with a fully verified simulator and a tuned controller. However, the original schedule required substantial revision at the beginning of September, as the effort needed to design a mechanism for transitioning from continuous to impulsive control (WP5) had been substantially underestimated and ultimately posed greater challenges than anticipated. Furthermore, it is relevant to mention that the original plan aimed to explore more advanced control methods and compare them with first-order sliding mode control theory. However, following a careful review of the requirements and research questions in early September, it was decided to shift the focus of the project towards a thorough robustness analysis of the designed system rather than a comparison between different approaches. Consequently, a new work package (WP6) was introduced and successfully executed.

Further observations can be made regarding the parallel management of reporting and design/implementation tasks. Although each work package allocated its final days to documenting the results, reporting tasks were often delayed until the end of the project due to challenges in finalizing decisions. In contrast, it is highlighted that maintaining a personal log to record ideas and reflections throughout the project proved highly effective and beneficial for thesis writing and meeting preparations. Finally, the inclusion of buffer periods within the project timeline (as shown in Figs. A.1 and A.2) was generally well-balanced. Specifically, the one-week buffer at the end of August proved critical for reassessing the project's direction and refining its primary objectives.

A.3 Gantt chart

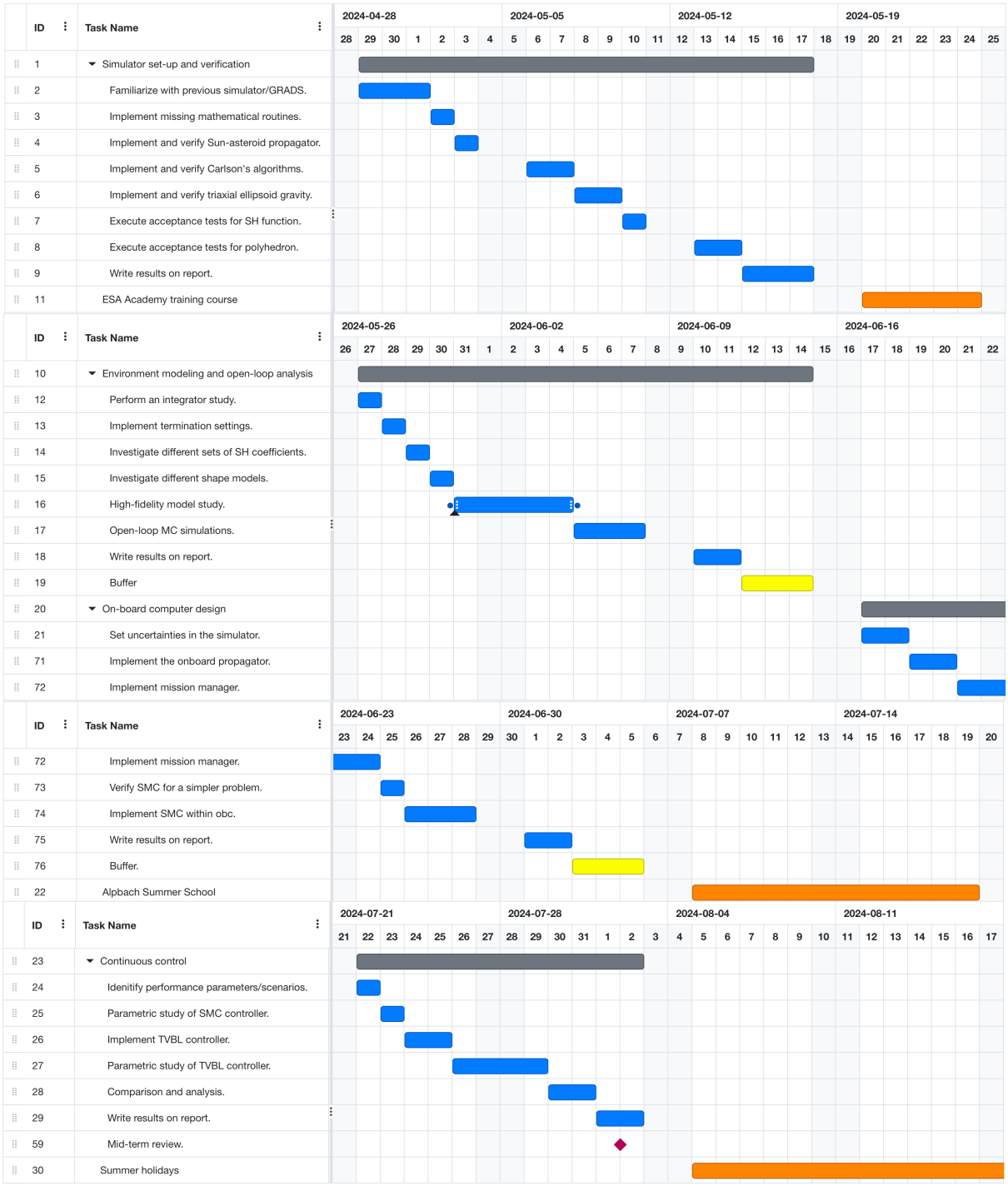

Figure A.1: Gantt chart up to the Mid-term Review: work packages are shown in gray, tasks in blue, pauses in orange, buffers in yellow, and milestones in purple.

Figure A.2: Gantt chart after the Mid-term Review: work packages are shown in gray, tasks in blue, pauses in orange, buffers in yellow, and milestones in purple.

B

Elliptic integrals

The gravity potential for a uniform-density triaxial ellipsoid (as represented in Fig. B.1) at exterior points can be computed according to Eq. (3.33). For illustration purposes, this is reformulated hereafter as follows:

$$\mathcal{U}(\boldsymbol{r}) = -\frac{3\mu}{4}\int_{\xi(\boldsymbol{r})}^{\infty}\phi(\boldsymbol{r},u)\frac{du}{\Delta u} \tag{B.1}$$

$$\phi(\boldsymbol{r},u) = \frac{x^2}{a^2+u}+\frac{y^2}{b^2+u}+\frac{z^2}{c^2+u}-1 \tag{B.2}$$

$$\Delta u = \sqrt{(a^2+u)(b^2+u)(c^2+u)} \tag{B.3}$$

where x, y, and z refer to a body-fixed coordinate system in the ellipsoid such that the x-axis lies along the largest dimension, the y-axis along the intermediate, and the z-axis along the smallest. The scalar ξ is solved for $\phi(\boldsymbol{r},\xi) = 0$, which identifies the ellipsoid passing through x, y and z and confocal to the body's ellipsoid. Whenever $\phi(\boldsymbol{r},0) > 0$, this results in a cubic equation with only one positive root ξ (Scheeres, 1994). Conversely, if $\phi(\boldsymbol{r},0) \leq 0$, the point at stake lies either on the body's surface or inside, and $\xi = 0$. Therefore, the ellipsoid's potential is valid both at the exterior and interior of the body, provided in this latter case ξ is set to zero.

Assuming $a > b > c$, MacMillan (1930) showed that Eq. (B.1) can be reformulated in terms of incomplete elliptic integrals of the first and second kind. Introducing the following parameters:

$$k^2 = \frac{a^2-c^2}{a^2-b^2} \tag{B.4}$$

$$\varphi = \arcsin\sqrt{\frac{a^2-c^2}{a^2+\xi}} \tag{B.5}$$

the potential can be expressed as:

$$\begin{aligned}\mathcal{U} = \frac{3\mu}{4}\frac{2}{\sqrt{a^2-c^2}}\Bigg\{&\left(1-\frac{x^2}{a^2-b^2}+\frac{y^2}{a^2-b^2}\right)F(\omega_\xi,k)\\ &+\left[\frac{x^2}{a^2-b^2}-\frac{\left(a^2-c^2\right)y^2}{\left(a^2-b^2\right)\left(b^2-c^2\right)}+\frac{z^2}{b^2-c^2}\right]E(\omega_\xi,k)\\ &+\left[\frac{c^2+\kappa}{b^2-c^2}y^2-\frac{b^2+\kappa}{b^2-c^2}z^2\right]\frac{\sqrt{a^2-c^2}}{\sqrt{\left(a^2+\kappa\right)\left(b^2+\kappa\right)\left(c^2+\kappa\right)}}\Bigg\}\end{aligned} \tag{B.6}$$

$F(\omega_\xi, k)$ and $E(\omega_\xi, k)$ are incomplete elliptic integrals of the first and second kind, respectively. Specifically, they can be expressed in their Legendre form as:

$$F(\omega_\xi, k) = \int_0^{\omega_\xi} \frac{d\varphi}{\sqrt{1 - k^2 \sin^2 \varphi}} \tag{B.7}$$

$$E(\omega_\xi, k) = \int_0^{\omega_\xi} \sqrt{1 - k^2 \sin^2 \varphi} d\varphi \tag{B.8}$$

As noted by MacMillan, the derivative of the potential with respect to ξ vanishes, therefore it is not necessary to regard ξ as a function of x, y, and z when computing the acceleration as $\nabla \mathcal{U}$. Thus, the components of the gravitational acceleration in a reference frame rotating with the asteroid are:

$$a_x = \frac{3\mu}{4} \frac{2}{\sqrt{a^2 - c^2}} \frac{2x}{a^2 - b^2} (E(\omega_\xi, k) - F(\omega_\xi, k)) \tag{B.9}$$

$$\begin{aligned} a_y = \frac{3\mu}{4} \frac{2}{\sqrt{a^2 - c^2}} \Bigg[& \frac{2y}{a^2 - b^2} F(\omega_\xi, k) + \frac{2(a^2 - c^2)y}{(a^2 - b^2)(b^2 - c^2)} E(\omega_\xi, k) \\ & + \left(2 \frac{c^2 + \xi}{b^2 - c^2} y \right) \frac{\sqrt{a^2 - c^2}}{\sqrt{(a^2 + \kappa)(b^2 + \kappa)(c^2 + \kappa)}} \Bigg] \end{aligned} \tag{B.10}$$

$$a_z = \frac{3\mu}{4} \frac{2}{\sqrt{a^2 - c^2}} \left[\frac{2z}{b^2 - c^2} E(\omega_\xi, k) - \frac{2\left(b^2 + \xi\right) z}{b^2 - c^2} \frac{\sqrt{a^2 - c^2}}{\sqrt{(a^2 + \kappa)(b^2 + \kappa)(c^2 + \kappa)}} \right] \tag{B.11}$$

Matlab provides the built-in functions[1] *ellipticF* and *ellipticE*, which allow to compute first- and second-kind elliptic integrals. However, these numerical routines are relatively slow and computationally inefficient. To show the attractiveness of this gravity field model for onboard applications, an alternative to the Legendre form of elliptic integrals has been considered. In fact, these latter can be also expressed in the Carlson form as (Press et al., 1992):

$$R_F(x, y, z) = \frac{1}{2} \int_0^\infty [(u + x)(u + y)(u + z)]^{-\frac{1}{2}} du \tag{B.12}$$

$$R_D(x, y, z) = \frac{3}{2} \int_0^\infty [(u + x)(u + y)]^{-\frac{1}{2}} (u + z)^{-\frac{3}{2}} du \tag{B.13}$$

where the variables x, y, and z are non-negative and at most one is zero. Based exclusively on rational operations and square roots, Carlson illustrated fast, robust numerical procedures based on the duplication theorem which can be used to compute the above expressions. For conciseness, the implemented version of these algorithms is not reported, but the interested reader can refer to Carlson (1979) for further insight. The Carlson's elliptic integrals can then be related to the Legendre form by the following relations:

$$F(\varphi, k) = \sin \varphi R_F \left(\cos^2 \varphi, 1 - k^2 \sin^2 \varphi, 1 \right) \tag{B.14}$$

$$E(\varphi, k) = \sin \varphi R_F \left(\cos^2 \varphi, 1 - k^2 \sin^2 \varphi, 1 \right) - \frac{1}{3} k^2 \sin^3 \varphi R_D \left(\cos^2 \varphi, 1 - k^2 \sin^2 \varphi, 1 \right) \tag{B.15}$$

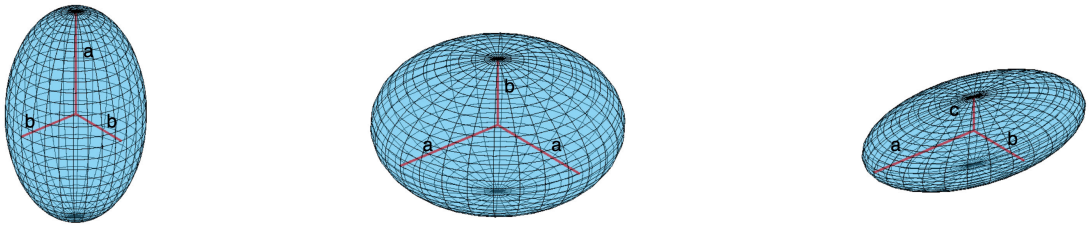

Figure B.1: Reference geometries: prolate spheroid (left), oblate spheroid (center), and triaxial ellipsoid (right).

[1] `https://nl.mathworks.com/help/symbolic/sym.ellipticf.html`, accessed on 8/05/2024.

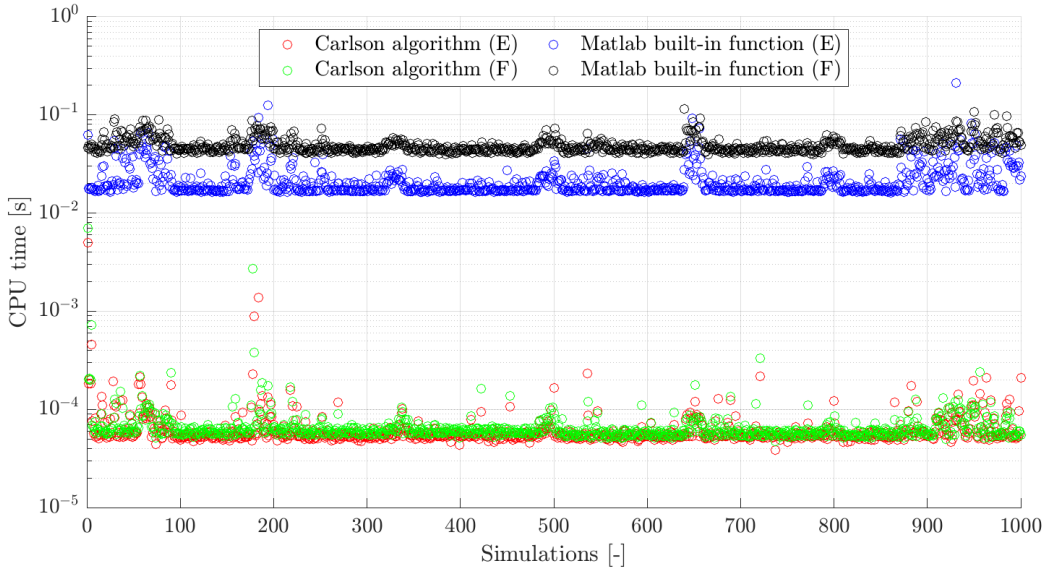

Figure B.2: Computational time required to evaluate random elliptic integrals using different algorithms.

The implemented algorithm has been tested over a batch of 1000 simulations and compared to the Matlab built-in functions. The results, displayed in Fig. B.2, show that Carlson's formulation is faster by approximately two/three orders of magnitude. In both cases, ξ was obtained by solving numerically $\phi(\boldsymbol{r}, \xi) = 0$ with a Newton method (attention needs to be paid to prevent the method from converging to one of the non-positive roots).

As a final note, it is mentioned that the reported formulation for the gravity potential and the corresponding gravity accelerations are formally not valid if two (or three) of the semi-axes are identical (a zero would appear at the denominator). In these cases, Eq. (B.1) can be still reformulated in terms of elliptic integrals but with a simpler expression. However, this was not implemented, therefore slightly different semi-axes were used to model Eros's short sides (or the sphere, during the verification test).

C

Orthogonal arrays

In this appendix, the full L_{27} orthogonal array used in Sec. 7.2.1 is reported. As visible in Table C.1, this matrix can host up to thirteen factors, varied over three levels, for 27 experiments in total. Furthermore, the corresponding interaction table is displayed in Table C.2. Given that the L_{27} array presents three levels per factor, each factor has two degrees of freedom, and each interaction has four degrees of freedom. Therefore, to avoid confounding, two three-level columns have to be kept empty, in contrast to only one needed for two-level orthogonal arrays. In particular, it has been highlighted that with a L_{27} array, the interaction A$\times$B confounds with the main effects of C and D. As a consequence, columns three and four have to be left empty. It can be verified that if this procedure is repeated for the other (four) factors, it will lead to leaving columns 3,4,6,7,8,9,10,11, and 13 empty.

Table C.1: L_{27} Taguchi array (Phadke, 1989).

Factor → **Experiment ↓**	**A**	**B**	**C**	**D**	**E**	**F**	**G**	**H**	**I**	**J**	**K**	**L**	**M**
1	-1	-1	-1	-1	-1	-1	-1	-1	-1	-1	-1	-1	-1
2	-1	-1	-1	-1	0	0	0	0	0	0	0	0	0
3	-1	-1	-1	-1	1	1	1	1	1	1	1	1	1
4	-1	0	0	0	-1	-1	-1	0	0	0	1	1	1
5	-1	0	0	0	0	0	0	1	1	1	-1	-1	-1
6	-1	0	0	0	1	1	1	-1	-1	-1	0	0	0
7	-1	1	1	1	-1	-1	-1	1	0	1	0	0	0
8	-1	1	1	1	0	0	0	-1	-1	-1	1	1	1
9	-1	1	1	1	1	1	1	0	0	0	-1	-1	-1
10	0	-1	0	1	-1	0	1	-1	0	1	-1	0	1
11	0	-1	0	1	0	1	-1	0	1	-1	0	1	-1
12	0	-1	0	1	1	-1	0	1	-1	0	1	-1	0
13	0	0	1	-1	-1	0	1	0	1	-1	1	-1	0
14	0	0	1	-1	0	1	-1	1	-1	0	-1	0	1
15	0	0	1	-1	1	-1	0	-1	0	1	0	1	-1
16	0	1	-1	0	-1	0	1	1	-1	0	0	1	-1
17	0	1	-1	0	0	1	-1	-1	0	1	1	-1	0
18	0	1	-1	0	1	-1	0	0	1	-1	-1	0	1
19	1	-1	1	0	-1	1	0	-1	1	0	-1	1	0
20	1	-1	1	0	0	-1	1	0	-1	1	0	-1	1
21	1	-1	1	0	1	0	-1	1	0	-1	1	0	-1
22	1	0	-1	1	-1	1	0	0	-1	1	1	0	-1
23	1	0	-1	1	0	-1	1	1	0	-1	-1	1	0
24	1	0	-1	1	1	0	-1	-1	1	0	0	-1	1
25	1	1	0	-1	-1	1	0	1	0	-1	0	-1	1
26	1	1	0	-1	0	-1	1	-1	1	0	1	0	-1
27	1	1	0	-1	1	0	-1	0	-1	1	-1	1	0

Table C.2: Interaction table for L_{27} array (Phadke, 1989).

Column	1	2	3	4	5	6	7	8	9	10	11	12	13
1	(1)	3,4	2,4	2,3	6,7	5,7	5,6	9,10	8,10	8,9	12,13	11,13	11,12
2		(2)	1,4	1,3	8,11	9,12	10,13	5,11	6,12	7,13	5,8	6,9	7,10
3			(3)	1,2	9,13	10,11	8,12	7,12	5,13	6,11	6,10	7,8	5,9
4				(4)	10,12	8,13	9,11	6,13	7,11	5,12	7,9	5,10	6,8
5					(5)	1,7	1,6	2,11	3,13	4,12	2,8	4,10	3,9
6						(6)	1,5	4,13	2,12	3,11	3,10	2,9	4,8
7							(7)	3,12	4,11	2,13	4,9	3,8	2,10
8								(8)	1,10	1,9	2,5	3,7	4,6
9									(9)	1,8	4,7	2,6	3,5
10										(10)	3,6	4,5	2,7
11											(11)	1,13	1,12
12												(12)	1,11
13													(13)